

---

CZECH TECHNICAL UNIVERSITY IN PRAGUE  
FACULTY OF MECHANICAL ENGINEERING

Habilitation Thesis

Experimental Research of Advanced  
Combustion Modes and Fuels in Internal  
Combustion Engines

Ing. Jiří Vávra, Ph.D.

2021

Prague

---



# Abstract

This work summarizes the knowledge acquired in several combustion engine research laboratories, within various research projects in the field of advanced combustion in spark ignition engines.

The first part will present studies on homogeneous charge compression ignition (HCCI), that has received much attention in recent years due to its ability to reduce both fuel consumption and NO emissions compared to normal spark-ignited (SI) combustion. However, due to the limited operating range of HCCI production feasible engines will need to employ a combination of combustion strategies, such as stoichiometric SI combustion at high loads and leaner burn spark-assisted compression ignition (SACI) and HCCI at intermediate and low loads. The goals of the first two studies were to extend the high load limit of HCCI into the SACI region while maintaining a stoichiometric equivalence ratio. Experiments were conducted on a gasoline-fueled single-cylinder research engine with fully flexible valve actuation. Attention was also given to a comparison of various methods for knock identification and quantification in various combustion modes.

The second part presents the experimental and simulation research of an advanced combustion system for a gas engine with indirect ignition using in-house developed actively scavenged prechamber. The concept was adopted from large stationary engines and was designed and optimized to fit the engine for a light duty truck. The work was initiated as an experimental work. However, during the project, it became obvious that a deeper insight into a complex flow and combustion process was needed. Therefore, a CFD simulation has been implemented into the process. In the first stage, the work was focused on the prechamber flow characterization using the CFD without the combustion process. The other two parts then involved a full engine working cycle simulation with a state-of-the-art combustion modeling and LES approach in CFD. Two design variants of the prechamber with different geometries and volume were analyzed.

The final part describes an investigation of a low temperature combustion of hydrogen in the internal combustion engine. A hydrogen fueled experimental single cylinder engine was tested in a steady state operation on an engine test bed. The engine was operated in a low-temperature combustion mode with a lean mixture with high air excess ratio  $\lambda$  between 2.6 and 3.0. without any irregular combustion phenomena. A high boost was necessary for achieving sufficient power density at the lean burn mode. The engine reached a high thermal efficiency. Molar fraction of NOx below 10 ppm was achieved within the whole range of operational points. Which means, that the low-temperature combustion showed a potential to comply with contemporary as well as future limits of NOx emission without any exhaust gas aftertreatment. Specific emission of  $CO_2$  even involving the  $CO_2$  inflow with

intake air was lowered by 2 to 3 orders of magnitude compared to state-of-the-art automotive diesel engines. Emission of other gaseous pollutants as well as emission of particulate matter were negligible.



# Acknowledgment

*At the first place I would like to thank my dear colleague and friend Professor Ing. Michal Takáts CSc. for his support, exceeding professional matters, Professor Ing. Jan Macek, DrSc. for his leadership, great management, and strategical thinking, the engine lab colleagues Ing. Zbyněk Syrovátka, Ing. Ivan Bortel and Ing. Miloš Emrich, Ph.D., docent Ing. Oldřich Vitek, Ph.D. and Ing. Vít Doleček, Ph.D. for their great support in CFD simulations, to Profesor Michal Vojtíšek, Ph.D. for consultations in the emission analysis and Dr. Marcel Diviš for many consultations. I would like to thank to all of my colleagues from the Department of Automotive Engineering and two engine laboratories for a friendly and inspiring environment.*

*Many thanks to my colleagues from the Autolab at the College of Engineering at the University of Michigan in Ann Arbor for a great cooperation during my research stay in the years 2010-2011. Many thanks to Dr. Stanislav Bohac, professor Dennis Assanis, Dr. George Lavoie, Dr. Jason Martz and Ph.D. students Laura Olesky and Stefan Klinkert.*

*I would like to thank my family for love, support, and patience.*



# List od Research Projects

This work has been realized with support by the following projects:

- Fulbright Commission, 2010
- DOE-EE0000203, “A University Consortium on Efficient and Clean High Pressure Lean Burn (HPLB) Engines.”, the U.S. Department of Energy, 2010-2011
- TE01020020 Josef Božek Competence Centre of Automotive Industry, Technology Agency of the Czech Republic, 2012-2018
- Project #CZ.1.05/2.1.00/03.0125 Acquisition of Technology for Vehicle Center of Sustainable Mobility, EU Regional Development Fund in OP R&D for Innovations (OP VaVpI) and Ministry for Education, Youth and Sports, Czech Republic, 2015
- Project #LO1311 Development of Vehicle Centre for Sustainable Mobility. The Ministry of Education, Youth and Sports program NPU I (LO), 2014-2019
- TG02010033, InovaFOND Gama, Subproject: Spark Ignition Gas Engine with an Advanced Combustion System, Technology Agency of the Czech Republic, 2017-2019
- TN01000026 National Competence Centre for a Surface Transport, Technology Agency of the Czech Republic, 2019-2020



# Contents

<b>Table of Contents</b>	<b>i</b>
<b>List of tables</b>	<b>vii</b>
<b>List of Figures</b>	<b>xv</b>
<b>Symbols and Abbreviations</b>	<b>xvii</b>
<b>1 Introduction</b>	<b>3</b>
1.1 Motivation for low temperature combustion . . . . .	3
1.1.1 Environment and climatic change . . . . .	3
1.2 Introduction of low temperature combustion in spark ignition engines	5
<b>2 Bridging the Gap between HCCI and SI: Spark-Assisted Compression Ignition</b>	<b>9</b>
2.1 Experimental Setup . . . . .	11
2.2 FFVA SYSTEM . . . . .	12
2.3 FUEL AND AIR . . . . .	14
2.4 ENGINE CONTROL AND MEASUREMENT . . . . .	15
2.5 EXPERIMENTAL PROCEDURE AND DATA ANALYSIS . . . . .	16
2.6 RESULTS AND DISCUSSION . . . . .	19
2.6.1 HCCI OPERATING REGIME . . . . .	19
2.6.2 THE SACI REGIME . . . . .	20
2.7 CONCLUSIONS . . . . .	33
<b>3 Knock In Various Combustion Modes in a Gasoline-Fueled Automotive Engine</b>	<b>35</b>
3.1 INTRODUCTION . . . . .	35
3.2 EXPERIMENTAL SETUP . . . . .	37
3.3 HCCI AND SI KNOCK . . . . .	39
3.4 KNOCK QUANTIFICATION METHODS . . . . .	40
3.5 RESULTS . . . . .	44

3.6	DISCUSSION . . . . .	50
3.7	SUMMARY AND CONCLUSION . . . . .	51
<b>4</b>	<b>Scavenged Pre-chamber on a Gas Engine for Light Duty Truck</b>	<b>53</b>
4.1	INTRODUCTION . . . . .	54
4.2	EXPERIMENTAL SETUP . . . . .	55
4.2.1	Experimental procedures and evaluation methods . . . . .	59
4.3	INITIAL TESTS – LIMIT SEARCH . . . . .	61
4.4	PRE-CHAMBER GEOMETRY VARIANTS . . . . .	62
4.5	HEAT RELEASE ANALYSIS RESULTS . . . . .	64
4.5.1	IMPACT OF PRE-CHAMBER FUEL RATE . . . . .	64
4.5.2	IMPACT OF IGNITION TIMING . . . . .	66
4.6	COMPARISON WITH SI ENGINE . . . . .	67
4.7	CONCLUSIONS . . . . .	68
<b>5</b>	<b>Analysis of Scavenged Pre-Chamber for Light Duty Truck Gas En-</b>	
	<b>gine</b>	<b>71</b>
5.1	Introduction . . . . .	72
5.2	Experimental Setup . . . . .	74
5.3	Pre-Chamber Design . . . . .	74
5.4	Experimental Procedures . . . . .	75
5.5	A GT-Power Model . . . . .	76
5.6	A CFD Model . . . . .	76
5.7	Simulation Results . . . . .	78
5.7.1	Pre-Chamber Scavenging . . . . .	81
5.8	Discussion . . . . .	90
5.9	Conclusions . . . . .	91
<b>6</b>	<b>Development of a Pre-chamber Ignition System for Light Duty</b>	
	<b>Truck Engine</b>	<b>93</b>
6.1	Experimental Setup . . . . .	94
6.2	Measurement Results . . . . .	94
6.3	1-D Flow Model for Boundary Conditions Generation . . . . .	96
6.4	CFD Model of Pre-Chamber Engine . . . . .	97
6.5	CFD Model Results . . . . .	103
6.6	Summary and Conclusions . . . . .	108
<b>7</b>	<b>Scavenged Pre-Chamber Volume Effect on Gas Engine Perfor-</b>	
	<b>mance and Emissions</b>	<b>111</b>
7.1	Experimental Setup and Procedures . . . . .	111
7.2	Mathematical Model . . . . .	115

7.3	Experimental Results . . . . .	117
7.4	Simulation Results . . . . .	127
7.5	Summary and Conclusions . . . . .	134
<b>8</b>	<b>Use of Hydrogen in a Combustion Engine with Advanced Combustion</b>	<b>137</b>
8.1	INTRODUCTION . . . . .	137
8.2	Experimental setup . . . . .	140
8.3	Methodology of experiments . . . . .	143
8.4	Experimental results . . . . .	143
8.5	Conclusions . . . . .	148
<b>9</b>	<b>Summary and Conclusions of the Thesis</b>	<b>151</b>
	<b>References</b>	<b>157</b>
	<b>Annexes</b>	<b>169</b>
A	UM-FFVA Engine . . . . .	169
B	Fuel supply into the pre-chamber . . . . .	170
C	Heat release analysis results for various Lambda values . . . . .	171
D	Results of natural gas composition analysis . . . . .	172
E	Scheme of the GT-power model . . . . .	173
F	Measured traces of ignition energy . . . . .	174
G	CFD Results . . . . .	175
H	Basic properties of various fuels . . . . .	181





# List of Tables

2.1	FFVA engine geometry. . . . .	11
2.2	Hydraulic valvetrain specifications. . . . .	13
2.3	Fuel specifications. . . . .	14
2.4	Experimental conditions during HCCI operation. . . . .	17
2.5	Experimental conditions during load extension (SACI mode). . . . .	18
4.1	Main engine parameters in original SI arrangement. . . . .	56
4.2	Tested variants of the pre-chamber geometry. . . . .	59
5.1	Pre-chamber heat release. . . . .	85
7.1	Main pre-chambers parameters. . . . .	114
7.2	Table 3. Main mesh parameters . . . . .	117
7.3	Pre-chamber heat release . . . . .	119
8.1	Basic parameters of the ŠKODA single cylinder research engine. . . .	141
I	Results of natural gas composition analysis using gas chromatograph HP 6980. . . . .	172
II	Basic properties of various fuels. * Composition determined by labo- ratory analysis. . . . .	181



# List of Figures

1.1	$CO_2$ emission reduction by gradual application of technical measures in the development of a natural gas fueled van [23] . . . . .	5
1.2	Energy and emission parameters of a gas spark ignition engine in low load mode depending on the dilution of the mixture. Colored dots correspond to exhaust gas recirculation dilution, marks without filling correspond to lean burn concept [86]. . . . .	6
2.1	FFVA engine schematic. . . . .	12
2.2	Example of a recompression valve strategy with a high degree of negative valve overlap (NVO). . . . .	13
2.3	The usable HCCI operating regime, (a) load vs. degree of NVO for various fueling rates (7-11.5 mg/cycle), and (b) load vs. combustion timing (CA50). . . . .	20
2.4	The effect of spark timing on (a) cylinder pressure, (b) cylinder temperature, and (c) apparent heat release rate at $\sim 5$ bar NMEP ( $\sim 16$ mg/cycle fueling rate). . . . .	21
2.5	The effect of spark timing on combustion characteristics including (a) CA10, CA50, and CA90, (b) NOx emissions, (c) ringing intensity. . .	22
2.6	The effect of spark timing on fuel economy, (a) NMEP vs. spark advance and (b) NSFC vs. spark advance. . . . .	23
2.7	Valve strategy for extending the high load limit (arrows indicate increasing load). . . . .	24
2.8	Control strategy for load extension at constant CA50, (a) required external and internal EGR percentages as load increased, (b) required spark advance as load increased. . . . .	25
2.9	The effect of increasing NMEP (using spark, external and internal EGR) on (a) cylinder pressure, (b) apparent heat release rate, and (c) cylinder temperature. . . . .	26
2.10	Combustion characteristics with increasing NMEP, including (a) CA10, CA50, and CA90, (b) ringing intensity, (c) NOx emissions. . .	27
2.11	The regions of HCCI and SACI combustion. . . . .	28

2.12	End-gas knock/unstable behavior for high load SACI (7.3 bar NMEP, CA50 10dATDC) – 200 consecutive cycles of cylinder pressure data.	29
2.13	Changes in residual gas content within the SACI regime as load is increased, including (a) NVO (deg), (b) internal EGR fraction, (c) external EGR fraction, and (d) phi prime ( $\phi'$ ).	30
2.14	Combustion characteristics in the SACI regime, including (a) ringing intensity ( $MW/m^2$ ), (b) COV of NMEP (%), and (c) EI-NOx (g/kg-fuel).	31
2.15	Efficiency characteristics in the SACI regime, including (a) NSFC (g/kW-hr) and (b) PMEP (kPa).	32
3.1	Conceptual model study results: pathways from low to high load using advanced combustion at naturally aspirated conditions.	36
3.2	Experimental study results [52] NSFC and NOx emission index vs. engine load for optimum combustion phasing points at various combustion modes.	37
3.3	Position of the spark plug, injector, valves and cylinder pressure transducer in the engine head.	38
3.4	HCCI “volumetric” knock at 3.7 bar NMEP (left), SI “end gas” knock at 7.1 bar NMEP (right).	39
3.5	Cycle-cycle FFT analysis of high pass cylinder pressure data for knock at HCCI 3.7 bar NMEP (left), and SI 7.1 bar NMEP (right).	40
3.6	“U filter” (left) and “A filter” characteristics (right).	44
3.7	a) negative valve overlap, b) fuelling rate, c) fuel to charge equivalence ratio $\phi'$ and d) peak rate of pressure rise vs. engine load. SI point denoted by single unconnected filled square.	45
3.8	SACI points a) Measured cylinder pressure traces and measured valve lift profiles over a crank angle, b) rate of heat release vs. Crank angle.	46
3.9	High pass ringing intensity (left) as a function of engine load for three combustion modes and standard deviations of ringing intensity (right).	47
3.10	Probability distribution of a) high pass ringing intensity, b) low pass ringing intensity.	48
3.11	Probability distribution of combustion noise for three combustion modes.	49
3.12	Average Low Pass, High Pass Ringing Intensities and Combustion Noise vs. load. SI point denoted by single unconnected filled square.	50
4.1	Testing engine layout and data acquisition schematic.	57
4.2	Cross sectional view of combustion chamber and pre-chamber installed into a modified cylinder head of the testing engine (left) and the prototype pre-chamber (right).	58

4.3	Basic performance of pre-chamber engine, pre-chamber fuel rate 5.5 sccm/cycle, 6 holes, ignition timing for $CA_{50} = 10^\circ$ aTDC. . . . .	62
4.4	Performance of engine with various pre-chamber alternatives with 4, 6 and 12 holes, pre-chamber fueling rates: 4 holes = 0.9 sccm/cycle, 6 holes = 3.7 sccm/cycle and 12 holes = 1.85 sccm/cycle. . . . .	63
4.5	Results of high speed data acquisition and heat release analysis, pre-chamber with 6 holes, $\Lambda = 1.91$ , pre-chamber fueling rate = 2.8 sccm/cycle = 7.7% of total fuel delivery. . . . .	65
4.6	Performance (IMEP) and indicated efficiency ( $\eta_{ai}$ ) of the pre-chamber engine – pre-chamber fueling rate study, 6 holes pre-chamber, pre-chamber fueling rate 1.8 – 4 sccm/cycle as a function of the air excess ratio ( $\Lambda$ ). . . . .	66
4.7	Performance of pre-chamber engine – spark timing study, 12 holes pre-chamber, pre-chamber fueling rate 1.8 sccm/cycle. . . . .	67
4.8	Performance of pre-chamber engine – comparison with SI engine. . . .	68
5.1	Cross-section of the pre-chamber with the highlighted boundary conditions (left), 3D geometry of the internal volume (middle), cross-section of the installation assembly (right). . . . .	77
5.2	Fuel delivery, Simulation of special motored mode - 3rd cycle. . . . .	79
5.3	Methane mass fraction. Simulation of special motored mode – 3rd cycle. . . . .	80
5.4	Pre-chamber scavenging simulation - 1st cycle. . . . .	82
5.5	$CO_2$ mass fraction and streamlines, Scavenging simulation - 1st cycle, crank angle 2700, perpendicular sections (A-A, B-B). . . . .	83
5.6	Comparison of volumetric flow rate through the orifices. Simulation of special motored mode (Mode B). . . . .	84
5.7	Sensitivity analysis of ignition timing and fuel quantity, (Mode C). . . .	85
5.8	Basic performance of pre-chamber engine, (Mode D). . . . .	87
5.9	Transient test - results of high speed data acquisition, pressure in pre-chamber. . . . .	89
6.1	Basic engine performance as a function of the air excess ratio ( $\lambda$ ). . . .	94
6.2	Engine-out emission as a function of the air excess ratio ( $\lambda$ ). . . . .	95
6.3	Running roughness & combustion phasing as a function of air excess ratio. . . . .	96
6.4	A snapshot of CFD mesh. . . . .	98
6.5	Comparison of measured and modeled pressure in the cylinder (pCyl - top) and in the pre-chamber (pChmbr - middle) and rate of heat release (RoHR - bottom) for the case of 1800 rpm and air excess of 1.05. Blue color corresponds to CFD calculation. Red color corresponds to measured data. . . . .	101

6.6	Comparison of measured and modeled pressure in the cylinder (pCyl - top) and in the pre-chamber (pChmbr - middle) and rate of heat release (RoHR - bottom) for the case of 1800 rpm and air excess of 1.9. Blue color corresponds to CFD calculation. Red color corresponds to measured data. . . . .	102
6.7	Measured instantaneous pressures in cylinder (pCyl), pre-chamber (pChmbr), intake port (pIn) and exhaust port (pEx) (top) and modeled mass of methane (mCH4) in the pre-chamber for the case of air excess 1.9 (bottom). . . . .	103
6.8	Modeled mass fraction of combustion products for the case of the air excess ratio 1.48. . . . .	104
6.9	Pre-chamber mixture composition. . . . .	105
6.10	Methane mass fraction at 3° bTDC. for $\lambda = 1.05$ . . . . .	106
6.11	Assessment of methane leakage to exhaust port. . . . .	107
6.12	Flame penetration into the cylinder volume. . . . .	108
7.1	Pre-chamber design: small pre-chamber (left), big pre-chamber (middle), geometry of orifices (right) for the connecting channel configuration of 12x d=1.2 mm. . . . .	113
7.2	Installation of big pre-chamber in research engine. . . . .	113
7.3	Indicated mean effective pressure (IMEP) and indicated efficiency as a function of the air excess ratio at engine speed of 1800 rpm. Comparison of the small and the big scavenged pre-chambers and the big un-scavenged pre-chamber. . . . .	120
7.4	Engine out emission as a function of the air excess ratio at constant engine speed of 1800 rpm. Comparison of small and big scavenged pre-chambers and big un-scavenged pre-chamber. . . . .	121
7.5	Coefficient of variation of indicated mean effective pressure (COV imep) as a function of the air excess ratio at constant engine speed of 1800 rpm. Comparison of small and big scavenged pre-chambers and big un-scavenged pre-chamber. . . . .	122
7.6	Comparison of average cycle rate of heat release for the air excess of 1.05 at engine speed of 1800 rpm. Comparison of conventional spark ignition (SI), small and big scavenged pre-chambers and big un-scavenged pre-chamber. . . . .	123
7.7	Comparison of average cycle rate of heat release for the air excess of 1.5 at IMEP = 7 bar and engine speed of 1800 rpm. Comparison of small and big scavenged pre-chamber and big un-scavenged pre-chamber. . . . .	124

7.8	Comparison of average cycle rate of heat release for the air excess of 2 at IMEP = 4.6 bar and engine speed of 1800 rpm. Comparison of small and big scavenged pre-chambers. . . . .	125
7.9	Spark timing, CA 5 and CA 90 at constant engine speed of 1800 rpm. Comparison of small and big scavenged pre-chambers and big un-scavenged pre-chamber. . . . .	126
7.10	GT-Power simulation – 1800 rpm, constant pre-chamber fuelling rate of 0.2 standard m <sup>3</sup> /h: air excess in the big scavenged pre-chamber as a function of the global air excess ratio. . . . .	127
7.11	In-cylinder rate of heat release for small scavenged pre-chamber at $\lambda = 1.05$ and engine speed of 1800 rpm. Comparison of the measured cycles with the highest and the lowest peak pressures (Max p meas and Min p meas) and CFD data. . . . .	129
7.12	In-cylinder rate of heat release for big scavenged pre-chamber at $\lambda = 1.05$ and engine speed of 1800 rpm. Comparison of the measured cycles with the highest and the lowest peak pressures (Max p meas and Min p meas) and CFD data. . . . .	130
7.13	In-cylinder rate of heat release for big un-scavenged pre-chamber at $\lambda = 1.05$ and engine speed of 1800 rpm. Comparison of the measured cycles with the highest and the lowest peak pressures (Max p meas and Min p meas) and CFD data. . . . .	131
7.14	CFD simulation of stoichiometric operation: air excess and residual gas content in the big pre-chamber as a function of crank angle. Scavenged and un-scavenged versions are compared . . . . .	132
7.15	Equivalence ratio as a marker of mixture quality at air excess of 1.5, ‘big version (12x d=1.2mm)’, 10 degCA bTDC (legend: blue color corresponds to value 0.0 while red one represents 2.0). . . . .	133
7.16	Equivalence ratio as a marker of mixture quality at air excess of 1.5, ‘small version (12x d=1.2mm)’, 10 degCA bTDC (legend: blue color corresponds to value 0.0 while red one represents 2.0). . . . .	134
8.1	Schematic of a test cell with an experimental single-cylinder ŠKODA-ČVUT engine in the CTU engine laboratory. . . . .	142
8.2	Influence of the air excess ratio on molar fraction of $NO_x$ and molar fraction of $H_2$ in the exhaust gas (top left), the boost pressure and the exhaust back pressure in the exhaust manifold (top right) and maximum cylinder charge temperature (bottom). Traces measured at a constant speed of 2000 rpm, at constant mean indicated pressure of 6 bar and at constant combustion phasing. . . . .	144
8.3	Crank angle indexed traces of the cylinder pressure and heat release rate in dependence of $\lambda$ values. . . . .	145

8.4	Performance maps of the four-cylinder engine: top left isolines of maximum cylinder pressure and top right isolines of the brake efficiency, lower left isolines of air excess ratio (determined from molar fraction of $O_2$ in the exhaust), lower right isolines of the crank angle of 50% of the mass fraction burned. . . . .	146
8.5	Plots the isolines of the absolute intake air pressure (left) and isolines of the absolute exhaust gas pressure (right). . . . .	147
8.6	Plot of isolines of NOX molar fraction in raw exhaust gas (left), isolines of specific NOX emission (right). . . . .	148
8.7	Isolines of the molar fraction of $CO_2$ in exhaust (left) and isolines of specific $CO_2$ emissions (right). . . . .	148
I	A FFVA engine test bed, a hydraulic system distribution rail for the Sturman valve system (in front), an exhaust plenum on the left and an egr line. . . . .	169
II	Schematics of the fuel supply into the pre-chamber. . . . .	170
III	Heat release analysis results for various Lambda values. . . . .	171
IV	Scheme of the GT-power TPA model. . . . .	173
V	Comparison of spark energy profiles measured at 1800 rpm and fully open throttle valve for various air excess ratio (lambda). Spark voltage was measured by high voltage probe Tektronics P6015A, the electric current was measured by Pearson Model 110 current probe, connected to digital oscilloscope. . . . .	174
VI	Comparison of individual cycle simulation data related to combustion (ROHR) at air excess of 1.0 while comparing different pre-chamber design configurations and scavenging strategies (scavenged/unscavenged) – top left subfigure corresponds to 1st calculated cycle while bottom right subfigure represents 4th calculated cycle. . . . .	175
VII	Comparison of individual cycle simulation data related to combustion (ROHR) at air excess of 1.5 while comparing different pre-chamber design – top left subfigure corresponds to 1st calculated cycle while bottom right subfigure represents 4th calculated cycle. . . . .	176
VIII	Comparison of cumulative released chemical energy in pre-chamber at air excess of 1.0 (left) and 1.5 (right) while comparing different pre-chamber design configurations – left subfigure corresponds to Fig. VI while right subfigure represents Fig. VII. . . . .	176



IX	Comparison of individual cycle simulation data related to mixing (equivalence ratio as a marker of mixture quality) at air excess of 1.0 while comparing scavenging strategies (scavenged/un-scavenged); presented data correspond to 2nd cycle – left column corresponds to variant ‘big version’, right one to ‘big version – un-scavenged’; 1st row corresponds to 180 °CA, 2nd one to 360 °CA, 3rd one to 540 °CA, 4th one 680 °CA and 5th one to 710 °CA. . . . .	177
X	Comparison of individual cycle simulation data related to heat transfer (local temperature as a marker of heat flux) at air excess of 1.0 while comparing different scavenging strategies (scavenged/un-scavenged); presented data correspond to 2nd cycle – left column corresponds to variant ‘big version’ right one to ‘big version – un-scavenged’; 1st row corresponds to 180 °CA, 2nd one to 360 °CA, 3rd one to 540 °CA, 4th one 680 °CA and 5th one to 710 °CA. . . . .	178
XI	Comparison of individual cycle simulation data related to mixing (equivalence ratio as a marker of mixture quality) at air excess of 1.5 while comparing different pre-chamber design configurations; presented data correspond to 2nd cycle – left column corresponds to variant ‘small version’, right one to ‘big version’– 1st row corresponds to 640 °CA, 2nd one to 680 °CA, 3rd one to 690 °CA, 4th one 700 °CA and 5th one to 710 °CA. . . . .	179
XII	Comparison of individual cycle simulation data related to mixing (CH <sub>4</sub> mass fraction as a marker of flame – blue color represents burnt zone) at air excess of 1.5 while comparing different pre-chamber design configurations; presented data correspond to 2nd cycle – left column corresponds to variant ‘small version’, right one to ‘big version’ – top row subfigures correspond to early combustion phase (flame front reaches connecting channels in pre-chamber), all other sub-figures represent increase by 2 °CA. . . . .	180



# List of Symbols and Abbreviations

## Acronyms

AHRR	Apparent (gross) heat release rate
AMEM	Advanced Multizone Eulerian Model
aTDC	after Top Dead Center
BC	boundary conditions
BMEP	brake mean effective pressure
bTDC	before top dead center
CA50	Crank angle at 50 % burned mass
CAD	Crank Angle Degree
CAS	Combustion analysis system
CCV	cycle-to-cycle variation(s)
CFD	computational fluid dynamics
CR	Compression Ratio
COV	Coefficient of variance
dATDC	Degrees after top dead center
DAQ	Data acquisition system
dBTC	Degrees before top dead center
°CA	degrees of crank angle
DI	Direct Injection
ECFM	extended coherent flame model
Eta, $\eta$	Efficiency

EGR	Exhaust gas recirculation
EI CH <sub>4</sub>	methane emission index ( $\text{kg}/\text{kg}_{fuel}$ )
HHV	Higher heating value
FFVA	Fully flexible valve actuation
FPGA	Field-programmable gate array
HCCI	Homogeneous charge compression ignition
HP	High Pass
iEGR	Internal EGR
eEGR	External EGR
ICE	internal combustion engine
IMEP	indicated mean effective pressure
IVC	Intake valve close
LHV	Lower heating value
LES	large eddy simulation
LP	Low Pass
MBT	maximum brake torque
MON	Motor Octane Number
MPRR	Maximum pressure rise rate
NMEP	Net indicated mean effective pressure
NOX	nitrogen oxides
NVO	Negative valve overlap
PC	pre-chamber
Phi, $\phi$	equivalence ratio
PP	Peak pressure
PRR	Pressure rise rate
Q <sub>fuel</sub>	Flow rate of natural gas into the prechamber
R	Gas constant
RGF, (RGC)	Residual gas fraction (content)

RI	Ringling Intensity
RMS	Root Mean Square
ROHR	rate of heat release
RON	Research Octane Number
SACI	Spark Assisted Compression Ignition
SI	Spark Ignition
TDC	top dead center
TWC	Three-way catalyst
VTG	variable turbine geometry



# Chapter 1

## Introduction

### 1.1 Motivation for low temperature combustion

#### 1.1.1 Environment and climatic change

As a result of social and economic development, the concentration of the population in cities is growing. The use of transport of all kinds is also growing, and as the bulk of transport uses fossil fuels as an energy source, the problem with air pollution on the number of vehicles is growing. Local pollutant emissions and the challenge of global climate change are forcing governments to tighten existing emission limits. Efforts by governments to keep the global average temperature rise within 2°C above the preindustrial levels to prevent or mitigate the effects of climate change (floods, droughts, heat waves, and fires) and the associated migration of people from affected areas to less affected and richer regions, resulted in the adoption of the so-called Paris Agreement of 2015 [2]. Substitutes for fossil fuels using renewable energy sources are being sought. This increases the production and consumption of liquid and gaseous renewable fuels. In recent decades, conventional petroleum fuels in transport and energy have been replaced by natural gas.

Natural gas is considered the most efficient, affordable, and immediately applicable solution to reduce air pollution in cities [26]. Combustion of methane produces 25 percent less carbon dioxide in the methane molecule due to the more favorable hydrogen to carbon mass ratio than the combustion of diesel fuel or gasoline. However, methane is considered as a major contributor to global warming. The Global Warming Index (GWI) of methane is 25 times the GWI of carbon dioxide. If there are leaks anywhere in the chain from the source to the wheels (Well-to-Wheel), the benefits of this fuel are eliminated from a global perspective. A tragic example is methane leaks in oil extraction. Due to the lack of infrastructure for the treatment and transport of methane from oil fields, the gas is at best burned in burners, at worst, it is immediately discharged in large quantities directly into the atmosphere

[98].

It is therefore necessary to work intensively to reduce losses in all links in the chain. The author and his collaborators are working to reduce losses in the so-called "Tank-to-Wheel", i.e., the conversion of energy from the vehicle's fuel tank to the wheels. The efficiency of the conversion of chemical energy in fuel into mechanical energy, which can be used to power the vehicle, is gradually being increased by technical development and the application of more sophisticated (and more expensive) measures. Figure 1.1 shows the benefit of applying various technical measures expressed by reducing the emission of  $CO_2$  in NEDC and WLTC driving cycles in a van powered by natural gas ICE. Compared to the initial state, i.e., the diesel engine, the emission reduction of  $CO_2$  can be achieved by optimizing the compressed natural gas drive by up to 20%.

The next step in the so-called "decarbonisation" of transport is to increase in the share of the use of low-carbon energy vectors. One potential solution is the use of hydrogen. However, the hydrogen economy cannot be started "overnight". The onset of hydrogen transport must be gradual. Therefore, it seems a logical step to build a hydrogen infrastructure with the use of so-called gray hydrogen, i.e., hydrogen, which was formed either as a by-product of the chemical industry or hydrogen from fossil sources. The long-term goal is to actually reduce greenhouse gas emissions. At the same time, the so-called zero emission vehicles cannot be immediately enforced.

The internal combustion engine is an affordable, robust, and long-term durable energy converter. At the same time, it can be adapted and optimized for various gaseous and liquid fuels. The internal combustion engine can be supplemented with an electric motor for bridging the low-efficiency modes (i.e., low loads) and for energy recovery during deceleration or when driving downhill. The results of recent research projects show that with a diesel engine for a truck, a thermal efficiency value very close to 50% [65], [54] can be achieved. This is comparable to the efficiency of a highly loaded hydrogen fuel cell at a significantly lower cost.

The dominant technology currently used in modern gas engines is the combustion of a homogeneous mixture of air and gas in an open combustion chamber above the piston, ignited by spark ignition with a conventional spark plug. Emissions of pollutants in the exhaust are treated up to almost zero using the so-called controlled three-way catalyst [9]. However, if we focus on the combustion system and the efficiency of the internal combustion engine, the conventional spark ignition engine is already reaching its limits. Another potential for improving efficiency on the thermodynamics side of an internal combustion engine is related to the use of advanced combustion systems, using so-called low-temperature combustion of extremely diluted air-fuel mixtures.



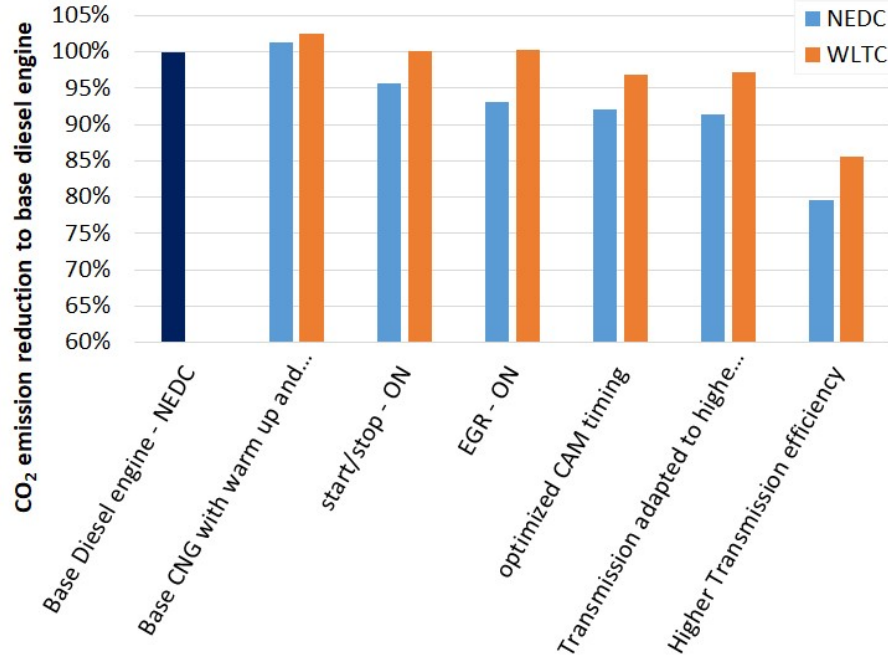


**Figure 1.1:**  $CO_2$  emission reduction by gradual application of technical measures in the development of a natural gas fueled van [23]

## 1.2 Introduction of low temperature combustion in spark ignition engines

The basis of low-temperature combustion is the combustion of an extremely diluted homogeneous mixture of air and fuel. Dilution can be performed with a high excess of air or with exhaust gas recirculation. In both cases, diluting the cylinder charge leads to a low combustion temperature. In terms of engine energy parameters, the low combustion temperature reduces the heat transfer to the combustion chamber walls. High dilution of the mixture and low combustion temperature increase the Poisson's constant  $\kappa$  or the ratio of the specific heat capacity of the cylinder charge. This leads to an increase in the thermal efficiency of the engine and a reduction in fuel consumption.

The low temperature combustion of the diluted mixture reduces the formation of nitrogen oxides and affects the proportion of other exhaust gas components, especially imperfect oxidation products such as carbon monoxide and  $CO$  and unburned hydrocarbons  $HC$ , see Fig. 1.2. The measured energy parameters and specific emissions of a gas spark ignition engine with conventional spark ignition in a low load

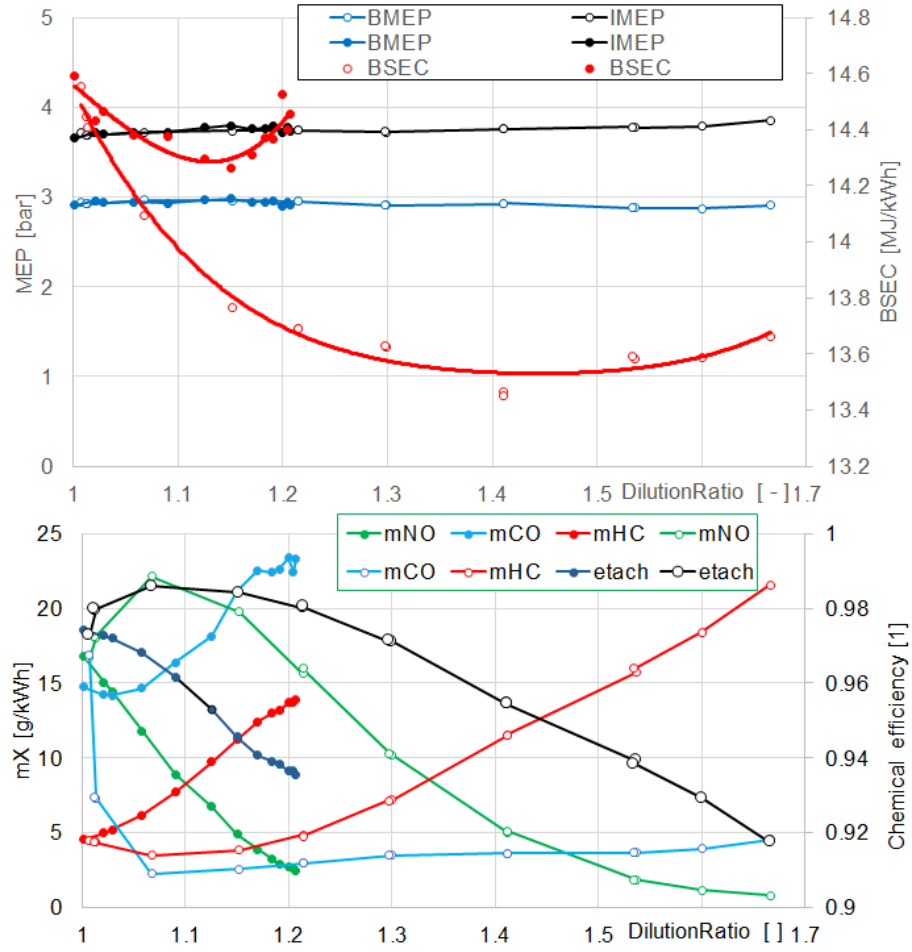


**Figure 1.2:** Energy and emission parameters of a gas spark ignition engine in low load mode depending on the dilution of the mixture. Colored dots correspond to exhaust gas recirculation dilution, marks without filling correspond to lean burn concept [86].

mode are shown here. It is clear that the dilution of the mixture in a real engine is limited by the chemical efficiency ( $\eta_{CH}$ ). The rate of chemical reactions and consequently chemical efficiency decreases proportionally to the degree of dilution. The lean burn engine concept with a conventional spark ignition combustion system and a premixed homogeneous mixture meets these limits.

This work will describe the methods of combustion of a homogeneous mixture in a gasoline engine and outside the area of the so-called lean flammability limits. The first part will be devoted to the concept of self-ignition of a premixed homogeneous charge, known as HCCI (Homogeneous Charge Compression Ignition) in a gasoline

engine. Research will focus on the combustion regime, which combines spark ignition with subsequent spontaneous combustion of the remaining unburned mixture. This combined mode is called SACI (Spark Assisted Compression Ignition) in the literature and makes it possible to bridge the area between conventional spark ignition and HCCI mode. The current work will compile the works created by the author at the University of Michigan in Ann Arbor [52], [83], [58], [32], [56].

The second part of this Habilitation thesis will deal with the research of an advanced ignition system with indirect ignition with a scavenged pre-chamber in gas engines to increase efficiency and reduce harmful exhaust emissions. These works were carried out at the Faculty of Mechanical Engineering of the Czech Technical University in Prague in the projects of the Josef Božek Research Center based on knowledge and research results and cooperation with industrial partners dating back to the 1990s. The concept of indirect ignition with a scavenged pre-chamber was taken from large gas stationary engines. It has been applied to the engine of a light truck. In the low and medium load regimes, a significant increase in thermal efficiency and a simultaneous reduction of nitrogen oxide emissions in raw exhaust gas to values comparable to the current legislative limit of EURO 6 was demonstrated. [73], [82] and [86] and two granted patents will be commented on in the second part of this publication.



## Chapter 2

# Bridging the Gap between HCCI and SI: Spark-Assisted Compression Ignition

HCCI has the potential to deliver high indicated thermal efficiencies relative to its spark-ignited counterpart [16]. These improvements are made possible partly through unthrottled operation at low load, which minimizes pumping loss. Thermal efficiency is also enhanced by the use of an increased compression ratio to promote auto-ignition, by the fact that combustion occurs at nearly constant volume (due to the fast burn rate of the mixture), and by the greater expansion stroke work (as a fraction of the fuel availability) provided by a low-temperature lean mixture [33].

In HCCI, combustion phasing is thermally controlled with intake temperature heating [67] or variable valve actuation to retain hot residual in-cylinder [99]. Peak combustion temperatures are kept relatively low due to high levels of charge dilution with air or residual gas. These lower temperatures elevate the ratio of specific heats  $\gamma$  of the mixture, leading to gains in thermal efficiency. Simultaneously, these low temperatures (achieved with either air or EGR dilution) greatly reduce the engine-out NO<sub>x</sub> concentrations, allowing the engine to meet emissions regulations without NO<sub>x</sub> after-treatment [16]. Heat loss through the cylinder walls is also reduced, improving engine efficiency [25]. These dilute mixtures are not normally accessible with traditional spark ignition; however, HCCI permits auto-ignition at lean equivalence ratios through charge preheating.

Despite its advantages, the maximum achievable load for naturally-aspirated HCCI is about 4.0-5.0 bar [16]. High load operation is restricted by the ringing/instability limit, beyond which slight changes in conditions can lead to excessive pressure rise rates (PRR) or misfire [20]. In order to take full advantage of the benefits of HCCI, the operating range must be expanded in order to cover an increased portion of the speed-load map. Several studies have attempted this using a variety

of strategies including boosting [20],[35] and [57], variable compression ratio [31], charge stratification [6], and spark assist [81]. This research focused on the latter method.

Spark-assisted compression ignition (SACI) uses spark as an additional means of combustion control. It is thought that the spark produces a propagating flame that consumes a portion of the charge and releases some of the fuel energy. This heat release by the flame increases the temperature of the remaining charge, causing it to auto-ignite earlier than it would have otherwise [49]. Since SI flame propagation has a longer burn duration than bulk auto-ignition, SACI can be used to reduce peak heat release rates at higher loads, thereby reducing ringing intensity. Wang et al. also demonstrated that implementing spark assist can improve the stability of gasoline HCCI near the misfire limit [93].

Urushihara et al. [81] accomplished SACI by injecting a small amount of additional fuel near the spark plug, facilitating a propagating flame that increased cylinder pressure and temperature and induced auto-ignition of the surrounding homogeneous lean mixture. As a result, precombustion temperatures necessary to achieve HCCI were reduced, and the engine was capable of operating at higher loads (up to 6.5 bar IMEP) before the ringing limit was reached. The moderating effect of SACI on heat release was confirmed by Yun et al. [96], who found that spark assistance was crucial to reducing combustion noise at higher engine loads. Spark advance resulted in a more gradual initial heat release, thought to be flame propagation, followed by autoignition of the remaining charge. Combustion noise was reduced by the increase in burn duration. Similar results were found by Szybist et al. [75], who used SACI to achieve loads up to 7.5 bar NMEP. Maximum cylinder pressure rise rates were controlled by spark timing, internal EGR, and late IVC to reduce the effective compression ratio. Under low load conditions, the combustion event was dominated by volumetric auto-ignition (similar to HCCI), while at higher loads, a larger portion of the heat release occurred during flame propagation, as in conventional SI.

Hyvonen et al. [36] have shown that SACI can also be used to control combustion phasing during a mode transfer between HCCI and SI. A modeling study by Lavoie et al. [49] attempted to define the regions of SI flame propagation, SACI, and HCCI in terms of unburned and burned gas temperatures near top dead center. HCCI requires high unburned temperatures to initiate combustion and has relatively low burned temperatures, while SI can be accomplished with low unburned temperatures but produces high burned temperatures. SACI can be used to achieve ignition when unburned temperatures are too low for complete auto-ignition (but high compared to conventional SI) and when the mixture is too lean for well-developed flame propagation. Under these conditions, a flame can be sustained when unburned temperatures are increased by a higher compression ratio, intake charge temperature, or internal residual fraction [89]. These high unburned temperatures allow HCCI and

SACI to be achieved at fuel-air mixtures significantly leaner than in conventional sparkignited combustion.

The objectives of this study were two-fold. The first goal was to extend the load range of SACI at maximum efficiency using dilute operation with EGR. The second goal was to obtain an understanding of the combustion regime that lies between low load HCCI and high load SI. This combustion regime should allow for smoother transitions from pure flame propagation to pure auto-ignition during a realistic drive cycle [96]. The following section introduces the test setup, fuel specifications, data acquisition systems, and experimental test procedures. Next, HCCI results from the engine are discussed and load limits for this combustion regime are quantified. Lastly, the results of load extension into the SACI regime are examined.

## 2.1 Experimental Setup

Experiments were performed on a single-cylinder gasoline direct-injected engine with a Ricardo Hydra crankcase. The engine is equipped with a fully-flexible valve actuation (FFVA) system from Sturman Industries. The engine geometry is listed in Tab. 2.1.

Parameter	Value
Displacement volume ( $cm^3$ )	550
Stroke (mm)	94.6
Bore diameter (mm)	86.0
Conrod length (mm)	156.5
Piston pin excentricity (mm)	0.8
Compression ratio (-)	12.5:1
Number of valves (-)	4
Piston shape	Shallow bowl
Head design	Pent-roof
Fueling method	Direct injection

**Table 2.1:** FFVA engine geometry.

The compression ratio for this engine is higher than that for a typical spark-ignited engine. This creates higher in-cylinder pressures and temperatures, aiding in the implementation of HCCI combustion. The piston contains an asymmetrical bowl for increased cylinder turbulence and reciprocates below a pent-roof type combustion

chamber. A spark plug is centrally mounted in the cylinder head. Fuel is delivered via a gasoline direct injector mounted between the two intake valves and aimed into the piston bowl. A detailed schematic of the engine setup is seen in Fig. 2.1.

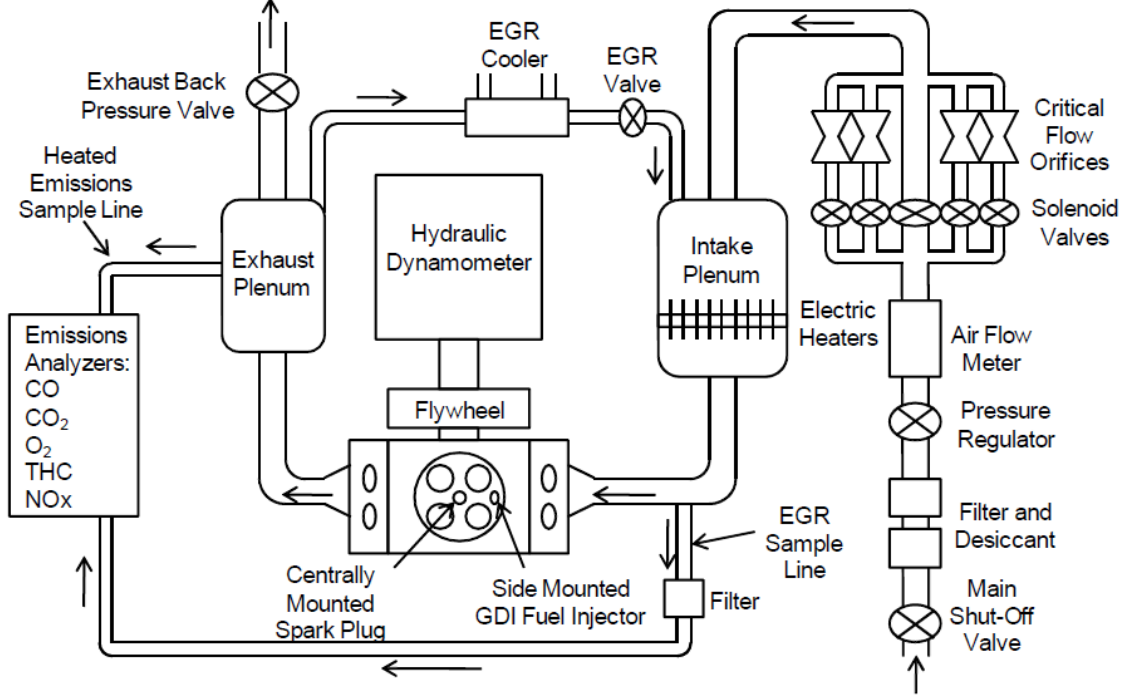


Figure 2.1: FFVA engine schematic.

## 2.2 FFVA SYSTEM

The Sturman electro-hydraulic valve actuation system allows the lift, timing, and duration of each valve event to be controlled independently. The system is capable of running two intake events and two exhaust events per engine cycle, at lifts up to 10.0 mm. The range of possible valve timings is limited only by physical interference between the piston and the valves, preventing large amounts of positive valve overlap from being achieved. Specifications for the FFVA system are listed in Tab. 2.2.

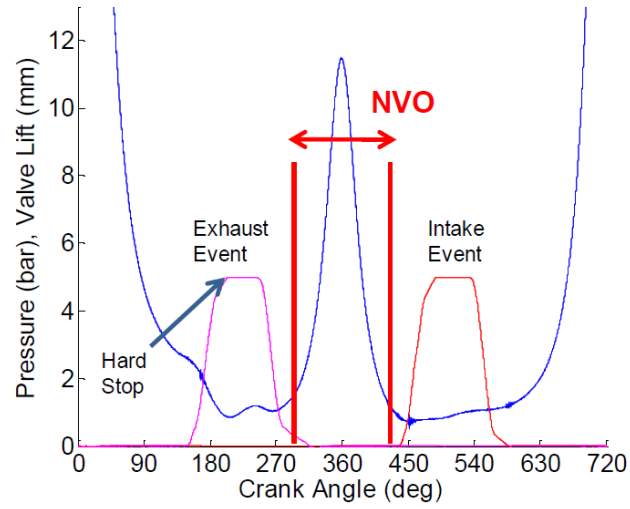
The lift of the primary valve event is controlled by an internal hard stop mechanism which gives the valve profiles a characteristic trapezoidal shape, as seen in Fig. 2.2. Due to physical limitations, the position of the hard stop cannot be changed mid-cycle, so valve lift and timing can only be varied on a cycle-resolved basis. In these experiments, a recompression valve strategy was used. Recompression relies



Parameter	Value
Manufacturer	Sturman Industries
Principle of operation	Electro-hydraulic
Number of valves	4
Maximum lift (mm)	10.0
Resolution of lift control (mm)	0.1
Resolution of timing control (CA°)	1.0
Maximum number of valve events per cycle (-)	2
Variability of opening (CA°)	$\pm 2.0$

**Table 2.2:** Hydraulic valvetrain specifications.

on a high degree of negative valve overlap (NVO) to retain hot residual gases in the cylinder. These hot residuals increase the pre-combustion temperature of the mixture and its tendency to auto-ignite.

**Figure 2.2:** Example of a recompression valve strategy with a high degree of negative valve overlap (NVO).

## 2.3 FUEL AND AIR

The fuel utilized in this experiment was research-grade gasoline supplied by Chevron Phillips. Fuel specifications are listed in Tab.2.3. The fuel system consists of a side-mounted direct injector and a large bladder accumulator which is pressurized with nitrogen up to 100 bar. Fuel flow is regulated based on a specified injection duration. End of injection is typically set to 30 degrees after intake TDC, giving the charge sufficient time to mix before ignition.

Parameter	Value
Research octane number (RON)	90.5
Motor octane number (MON)	82.6
Antiknock index (R+M)/2	86.6
Carbon (Wt. %)	86.38
Hydrogen (Wt. %)	13.62
Oxygen (Wt. %)	0.0
H/C atomic ratio	1.879
Stoichiometric air-fuel ratio	14.61
Lower heating value (MJ/kg)	43.043
Specific gravity (kg/dm <sup>3</sup> )	0.745
Grabner vapor pressure (kPa)	48.1
Molar mass (g/mol)	93.04

**Table 2.3:** Fuel specifications.

The engine is supplied with compressed shop air, which is regulated upstream of the intake plenum to achieve the desired intake pressure (measured in the intake runner). The system is capable of running boosted pressures, but for these experiments the intake pressure was limited to an unthrottled 1.0 bar absolute. Three electric heaters inside the intake plenum can be used to heat the intake charge. However, for these experiments, the intake heaters were not used, and the temperature of the charge at intake valve closing was controlled by varying the amount of internal EGR using negative valve overlap. A butterfly valve in the exhaust system was used to regulate exhaust manifold pressure, thereby adjusting the flow of external EGR into the intake manifold. To achieve flow, exhaust pressure was maintained about 5 kPa above intake pressure throughout the experiment, and EGR percentage was varied

by finely adjusting a needle valve in the EGR line. The EGR cooler was necessary to maintain constant intake temperature at a target value of  $\sim 40^\circ\text{C}$ .

An array of critical flow orifices and a thermal mass flowmeter are used to measure the air mass flow rate into the engine. Fuel flow rate is measured with a piston-type positive-displacement flow meter. A wide range lambda sensor mounted in the exhaust manifold is used to quantify equivalence ratio.

Full exhaust constituents are measured with a Horiba emissions analysis system. Gases are probed in the exhaust plenum and transferred to the various analyzers via a heated line, where molar fractions of NO<sub>x</sub> (chemiluminescence), THC (flame ionization), CO, CO<sub>2</sub> (non-dispersive infrared), and O<sub>2</sub> (paramagnetic) are measured. Air-fuel ratio is also determined from calculations involving these quantities [70]. Additionally, CO<sub>2</sub> is measured in the intake runner and the external EGR percentage is computed based on the ratio of molar fractions of CO<sub>2</sub> in the intake and exhaust manifolds.

## 2.4 ENGINE CONTROL AND MEASUREMENT

A hydraulic dynamometer is used to provide load and regulate engine speed. The engine's crankshaft is mechanically connected to a hydraulic motor which is connected to the pump via hydraulic lines. The engine controller is composed of hardware from National Instruments and Drivven, Inc. Lab View based software provided by Drivven was modified for our particular application. The NI FPGA controller regulates spark and fuel injection timing and duration via Drivven spark and fuel injector drivers. Equivalence ratio is easily adjusted with the fuel injection pulse duration. The spark plug is fired by a MoTeC M DEN-580 inductive smart coil, which is capable of only one ignition event per cycle. The coil is mounted just above the engine head, and a short spark plug wire and boot connect the coil to the plug terminal.

The low-speed data acquisition system (DAQ), which is also based on NI hardware and Lab View, provides signal conditioning for flow rates and temperatures with thermocouples and RTD sensors. Measured values include oil and coolant temperatures, fuel and air mass flow rates, and temperatures at the intake and exhaust ports.

The high-speed AVL combustion analysis system (CAS) samples pressure data at 0.1 crank angle degree (CAD) resolution for 200 consecutive engine cycles. A Kistler crank angle encoder is used to keep the CAS synchronized with the engine. Absolute intake and exhaust manifold pressures are measured using Kistler piezoresistive pressure sensors. The exhaust sensor is mounted in a cooled switching adapter which helps to protect it from overexposure to high exhaust temperatures. In-cylinder pressure is measured with a Kistler piezoelectric pressure transducer

with a flame shield, which is pegged once per cycle near bottom dead center (BDC) from the intake pressure sensor. It has been shown experimentally that the use of a flame shield improves the sensor thermal characteristics by preventing hot burned gas products from contacting the transducer face [59]. The highspeed DAQ also monitors the valve lift signals from the Sturman controller unit.

## 2.5 EXPERIMENTAL PROCEDURE AND DATA ANALYSIS

The experiment focused on two primary combustion regimes: HCCI and SACI. Before attempting load extension, the engine was mapped in HCCI mode. The engine was operated at unheated naturally-aspirated conditions using air and internal EGR dilution to control load. Spark was not implemented and NVO sweeps were performed at several different fueling rates (7-11.5 mg/cycle). For each fueling rate the upper and lower NVO limits were set by ringing intensity and stability constraints, respectively. A larger degree of NVO phased combustion earlier by increasing the internal residual fraction, raising pre-combustion temperature. Earlier combustion led to high rates of pressure rise, greater NO<sub>x</sub> emissions, and a higher ringing intensity. Combustion was retarded through reduced amounts of NVO, resulting in a lower charge temperature, slower rate of pressure rise, and longer burn duration. The reduced pressure rise rate from combustion retard allowed fueling to be increased again, and the process was continued until the viable range of NVO steadily diminished and the limits of combustion were reached. Load was increased up to the maximum load limit, at which point no NVO settings were possible to achieve acceptable combustion. Tab. 2.4 lists the operating conditions for the first part of the experiment.

The load extension portion of the study focused only on stoichiometric operating conditions, similar to previous studies [16], [96] and [75]. As more fuel was injected into the cylinder and temperatures increased, unacceptable levels of NO<sub>x</sub> emissions were produced. By making the mixture stoichiometric at these higher loads through the addition of external EGR, practical after-treatment with a standard threeway catalyst (TWC) can be used. Accordingly, this study concentrated only on stoichiometric operation, so that NO<sub>x</sub> emissions were no longer a concern.

Load extension into the SACI regime was achieved using a combination of spark assist, negative valve overlap, and cooled external EGR. As fueling rate was increased beyond the limit of HCCI, cooled external EGR was added to decrease pressure rise rates and avoid ringing; however, it also resulted in late and unstable combustion. Small amounts of internal EGR were then added (via increased NVO) to phase combustion earlier and achieve a stoichiometric mixture. External and internal EGR

Parameter	Value
Engine speed (rpm)	2000
Fuel flow rate (mg/cycle)	7 - 11.5
Fuel pressure (bar)	$\approx 100$
Intake pressure ( $bar_a$ )	1.0
Exhaust pressure ( $bar_a$ )	1.05
Intake temperature ( $^{\circ}C$ )	40
Negative valve overlap ( $CA^{\circ}$ )	150 - 250
Coolant temperature ( $^{\circ}C$ )	90
Oil temperature ( $^{\circ}C$ )	90
Valve lift height (mm)	4.0
Fuel injection timing (dBTDC)	48.1
External EGR (%)	0

**Table 2.4:** Experimental conditions during HCCI operation.

were adjusted until barely stable, stoichiometric combustion was obtained. Finally, the spark was implemented to fine-tune the combustion phasing and provide further stabilization. While internal and external EGR can also phase combustion, spark is adjusted more finely and easily than the former parameters, making it a valuable method of control.

This load extension strategy differs somewhat from other previously implemented strategies. Szybist et al. [75] used only internal residual and late IVC to control the effective compression ratio and combustion timing at spark-assisted high load operation; no external EGR was used. Knock mitigation was also assisted by the relatively low geometric compression ratio of the engine (11.85:1) as well as the use of a high octane fuel. Cairns et al. [16] achieved 5.5 bar BMEP by modulating only internal and external EGR. Spark was implemented at a constant timing, but it was not the focus of the control strategy. The study presented here builds on these two former strategies to combine the effects of iEGR, eEGR, and spark advance. Tab. 2.5 provides more details about the experimental conditions during this portion of the study.

Heat release analysis was carried out to determine combustion characteristics, estimated temperatures, and residual gas fractions. Combustion phasing was determined by CA50, the crank angle at which 50% of the fuel mass was burned. This quantity was determined from the apparent heat release rate (AHRR) computed

Parameter	Value
Engine speed (rpm)	2000
Fuel flow rate (mg/cycle)	12.5-24
Fuel pressure (bar)	100
Intake pressure (bar)	1.0
Exhaust pressure (bar)	1.05
Intake temperature ( $^{\circ}\text{C}$ )	40 – 50 (varies with eEGR)
Degrees of negative valve overlap	175 to -5
Coolant temperature ( $^{\circ}\text{C}$ )	90
Oil temperature ( $^{\circ}\text{C}$ )	90
Spark advance (dBTDC)	22-43
Spark Dwell (ms)	5.4
Fuel injection timing (dBTDC)	330
External EGR (%)	12-25
EGR Coolant Temperature ( $^{\circ}\text{C}$ )	60

**Table 2.5:** Experimental conditions during load extension (SACI mode).

from an average of 200 cycles of cylinder pressure data, to which a 5 kHz low-pass filter was applied. A modified Woschni heat transfer correlation with variable mixture properties was used to calculate the apparent (gross) heat release and determine the curve of mass fraction burned [17].

Accurate temperature determination is important for the study of HCCI combustion since it is highly sensitive to this parameter; however, this process can be difficult for NVO operation since the residual mass is often a large portion of the total inducted mass. Therefore, trapped mass (including fuel, air, and residual) was computed using the methodology by Fitzgerald et al. [27], which was developed for an HCCI engine with NVO. Average in-cylinder temperature was then determined using the equation of state and in-cylinder pressure averaged over 200 cycles.

Combustion stability was quantified by cycle-to-cycle variability of NMEP over 200 engine cycles. For this experiment, the limit was defined by a COV of NMEP greater than 5.0%. At retarded combustion timings, high rates of expansion were encountered, causing temperature rise rates to decrease. Eventually, small variations in precombustion temperature caused large variations in combustion timing.

The engine was also limited by high rates of pressure rise, which caused un-

acceptable ringing that could lead to engine damage. For this experiment, ringing intensity  $RI$  ( $MW/m^2$ ) was determined from the average filtered pressure trace using the following equation developed by Eng [24]:

$$RI [MW/m^2] = \frac{1}{2\gamma} \frac{(0.05 \frac{dP}{dt_{max}})^2}{P_{max}} \sqrt{\gamma R T_{max}}. \quad (2.1)$$

In this expression,  $(dP/dt_{max})$  is the maximum pressure rise rate ( $kPa/msec$ ),  $P_{max}$  is the peak cylinder pressure ( $Pa$ ),  $T_{max}$  is the peak cylinder temperature ( $K$ ),  $\gamma$  is the ratio of specific heats, and  $R$  is the gas constant ( $J/kg/K$ ). Ringing intensity was limited to  $4.0 MW/m^2$  based on the appearance of large pressure fluctuations near TDC and the onset of disconcerting combustion noise. NOx emissions were also a concern for these advanced combustion regimes. For lean operation, the NOx index was limited to  $1.0 g/kg\text{-fuel}$ , which provided a good estimation for the US-2010 emission standard [20]. However, the NOx constraint was relaxed when the mixture was stoichiometric.

## 2.6 RESULTS AND DISCUSSION

### 2.6.1 HCCI OPERATING REGIME

With the limits of combustion in mind, the usable range of HCCI was mapped. Fig. 2.3 (a) shows load plotted against NVO while Fig. 2.3 (b) shows load plotted against CA50 (combustion timing) for the usable HCCI regime. As indicated in Fig. 2.3 (a), at low loads, a large range of NVO could be spanned before the limits of combustion were reached. However, at high loads, slight changes in NVO had a greater effect on combustion. As fueling was increased, the limits of ringing intensity and instability converged and the operating range became narrower. At the maximum achievable load, only four degrees of NVO separated heavy ringing from unstable combustion. Beyond this fueling rate, combustion phasing could not be adjusted (to mitigate ringing intensity) while still maintaining acceptable combustion stability. NOx emissions for the entire region did not exceed  $1.0 g/kg\text{-fuel}$ .

In this HCCI regime, the maximum achieved load was  $\sim 3.7$  bar NMEP. Others, notably Dec et al. [20] have managed to achieve naturally-aspirated HCCI up to  $5.0$  bar IMEP, possibly due to a different HCCI strategy, which relied on a high compression ratio and intake air heating, rather than internal residual. In this experiment, NVO added another degree of complexity to the engine by introducing cycle-to-cycle feedback. Combustion behavior was affected mostly by the thermal properties of the gases from the previous cycle and not by the incoming conditions, which can be controlled more easily. For partial-burn cycles at high loads, the NVO retained excess unburned fuel for the following cycle, causing advanced combustion

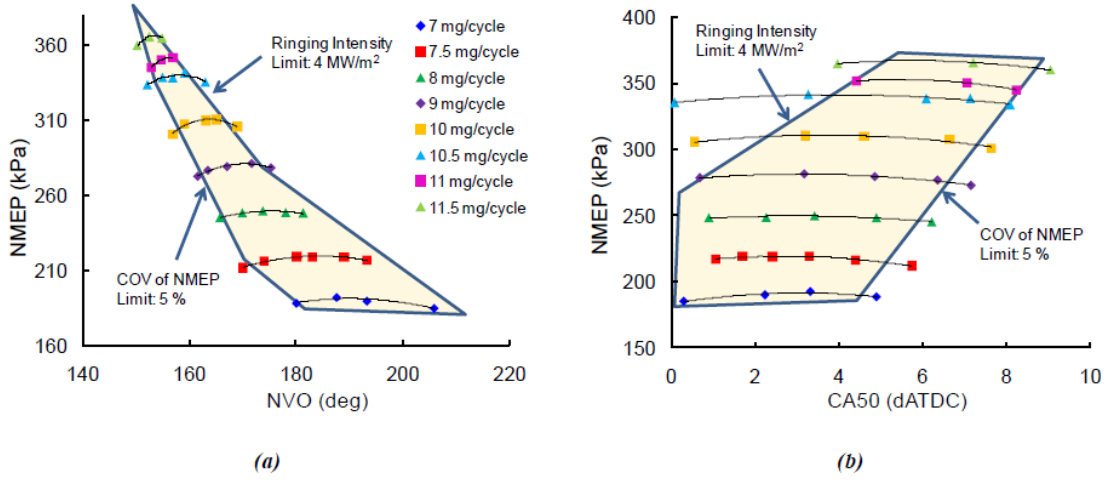


**Figure 2.3:** The usable HCCI operating regime, (a) load vs. degree of NVO for various fueling rates (7-11.5 mg/cycle), and (b) load vs. combustion timing (CA50).

and ringing. Oscillations between early and late combustion continued, eventually leading to misfire. Thus, the current setup is inherently less stable than that of Dec et al.

## 2.6.2 THE SACI REGIME

### Spark Advance Sweep at Constant Load

This load extension strategy relied heavily on spark assist to control the start of ignition and combustion phasing. To show the spark effect, a spark sweep was performed at constant NVO (shown in Fig. 2.2) at  $\sim 5$  bar NMEP, well into the SACI regime. Spark timing was set at 28 dBTDC and NVO and external EGR were adjusted to establish stable combustion while maintaining a stoichiometric equivalence ratio. Fuel flow was  $\sim 16$  mg/cycle, and the internal and external EGR fractions were  $\sim 29\%$  and  $\sim 16\%$ , respectively. Under these conditions, the spark timing was then varied and its effect on combustion phasing was studied.

Fig. 2.4 shows the effect of spark timing on cylinder pressure, temperature, and apparent heat release rate as the spark was advanced from 28 to 35 dBTDC. As seen in Fig. 2.4(a), the in-cylinder pressure trace changed noticeably as spark was advanced. Earlier spark timing resulted in earlier combustion, higher rates of pressure rise, and higher incylinder pressures and temperatures, as seen in Fig. 2.4(b). Spark advance also resulted in earlier, more rapid heat release, seen in Fig. 2.4(c). These results agree with Persson et al. [60], who showed that spark advance can be



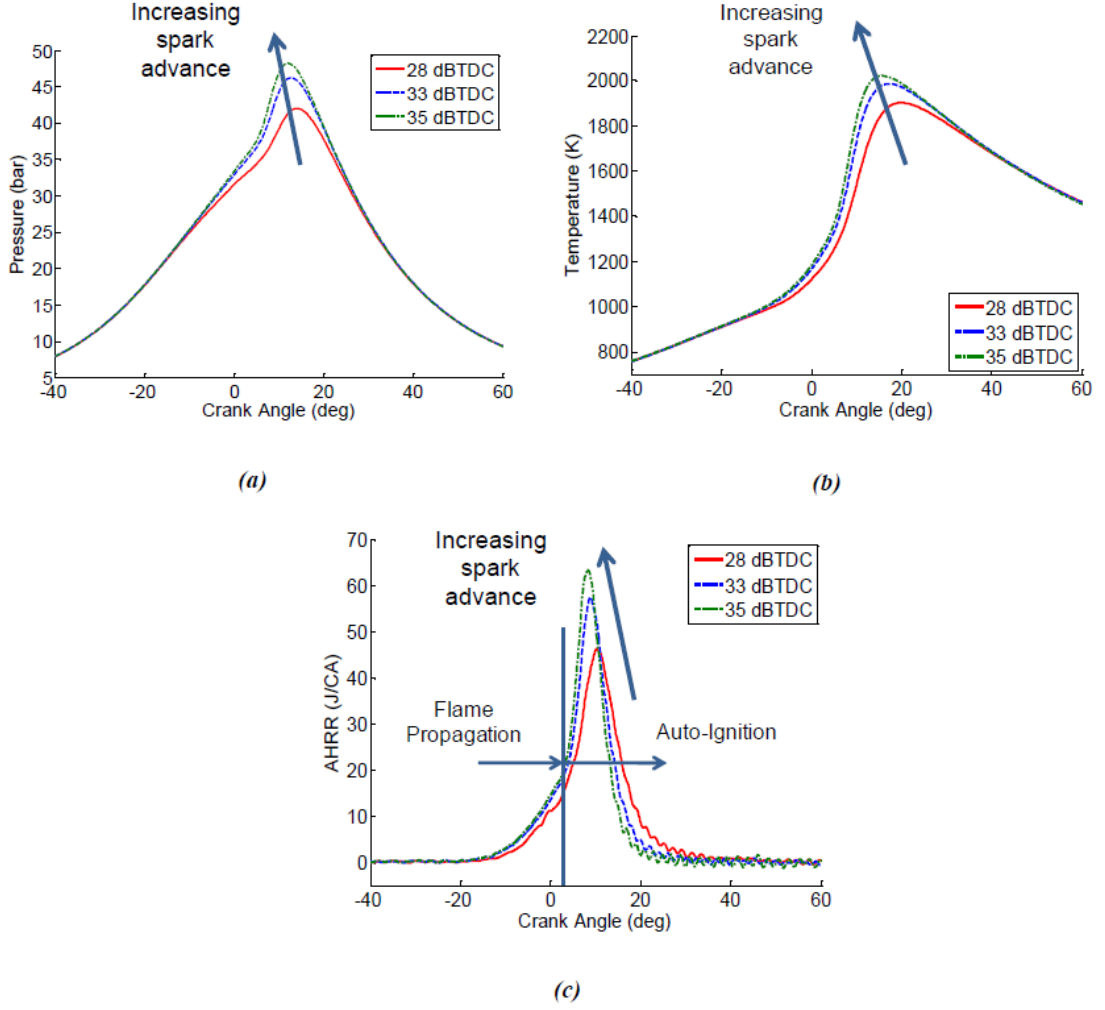


**Figure 2.4:** The effect of spark timing on (a) cylinder pressure, (b) cylinder temperature, and (c) apparent heat release rate at  $\sim 5$  bar NMEP ( $\sim 16$  mg/cycle fueling rate).

used to phase combustion even when the majority of the heat release comes from auto-ignition. The heat release curves of Fig. 2.4(c) show two distinct regions: an initial region of slow heat release, consistent with flame propagation, is followed by rapid heat release, characteristic of bulk auto-ignition. These combined combustion modes are representative of SACI, and optical experiments have noted similar behavior within this region [92], [42]. The transition from one mode to the other can be defined by a rapid change in slope of the heat release rate, as described by Persson et al. [60]. While SACI flame propagation is perhaps slower than SI flame propaga-

tion, it can be tolerated due to increased burn rates from autoignition. These results show that SI flame propagation and HCCI auto-ignition can exist together at these operating conditions.

Fig. 2.5(a) shows the effect of spark advance on CA10, CA50, and CA90. The 10% burn point (CA10) is typically used to represent the start of combustion. As spark was advanced, combustion was initiated earlier and CA10 decreased. CA50 also decreased at a similar rate. As the autoignition event occurred earlier in the cycle, the overall heat release became faster and burn duration was shortened. As a result, CA90 decreased at a faster rate than both CA10 and CA50.

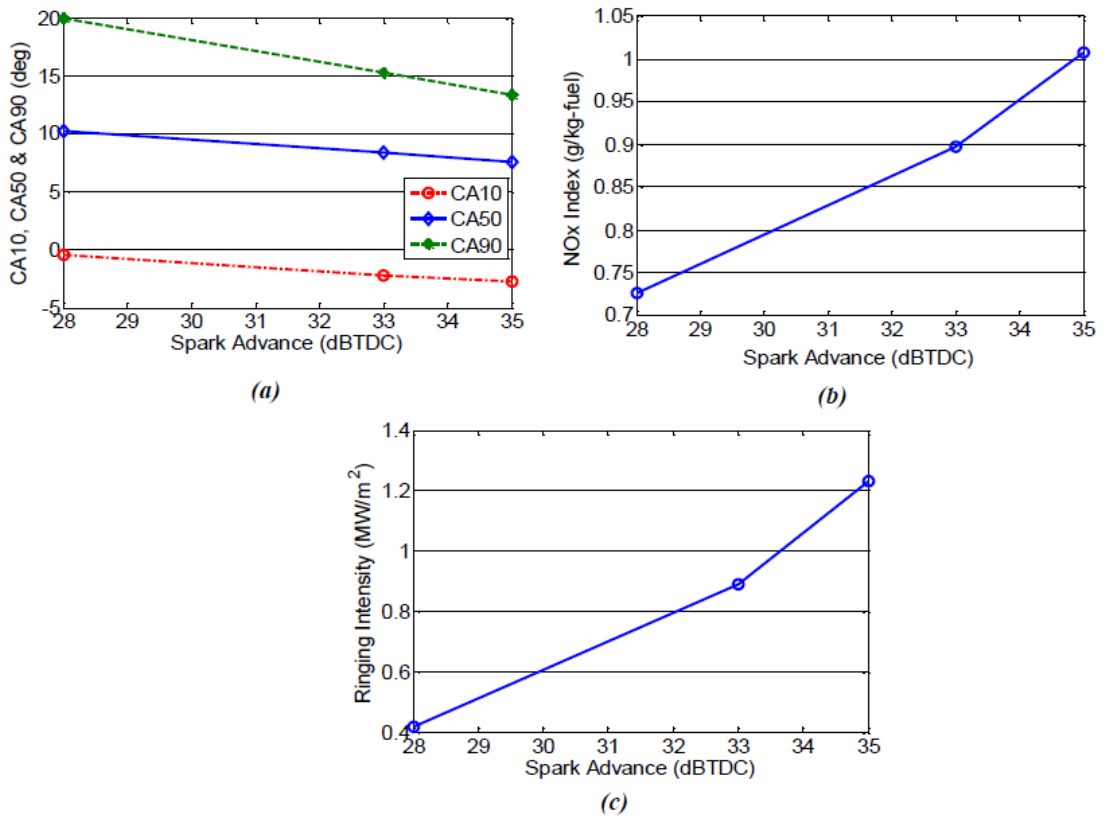


**Figure 2.5:** The effect of spark timing on combustion characteristics including (a) CA10, CA50, and CA90, (b) NOx emissions, (c) ringing intensity.

Fig. 2.5(b) and Fig. 2.5(c) show the effect of spark advance on NOx emissions and ringing intensity, respectively. Both plots show the same increasing trend with spark advance. Earlier combustion produced higher cylinder pressures and temperatures that resulted in increased NOx concentrations, yet these temperatures remained relatively low due to high levels of charge dilution. As a result, the NOx emissions

never exceeded 1.0 g/kg-fuel. Ringing intensity also increased with spark advance due to higher pressure rise rates. However, the increased burn duration (due to flame propagation) compared to normal HCCI kept ringing intensity well below the acceptable limit of 4.0 MW/m<sup>2</sup> at the most advanced spark timing.

Fig. 2.6(a) and Fig. 2.6(b) show engine load and net indicated specific fuel consumption (NSFC) consistent with the combustion phasing seen in Fig. 2.5. Load increased with spark advance at a constant fueling rate, indicating a higher thermal efficiency. As a result, NSFC (fuel energy input per engine power output) decreased.

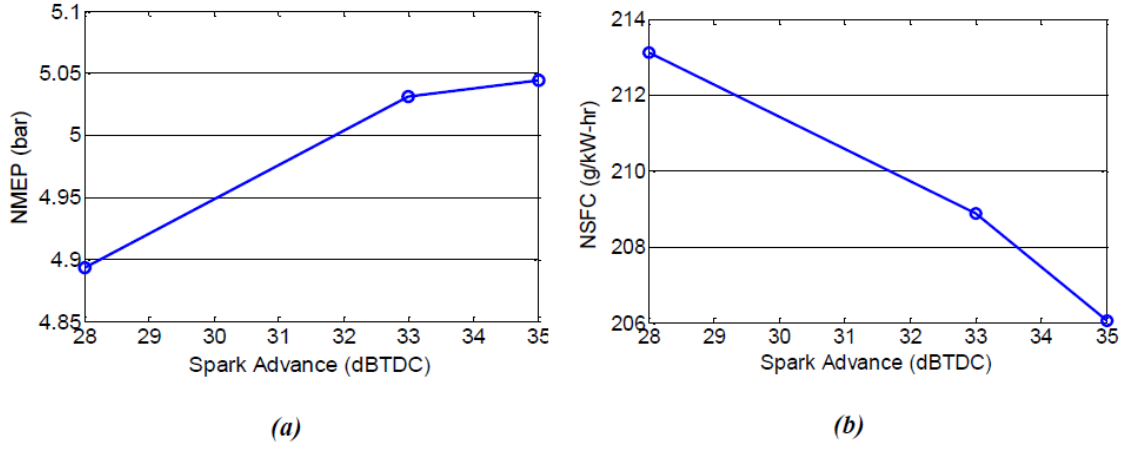


**Figure 2.6:** The effect of spark timing on fuel economy, (a) NMEP vs. spark advance and (b) NSFC vs. spark advance.

## Load Sweep at Constant CA50

A sweep in which load was varied while maintaining constant combustion timing was also conducted. At each load, iEGR, eEGR, and spark timing were adjusted to achieve a CA50 of  $\sim 10$  dATDC. Fig. 2.7 depicts the valve control strategy used as fuel and air were increased in equal ratio to maintain a stoichiometric mixture. At higher load, the required airflow was achieved by decreasing NVO and raising the valve lift. This change in NVO decreased the internal residual fraction and lowered maximum cylinder pressure during the recompression portion of the cycle. To achieve the required stoichiometric mixture, cooled external EGR was increased slightly to replace part of the internal EGR. This effect, as well as the decrease in NVO, helped to decrease precombustion temperatures, retard combustion, and prevent knock at higher load. As load increased, the valve profiles transitioned from high NVO, low lift (typical for HCCI) to high lift, full duration events.

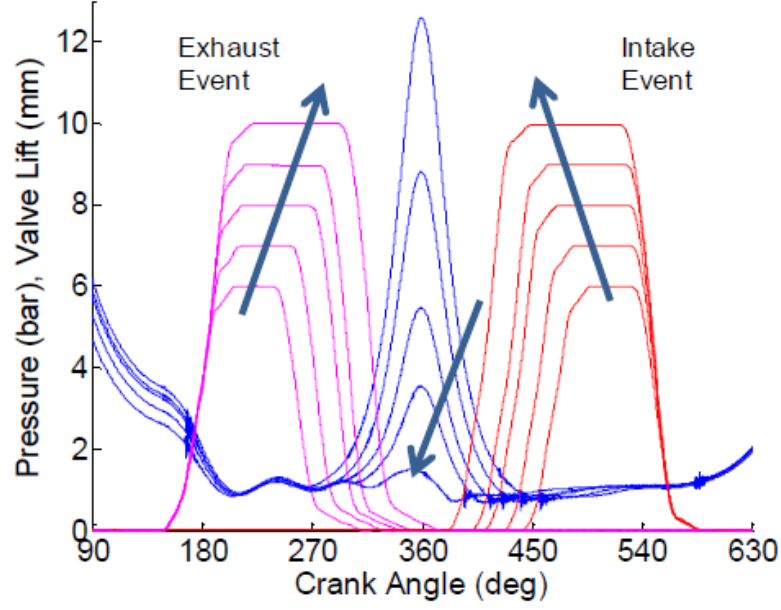


**Figure 2.7:** Valve strategy for extending the high load limit (arrows indicate increasing load).

Fig. 2.8(a) depicts the variation in internal and external EGR as load was increased. As load increased, the sum of internal and external EGR was required to decrease in order to obtain the necessary airflow. In addition, external EGR replaced a portion of the internal EGR. This additional external EGR helped to maintain a stoichiometric mixture, lower the incylinder temperature, and prevent the onset of knock as load increased. Fig. 2.8(b) shows that the required spark advance also increased with load. At higher loads, pre-combustion temperatures decreased (due to less thermal energy from the internal residual), and the combustion process required more time for completion. Therefore, a more advanced spark was required to maintain constant CA50.

Fig. 2.9 represents the combustion characteristics of the load sweep. In Fig. 2.9(a), as load was increased from 4.9 bar to 7.3 bar NMEP, combustion appeared to transition from HCCI-like to SI-like. The heat release curves show a similar trend, as seen in Fig. 2.9(b). As load increased, overall burn duration increased due to more flame propagation, and combustion was initiated earlier to maintain constant CA50. The heat release occurred more slowly and peak heat release rate decreased. Moreover, as load increased, less energy was released during the late bulk auto-ignition process. From the temperature curves in Fig. 2.9(c), it is apparent that pre-combustion

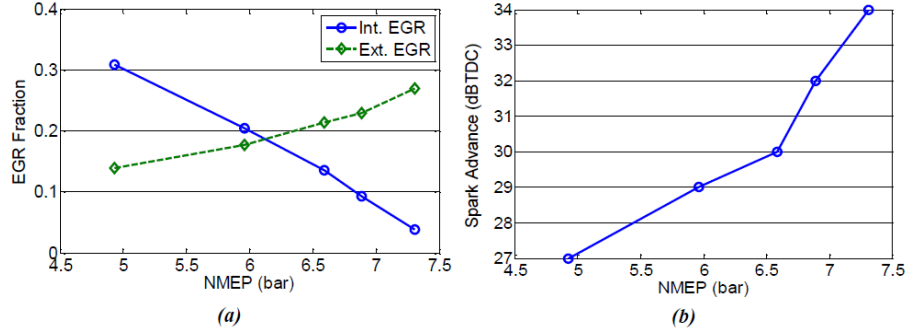


**Figure 2.8:** Control strategy for load extension at constant CA50, (a) required external and internal EGR percentages as load increased, (b) required spark advance as load increased.

temperatures decreased as load increased. This was due to a lower fraction of hot internal residual (a result of decreased NVO) and a higher percentage of cooled external EGR. These lower pre-combustion temperatures were necessary to prevent engine knock at higher load. As pre-combustion temperature decreased, the region of flame propagation became a larger portion of the overall combustion process. As a result, the pressure and heat release curves began to resemble those of SI combustion. For each load point, peak cylinder temperatures were kept relatively low, consistent with dilute operation.

Fig. 2.10(a) shows the variation in CA10, CA50, and CA90 during the load sweep. CA10 occurred earlier as load was increased due to the advance in spark timing. CA50 was held constant throughout the load sweep, as required by the control strategy. CA90 increased with load due to an increase in burn duration as fast auto-ignition was replaced by flame propagation. Although combustion began earlier, it ended later due to the slow nature of the flame.

Fig. 2.10(b) shows ringing intensity and maximum rate of pressure rise (MPRR) as load was increased. Ringing intensity is a function of the MPRR of the average low-pass filtered cylinder pressure trace. At the lower end of the SACI regime, where the pressure trace resembled HCCI, there was a distinct region of auto-ignition, which had a high MPRR. As flame development increased with load, the MPRR decreased dramatically. As spark was advanced further to counteract the effect of flame speed, combustion was initiated earlier in the cycle and the maximum rate of pressure rise steadily increased. At high load SACI, ringing intensity became a tradeoff between the maximum heat release rate (depending on combustion mode) and spark timing. Ringing intensity did not exceed 4.0 MW/m<sup>2</sup> for any of these operating conditions.

Despite the behavior of ringing intensity, NO<sub>x</sub> emissions in Fig. 2.10(c) followed

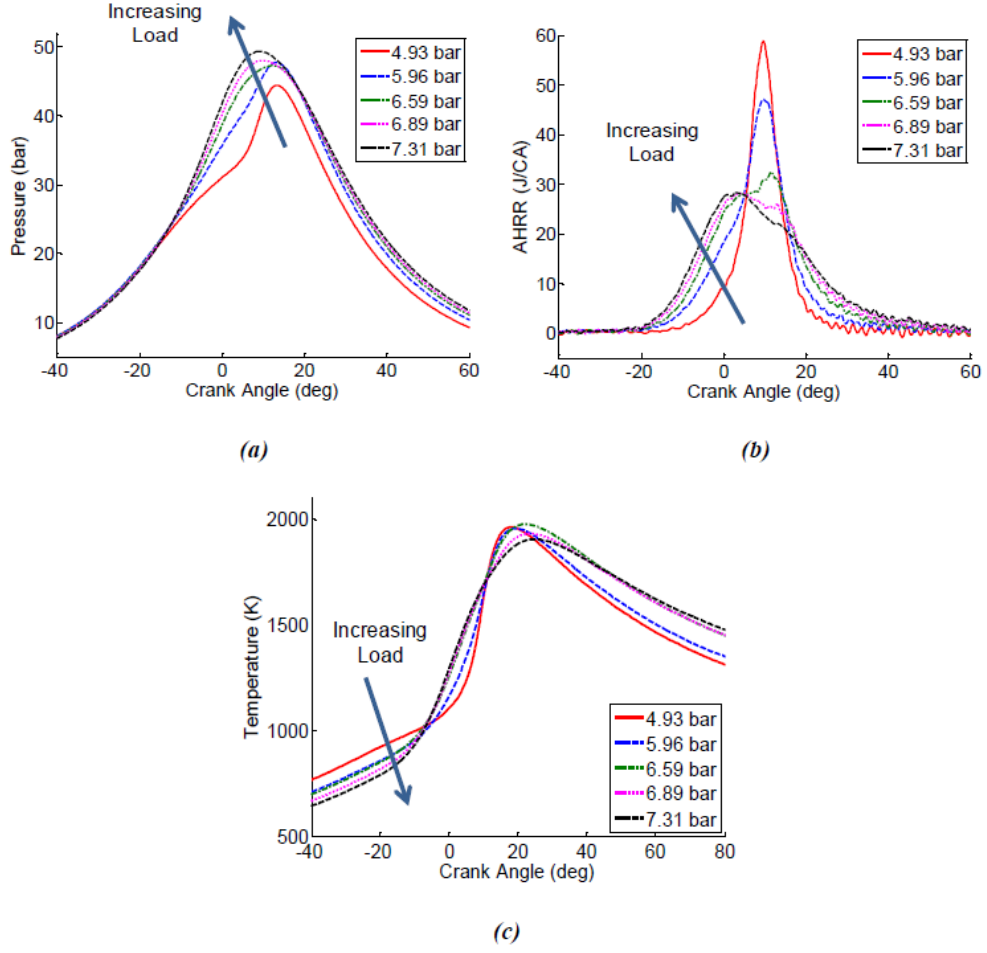


**Figure 2.9:** The effect of increasing NMEP (using spark, external and internal EGR) on (a) cylinder pressure, (b) apparent heat release rate, and (c) cylinder temperature.

an increasing trend with load. Although average temperatures remained low due to heavily dilute operating conditions, it is thought that in-cylinder temperature gradients became larger as flame propagation became more prominent. The burned region around the flame was much hotter than the region near the walls, and these high temperatures were responsible for the increase in engine-out NO<sub>x</sub> emissions. Although these levels exceeded the US-2010 standard, they could still be treated effectively since the overall mixture was stoichiometric.

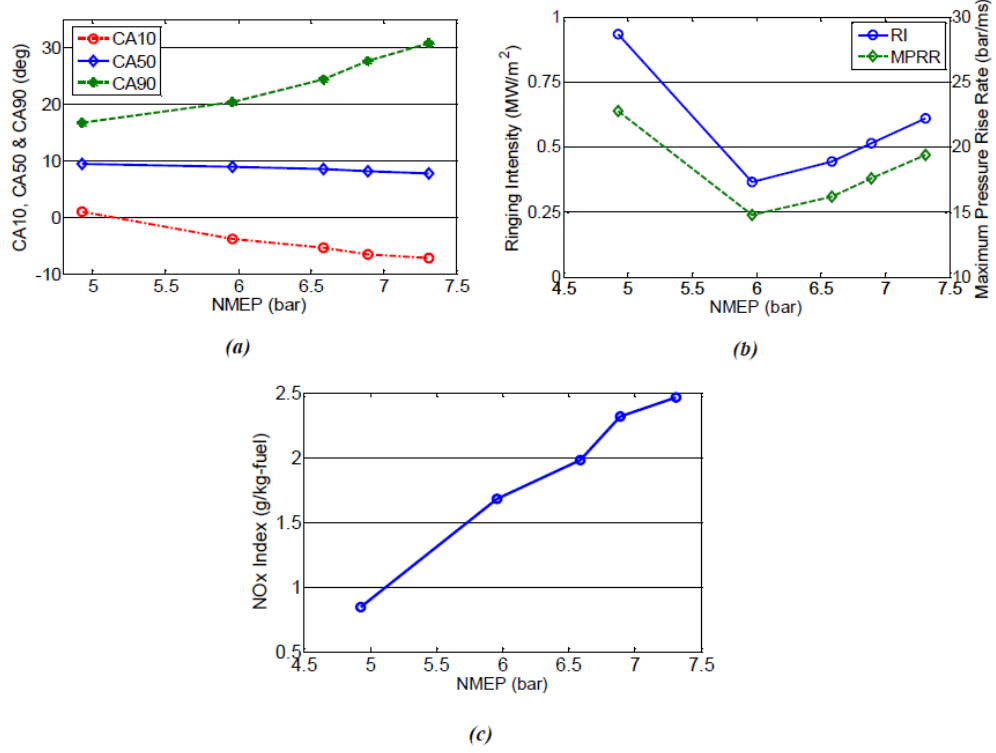


**Figure 2.10:** Combustion characteristics with increasing NMEP, including (a) CA10, CA50, and CA90, (b) ringing intensity, (c) NOx emissions.

## Mapping the SACI Regime

In Fig. 2.11, the regions of HCCI and SACI combustion are plotted with respect to load and combustion timing. SACI was achieved at several fueling rates (12.5-24 mg/cycle), which correspond to the various lines on the plot. With each increase in fueling rate within the SACI region, internal and external EGR were adjusted to maintain a stoichiometric mixture and provide the pre-combustion temperatures necessary for barely stable operation. Spark was then advanced until the ringing intensity limit was reached or endgas knock became apparent. As load increased, the acceptable range of CA50 shifted later in the cycle to avoid high pressure rise rates. A maximum load of about 7.5 bar NMEP was achieved in the SACI combustion regime.

Fig. 2.12 shows the combustion behavior at 7.3 bar NMEP and CA50  $\sim$  10 dATDC. At this condition, end-gas knock developed due to the high compression ratio of the engine (12.5:1). This condition was not accompanied by a high ringing intensity and resembled traditional SI knock. Attempts to mitigate this knock

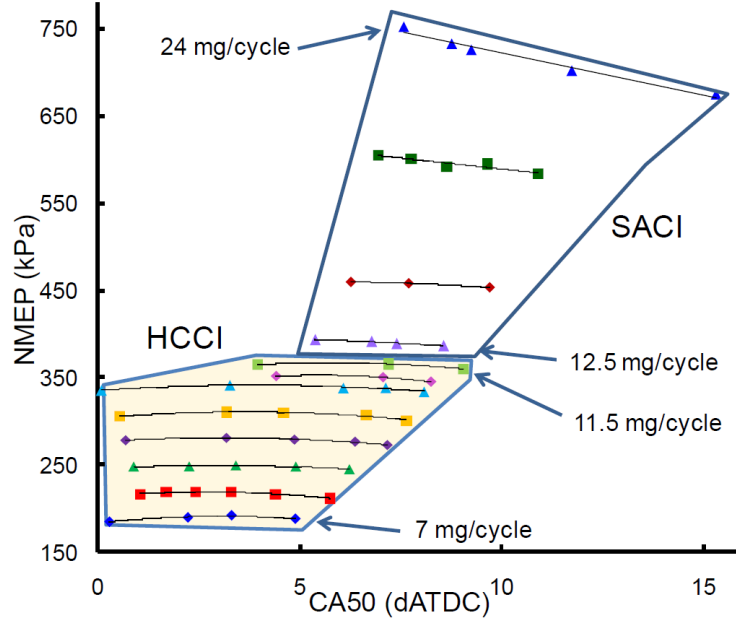


**Figure 2.11:** The regions of HCCI and SACI combustion.

through spark retard were unsuccessful and led to significant deterioration in combustion stability. Increasing external EGR fraction was not possible while maintaining a stoichiometric mixture, as the valves were at full duration and lift, ensuring a minimal internal EGR fraction. A late IVC strategy was attempted to decrease the effective compression ratio, but this led to a decline in NMEP, as the engine appeared to be limited by air induction.

Various contour plots of the SACI regime are seen in Fig. 2.13, 14, and 15. Fig. 2.13(a) shows the decrease in NVO as load was increased. This decrease occurred so that air induction into the cylinder could be increased at higher fueling rates. The lower internal residual fraction that resulted was responsible for decreasing pre-combustion temperatures and lowering the tendency of the mixture to auto-ignite. At the highest loads, positive valve overlap was achieved, resulting in a very small internal residual fraction, as seen in Fig. 2.13(b). Fig. 2.13(c) shows that external EGR fraction increased with load to dilute the charge, maintain a stoichiometric mixture, and prevent the onset of knock. While external EGR increased, internal EGR decreased more substantially, causing a reduction in total in-cylinder residual as load increased.

To quantify the limits of the various combustion regimes, including both air and EGR dilution, the metric phi prime ( $\phi'$ ) was used, defined as



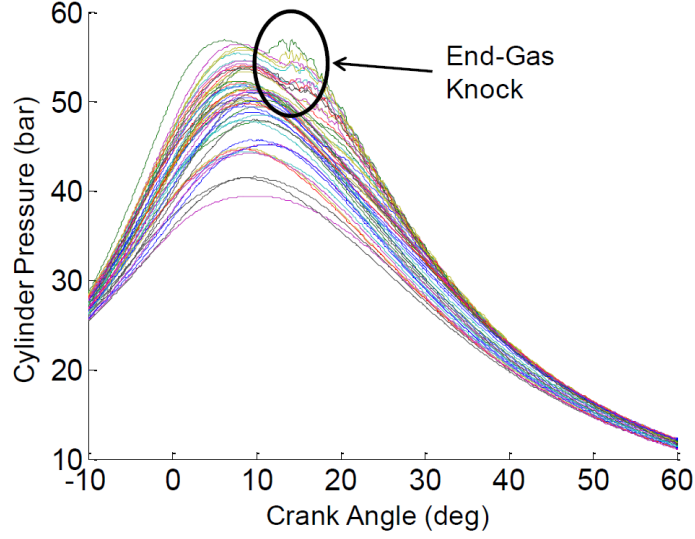


**Figure 2.12:** End-gas knock/unstable behavior for high load SACI (7.3 bar NMEP, CA50 -10dATDC) – 200 consecutive cycles of cylinder pressure data.

$$\phi' = \frac{\frac{F}{A+R}}{\left(\frac{F}{A}\right)_{ST}} = \frac{\phi \cdot (1 - RGF)}{1 + RGF \cdot \phi \cdot \left(\frac{F}{A}\right)_{ST}} \approx \phi \cdot (1 - RGF). \quad (2.2)$$

where mass of fuel, air, and residual are denoted by  $F$ ,  $A$ , and  $R$  respectively, and  $\phi$  is the operating equivalence ratio. The subscript  $ST$  denotes stoichiometric conditions.  $RGF$  is the total residual gas fraction, including both internal and external EGR. The approximation holds because the second term in the denominator is small compared to one. Essentially,  $(\phi')$  is a measure of the specific energy of the charge (the amount of fuel compared to air and residual) and approximates IMEP well for a naturally-aspirated engine operating under dilute conditions [49]. Since  $(\phi)$  was equal to  $\sim 1.0$  for the entire experiment,  $(\phi')$  provided a measure of EGR dilution at each load condition. Since EGR dilution decreased as load increased, a higher  $(\phi')$  was achieved.

Fig. 2.13(d) shows  $(\phi')$  at various SACI conditions. From the graph, the maximum  $(\phi')$  reached for this experiment was  $\sim 0.7$ . According to the literature [41], this value is approximately the lean limit for SI combustion. Therefore, SACI can be used to bridge the gap between unassisted HCCI and conventional SI by relying on increased unburned temperatures to sustain flame propagation. As  $(\phi')$  increases, so does the strength of the flame. This was noticed in Fig. 2.9(b), where the fraction of the flame propagation heat release increased with  $(\phi')$ . Zigler [100] showed with optical engine experiments that spark-initiated reaction fronts are weak for low  $(\phi')$

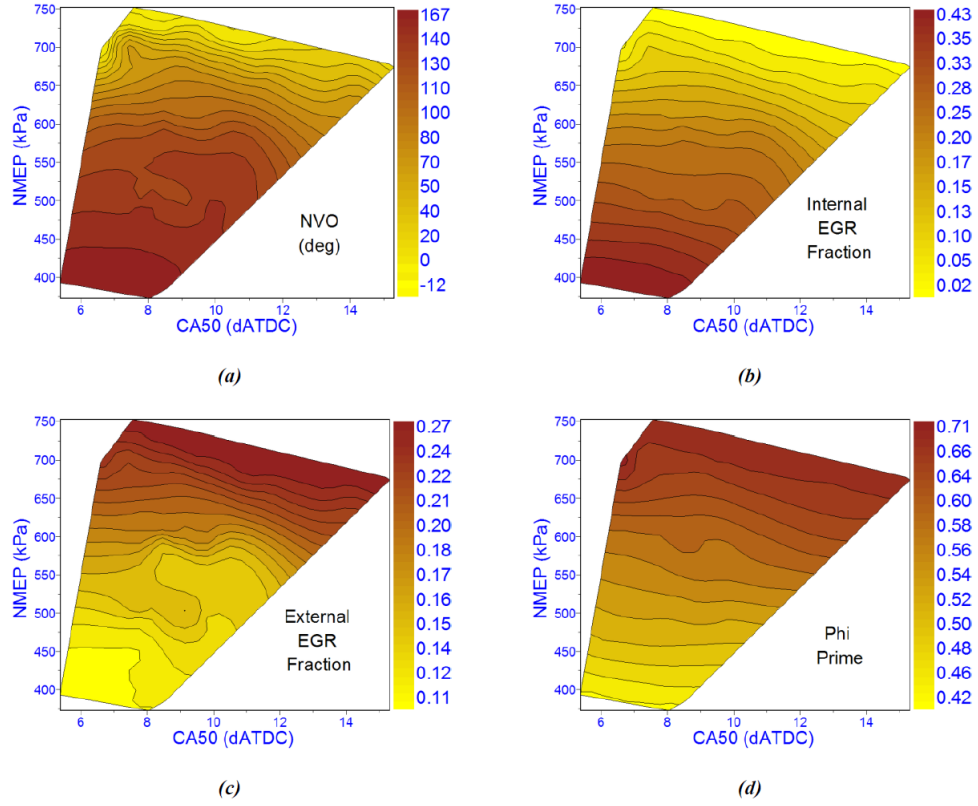


**Figure 2.13:** Changes in residual gas content within the SACI regime as load is increased, including (a) NVO (deg), (b) internal EGR fraction, (c) external EGR fraction, and (d) phi prime ( $\phi'$ ).

values and become more well-defined as ( $\phi'$ ) increases.

Ringling intensity, as shown in Fig. 2.14(a), appears to only be an issue at low load conditions with advanced spark timings. At these points, the combustion was still primarily volumetric and resembled that of HCCI. The early autoignition event caused a rapid increase in cylinder pressure, which correlated to a high ringling intensity. Ringling was evaluated with Eng's equation [24] based on the slope of the main combustion event. As noted earlier, as load increased and flame propagation became more prominent, end-gas knock began to occur due to the engine's high compression ratio. This high load knock was not captured in Fig. 2.14(a) because it occurred intermittently from cycle-to-cycle; therefore, the average magnitude of the knock over 200 cycles was much lower than that of the cycle-based ringling events. The peak rate of pressure rise in SI knock was also much lower than in HCCI auto-ignition, as the majority of the mass had already been burned when the SI knock occurred. Ringling and end-gas knock are different phenomena and should be

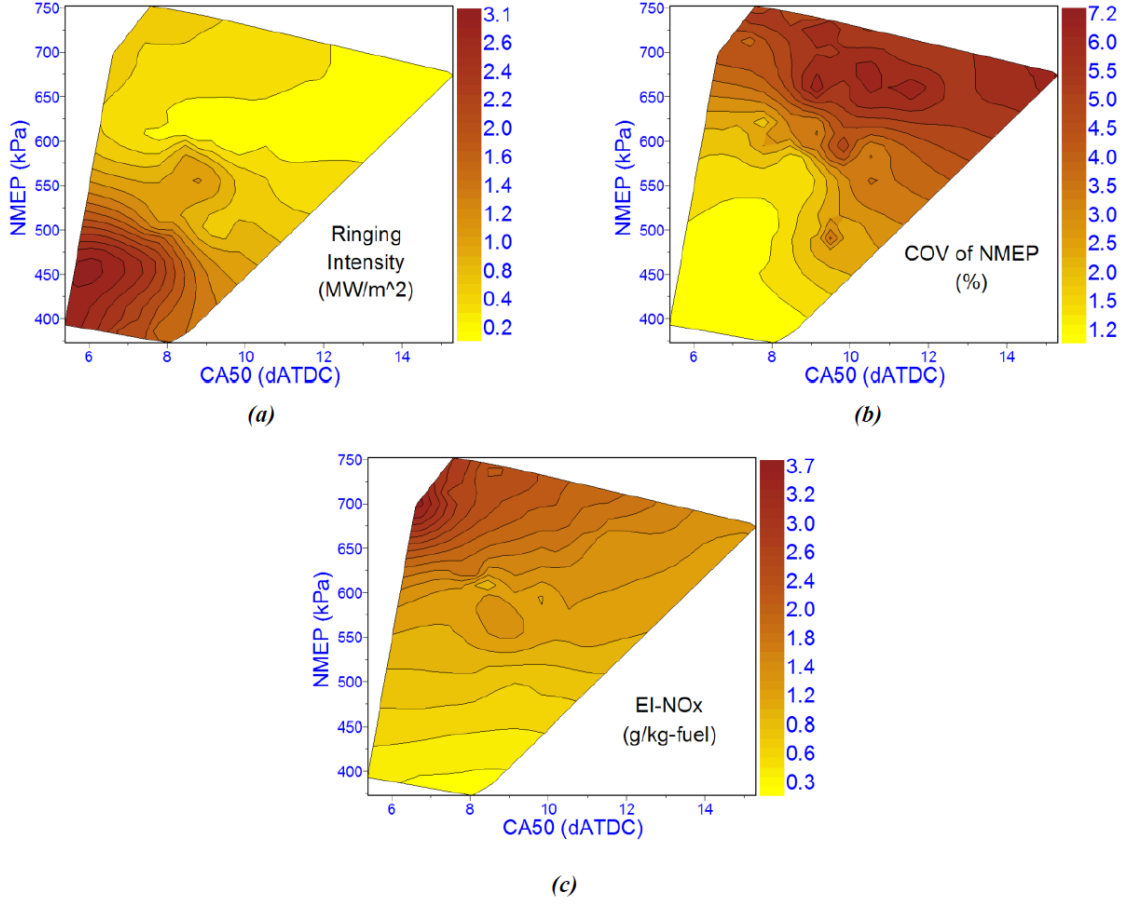


**Figure 2.14:** Combustion characteristics in the SACI regime, including (a) ringing intensity ( $MW/m^2$ ), (b) COV of NMEP (%), and (c) EI-NOx ( $g/kg\text{-}fuel$ ).

evaluated using different methods. Ringing appears to be an appropriate measure of potentially harmful energy release when a relatively dilute charge ignites more or less homogeneously, while end-gas knock refers to auto-ignition of a small portion of the charge, but with a relatively high local energy content ( $\phi$ ) as seen here at high load.

Fig. 2.14(b) shows combustion stability as quantified by COV of NMEP throughout the SACI regime. In an attempt to avoid the knocking behavior at high load, spark timing was retarded. However, this resulted in late and unstable combustion. These knock problems could potentially be solved through the addition of more external EGR. However, at the high load conditions, it was impossible to do this and maintain a stoichiometric mixture, as the valve events were at full lift and duration. A late IVC strategy led to a decrease in NMEP.

Fig. 2.14(c) shows that NO<sub>x</sub> emissions increased significantly at higher loads. This was due to stronger flame development and higher burned zone temperatures as load was increased. As seen in Fig. 2.9(c), average in-cylinder temperatures remained low throughout the load sweep due to charge dilution with EGR. However, as flame propagation became more prominent, two distinct burned and unburned zones developed, the temperature of the burned zone (consumed by the flame) being much higher than the temperature of the unburned zone (not yet consumed by the flame). As flame development increased with load, the temperature of the burned zone increased significantly, leading to greater NO<sub>x</sub> emissions. The US-2010 standard was exceeded for the majority of the SACI regime. However, since the overall mixture was stoichiometric, these emissions could be treated with a three-way catalyst.

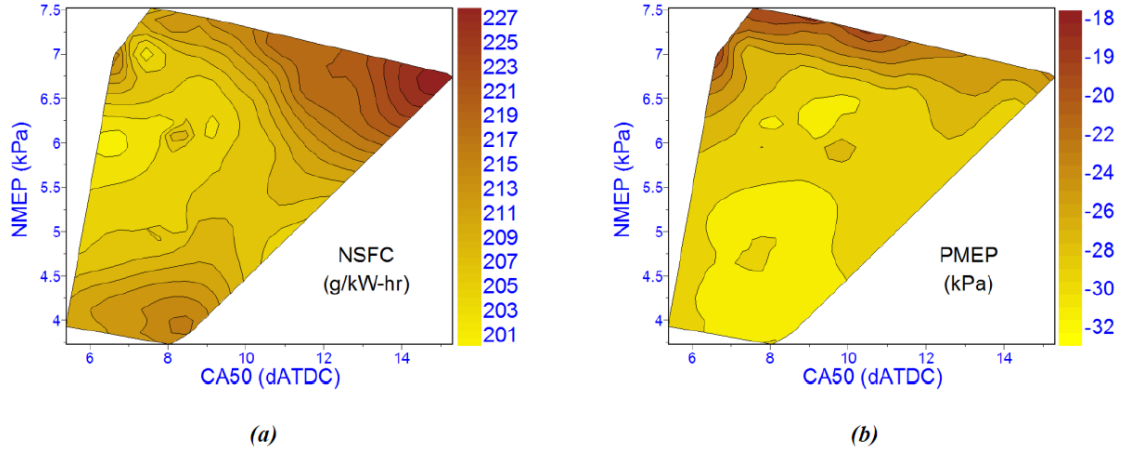


**Figure 2.15:** Efficiency characteristics in the SACI regime, including (a) NSFC (g/kW-hr) and (b) PMEP (kPa).

Fig. 2.15(a) shows the variation in NSFC with load and combustion timing. Overall, it appears that NSFC increased as combustion was retarded. NSFC was especially high at the high load conditions, possibly due to the increased COV of NMEP encountered at these operating points. Although the range of PMEP was relatively low, as shown in Fig. 2.15(b), it could help explain the shape of the NSFC diagram. The increase in NSFC at low load can be explained by the increase in pumping work as the result of a high degree of NVO. Pumping work decreased as load increased, and NSFC became heavily affected by combustion timing in this region.

## 2.7 CONCLUSIONS

The engine was mapped first in lean HCCI mode, and fueling rate was steadily increased until the ringing/instability limit of combustion was reached. Load extension into the SACI regime was then accomplished by increasing fueling rate and using a combination of spark assist, internal EGR, and cooled external EGR to control pressure rise rates. The engine was operated at unheated, naturally-aspirated conditions throughout the experiment, and engine speed was maintained at 2000 rpm.

This study showed that stable, dilute, and efficient combustion could be achieved with SACI at loads above the allowable limits for naturally-aspirated HCCI. The SACI combustion mode provided a pathway of transition from pure HCCI to pure SI. The following results were also obtained.

1. Lean HCCI without spark assistance was achieved up to  $\sim 3.7$  bar NMEP. Combustion phasing was heavily dependent on the degree of NVO and the fraction of hot internal residual under certain conditions. A large degree of NVO introduced complex cycle-to-cycle feedback, which greatly affected combustion stability at higher loads.

2. Load extension was achieved using a combination of spark assist and EGR dilution. Maintaining a dilute mixture limited maximum in-cylinder temperatures, increasing Poisson's constant of cylinder charge and allows for more efficient operation than conventional SI at the same load conditions. A maximum load of  $\sim 7.5$  bar NMEP was achieved within the SACI region. At these loads, NO<sub>x</sub> emissions exceeded current emission standards; however, conventional after-treatment could be used due to the stoichiometric mixture.

3. Within the SACI regime, spark advance had a major effect on combustion behavior, causing an increase in peak cylinder pressure and temperature. CA<sub>50</sub> was advanced, heat release occurred earlier, and burn duration decreased as spark was advanced. Ringing intensity and NO<sub>x</sub> emissions also increased due to higher rates of pressure rise and in-cylinder temperature. Expansion work and engine efficiency increased as combustion became more "constant volume" for a given fueling rate.

4. Within the SACI regime, heat release analysis showed a noticeable region of flame propagation followed by autoignition. Features of HCCI combustion and SI combustion co-exist throughout the regime.

5. It was possible to transition from low load HCCI combustion to high load SI combustion. As load increased, rapid auto-ignition was replaced by flame propagation, burn duration increased, and spark timing was advanced to maintain constant combustion phasing. Pre-combustion temperatures decreased as a portion of the hot internal EGR was replaced by cooled external EGR. At higher loads, flame propagation became more effective in reducing pressure rise rates and combustion noise.

Peak combustion temperatures were kept relatively low due to air and EGR dilution, resulting in high thermal efficiency.

6. The ringing intensity calculation of Eng [24] was appropriate mainly to describe the combustion noise associated with homogeneous auto-ignition. The resulting value depended heavily on the maximum rate of pressure rise associated with the primary combustion event. This equation was not effective at identifying the presence of end-gas knock at higher load SACI conditions. Ringing was only apparent at lower load where the combustion resembled that of HCCI. In this sense, ringing intensity can actually be used to differentiate between HCCI-like combustion and Si-like combustion, since the ringing intensity for the latter mode was always quite low.

7. The relatively high compression ratio (12.5:1) of this engine created problems with end-gas knock at the higher load operating conditions. Retarding the spark in an attempt to mitigate this phenomenon only resulted in unstable combustion. Decreasing the effective compression ratio through late IVC created challenges with maintaining high IMEP.

8. NOx emissions increased significantly at high load SACI conditions due to the greater proportion of flame propagation heat release and the appearance of distinct burned and unburned mixture zones. Average in-cylinder temperatures remained low, but temperature gradients became larger as a result of stronger flame development.

9. SACI allowed for successful engine operation above the HCCI ringing limit and below the SI misfire limit, bridging the gap between the two combustion regimes. Just above the HCCI limit, increased unburned temperatures allowed weak flames to be sustained at very diluted mixtures. These flames helped induce auto-ignition when the mixture was too cold to auto-ignite consistently without spark. As load increased, flame development became stronger and total internal residual was reduced, resulting in lower unburned temperatures.

## Chapter 3

# Knock In Various Combustion Modes in a Gasoline-Fueled Automotive Engine

### 3.1 INTRODUCTION

Recent research shows that spark-assisted compression ignition (SACI) can bridge the gap between HCCI combustion at low load and SI combustion at full load engine operation [96], [52], [75]. Within the SACI region, a portion of the mixture is burned by flame propagation, followed by controlled auto-ignition of the remaining charge. A conceptual modeling study was carried out for a naturally aspirated gasoline fueled automotive engine with a 12:1 compression ratio [50]. The results of this study are shown in Fig. 3.1, which maps the pathway from low load to full load operation using various methods of load control. The lowest (baseline) thermal efficiency corresponds to throttled spark ignition (SI) stoichiometric operation. Unthrottled operation using an early intake valve closing (EIVC - dashed line) strategy can slightly improve this efficiency. Advanced combustion, such as HCCI with air and/or EGR dilution, has the potential to significantly improve thermal efficiency (top two lines in Fig. 3.1), not only because pumping losses are minimized, but because peak combustion temperatures remain low, resulting in a high ratio of specific heats  $\gamma$ . Fuel-to-charge ratio  $\phi' \approx \phi(1 - EGR)$  is displayed in the figure along the advanced combustion curve as a measure of the charge dilution with the EGR (Exhaust Gas Recirculation).

Fig. 3.2 shows the results from an experimental study [52] performed on the FFVA (Fully Flexible Valve Actuation) single cylinder research engine at the University of Michigan. Net specific fuel consumption (NSFC) and specific NO<sub>x</sub> production for points of optimum combustion phasing in HCCI and SACI are plotted

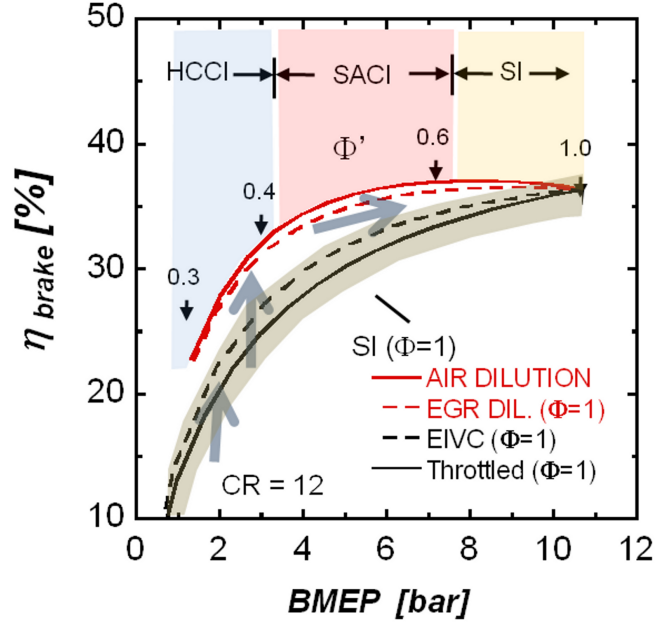


**Figure 3.1:** Conceptual model study results: pathways from low to high load using advanced combustion at naturally aspirated conditions.

as a function of engine load (net mean effective pressure). Approximately 400 kPa is the load limit for HCCI combustion controlled solely by negative valve overlap (NVO). Beyond this point stable HCCI combustion was no longer possible because of the simultaneous occurrence of misfire and knock.

A practical limit in NO<sub>x</sub> emissions (1.0 g/kg fuel) was reached for lean operation ( $\phi < 1$ ) without exhaust aftertreatment at this point as well. For this reason, a stoichiometric air-fuel mixture strategy ( $\phi = 1$ ) was used as load was increased beyond the limits of HCCI and into the SACI regime. This strategy is compatible with three way catalyst aftertreatment and effectively removes the NO<sub>x</sub> constraint. Recent studies [96] and [75] show similar conclusions. Spark and external EGR had to be introduced to achieve stable combustion and avoid knock within the SACI regime, where a portion of the mixture is first consumed by flame propagation, followed by controlled auto-ignition of the remaining charge. Load was increased by varying the proportions of cooled external to hot internal EGR together with spark timing control. The ratio between flame propagation and auto-ignition was gradually increased with load, until SI-like combustion was reached at the highest load condition. For both of the aforementioned combustion modes, high load operation was limited by the presence of knock as seen in Fig. 3.2.

The objectives of this study are to explore the differences between HCCI and



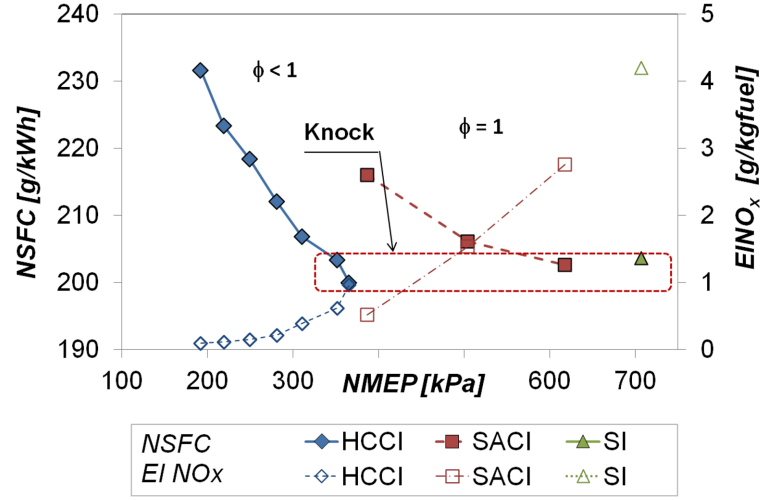


**Figure 3.2:** Experimental study results [52] NSFC and NOx emission index vs. engine load for optimum combustion phasing points at various combustion modes.

end gas knock and to apply and compare a number of commonly used metrics for knock and noise over the range of HCCI, SACI and SI combustion. In view of the importance of knock limiting the HCCI, SACI and SI combustion, numerous knock metrics have been developed and used in the combustion engine community. It is unclear whether the different commonly used metrics agree with one another within and between different combustion modes. To our best knowledge, this is the first time these different metrics have been applied and compared for various combustion modes.

## 3.2 EXPERIMENTAL SETUP

All experimental data presented in this study were acquired with a FFVA single cylinder research engine at the Walter E. Lay Automotive Laboratory at the University of Michigan. Tab. 2.1 lists the specifications of the engine.

The engine is equipped with a Sturman Hydraulic Valve System that allows independent control of all intake and exhaust valves. The system allows continuously variable lift and valve event duration, with up to two valve events per cycle. Fig. 2.1 shows a schematic of the FFVA engine setup. A sketch at the figure Fig. 3.3 shows the position of the spark plug, injector, valves and cylinder pressure transducer in the engine head. Cylinder pressure is measured with a Kistler 6125A uncooled piezoelectric pressure transducer mounted in the corner of the cylinder head along the axis of the pent-roof. The pressure transducer is connected to the combustion

chamber via a  $\varnothing 4.0$  mm x 4.0 mm passage in the cylinder head. A heat shield with multiple holes is installed over the diaphragm of the sensor to protect it from thermal shock [91] caused by fast change in temperature of burned gas products. Natural frequency of the pressure sensor itself is 75 kHz. Natural frequency of the Helmholtz resonator model [91] of the passage and the cavity varies between 34 to 60 kHz within the temperature range between 500 and 1500 K. For a multiple slots heat shield Randolph [62] reports Helmholtz resonance at 84 kHz at 200°C. Since acoustic-wave frequencies for the passage and the sensor heat shield are significantly higher than the expected acoustic frequencies of the waves caused by knock, the distortion of the pressure signal has been neglected.

The signal from the transducer is amplified using an IFEM AVL charge amplifier. Crank angle based cylinder pressure is sampled with a resolution of 0.1 crank angle degrees. A 2613B Kistler crank angle encoder is installed at the free end of the crankshaft. All measured points reported in this study are taken at steady state at a constant engine speed of 2000 rpm. Uniform crankshaft angular speed over the cycle is assumed during cylinder pressure analysis. The engine is equipped with a heavy flywheel thus limiting crankshaft speed variation within  $\pm 20$  rpm during the cycle. This variation at the average engine speed 2000 rpm is considered not to significantly affect any of the results shown in this paper.

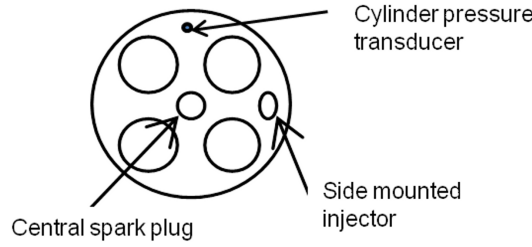


**Figure 3.3:** Position of the spark plug, injector, valves and cylinder pressure transducer in the engine head.

Pressure records of 200 consecutive cycles are acquired for each operating point. An AVL Indiset 642 high-speed data acquisition system is used for all crank angle based measurements. A low speed data acquisition system based on National Instruments hardware and LabView software is used for all time based measurements of pressures, mass flows and temperatures in the engine's peripheral systems. Coolant and lubrication oil flow and temperatures are maintained at constant values using PID controllers. Engine injection, spark timing and dwell are adjusted manually. A more detailed description of the experimental setup, data acquisition systems and post processing tools used in this study can be found in Manofsky et al. [52]. An automated and integrated low and high speed postprocessing code, developed in-house,

is used for heat release analysis.

### 3.3 HCCI AND SI KNOCK

The high load operation of HCCI and SI combustion is limited by knock, which is caused by elevated temperatures that lead to rapid auto-ignition, resulting in in-cylinder pressure oscillations. The transfer of these oscillations to the engine structure causes vibrations. Excessive noise caused by structure vibration is usually the first symptom of knock. Knock also increases heat transfer from the working fluid to the walls and if left uncontrolled it can lead to severe engine damage. Two examples of knock from this study are shown in the cylinder pressure traces of Fig. 3.4. The image on the left depicts high load HCCI knock, while the one on the right resembles SI knock. The shaded area represents the envelope of unfiltered pressure traces in the record of 200 cycles. The size of the area corresponds to the magnitude of the cylinder pressure variation at each crank angle. The smooth curves that lie within the envelope represent the filtered average cycle and the curve that lies at the upper boundaries of the envelope represents the unfiltered pressure trace of the cycle with the highest peak cylinder pressure.

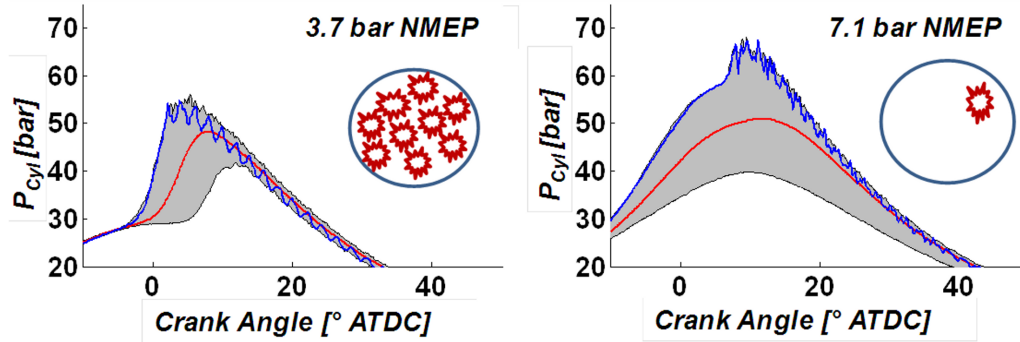


**Figure 3.4:** HCCI “volumetric” knock at 3.7 bar NMEP (left), SI “end gas” knock at 7.1 bar NMEP (right).

The “volumetric” HCCI knock case, in which auto-ignition is generally believed to be initiated simultaneously at multiple locations within the cylinder, is displayed on the left-hand side of Fig. 3.4. On the right, SI “end gas” knock can be described as a small autoignition pocket near the wall, where the energy density, pressure, and unburned temperature are higher than the energy density in diluted HCCI operation. To illustrate the differences, a Fast Fourier Transformation (FFT) on a cycle-to-cycle basis was applied to the two aforementioned cases to analyze the knock and describe the main difference between “volumetric” and “end gas” knock.

High-pass filtered pressure traces (5 kHz cutoff frequency) were cropped within the crank angle window from  $-20^\circ$  to  $+120^\circ$  aTDC and were used as an input to the FFT analysis. Fig. 3.5 depicts the amplitude-frequency spectrum of the pressure oscillations over 200 consecutive engine cycles. The frequency distribution of the HCCI “volumetric” knock shows a steady knock pattern with one dominant frequency of the first circumferential oscillation mode. Other oscillation modes show uniform decrease in amplitude. SI “end gas” knock on the other hand shows a less uniform distribution in frequencies, a larger difference in knock magnitude from the first to the second circumferential modes and cycle-to-cycle behavior with irregularly distributed peaks. SI knock is believed to show more variation because it starts at one, localized location that moves from cycle to cycle. SI knock also typically begins after TDC, while the cylinder charge is expanding. If an auto-ignition does not occur near TDC, it is less and less likely to occur at a later time. HCCI knock, on the other hand, begins in the bulk gas and is less likely to vary as much spatially. HCCI knock also occurs closer to TDC, so if it doesn’t occur at one crank angle, the likelihood of it occurring in subsequent crank angles is high.

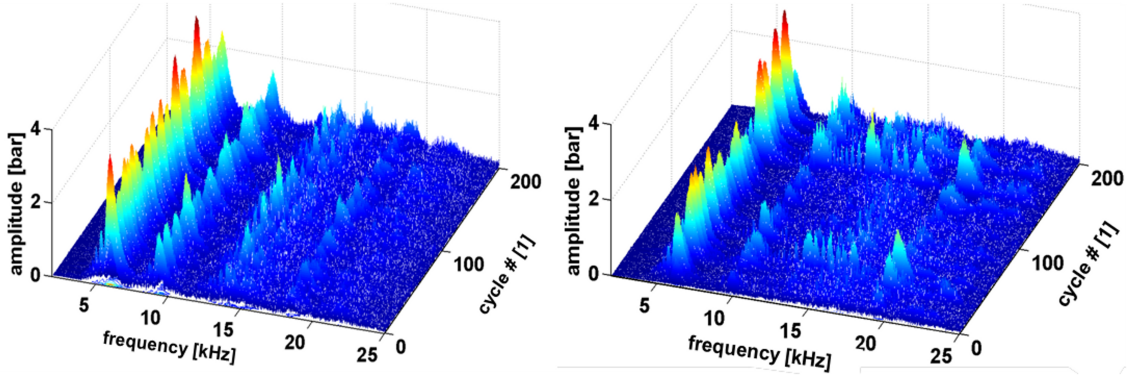


**Figure 3.5:** Cycle-cycle FFT analysis of high pass cylinder pressure data for knock at HCCI 3.7 bar NMEP (left), and SI 7.1 bar NMEP (right).

### 3.4 KNOCK QUANTIFICATION METHODS

The following section summarizes the most commonly used filtering techniques for knock identification. To be used in real time in the laboratory, these methods should be fast and simple enough to be carried out on a cycle-to-cycle basis so that knock can be detected quickly to avoid engine damage. Runaway knock can damage the engine within several cycles, so it is important that the robustness of the knock evaluation method and computational effort be optimized. Various filtering

techniques applied to measured cylinder pressure traces are used to quantify knock.

According to König et al [48] mechanical and thermal wall stress during developing detonation increased four and three times respectively compared to deflagration. Syrimis et al [72] show a correlation between heat flux and knock intensity at light and heavy knock. Light knock shows the increase in heat transfer in the piston area inside the end-gas region, while heavy knock results show heat transfer increases over the entire piston. They used two knock parameters based on the band pass filtered pressure data RMS (PRMS) and max amplitude ( $\Delta P_{max}$ ) of the band pass filtered cylinder pressure oscillation. The PRMS was found to be more reliable knock indicator than other indices. Chun et al calculated the knock intensity from the cylinder pressure data using a digital bandpass filter with 5 to 10 kHz bandpass [18]. The maximum amplitude ( $P_{max}-P_{mean}$ ) of the filtered pressure was used as a measure of the knock intensity. Börje et al. [30] report increased heat flux for selected cycles with knock intensity. The maximum amplitude of the high pass pressure oscillation ( $\Delta P_{max}$ ) was determined as a knock intensity measure in their study. König and Sheppard [47] adopted the “knock intensity factor” Eq. (3.1) which had been found by earlier workers to correlate with the development knock damage in combustion chamber.

$$KI_{20} = \sum_{i=1}^{N_{samp}} (P(i) - P_{mean})^2 \frac{1}{N_{samp}}. \quad (3.1)$$

(where  $P_{mean}$  is the average pressure value – zero level of the high pass filtered data and  $N_{samp}$  is the number of pressure samples within  $20^\circ$  crank angle range following the offset of the first pressure pulse). All of the above methods have in common, a reliance on various forms of high pass filtering of the pressure trace.

## High Pass Ringing Intensity

According to [5], the excitation of the engine structure is due to the first few waves of pressure oscillations, and it is proportional to the acoustic intensity of these waves. The intensity of acoustic waves can be expressed as Eq. (3.2)

$$I = \frac{1}{2\gamma} \frac{(\Delta P)^2}{P} \sqrt{\gamma R T}, [W m^{-2}] \quad (3.2)$$

where  $\gamma$  is the ratio of specific heats,  $\Delta P$  is the pressure fluctuation amplitude,  $P$  is pressure,  $R$  is the gas constant, and  $T$  is temperature.

Eng [24] named this quantity ringing intensity. In this study, we will use the term High Pass Ringing Intensity to describe this equation, because a high pass filtered pressure trace is used as the input.

In our implementation of the *High Pass Ringing Intensity* formula, a 5 kHz two pole Butterworth high pass filter is applied to a measured cylinder pressure trace. For each individual cycle a maximum amplitude (peak-to-peak)  $\Delta P_{max}$  of filtered pressure data is found and used as an input into equation Eq. (3.2).  $P_{max}$  is the peak cylinder pressure,  $R$  is the gas constant, and  $T_{max}$  corresponds to peak cylinder temperature.

$$RI_{HP} = \frac{1}{2\gamma} \frac{(0.05 \frac{dP}{dt_{max}})^2}{P_{max}} \sqrt{\gamma R T_{max}} [W/m^2]. \quad (3.3)$$

To be able to calculate this quantity in real-time without having to evaluate composition and maximum temperature, a simplified form Eq. (3.4) has been derived from equation Eq. (3.2), using kPa as units of pressure.

$$RI_{HP} = 3200 \frac{(\Delta P_{max})^2}{P_{max}} [MWm^{-2}]. \quad (3.4)$$

The formula was compared to the more complete version and found to be valid over a wide range of operating conditions (NMEP=100-750 kPa,  $\phi=0.3-0.8$ ) with a negligible error.

## Low Pass Ringing Intensity ( $RI_{LP}$ )

This method, known also as the ringing index Eq. (3.5), was derived by Eng [24] and has been widely accepted as the primary metric for HCCI knock [96], [68], [39], [20], [40], [21]]. It is an empirical correlation between a low pass filtered  $(dP/dt)_{max}$  and  $\Delta P_{max}$ , Eq. (3.3) and uses  $\beta$  as a correlation coefficient. According to Eng,  $\beta$  is a fixed value determined from engine geometry. A value of  $\beta = 0.05$  ms has been commonly used. The main advantage of the low pass ringing intensity equation is that it can easily be used to quantify knock in HCCI engine simulations, as most models do not capture high frequency oscillations. There are many ways to calculate the low-pass ringing intensity from measured pressure traces. For this study, a low-pass filter with a cutoff frequency of 5 kHz was applied to individual cycles of pressure data from -20 to 120 CAD aTDC. A numerical derivative method is then applied to each of the filtered pressure signals to determine the maximum rate of pressure rise. The time-based rate of pressure rise should be calculated as opposed to the crank angle based rate in order to eliminate engine speed dependence. The average crankshaft speed can be used for this conversion, neglecting the crankshaft speed variation over the cycle. Once the maximum value of the rate of pressure rise is found, the ringing intensity is calculated using Eq. (3.5). The other terms in this formula are identical to the terms used in Eq. (3.6). Yun et al. [96] suggest using a simplified form of this calculation Eq. (3.6), where cyclic variation in cylinder properties and

peak cylinder temperature can be neglected, as in the case of the simplified version of the high pass ringing intensity Eq. (3.4).

$$RI_{LP} = \frac{1}{2\gamma} \frac{(\beta (\frac{dP}{dt})_{max})^2}{P_{max}} \sqrt{\gamma R T} [W m^{-2}], \quad (3.5)$$

$$RI_{LP} = 2.88e-8 \frac{((\frac{dP}{d\theta})_{max} rpm)^2}{P_{max}} [W m^{-2}]. \quad (3.6)$$

The limit value in ringing intensity varies from author to author. Numbers in the range between 2 up to 6  $MW m^{-2}$  are usually reported [48] [5] and [20]

## Combustion Noise Evaluated from Cylinder Pressure

The combustion noise measurement is a simple filtering technique developed for the measurement of the noise radiated by engine surfaces in response to combustion excitation [64]. The arrival of diesel direct injection technology into the passenger vehicle sector in the 1980's made the use of this technique necessary in R&D to cope with the strict vehicle noise limits. A FFT of the pressure signal is taken and filtered by two filters in series: a "U filter" that emulates the attenuation by the engine mass and an "A" filter that emulates the noise reception by the human ear. Fig. 3.6 shows the characteristics of the two filters. The RMS value is calculated and the result is scaled and reported in dB [8]. The commercially available combustion noise meter uses analog electronic circuitry with no crank angle position synchronization during measurement. Not measuring crank speed may lead to problems in distinguishing between cylinder pressure oscillations and other sources of vibration, such as valve closing events. In this study combustion noise evaluation was performed digitally on a cycle-cycle base as an embedded function in the high speed data acquisition system [68].

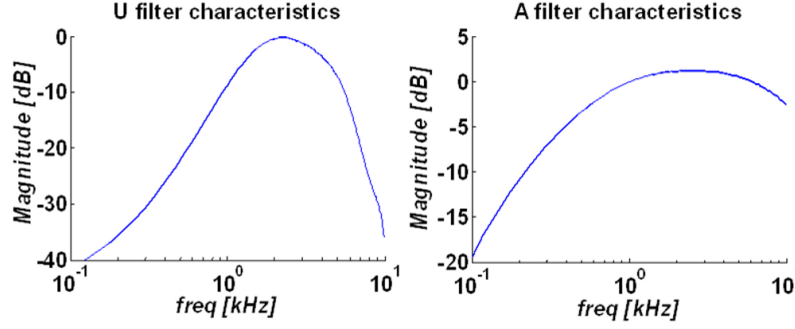


**Figure 3.6:** “U filter” (left) and “A filter” characteristics (right).

## 3.5 RESULTS

### Operating condition description

Fig. 3.7 describes the operating regimes used in this study. The engine was operated at constant speed of 2000 rpm. The individual data points correspond to the optimum combustion phasing for each load level. For the HCCI mode the optimum combustion phasing expressed by parameter CA50 was  $3.5^\circ$  aTDC and SACI and SI points this parameter was  $8.5^\circ$  aTDC.

### HCCI mode

HCCI combustion phasing was controlled by capturing hot internal residual using NVO levels up to 187 CAD, as shown in Fig. 3.7a). Neither spark nor external EGR were implemented as part of the control strategy. Fueling rate varied from 7.5 mg/cycle up to 11.5 mg/cycle, seen in Fig. 3.7b).

A maximum fuel-air equivalence ratio of  $\sim 0.65$  was achieved, however due to the presence of internal EGR, the maximum fuel to charge ratio  $\phi_f \approx \phi(1 - EGR)$  was  $\approx 0.45$ , as shown in Fig. 3.7c). From Fig. 3.7d), it is clear that the rate of pressure rise gradually increased as load increased, reaching a maximum value of around 60 bar/ms at 4 bar NMEP.

### SACI to SI Transition

Extending the load beyond HCCI and into the SACI regime requires fine control over spark advance, internal EGR, and external EGR. Throughout the SACI regime, a combination of internal EGR and external EGR was used to maintain a



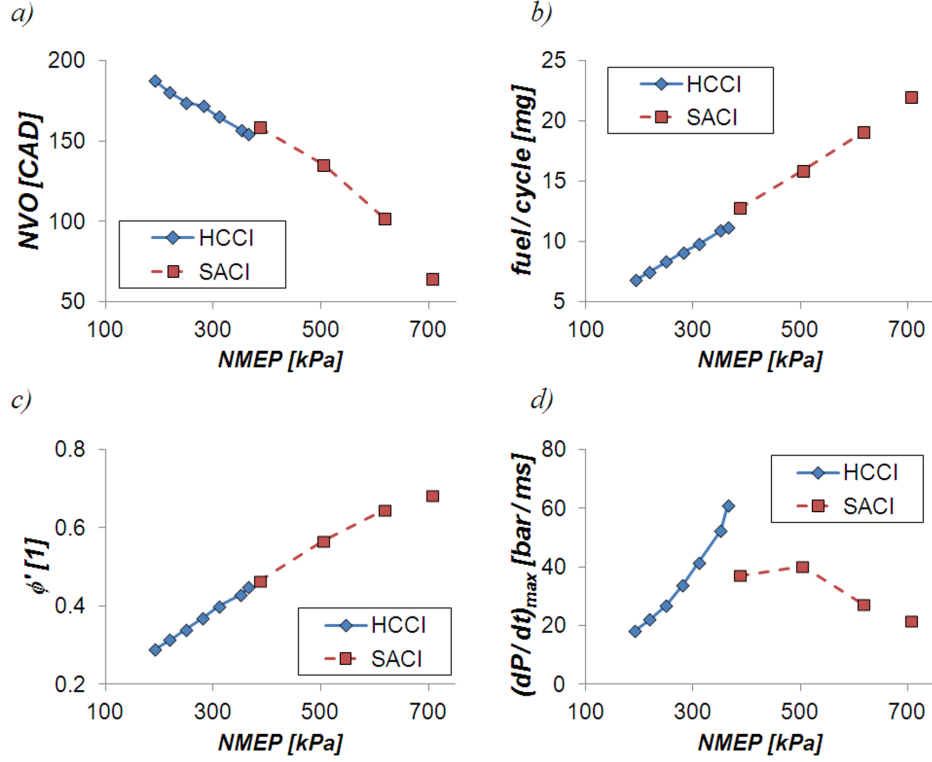


**Figure 3.7:** a) negative valve overlap, b) fuelling rate, c) fuel to charge equivalence ratio  $\phi'$  and d) peak rate of pressure rise vs. engine load. SI point denoted by single unconnected filled square.

stoichiometric air-fuel mixture. At low load SACI operation, the valve lifts were set to achieve symmetrical NVO for trapping the hot residual. As load increased, more fuel was injected per cycle; at the same time more air was inducted into the cylinder by decreasing the amount of NVO and increasing the valve lift in small increments from 4 to 10 mm, as seen in the valve traces of Fig. 3.8(a). The percentage of external EGR was increased slightly with load to maintain this stoichiometric mixture, reaching a maximum value of about 25%. This external EGR was also helpful in preventing knock at higher load operation.

As load increased and NVO decreased, the proportion of internal EGR to external EGR was gradually reduced, and flame propagation began to play a larger role in the overall heat release, seen in Fig. 3.8(b). At the lowest load condition, auto-ignition was the primary method of heat release, while the highest load condition resembled SI heat release with a small amount of auto-ignition near the end of the combustion process. This highest load condition of 7.1 bar NMEP corresponded to a fueling rate of 24 mg/cycle. At each load condition, combustion phasing was controlled by spark

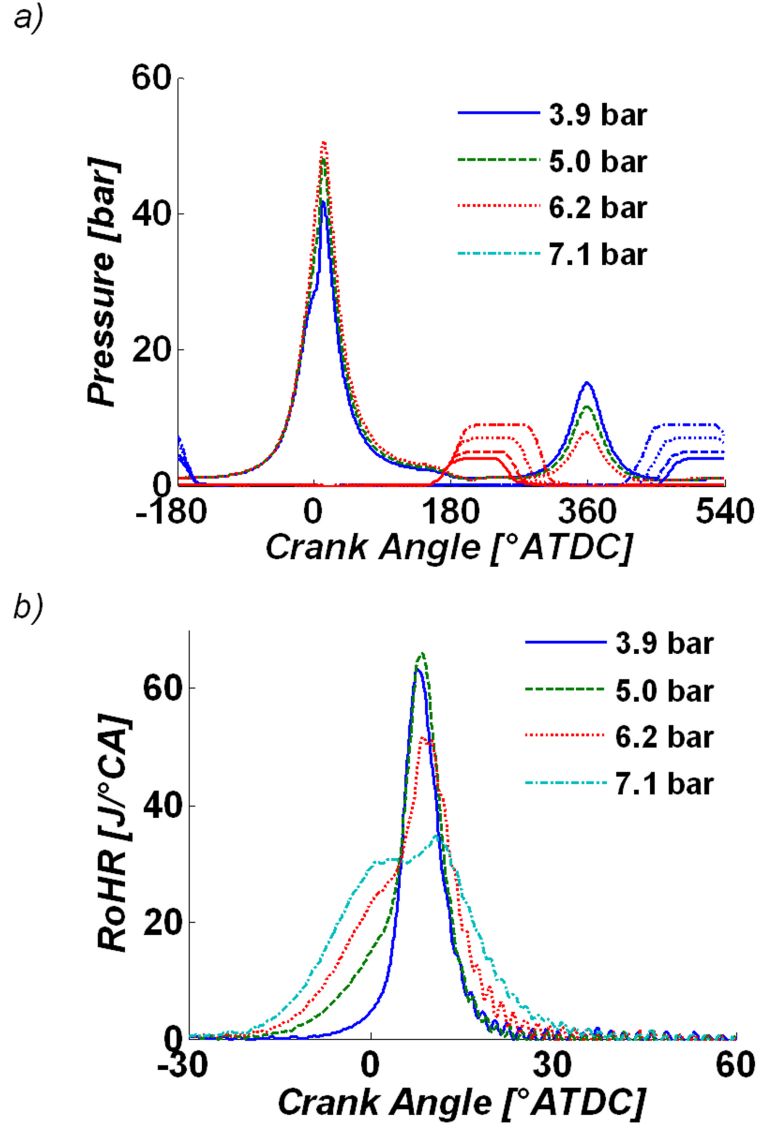


**Figure 3.8:** SACI points a) Measured cylinder pressure traces and measured valve lift profiles over a crank angle, b) rate of heat release vs. Crank angle.

timing. For all cases in both the HCCI and SACI regions, only one fuel injection event was utilized with the end of injection occurring 330 CAD before firing TDC. Completely knock free SI combustion was not achievable in these experiments due to combustion instability, however the heat release characteristics of the highest load point resembled normal SI knock. Accordingly in what follows this point is considered “SI” while the SACI point corresponds to 6.2 bar in Fig. 3.8. The HCCI

point is taken from pure HCCI data reported in Manofsky et al [52] at 3.7 bar.

## Probability Distribution of Knock

The goal of this section is to compare knocking behavior and distribution of knocking cycles for three different combustion modes: HCCI, SACI, and SI. Fig. 3.9 shows average high pass ringing intensity values and their standard deviations for HCCI, SACI, and SI operation. High Pass Ringing Intensity increases nonlinearly with load in HCCI combustion mode. Extending the load into the SACI regime results in a sharp decrease in ringing intensity, followed by a less steep linear increase than was seen with HCCI. Extending the load further into SI operation results in another step decrease in ringing intensity.

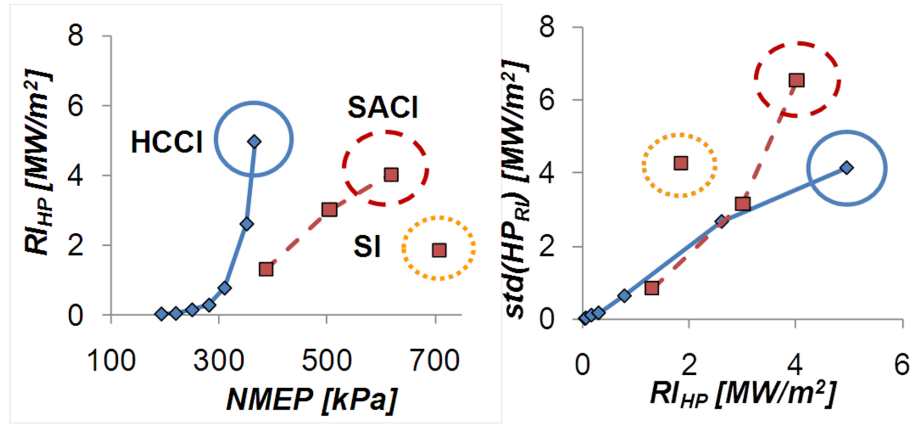


**Figure 3.9:** High pass ringing intensity (left) as a function of engine load for three combustion modes and standard deviations of ringing intensity (right).

On the right side of Fig. 3.9, the standard deviation of the ringing intensity is seen to increase proportionally with its average value. With SACI combustion, this standard deviation rises more steeply than in HCCI. For the same ringing intensity, the SACI points show more cyclic variation than those associated with HCCI. For a ringing intensity of  $\sim 2 MW/m^2$ , the SI point shows the highest deviation. The magnitude of the standard deviation for this SI case is higher than the average value. The standard deviation of NMEP for this case was 27 kPa, which corresponds to a COV of NMEP of about 3.8%.

The probability distribution of the ringing intensity was calculated for all three circled points showed in Fig. 3.9. Ten bins were used covering the range of the ringing intensity values for each mode for 200 consecutive cycles in the pressure records. Distribution calculation has been done in logarithmic transformation for both the

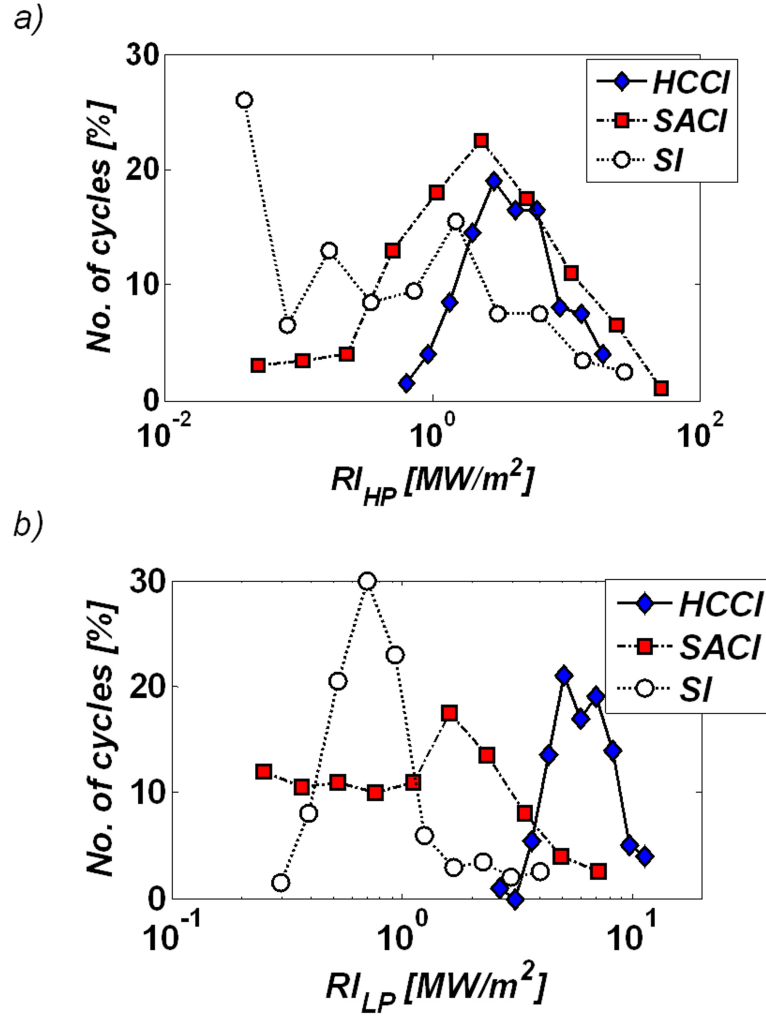


**Figure 3.10:** Probability distribution of a) high pass ringing intensity, b) low pass ringing intensity.

ringing intensities so that all three metrics can be compared on the same basis. The resulting histograms of the two knock measures are plotted for each combustion mode in Fig. 3.10a) for  $RI_{HP}$ , Fig. 3.10b) for  $RI_{LP}$ .

Knocking HCCI combustion shows a narrow distribution of High Pass Ringing Intensity Fig. 3.10a). As load increases and combustion mode switches to SACI and SI, the spread in ringing intensity becomes larger. These modes show a larger cyclic variability in this ringing intensity. Although most cycles (SACI 81% and SI 86%) are in the lowest bin, the rest of the cycles show ringing intensity values significantly larger than the accepted limit of 5 MW/m<sup>2</sup> [52]. Although this knock occurs

intermittently, it is likely to be more dangerous for the engine structure since the energy density of the end-gas SI knock is significantly higher than the energy density of dilute, low temperature HCCI combustion. The Low Pass Ringing Intensity Fig. 3.10b) resembles “Gaussian” distribution for HCCI mode. As load increases and combustion mode switches to SACI and SI Fig. 3.10b), this ringing intensity diminishes suggesting that knock is not significant, in contrast to the high pass ringing intensity. This is a consequence of the fact that the main contributor to the index comes from the high frequency part of the pressure trace.

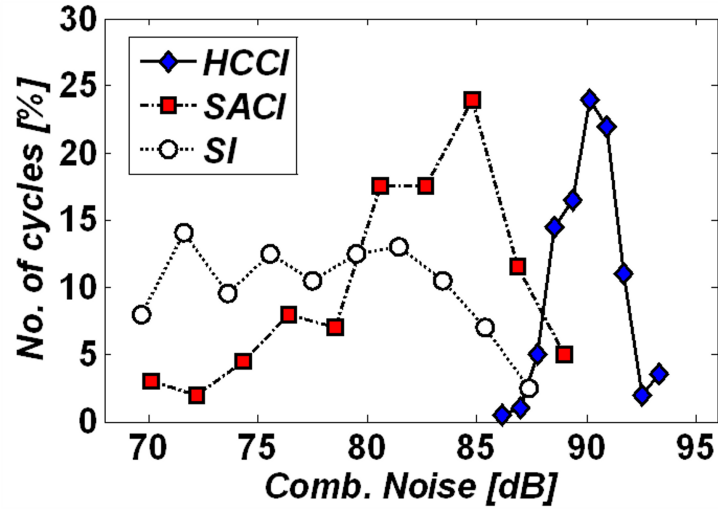


**Figure 3.11:** Probability distribution of combustion noise for three combustion modes.

Combustion noise Fig. 3.11 for HCCI case shows small variations. The shape of the distribution is narrow with the mean value around 90 dB. For SACI mode and SI mode the noise distribution becomes wider. This is in contrast to the skewed shapes for both of the ringing intensities. The SACI Fig. 3.11 with the mean combustion noise value around 80 dB is more quiet combustion than the 90 dB of HCCI. The SI end gas knock combustion Fig. 3.11 shows more stochastic distribution of combustion noise over the whole range than the two other combustion modes. The combustion noise metric shows more differentiation among combustion modes than the other two metrics.

## LP vs. HP Ringing Intensity vs. Combustion Noise

Fig. 3.12 directly compares the average low pass and high pass ringing intensity values over the engine load range. The colored boxes indicate the points analyzed in Fig. 3.10 and Fig. 3.11. For HCCI, the Low Pass Ringing Intensity metric shows

a similar trend to the High Pass Ringing Intensity, with the exception that the values for the RILP are greater at low load. However, the results from both metrics converge at the HCCI high load limit.

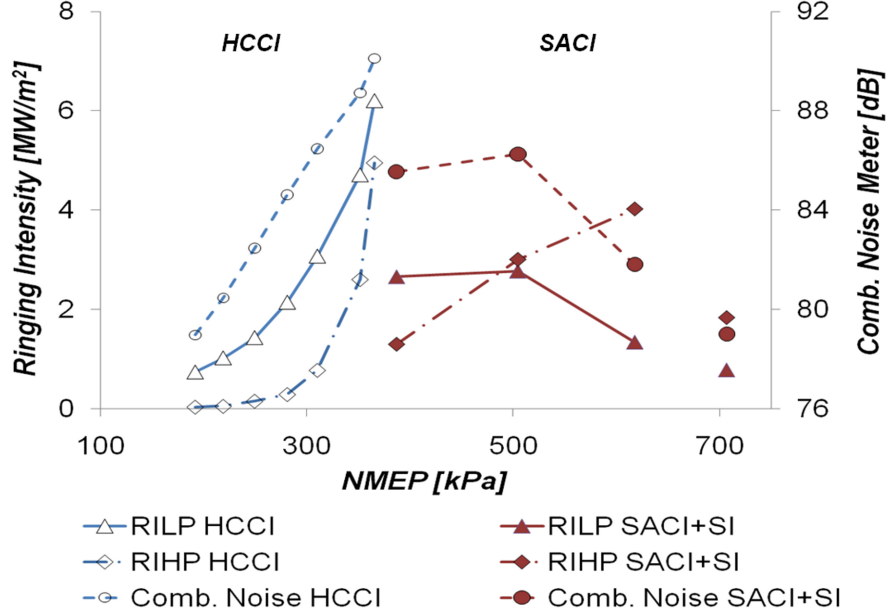


**Figure 3.12:** Average Low Pass, High Pass Ringing Intensities and Combustion Noise vs. load. SI point denoted by single unconnected filled square.

For SACI operation, the High Pass Ringing Intensity rises with a smaller slope than in HCCI mode. The Low Pass Ringing Intensity is initially flat in the SACI mode and then decreases as the SI region is approached. Both ringing intensities are much less in the SI region. Combustion noise follows the trend of the RILP, rising in the HCCI region and flat then falling in the SACI and SI region.

### 3.6 DISCUSSION

All measurements showed similar trends in the pure HCCI region. In particular, the low pass method with proper calibration can be a useful tool in defining combustion limits for both modelers and experimental investigators. However in the SACI and SI region, the low pass and combustion noise trends were opposite that of the high pass method. Furthermore all metrics in SACI and SI mode gave lower values than in HCCI mode despite the fact that the engine exhibited audible knock, especially at the highest load point. It is clear that new metrics are required to take into account the critical features of this advanced combustion mode.

As demonstrated in the statistical analysis, SACI and SI knock are qualitatively different from HCCI knock, likely due to the different combustion mechanisms. While pure HCCI combustion generally features relatively uniform phasing, when a flame is introduced with spark assist it introduces an independent source of stochastic behavior which apparently changes the occurrence of knock. Previous work on SI knock for the most part concentrates on higher frequency pressure oscillations because of its connection with pressure wave energy and potential engine damage. Any new approach should be based on the high pass analysis. While the low pass method is of some practical use for HCCI, it is also based on the high pass phenomena through an empirical correlation. Heat transfer is also a critical factor related to the energy content of the charge as reflected by load. This latter element is not taken into account by any of the metrics considered here and is a fruitful avenue for future research.

### 3.7 SUMMARY AND CONCLUSION

Three knock metrics have been applied to HCCI, SACI and SI combustion in a FFVA engine and the results compared over a range of loads. The results show:

1. For all metrics, the transition from HCCI to SACI, and from SACI to SI results in a reduced knock values.
2. Variability as measured by standard deviation and frequency distribution is increased as the combustion transitions from HCCI through the SACI region to SI, consistent with the increasing proportion of flame induced heat release.
3. The high pass ringing intensity gives higher values compared to the low pass method in all three combustion regions.
4. In the HCCI region, all three metrics show the same rising trend depending the load. In the SACI region, the high pass method shows increasing values while the low pass and combustion noise measure decrease with increasing load.
5. The combustion noise method shows the most differentiation among combustion modes ranging from a narrow distribution in HCCI mode to a more stochastic behavior in SI mode.
6. An FFT analysis shows a steady knock pattern with one dominant frequency of the first circumferential oscillation mode in HCCI combustion. SI knock on the other hand shows a less uniform distribution in frequencies, a larger difference in

knock magnitude from the first to the second circumferential modes, and more cycle-to-cycle behavior with irregularly distributed peaks.

7. In the SACI combustion mode, no general agreement was found among the metrics. Further all metrics showed a significant decrease as the engine transitioned between HCCI through SACI to SI despite the presence of significant audible knock as SI combustion was approached. Future work is needed.



## Chapter 4

# Scavenged Pre-chamber on a Gas Engine for Light Duty Truck

This chapter presents an experimental investigation of advanced combustion of extremely lean natural gas / air mixture in a gas fueled automotive engine with a scavenged pre-chamber. The pre-chamber, which was designed and manufactured in-house, is scavenged with natural gas and is installed into a modified cylinder head of a gas fueled engine for a light duty truck.

For initial pre-chamber ignition tests and optimizations, the engine is modified into a single cylinder one. The pre-chamber is equipped with a spark plug, fuel supply and a miniature pressure transducer. This arrangement allows a simultaneous crank angle resolved pressure measurement in the pre-chamber and in the main combustion chamber and provides important validation data for computational fluid dynamics (CFD) simulations.

The results of the tests and initial optimizations show that the pre-chamber engine is able to operate within a significantly wider range of mixture composition than the conventional spark ignition engine.

Full load operation of the pre-chamber engine is feasible with stoichiometric mixture (compatible with a three-way catalyst), without excessive thermal loading of components. At low load operation, the results show low  $NO_X$  emissions with a high potential to fulfill current and future  $NO_X$  limits without lean  $NO_X$  exhaust gas after-treatment. The scavenged pre-chamber helps to increase the combustion rate mainly in the initial phase of combustion. However, significant unburned hydrocarbons emissions due to incomplete combustion need further optimizations. Thermal efficiency of lean operation of the engine with the pre-chamber compared to the conventional spark ignition system operated in stoichiometric conditions shows approximately 13 % improvement.

## 4.1 INTRODUCTION

An extremely high air excess ratio ( $\lambda$ ) value near the flammability limit enables to achieve low content of nitrogen oxides ( $NO_X$ ) in raw exhaust gas in homogeneous mixture spark ignition combustion. Low  $NO_X$  emission is achieved due to low peak cycle temperature. Additional air in the lean mixture increases the specific heat ratio which leads to an increase in thermal efficiency [84]. This strategy (called lean burn concept - *LB*) is frequently used in stationary natural gas fueled engines within the whole operating range.

On the other hand, an extremely lean mixture leads to lower burning velocity, high hydrocarbons emission and poor combustion stability. These challenges require an ignition system with a high energy combustion initiation.

A pre-chamber ignition is a technology frequently used in the field of stationary large bore gas engines. It allows to burn extremely lean homogenous mixtures with a high combustion rate. Extremely lean engine operation allows reduction of nitrogen oxides ( $NO_X$ ) emissions to levels below the legislative limits without the need of  $NO_X$  after-treatment system. At the same time, lean mixture combustion reduces the peak cylinder temperature, hence heat losses are reduced and thermal efficiency of the engine is increased.

There have been several attempts in the past to develop and investigate this technology for automotive applications [12], [28] and [80]. The packaging of a scavenged pre-chamber into a limited space in the cylinder head of the small engine is a cumbersome task.

Beatty et al. [12] investigated the application of scavenged pre-chamber in a Volvo 9.6 liter natural gas bus engine. Various pre-chamber and nozzle geometries were investigated. They achieved emission levels which complied with, at the time, valid emission limits with the use of the oxidation catalyst primarily dedicated for hydrocarbon afterburning. Geiger et al. [28] tested methane scavenged swirl pre-chamber in a small gasoline engine with a cylinder displacement of 0.5 liter in a low load operation. They concluded with "excellent lean operation qualities". They extended the lean limit to the  $\lambda = 1.96$ . Toulson et al. [80] presented a wide literature and patents review of pre-chamber ignition systems. It states a Diesel like peak engine efficiency is achievable with pre-chamber ignition lean engine operation.

In this work the authors developed a scavenged pre-chamber that contains a well ignitable mixture in time and location of the spark. The basic principle is a multipoint ignition of the cylinder charge by a several high energy jets leaving the pre-chamber. A pre-chamber system with a small volume (less than 3% of engine compression volume) was chosen for the ongoing research project based on a previous work by the authors on the development of scavenged pre-chamber for a large bore stationary gas fueled engine [69]. Scaling of this system to the size of a light duty

truck engine was a challenging task. Based on previous works [88] the design for a light duty truck engine was modified.

## 4.2 EXPERIMENTAL SETUP

### Testing Engine

The test setup is described in [84] and [86]. Tab. 4.1 shows main engine parameters in its four cylinder turbocharged version before modifications to the pre-chamber configuration.

The engine is equipped with a central mixer for metering and delivery of gaseous fuel into the compressor inlet. It is possible to manually control the fuel flow or to operate with a closed loop lambda control using the conventional oxygen sensor output signal as feedback. Mixture inflow is controlled by a conventional throttle valve (*THR*) located downstream from the intercooler (*IC*) and actuated by a stepper motor (see Fig. 4.1).

A capacitive ignition system (UNIMA TC+) enables an independent adjustment of spark timing and spark energy. All actuators and selected set of sensors are connected to the engine electronic control unit (*ECU*) purposely developed in the author's department using a Field-Programmable-Gate-Array as a *HW* platform. The *ECU* is fully accessible and allows an open loop control as well.

For the initial stage of experimental research, the testing engine was converted to a single cylinder one by closing the intake and exhaust, using by plates installed into the ports of 3 other cylinders as indicated (by red lines) in Fig. 4.1.

### Pre-chamber design

The cylinder head of one cylinder was modified and the newly developed scavenged pre-chamber was installed into it as shown in Fig. 4.2.

The pre-chamber is filled with additional gaseous fuel through a check valve. The schematics of the fuel supply line to the pre-chamber are presented in ANNEX B. The laboratory is equipped with a compressed natural gas (*CNG*) line with gas pressure up to 200 bar. The pressure is reduced approximately to 3 bar using a pressure regulator. Fuel flow is measured and controlled by an OMEGA FMA2610A mass flow controller. Average volumetric flow rate can also be visually inspected by a rotameter. Pressure oscillations are damped into a small damping vessel and the fuel enters the pre-chamber through a drilled passage with diameter of 1.5 mm with built in miniature check valve (opening gauge pressure  $\sim 20$  kPa).

The filling of the pre-chamber with a fresh fuel and scavenging the residual gas is controlled by a pressure difference between the fuel supply and the pre-chamber

Basic Engine Geometry	
No. of cylinders	4
Bore / Stroke	102 / 120 mm
Displacement	3.92 dm <sup>3</sup>
Compression ratio	12:1
Valves /cylinder	4
Valve timing	(at 0.1 mm clearance)
EVO/EVC	122 / 373 °CA after firing TDC
IVO/IVC	342 / 595 °CA after firing TDC
Engine Performances	
Maximum Speed	2800 rpm
Maximum Torque	600 Nm @ 1500 – 1600 rpm
Maximum Power	125 kW @ 2400 – 2800 rpm
Turbocharger	
Make	CZ C12
Control	Variable Turbine Geometry (VTG)
Intercooler	Air-to-Water
Mixture Formation	
Arrangement	Common (central) mixer
Control units	
Electronic control units	Manual/closed loop $\lambda$ control ( $\lambda \geq 1$ )
Ignition	Capacitive ignition
Throttle	Electronic throttle control
TC control	VTG rack control

**Table 4.1:** Main engine parameters in original SI arrangement.

instantaneous pressure. This arrangement allows that the level of scavenging can be controlled almost continuously by a mass flow controller. Ideally, the fuel pressure control should be adjusted to ensure the start of fuel flow at the end of the exhaust stroke and fuel inflow should last the whole intake stroke to maximize the pre-chamber scavenging from the residual gas.

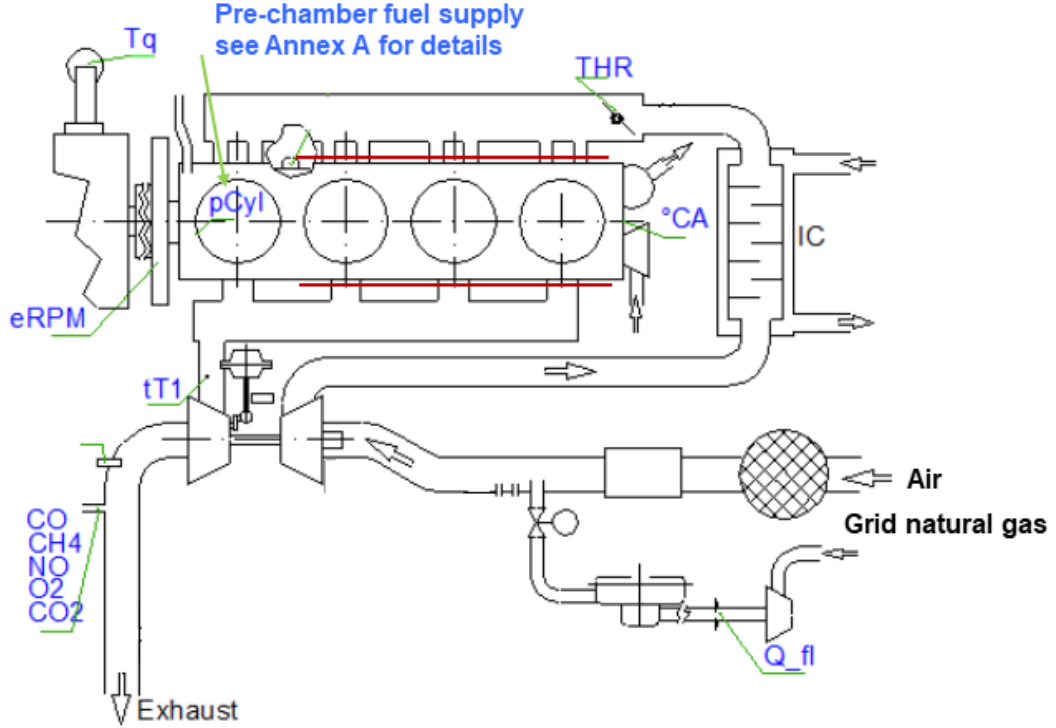


**Figure 4.1:** Testing engine layout and data acquisition schematic.

The fuel leak to the exhaust manifold should be completely avoided. The combustible mixture in the pre-chamber is formed in the compression stroke in which the pre-chamber is being filled with the lean mixture from the main combustion chamber. Ideally, a stoichiometric or moderately rich mixture should be present in the vicinity of the spark gap at the time of spark discharge.

Besides of the spark plug and fuel supply line, a miniature pressure transducer is installed in the pre-chamber. The installation of the miniature pressure transducer allows a crank angle resolved pressure measurement in the pre-chamber simultaneously with the pressure measurement in the main combustion chamber. It gives an important insight into the pre-chamber thermo and fluid dynamics. The measured pressure data also serves as a validation data for ongoing computational fluid dynamic (CFD) study that will help to understand the physics of the pre-chamber gas exchange. Further steps will include the reaction kinetics and a flame propagation modeling. The goal is to create a theoretic background for future design optimizations.

The pre-chamber assembly was designed in a modular way and allows modifica-

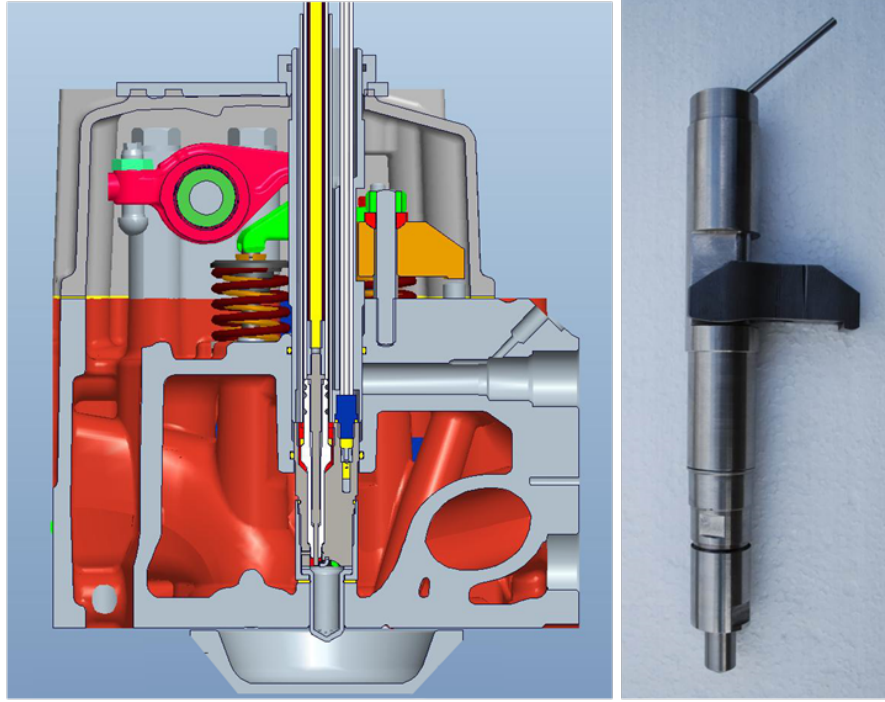


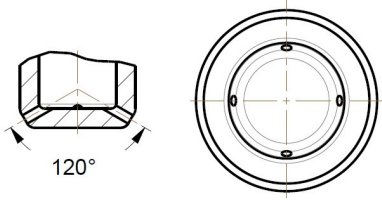
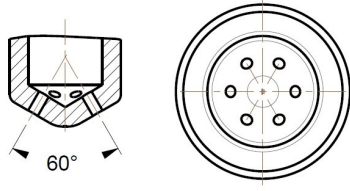
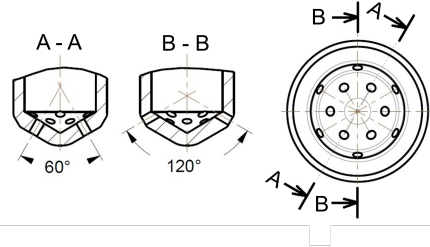
**Figure 4.2:** Cross sectional view of combustion chamber and pre-chamber installed into a modified cylinder head of the testing engine (left) and the prototype pre-chamber (right).

tions of size and geometry of the pre-chamber and jet nozzles. The three configurations of jet nozzles that were tested in this study are shown in Tab. 4.2.

## Measuring equipment

An AVL GU13Z-24 uncooled miniature cylinder pressure transducer with M5 thread was installed in the cylinder head. Another uncooled AVL GH15D pressure transducer was installed in the pre-chamber. The pressure signals were amplified using a two-channel Kistler charge amplifier. High speed data recording was performed using an in-house developed data acquisition software and an angle calculator system compiled in a National Instruments (NI) LabVIEW integrated development environment and NI hardware. An in-house low speed data acquisition (DAQ) also compiled in LabVIEW records the signals from the sensors of slowly changing physical quantities.

The main gaseous emission components have been measured in a raw exhaust gas sample. The test cell is equipped with an emission bench based on ABB gas

No. of holes / hole diameter [mm]	Geometry of jet nozzles	P-C volume [cm <sup>3</sup> ] / % of compression volume
4 / 1		1.33 / 1.66 %
6 / 1.2		1.33 / 1.66 %
12 / 1.2		1.95 / 2.43 %

**Table 4.2:** Tested variants of the pre-chamber geometry.

analyzers that sampled a raw and dried exhaust gas (NDIR for  $CO$ ,  $CO_2$ ,  $CH_4$  and  $NO$  and  $PMD$  for  $O_2$ ).

#### 4.2.1 Experimental procedures and evaluation methods

All engine tests presented in this paper were acquired on engine dynamometer at steady state and at constant engine speed of 1800 rpm and fully open throttle valve. VTG rack position was kept constant at maximum stator nozzle area (minimum boost pressure). No exhaust gas recirculation ( $EGR$ ) was applied for all measurements in this study.

The engine was fueled with natural gas with 97.1 % of methane. Complete re-

sults of gas analysis using a gas chromatograph is presented in ANNEX D. Where not explicitly stated the ignition timing was adjusted to keep combustion phasing of 50 percent mass fraction burned constant ( $CA_{50} = 10^\circ$  aTDC). This is an optimum combustion phasing of this engine with a conventional spark plug. It is consistent with a long term experience from combustion engine research and development (R&D) activities and is generally accepted as a simple guideline for optimal power and efficiency depending on ignition timing.

To be able to control the combustion phasing during the test an in-house code for simple thermodynamic (on-line) evaluation of heat release was developed. This code assumes constant charge properties and does not take into account the heat loss to the walls. The HR scope is normalized to  $<0;1>$  range by dividing by its maximum.

For a detailed (off-line) analysis of indicator diagram, a single zone heat release computation code was developed which operates with the temperature dependent specific heat capacity and variable cylinder charge composition. The code also accounts for the heat losses to the walls using Eichelberg's heat transfer coefficient correlation [95].

The evaluation of working cycle thermodynamics was adapted to the possibility to cope with the extremely high content of unburned fuel in raw exhaust. It would be useful to mention several specific aspects.

The calculating procedure generates the angle resolved sequence of net heat release (HR) in Joules. In each calculating step the value is amended by the heat transfer to the wall and gross heat release is quantified. The value of absolute gross heat release is normalized by dividing by the absolute total heat delivery per one working cycle calculated as:

$$\text{Fuel lower heating value} \times \text{Fuel mass per cycle} \times \text{Chemical efficiency}$$

To determine the chemical efficiency the composition of reaction products is considered to be the composition of equilibrium mixture which contains the same molar fraction of CO as measured by the exhaust gas analysis and the molar fraction of H<sub>2</sub> originating from the equilibrium calculation. However the equilibrium calculation gives very low content of CH<sub>4</sub> (and any other hydrocarbons if relevant) in the equilibrium mixture. Therefore, the calculated equilibrium mixture has to be additionally amended by the correct amount of unburned mixture consisting of CH<sub>4</sub> (determined in exhaust by analysis) and a corresponding amount of the air. It means that a part of the combustion products is of the same composition as the fresh mixture. At the end of combustion the content of the reaction products in the cylinder charge reaches 100% regardless of the quality of the combustion process itself. In this way the value of normalized HR is directly equal to the burned fuel fraction and the value is imposed into calculation of the value of gas constant and



specific heat capacity for subsequent calculation step.

A possible difference between the final value of the normalized heat release and the expected value of  $HR = 1$  are compensated by a modification of the cylinder charge mass imposed into the thermodynamic calculations. Finally, the modified charge mass value is crosschecked with the value calculated from experimentally determined mass flow of engine working substance. According to the previous experience with evaluation of the thermodynamics of the engine working cycle in the author's laboratory the deviation within the range of  $\pm 3\%$  is acceptable. In all cases presented in the paper, the data passed this crosscheck successfully.

Based on the long term experience with unthrottled engines a typical value of 5% of residual gas content is imposed into all thermodynamic calculations.

For each measured point a pressure record of 80 consecutive cycles with 0.295 crank angle degree resolution (1/10 of flywheel teeth pitch) was acquired. Average cycle was used for all subsequent evaluations.

### 4.3 INITIAL TESTS – LIMIT SEARCH

At the beginning of the experimental campaign, the basic set of engine performance parameters has been acquired and evaluated in order to determine the meaningfulness of the pre-chamber approach and to outline the main challenges.

The results of the initial phase for a 6 hole pre-chamber with ignition timing adjusted for constant combustion phasing ( $CA_{50} = 10^\circ \text{aTDC}$ ) and constant pre-chamber fueling rate of 5.5 sccm/cycle are summarized in Fig. 4.3.

The engine is able to operate within a wide range of mixture composition with lambda values far above the lean limit of inflammability ( $\lambda = 1.65$ ) as it was determined on the testing engine in its conventional SI version [86].

At extremely lean operation the content of nitrogen oxides in raw exhaust gas is very low (see the plots of indicated specific nitrogen oxides –  $IS_{NOx}$ ), giving good prospects to comply with demand of contemporary and predicted emission legislative for road vehicles without exhaust gas  $NO_X$  aftertreatment. On the other hand the testing engine demonstrated ability to operate with the mixture composition close to the stoichiometric one ( $\lambda = 1$ ), creating good condition to use a Three Way Catalyst (TWC) configuration.

The test results in Fig. 4.3 demonstrate possibility to achieve excellent environmental performances regarding  $NO_X$  emission in the whole operational range maintaining the demands for a size, complexity and cost of additional exhaust gas aftertreatment within a reasonable range.

Peak in-cylinder temperature ( $T_{MAX}$ ) at the engine operating with the lean mixture shows the typical values for so-called low temperature combustion allowing to benefit from main advantages (i.e. low  $NO_X$  emission), low thermal losses and

favorable ratio of specific heats for a high thermal efficiency.

During the initial phase of the experimental activity the engine showed a good reproducibility and repeatability of its performance and viability of the design of particular details as well as design approach as a whole.

However, several challenges have been revealed. At the right end of the graphs the engine indicated efficiency ( $\eta_i$ ) is low, the cycle-to cycle variability (coefficient of variability - cov of IMEP and standard deviation - std of IMEP) is high and considerable amount of delivered fuel does not burn at all. Amount of unburned fuel is expressed in terms of methane emission index ( $EICH_4$  = mass flow of  $CH_4$  in exhaust / total fuel consumption in kg/hour).

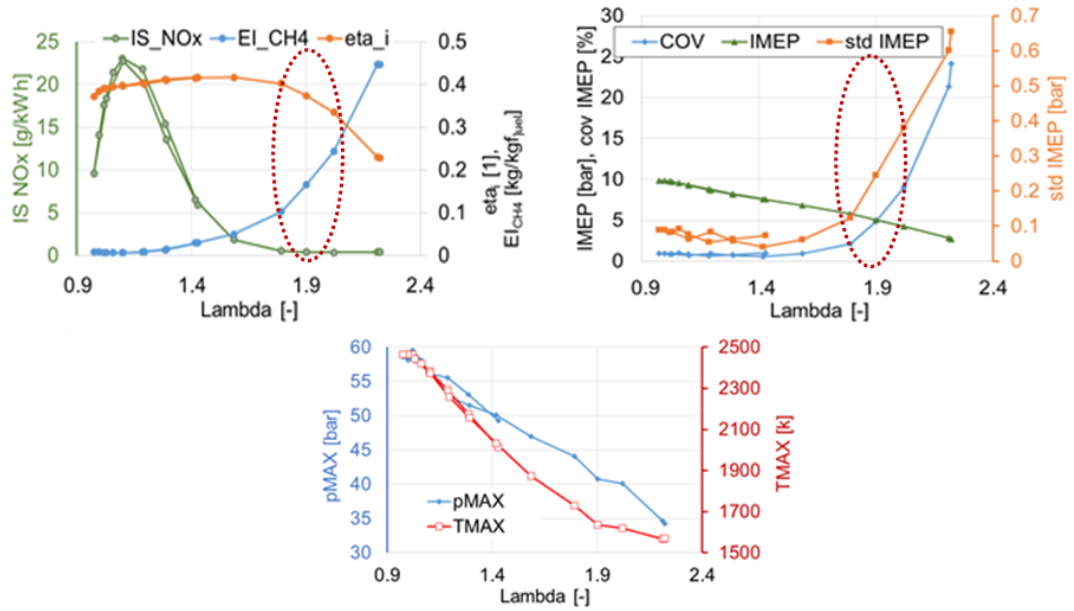


**Figure 4.3:** Basic performance of pre-chamber engine, pre-chamber fuel rate 5.5 sccm/cycle, 6 holes, ignition timing for CA50 = 10° aTDC.

## 4.4 PRE-CHAMBER GEOMETRY VARIANTS

After initial experiments with the 6 holes pre-chamber (6 x 1.2 mm diameter holes, 60° drill angle) the sensitivity study on pre-chamber geometry was performed. Taking into account the complexity of part manufacturing and pre-chamber installation, only limited amount of variants were investigated.

For the first modification (4 x 1 mm diameter holes, 120° drill angle) the chamber volume was kept constant. This variant showed deterioration of engine performance at extremely lean (low  $NO_X$ ) operation.

Based on these results and former experience [69] final version was designed with efforts for maximizing the pre-chamber volume for increasing ignition energy respecting the available space in the cylinder head. At the same time number of nozzles was increased to support the flame penetration of the main combustion chamber.

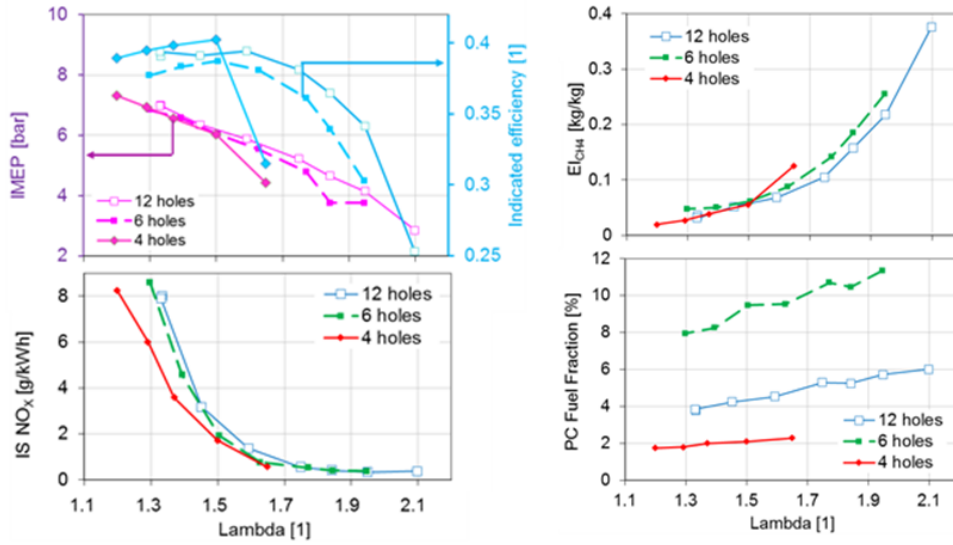


**Figure 4.4:** Performance of engine with various pre-chamber alternatives with 4, 6 and 12 holes, pre-chamber fueling rates: 4 holes = 0.9 sccm/cycle, 6 holes = 3.7 sccm/cycle and 12 holes = 1.85 sccm/cycle.

The description of the variants of the pre-chamber geometry is introduced in Tab. 4.1. The main results of the engine experiments with various pre-chamber arrangements are summarized in Fig. 4.4. In this figure the values are presented (from top to bottom): Indicated mean effective pressure ( $IMEP$ ), Indicated specific  $NO_X$  emission ( $IS_{NOx}$ ), relative amount of unburned fuel in exhaust (methane emission index  $EICH_4$ ), relative pre-chamber fueling rate to total fuel delivery (P-C fuel fraction).

Measurement of each curve was performed with stepwise increase of Lambda value till the significant deterioration of engine performance was observed. For each pre-chamber alternative the best efficiency fueling rate to pre-chamber was adjusted. The ignition timing was adjusted to maintain CA50 at 10° aTDC for all cases.

The pre-chamber with 12 holes features the greatest volume and the greatest

cross section area of the nozzles. With this alternative the best engine performance was achieved. At extremely lean operation it shows the best efficiency and the lowest emissions of hydrocarbons still maintaining favorable  $NO_X$  emission.

The main challenges mentioned at the end of the previous section (mainly the excessive unburned hydrocarbon emissions) unfortunately still remain and further improvements should be pursued.

## 4.5 HEAT RELEASE ANALYSIS RESULTS

A high speed pressure indication was engaged as a tool that offers an insight into the behavior of the engine working substance.

Angle indexed scopes of relevant physical quantities in Fig. 4.5 describe the thermodynamic behavior of the working substance during engine operation with the mixture composition well beyond the lean limit of flammability as it was repeatedly observed at conventional SI operation ( $\lambda > 1.9$ ). Spark discharge timing can be easily identified as the position of steeply descending slope of the voltage ( $Ign_{Volt}$ ) sensed at the high voltage cable close to the spark plug terminal. The local peak on a pre-chamber pressure trace ( $pChamb$ ) describes combustion of enriched mixture inside the pre-chamber. Ignition delay in the pre-chamber can be assessed from these two signals. The plot of the pressure sensed in cylinder ( $pCyl$ ) almost does not reflect the combustion in the pre-chamber.

The plot of angle dependent scope of locally averaged temperature (single zone evaluation) of the cylinder charge well illustrates the favorable condition for a low reaction rate of formation of  $NO_X$ . Normalized heat release ( $N_{HR}$ ) and its derivative ( $N_{RoHR}$ ) indicate burning rate as usually observed at conventional SI engine operation with significantly richer mixture strength. The extremely steep rising edge of the rate of heat release curve immediately after the combustion start is a typical feature of the pre-chamber ignition.

The results of evaluation of the high speed data acquisition record acquired at various operational regimes are introduced in ANNEX C.

The scopes of heat release and its derivative confirm the ability of pre-chamber ignition to initiate the combustion process in the main combustion chamber and to accelerate the starting phase of the combustion process. Even at the leanest investigated condition the extremely slow final phase of combustion was not observed.

### 4.5.1 IMPACT OF PRE-CHAMBER FUEL RATE

Fig. 4.6 introduces the main relevant aspects of engine performances for various amount of the fuel delivered into the pre-chamber ( $QfPC = 1.8, 3$  and  $4$  standard  $cm^3$  per cycle). The dependence on the air-excess ratio is plotted in this figure.

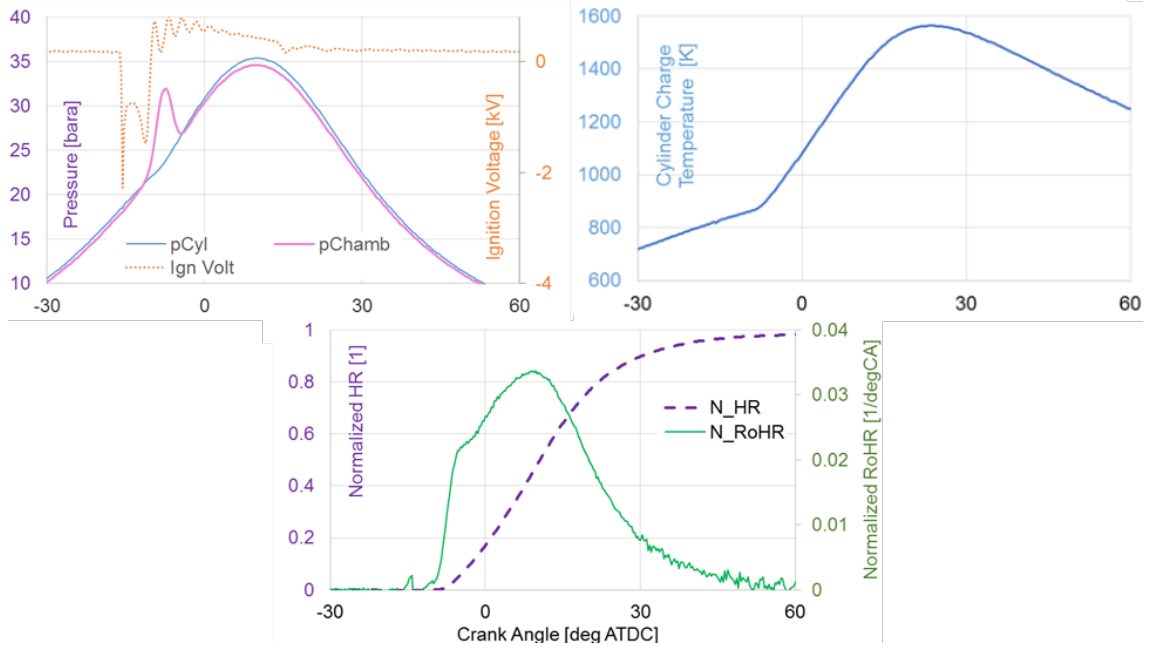


**Figure 4.5:** Results of high speed data acquisition and heat release analysis, pre-chamber with 6 holes,  $\Lambda = 1.91$ , pre-chamber fueling rate = 2.8 sccm/cycle = 7.7% of total fuel delivery.

Little or none impact of the pre-chamber fuel delivery on mean indicated pressure ( $IMEP$ ) and indicated efficiency ( $\eta_{ai}$ ) can be derived from this figure. A negative consequence of this statement is that the pre-chamber fueling rate does not introduce a tool to improve engine performance. On the other hand the insensitivity to pre-chamber fueling rate minimizes the demand for a complex injection rate control. No stressing demand for minimizing the cylinder-to-cylinder variability of fuel distribution to pre-chamber is the encouraging expectation for a future implementation of the pre-chamber ignition on a multi cylinder engine. Under the steady state conditions this finding is in the contrary to the findings of Beaty at al. [12] who stressed the need for the accurate control of extremely small gas flow rates to the pre-chamber and the need for a complex control system for achievement of extremely low  $NO_X$  emissions.

Only remarkable influence of the pre-chamber fuel delivery can be seen from a demand for advanced spark timing (bottom graph in Fig. 4.6) to maintain the crank angle position at which 50% of cylinder charge has been burnt ( $CA_{50}$  in Fig. 4.6) at  $10^\circ$  CA after TDC. The difference in ignition timing for various pre-chamber fueling rates is caused by variable composition (and possible charge stratification) in the pre-chamber when the spark discharge takes place.

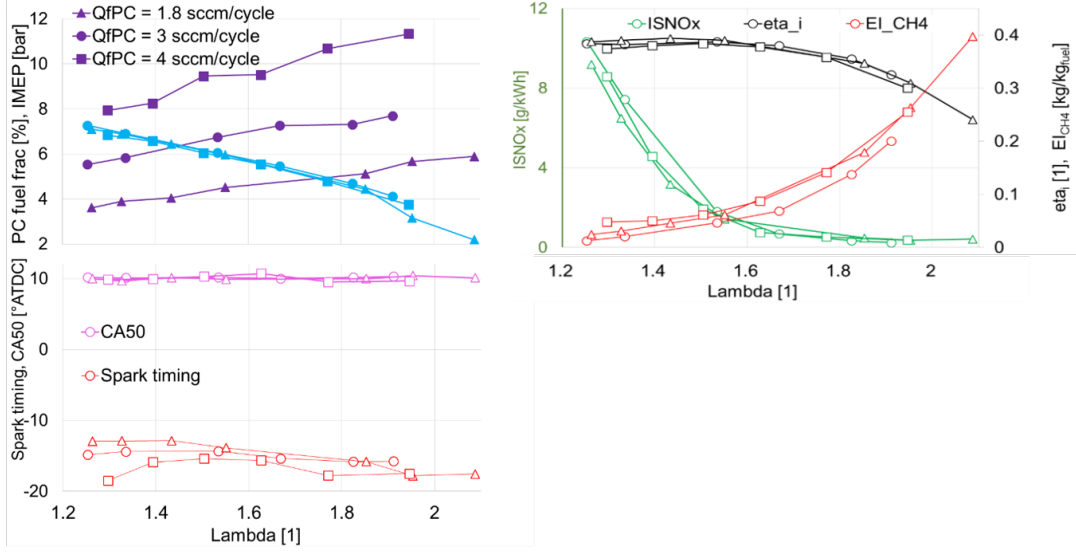


**Figure 4.6:** Performance (IMEP) and indicated efficiency ( $\eta_i$ ) of the pre-chamber engine – pre-chamber fueling rate study, 6 holes pre-chamber, pre-chamber fueling rate 1.8 – 4 sccm/cycle as a function of the air excess ratio (Lambda).

#### 4.5.2 IMPACT OF IGNITION TIMING

Adjustment of ignition timing is an important control measure which has decisive influence on the combustion phasing. The combustion phasing influences the angle-depending in-cylinder pressure course and effective work of engine working cycle.

As already mentioned in the previous paragraph the adjustment of ignition timing to maintain condition  $CA50 = 10^\circ CA$  ATDC was considered to be a good practice at least as a first approach.

During the compression stroke the pre-chamber volume is continuously pressurized by delivery of leaner mixture from the cylinder and therefore the pre-chamber charge becomes leaner as the piston approaches the top dead center ( $TDC$ ). The spark timing has to be adapted correspondingly, even if combustion phasing might differ from the apparent optimum value.

The influence of ignition timing on engine behavior is described in Figure 7 for 4 various adjustments of total mixture composition, covering the whole acceptable operation range ( $1 < \lambda < 2$ ). The pre-chamber fueling rate was kept constant at 1.8 sccm/cycle for this study. It is obvious that leaner mixture calls for more advanced ignition timing as long as engine power and efficiency are subject of optimization (see upper part of Fig. 4.7). Only the curves valid for the high Lambda values are relevant for future practical implementation because at lower excess air values (but still

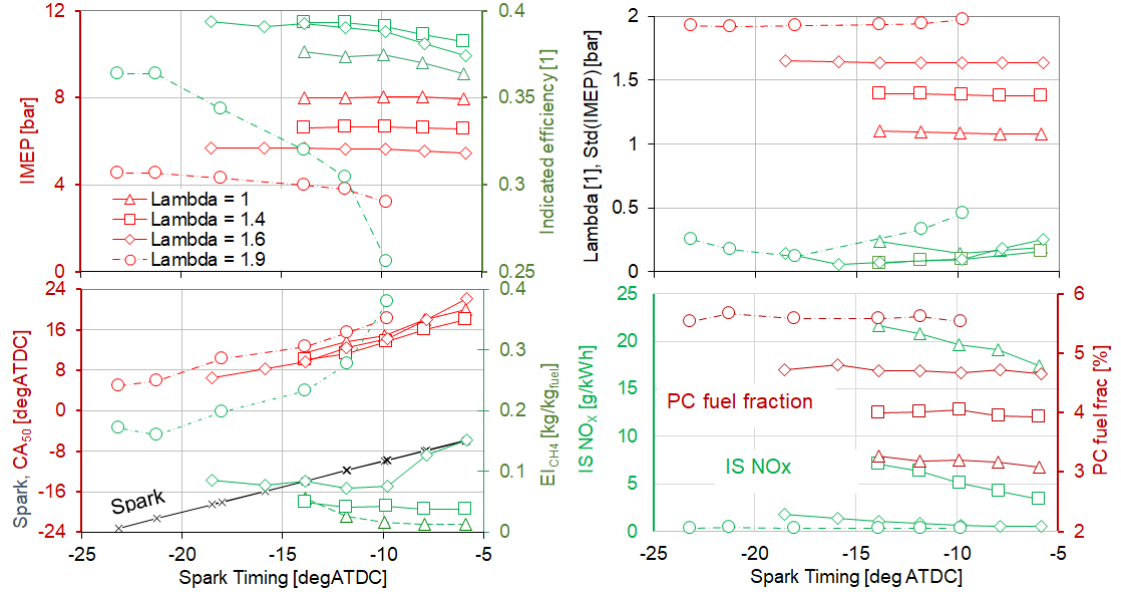


**Figure 4.7:** Performance of pre-chamber engine – spark timing study, 12 holes pre-chamber, pre-chamber fueling rate 1.8 sccm/cycle.

higher than  $\lambda = 1$ ) neither achieving of acceptable  $NO_X$  level without aftertreatment (bottom graph in Fig. 4.7) nor implementation of the *TWC* are possible. Optimum spark advance for  $\lambda \approx 1.95$  accounts approx.  $22^\circ$  BTDC leading to  $CA_{50} \approx 6^\circ$  ATDC. The curves of  $IS_{NO_x}$  show descending tendency with retarding ignition for lower excess air values. During the operation with  $\lambda$  above 1.9 the slope of  $IS_{NO_x}$  curve is almost invisible and values of specific  $NO_X$  formation remain below the threshold of 0.5 g/kWh which is considered to be decisive for assessment of acceptability of  $NO_X$  emission from the point of view of contemporary and future emission legislature.

## 4.6 COMPARISON WITH SI ENGINE

Fig. 4.8 shows comparison of SI and pre-chamber ignition engine in a low load conditions. The red curves show a performance of the conventional SI engine throttled at 4 bar IMEP with the optimal combustion phasing. Green curves show the results of the unthrottled engine with a pre-chamber with 12 holes nozzle variant. Indicated efficiency of lean operation at  $\lambda \sim 1.9$  of the engine with the scavenged pre-chamber shows approximately 13% relative improvement compared to the efficiency of the conventional SI engine operated in stoichiometric conditions.  $NO_X$  emissions of lean burn pre-chamber engine show a good prospect to fulfill the current and

future legislative demands without the  $NO_X$  reducing aftertreatment.

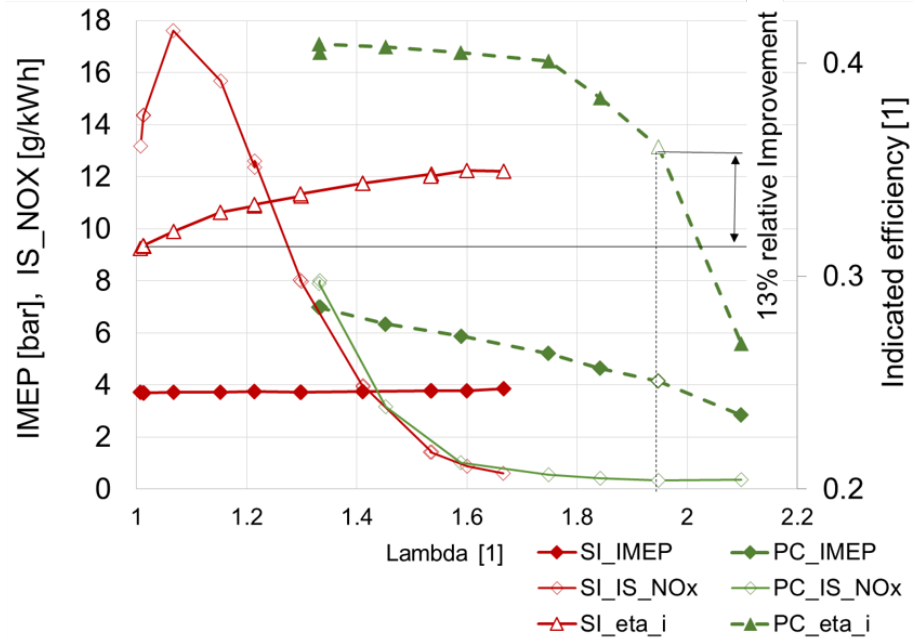


Figure 4.8: Performance of pre-chamber engine – comparison with SI engine.

## 4.7 CONCLUSIONS

Three geometries of scavenged pre-chamber equipped with a miniature pressure sensor were designed and tested on a natural gas light duty truck engine in a fixed engine speed under the steady state operation.

The best engine performance was achieved with the pre-chamber with the largest volume and the greatest cross section area of the nozzles. At extremely lean operation it shows the best efficiency and the lowest emissions of hydrocarbons with favorable  $NO_X$  emissions.

Despite high amount of unburned hydrocarbons in exhaust, the tested engine equipped with the scavenged pre-chamber showed significant improvements compared to the engine with a conventional spark plug.

The pre-chamber engine was able to operate at high load with a stoichiometric mixture strategy that is compatible with a three way catalyst.

At low loads the scavenged pre-chamber allows to ignite extremely lean fuel air mixtures with high combustion rate. Lean operation potentially allows reduction of



nitrogen oxides ( $NO_X$ ) emissions to levels below the legislative limits without the need of using a  $NO_X$  after-treatment system. At the same time, lean mixture reduces the combustion temperature, hence heat losses are reduced and thermal efficiency of the engine is increased.

Appropriately designed catalytic exhaust gas aftertreatment will probably be able to mitigate unburned hydrocarbons in all operational regimes.

## NEXT STEPS

During experimental investigation described in this paper a large database of experimental data was acquired. Next chapters will present CFD simulations, exploiting experimental data for calibration and verification. Deeper insight into the phenomena will be subsequently exploited for design modification towards improved system performance.

#### 4 Scavenged Pre-chamber on a Gas Engine for Light Duty Truck

## Chapter 5

# Analysis of Scavenged Pre-Chamber for Light Duty Truck Gas Engine

An ongoing research and development activities on the scavenged pre-chamber ignition system for an automotive natural gas fueled engine is presented in this chapter. The experimental works have been performed in engine laboratory at steady state conditions on a gas engine with 102 mm bore and 120 mm stroke, converted to a single cylinder engine as was explained in chapter 4. The in-house designed scavenged pre-chamber is equipped with a spark plug, fuel supply and a miniature pressure sensor for detailed combustion diagnostics. The engine was operated at constant speed, fully open throttle valve and four different fueling modes with or without spark discharge. A partly motored mode allowed direct evaluation of the pre-chamber heat release. The experimental data acquired in this research served as a validation data for the numerical simulations. The performed tests of prototypes and calculations have recently been expanded to include 3-D flow calculations in the Ansys Fluent software. The work presents results from the coupled 1-D and 3-D numerical simulation of the flow in the pre-chamber. The main goal of the computational fluid dynamic (CFD) simulation was to describe the fluid dynamics inside the pre-chamber (without combustion), mixture distribution and assessment of the scavenging quality. The pre-chamber interior volume is analyzed in detail for the operating condition. The outputs of the simulation serve as a base for optimization of the pre-chamber design. It is also a valuable input for the optimal control setting to improve overall functionality of the scavenged pre-chamber. The simulation results were compared with the experiments.

## 5.1 Introduction

An extremely lean homogeneous mixture of the natural gas in a spark ignition engine leads to a low temperature combustion, which results in a low level of  $NO_X$  emissions. Additional air in the lean mixture increases the specific heat ratio which leads to an increase in thermal efficiency [33]. This strategy (called lean burn concept) is frequently used in stationary natural-gas fueled engines within the whole operating range. The pre-chamber ignition system allows considerable extension of the lean flammability limit of the mixture. This is enabled by the enhanced ignition energy which results from multipoint ignition of the mixture via burning jets that are leaving the pre-chamber through the orifices [7]. The interior of the pre-chamber is partly separated from the main combustion chamber and thus is protected from the intensive in-cylinder mixture motion. That is important for maintaining high ignition stability [33]. The in-house designed scavenged pre-chamber is equipped with a stand-alone gas supply as can be seen in Fig. 5.1. Additional gas leads in local enrichment of the pre-chamber charge. All these mechanisms provide better conditions for combustion initiation and flame propagation.

The pressure difference between the pre-chamber and engine cylinder is continuously balanced through the interconnecting channels. The overall mass of the mixture in the pre-chamber depends on its volume and thermodynamic state. The composition of the mixture and its stratification in the pre-chamber is a complex phenomenon. This phenomenon is determined by the gaseous fuel inflow through the check valve, outflow of fuel due to the short circuit scavenging, amount of residual gases from the previous cycle, by the charge concentration entering the pre-chamber from the cylinder and mixing of all components. The evaluation of the mixture distribution is one of the main interests of this research and it depends on the nature of the flow and its motion intensity inside the pre-chamber.

The advantages of the pre-chamber ignition system were confirmed at low load by the experimental results described in chapter 4. The results of experiments have shown that the scavenged pre-chamber significantly expands the flammability limit compared to the conventional SI engine. Extremely low  $NO_X$  emissions in a low load eliminate the necessity of using a special  $NO_X$  after-treatment to comply with the current and future  $NO_X$  emission limits. At full load operation, the pre-chamber engine is able to operate with the stoichiometric mixture, compatible with a three-way catalyst (TWC).

On the other hand, the extremely lean mixture (far beyond the ignitibility limit of a conventional spark ignition engine) leads to a low burning velocity, poor combustion stability, which results in high unburned hydrocarbons emissions. Therefore, the next step was focused on the pre-chamber development supported by the CFD simulation approach to globally optimize the functionality of the ignition system.

Simulation of the charge motion in the combustion engine with the torch ignition system during the intake and compression stroke is described in [14]. The calculation model contains the engine geometry, including the moving mesh, taking into account the movement of the piston and the valves. The work presents motored operation only.

The flow and the mixture formation within the pre-chamber as well as the turbulent kinetic energy was investigated and presented in [11]. The orifice diameter has an important influence on the flow within the pre-chamber and between the spark plug electrodes and therefore the ignition and first flame propagation. Small diameters below 0.9 mm seem to intensify the velocity field, deteriorating and very likely to extinguish the combustion in the pre-chamber. Shah et al. [66] evaluated the interaction of the pre-chamber jets and the main chamber charge. The rate and the depth of the penetration of pre-chamber jets are mainly governed by the jet momentum and hence increase with the volume of pre-chamber and decrease with the nozzle diameter. Increasing the pre-chamber volume increases the absolute mass flow rate from the pre-chamber and reducing the nozzle diameter increases jet velocity, both increasing the jet momentum.

The structure and behavior of the flame jet from the pre-chamber and the flame propagation of lean mixture in the main chamber were investigated by Kawabata et al. is described in [43]. The flame jet is ejected toward the outer radius of the main chamber with high speed and strong penetration. It spreads over the main chamber by impinging on the main chamber cavity wall and undergoing radial bend subjected to the influence of the swirl. To achieve optimized pre-chamber combustion, the optimization of both chambers (pre- and main) has to be done simultaneously.

A computational study of the effects of the spark location on the performance of a turbulent jet ignition system is solved in [78]. The simulations show, that locating the spark further from the connecting orifices in the pre-chamber produces a jet that is more effective and results in a faster ignition in the main chamber. Since the pre-chamber flames must propagate a greater distance through the chamber to reach the orifice, more pre-chamber gas is burned in the process generating a higher pressure difference between the two chambers. Combustion visualization in a rapid compression machine and study of the early flame development on the large bore optical engine Wärtsilä 34SG can be found in [78] and [94].

Investigation of the pre-chamber interior behavior only has been described in this chapter. Simplified model (without moving walls) is used for faster evaluation of different variants with lower computational requirements.

## 5.2 Experimental Setup

### Test Engine

Experiments were performed on a 4-cylinder 4-stroke natural gas engine which was converted to a single cylinder one by closing the intake and exhaust runners. Fig. 4.1 shows the plates installed between the intake and the exhaust flange and the cylinder head as indicated by the red lines. Otherwise the engine configuration remains unchanged from the original four-cylinder including the turbocharger with variable turbine geometry (VTG) and intercooler (IC). The main engine parameters can be found in Tab. 4.1.

A central mixer for metering and delivery of gaseous fuel is located upstream of the compressor. It is possible to manually control the fuel flow or to operate with a closed loop lambda control using the conventional oxygen sensor output signal as a feedback. The engine was fueled with natural gas with the content of 98.4% (by volume) of methane. Mixture inflow is controlled by a conventional throttle valve located downstream from the intercooler and actuated by a stepper motor.

A capacitive ignition system (UNIMA TC+) enables independent adjustment of the spark timing. All actuators and selected set of sensors are connected to the engine electronic control unit (ECU) developed in the authors' department using Field-Programmable-Gate-Array as a HW platform. The ECU is fully accessible and allows an open loop control as well. The detailed test setup description can be found in [84].

### 5.3 Pre-Chamber Design

The cylinder head of one cylinder was modified, and the newly developed scavenged pre-chamber was installed into it. The pre-chamber assembly was designed in a modular way and allows modifications of its size, geometry and its orifices. The pre-chamber shape is cylindrical (Fig. 5.1) and the specifications of its geometry are shown in bottom row in Tab. 4.2. The orientation of the orifices was designed with regard to the shape of the main combustion chamber and the uniform distribution of jets leaving the chamber. The pre-chamber with twelve orifices were selected as the best of the tested variants. The experimental sensitive study of three variants with different numbers of orifices (4, 6, 12) was performed and can be found in Chapter 4.

The pre-chamber is filled with additional gaseous fuel through a check valve. The schematics of the fuel supply line to the pre-chamber are presented in the Annex A. Fuel flow is measured and controlled by an OMEGA FMA2610A mass flow controller. The combustible mixture in the pre-chamber is formed during the

compression stroke in which the pre-chamber is being filled with the lean mixture from the main combustion chamber. Ideally, a stoichiometric or moderately rich mixture should be present in the vicinity of the spark plug gap at the time of spark discharge. Standard spark plug (Brisk CR10YS) with 0.5 mm spark gap was used. Besides the spark plug and fuel supply line, a miniature pressure transducer is installed in the pre-chamber.

## 5.4 Experimental Procedures

All engine test results presented in this paper were acquired on an engine dynamometer at constant engine speed of 1800 rpm and fully open throttle valve. The experimental arrangement allows measurement of the combustion pressure in the pre-chamber and in the cylinder simultaneously. Detailed heat release analysis was performed using the cylinder pressure trace only, including the volumes of both the main combustion chamber and the pre-chamber. The separate heat release analysis for pre-chamber and main chamber was impossible, because the instantaneous mass of the pre-chamber charge is unknown. However, the pressure difference between both mentioned volumes is an important calibration parameter for both the 3-D CFD and 1-D modelling.

Spark voltage and current at the secondary circuit of the ignition coil were measured directly. The spark energy was evaluated as an integral value of spark electric power. Annex C shows the traces of spark energy for various charge compositions. In most cases the spark energy value reaches 30 mJ. Operational modes used during the experiments were as follows:

- Mode A: Motored mode - no fuel was delivered, no spark was actuated. Simplified conditions were used for an initial calibration of the models.
- Mode B: Special motored mode - fuel was delivered only into the pre-chamber, no spark was actuated, no combustion occurred. A fuel quantity necessary for the scavenging of the pre-chamber was investigated in this mode.
- Mode C: Partly motored mode - fuel was delivered only into the pre-chamber, spark was on. This mode was investigated experimentally to evaluate the combustion efficiency of the combustion in the pre-chamber only, to quantify ignition energy from the pre-chamber combustion.
- Mode D: Full combustion mode - fuel was delivered into the pre-chamber and into the inlet manifold, spark was on. This mode represents the typical operation of the engine with the pre-chamber.

## 5.5 A GT-Power Model

GT-Power model of the investigated system was built and used for obtaining knowledge of physical quantities which are not available from direct measurement (e.g., instantaneous mass flow rate of gas through the check valve which was used as a boundary condition in CFD simulation) and for computational validation. The simulation of the “pre-chamber engine” requires modeling of two divided combustion chambers (one for the cylinder and second for the pre-chamber). For both volumes, the modeling of combustion, heat transfer and emission formation is needed and therefore the cylinder objects were used. At the first stage, a scavenging reference object was not used, i.e., the gases in the investigated volume are assumed to be ideally homogeneously mixed (0-D approach).

The influence of throttling in communication ports (orifices) is respected by several pipes with appropriate dimensions (1-D approach). The pressure losses are represented by flow coefficients calibrated by data of pressure traces that are directly measured in the cylinder and pre-chamber from motored engine (Mode A). The amount of additional gas flowing into the pre-chamber is controlled by the pressure upstream of the check valve. The mechanical check valve prevents backflow from the pre-chamber into the fuel system. This part was modeled by the valve object (connection) with two dimensional array of pressure difference and discharge coefficients (determined experimentally). The rest of the model is a standard three pressure analysis (TPA) procedure [15]. The Fig. IV in ANNEX E shows the scheme of the model.

## 5.6 A CFD Model

The complexity and computational demands of the simulations of all of the physical processes inside the pre-chamber would be too large, therefore the CFD simulations were limited to the scavenging without combustion in the initial phase. Calculations are focused on the pre-chamber interior only at motored engine operation. The internal volume of the pre-chamber was modelled in detail. Small external volume (hemispheres) at the outlets of the connection orifices serve to respect pressure losses associated with the flow from the main chamber to the pre-chamber. The external volume was chosen as small as possible to prevent accumulation of gas due to missing swirl of the cylinder charge. The whole geometry was meshed using the Ansys Meshing software, including the boundary layer (inflation) along the walls, using “tetra” elements. Subsequent conversion of the generated mesh by using “polyhedral” elements, which effectively fill the volume, resulted in a significant reduction of total number of cells (i.e. from 633.000 to 252.000).

The engine is usually operated with the two independent gaseous fuel inlets



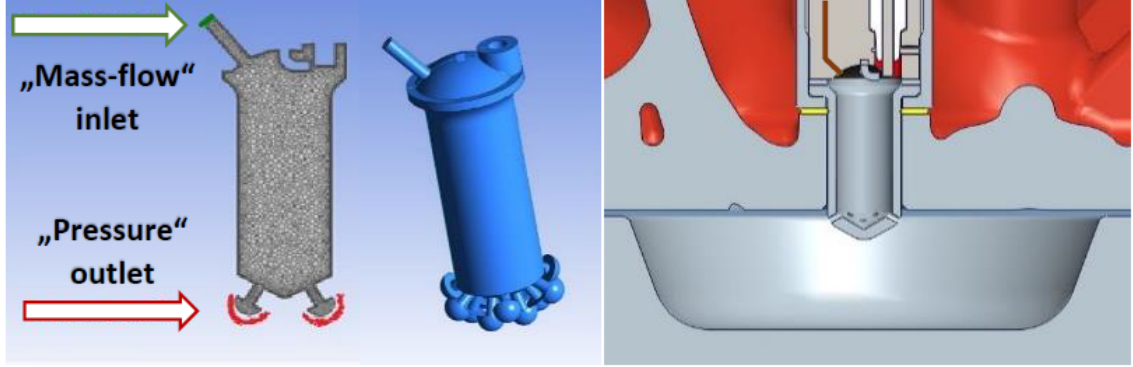


**Figure 5.1:** Cross-section of the pre-chamber with the highlighted boundary conditions (left), 3D geometry of the internal volume (middle), cross-section of the installation assembly (right).

(Mode D). The main part of fuel is delivered into the common mixer upstream of the compressor and the second part (much less) into the pre-chamber. For the description of the events inside the pre-chamber, the special motored engine mode (Mode B) was assumed, and gas was delivered only into the pre-chamber. In this case, the pre-chamber charge is diluted by the pure air from the cylinder during the compression stroke.

The boundary conditions of this task were specified by the crank angle indexed profiles of pressure, temperature and mass flow. The cylinder interface was defined by the “Pressure outlet” boundary Fig. 5.1 with variable values of pressure and temperature. The record of in-cylinder pressure trace was taken from the real engine experiment at 1800 rpm at special motored mode (Mode B) with fully open throttle valve. In the laboratory, the fuel delivery into the pre-chamber was controlled by the gas pressure in the gas rail. This pressure was controlled by the mass flow meter. A backflow from the pre-chamber is prevented by the installation of the miniature check valve. During the experiment the average mass flow rate was measured at steady operation. For the simplification of the CFD evaluation the check valve was simulated by a boundary condition “Mass-flow inlet.” The required instantaneous profile of the mass flow rate of fuel was obtained from the numerical simulation of the pre-chamber with check valve on the tested engine in GT-Power software. According to the experiments, natural gas average flow rate was set to 0.2 Nm<sup>3</sup>/h. A similar analysis of pre-chamber engine using 1-D/0-D approach can be found in [88]. The transient calculation is solved with the following assumptions and simplifications: Mixture of methane and air is considered as an ideal compressible gas. The heat transfer between the charge and the pre-chamber walls was neglected. A  $k - \epsilon$  turbulence model and a “SIMPLE” algorithm for the pressure-velocity coupling

were used. Time step of the calculation was chosen to the value that corresponds to 0.5 degrees of the crankshaft rotation (i.e.  $46 \mu\text{s}$  at 1800 rpm). Longer time step frequently causes a divergence of the calculation due to steep changes in the values of boundary conditions. Each simulation was performed for at least two consecutive engine cycles, in order to be able to monitor the convergence and the progress of the individual parameters.

## 5.7 Simulation Results

### Special Motored Mode

The special motored mode (Mode B) without combustion was chosen for the investigation of the mixture formation in the pre-chamber. Natural gas was delivered only into the pre-chamber, and the cylinder contained only fresh air. This simulation represents the situation before combustion occurs (up to the ignition). Since the CFD simulation does not solve chemical reactions (burning) in this work, the scavenging of the pre-chamber was simulated by substituting the mixture charge in the pre-chamber by carbon dioxide (as a combustion product) at the top dead center (TDC), and the simulation continued under prescribed conditions, defined by mode B. Thus, the scavenging quality of the pre-chamber was assessed.

### Fuel Supply/Leakage Assessment

Fuel flow into the pre-chamber is given by pressure difference in the gas line (fuel pressure) upstream of the check valve and the pre-chamber pressure. When the pressure in the pre-chamber ( $p_{cham}$ ) falls below the value of the pressure loss at the check valve ( $\Delta p = 20\text{kPa}$ ) the fuel starts flowing into the pre-chamber. The Fig. 5.2 shows the instantaneous fuel mass flow rate profile (fuel) predicted by the GT-Power simulation with the average flow value of  $0.2 \text{ Nm}^3/\text{h}$ . The experimental setup only enables measurement of average mass flow of fuel into the pre-chamber. GT-power model of fuel line including the check-valve allowed the authors to evaluate the instantaneous mass flow profile. This model was calibrated by experimental data according to average fuel flow. Resulting mass-flow profiles were imposed as a boundary condition into the Fluent CFD simulation.

The middle plot in Fig. 5.2 shows the integral fuel mass inflow (integral) and outflow that corresponds to the fuel mass that dissipates due to the short circuit scavenging into the cylinder (Fuel leakage). In this particular case, this loss accounts for 37% of supplied fuel in the pre-chamber. From the curve of fuel leakage, it can be observed that massive outflow of the fuel from pre-chamber (to the cylinder) starts to take place within the intake stroke after the exhaust valve has been already closed.

The loss of fuel, by its direct leak during the exhaust event from pre-chamber to the main combustion chamber, is about 6%. It is a question whether this amount of fuel will be lost in the exhaust port and affect the unburned hydrocarbons. CFD simulations including the complete engine geometry, which is currently in progress, will help to find the answer for this question.

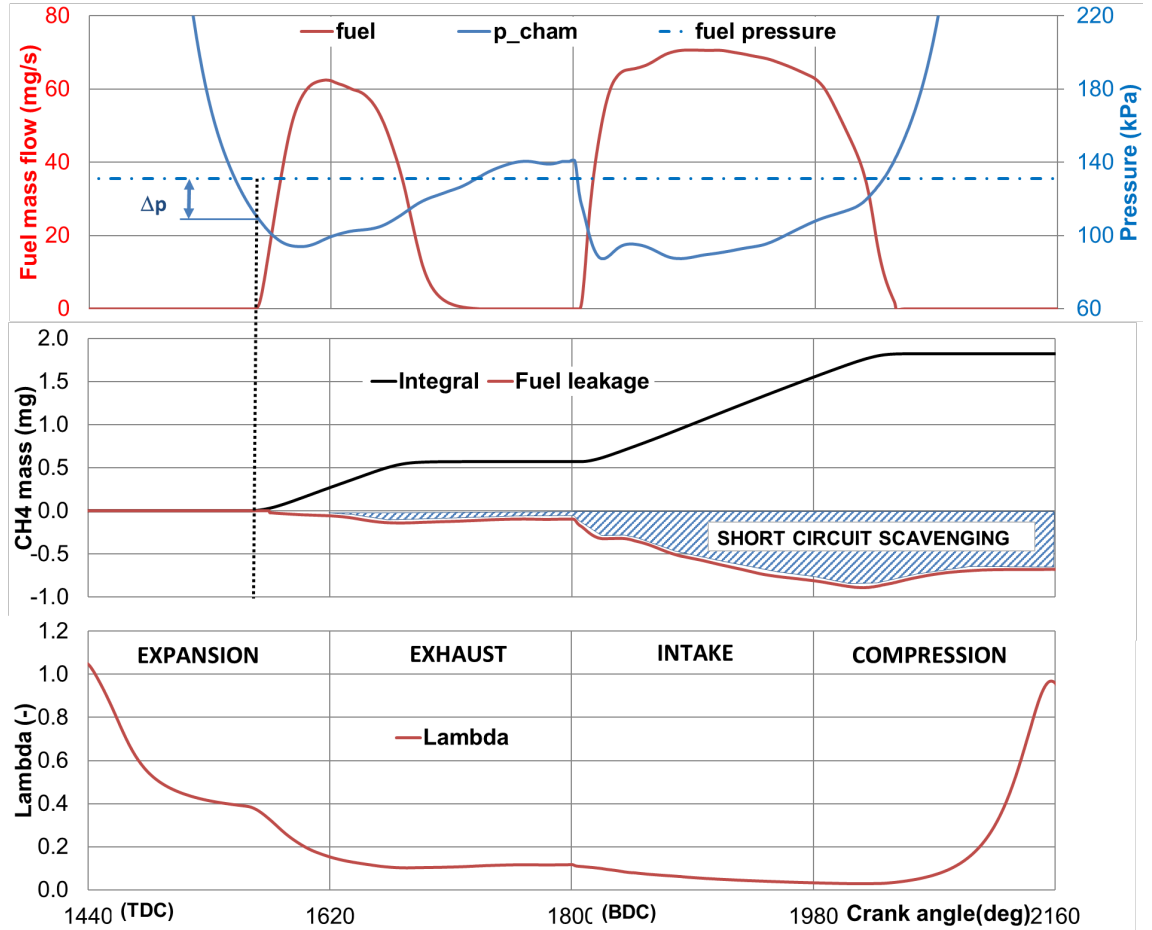


**Figure 5.2:** Fuel delivery, Simulation of special motored mode - 3rd cycle.

The charge inside the pre-chamber (ideally pure fuel) is diluted by the air (or by the mixture, if it is the case) coming from the cylinder during a compression stroke. Mixture formation in the pre-chamber terminates as a result of the pressure rise in the pre-chamber above the main combustion chamber as soon as the combustion starts. Instantaneous value of the total mass of the pre-chamber charge is determined by the course of the compression pressure and temperature. Air excess ratio ( $\Lambda$ ) was evaluated from the average mass concentration of fuel and oxy-

gen inside the pre-chamber. A bottom plot in Fig. 5.2 shows that lambda reaches the stoichiometric value at the TDC. It seems that the conditions for combustion initiation are optimal, however, a look at the spatial distribution of the charge in the pre-chamber will show a more complex picture.

## Mixture Spatial Distribution

For a conventional spark ignition (SI) engine, according to [50], the optimum ignition timing corresponds to combustion phasing of 50% of normalized heat release value at 10 crank angle degrees after the compression top dead center. For the pre-chamber ignition system more factors must be taken into account. One of them is mixture composition in the vicinity of the gap between the electrodes of the spark plug. Mixing depends on the character of the flow and the intensity of turbulence which is primarily determined by the geometry of inlet channels (orifices). Investigated pre-chamber was designed with regard to the shape of the main combustion chamber and the uniform distribution of jets leaving the chamber. Fig. 5.3 shows the mass concentration of methane in the pre-chamber cross-section for the three crank angle positions near the top dead center which is the typical range of spark event. Red color marks the region of rich mixture ( $\lambda \leq 0.5$ ) whereas the region with lean mixture ( $\lambda \geq 2$ ) is colored in blue. Stoichiometric mixture corresponds to 5.5 % of mass fraction of methane.

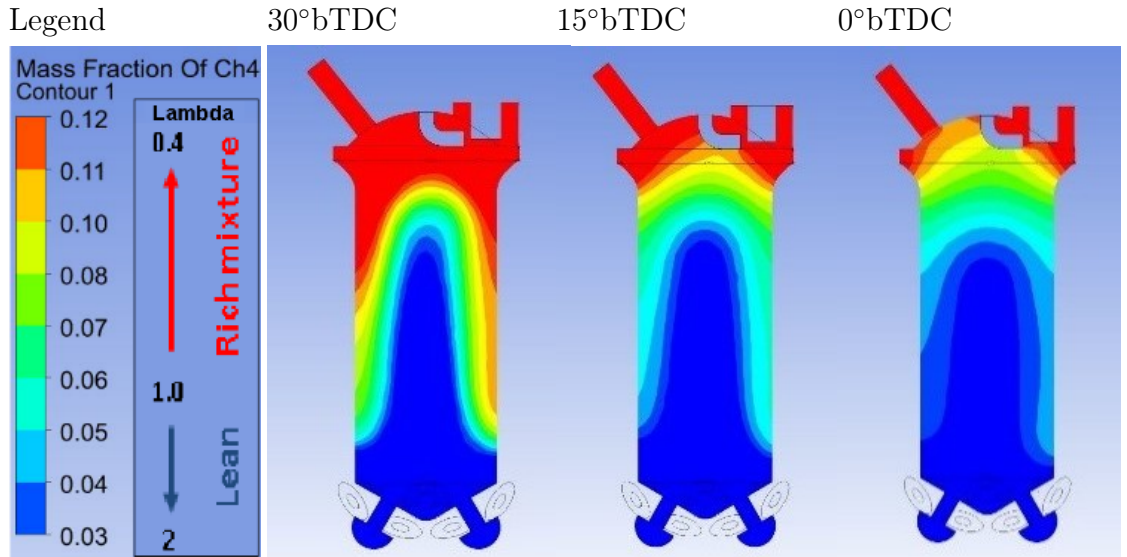


**Figure 5.3:** Methane mass fraction. Simulation of special motored mode – 3rd cycle.

Simulation results show significantly stratified mixture along the axis of the pre-

chamber. This is caused by concentric arrangement of the orifices, relatively long and small inner diameter of the pre-chamber. Due to this fact the ignition timing could be more sensitive to the determination of its optimal value compared to the case of ideal mixing described only by trend of  $\lambda$  presented in Fig. 5.2. Dashed-line marks the region with a good ignitability of the mixture. This area is relatively small and can be assumed that only this portion will burn optimally. It divides the volume into the rich mixture in the upper part of the pre-chamber and lean mixture in the bottom. It can be found in [10] that the minimum ignition energy increases with increasing velocity of flow and changes rapidly with increasing fuel/air ratio and turbulence intensity. The velocity of the flow (about 5 m/s at 15° bTDC by CFD results) and rich mixture ( $\lambda \geq 0.5$ ) in the vicinity of the spark plug gap several times increased the required minimal ignition energy (according to Figure 9-45 presented in [33]). For this reason, the amount of additional gas must be limited to avoid occurrence of these adverse conditions. Another important aspect of this arrangement, which is currently being investigated, but will not be mentioned in this study, is the position of the spark plug and the protrusion of the spark plug electrodes into the pre-chamber.

### 5.7.1 Pre-Chamber Scavenging

The scavenging quality is influenced by the pre-chamber geometry, pressure loss at the orifices (discharge coefficients), location and amount of gas supply. The curves in the graph in Fig. 5.4 illustrate the locally average composition of the pre-chamber charge. In this way, the effectiveness of exploitation of incoming fuel to remove the products of the former combustion process is emulated. For simplicity, the appearance of combustion products was emulated by imposing of 100% of  $CO_2$  in compression TDC. The massive scavenging starts after the check valve opens before expansion bottom dead center and stops at the beginning of the compression stroke. Pressure increase in the cylinder during the exhaust stroke is caused by the pressure pulsations in the exhaust port (visible on the pre-chamber pressure trace in upper part of the Fig. 5.2). Due to this fact, the additional gas flow stops and fresh air start flowing into the pre-chamber for certain time period of exhaust stroke. At the gas exchange TDC there is a visible sharp drop in air mass fraction inside the pre-chamber. It can also be explained by the pressure trace plotted in Fig. 5.2. A sharp pressure drop evacuates more air than  $CO_2$  from the pre-chamber volume. Therefore, air mass fraction sharply drops and  $CO_2$  fraction temporarily rises. During the compression stroke the air coming from the cylinder dilutes the mixture in the pre-chamber.

The residual amount of  $CO_2$  in the pre-chamber is 0.84 mg that corresponds to 3.3% of the total mass fraction at the end of the compression cycle. Gaseous fuel supply is essential for the pre-chamber scavenging. Exhaust gas residuals remain

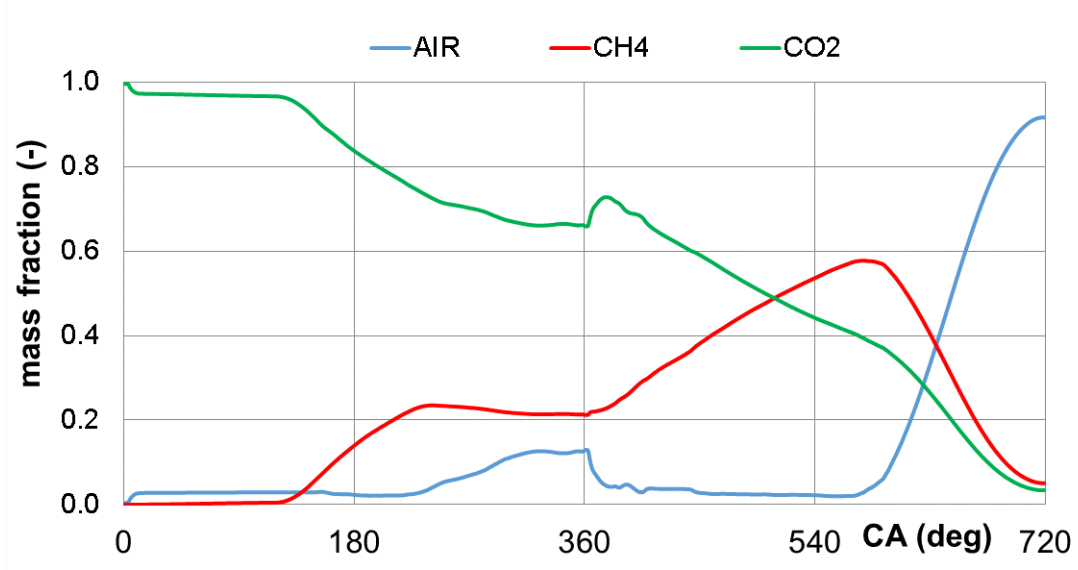


**Figure 5.4:** Pre-chamber scavenging simulation - 1st cycle.

near the electrodes due to the direction of gas inlet and the spark plug eccentricity. Fig. 5.5 shows the concentration of  $CO_2$  together with streamlines to visualize the flow profile during the exhaust stroke (at  $CA = 270^\circ$ ).

## Computational Validation

Selected parameters were validated by means of the 1-D numerical simulation results. Good correlation between the Fluent and GT-Power was achieved, regarding the values of flow velocities and flow rates. Fig. 5.6 presents the comparison of volumetric flow rate through the orifices. The GT-Power simulation uses the 1-D discretization for pipes and 0-D for the cylinder and pre-chamber. The 0-D approach assumes the ideal mixing of all components in the evaluated volume. Due to this fact, the resulting values can be different from the full 3-D flow model. Especially the composition of charge in the pre-chamber and the gas leakage assessment might give different results.

Some improvement of 0/1-D plausibility can be achieved by the use of a scavenging object for the pre-chamber in the GT-Power simulation. It describes the relationship between the cylinder residual ratio and the exhaust residual ratio which defines scavenging function. This object must be used in two-stroke engines and must be calibrated from experiments or CFD simulations. The example of the simulation model of two-stroke diesel engine and its calibration is described in [61]. The scavenging function can improve the information about exhaust gas residual

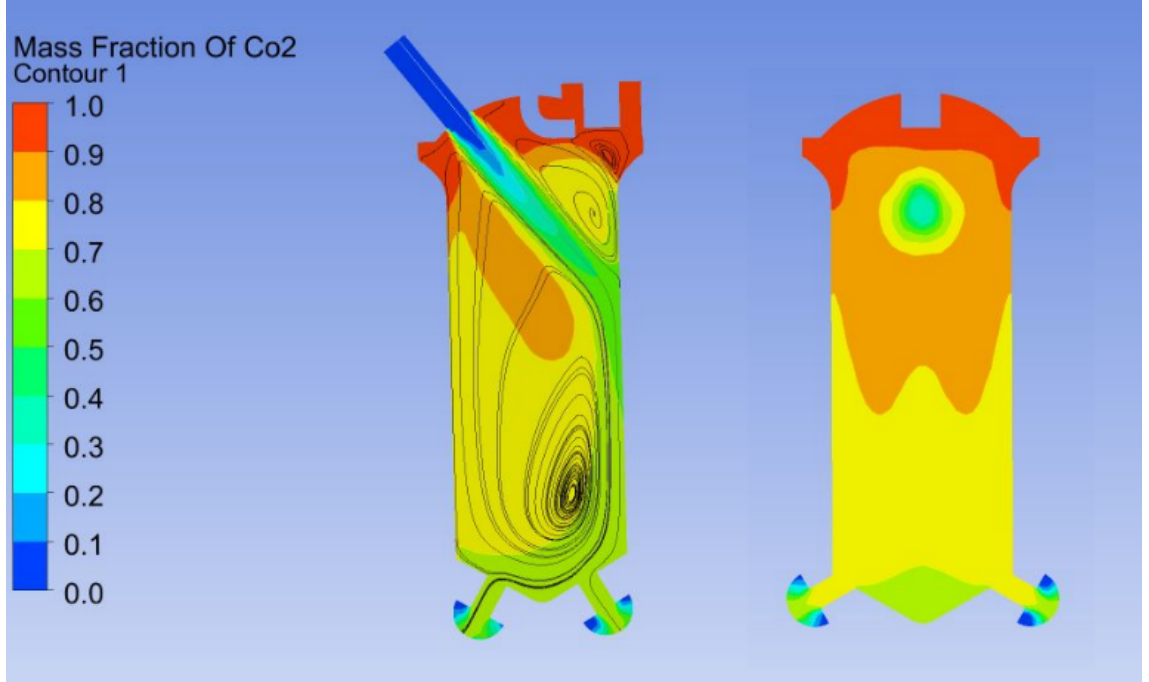


**Figure 5.5:**  $CO_2$  mass fraction and streamlines, Scavenging simulation - 1st cycle, crank angle 2700, perpendicular sections (A-A, B-B).

and average composition in the pre-chamber. Authors are currently working on the calibration of scavenging function by means of the CFD.

## Experiments

The data from experiments of the motored (Mode A) and special motored engine mode (Mode B) was used as an input for numerical calculations. Additional experiments with combustion, described below, were carried out in order to confirm the CFD simulation results and demonstrate the functionality of the designed pre-chamber ignition system.

## Combustion only in the Pre-Chamber

Sensitivity analysis of ignition timing and fuel quantity study at partly motored mode (Mode C) was carried out with the combustion and the results are shown in Fig. 5.7. Optimal value of ignition advance timing (before TDC) decreases as the fuel quantity rises. This is caused by the time needed for the sufficient dilution of the pre-chamber charge during the end of the compression stroke.

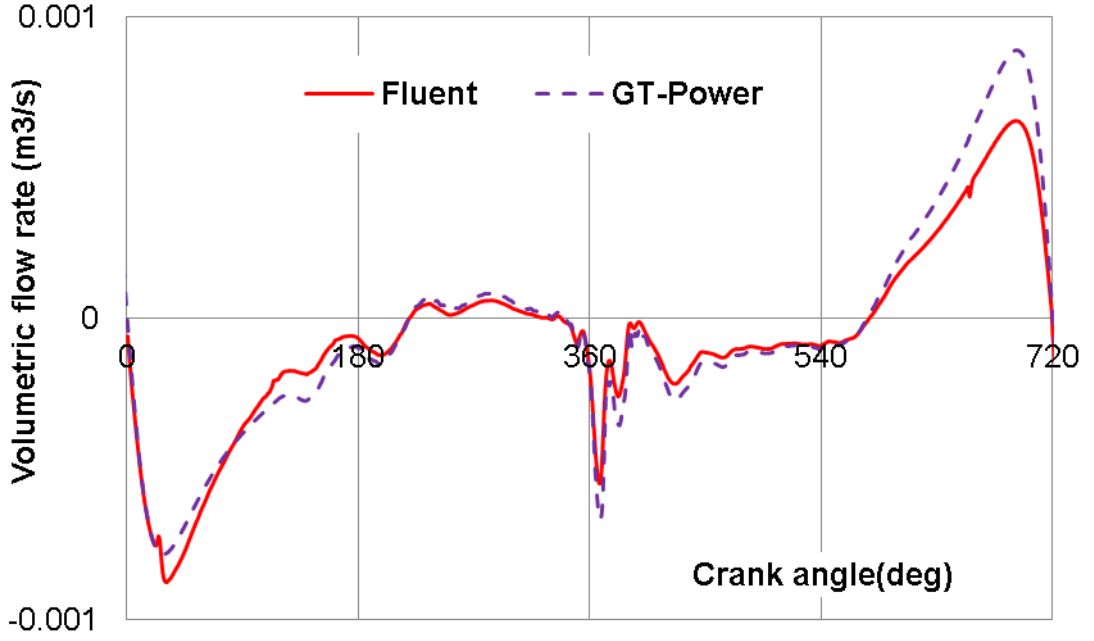


**Figure 5.6:** Comparison of volumetric flow rate through the orifices. Simulation of special motored mode (Mode B).

The amount of unburned fuel is expressed in terms of methane emission index ( $EICH_4 = \text{mass flow of } CH_4 \text{ in exhaust} / \text{total fuel consumption in kg/hour}$ ). The best result shows that maximum of 30% of supplied fuel into the pre-chamber is burned for gas average flow rate  $Q=0.1 \text{ Nm}^3/\text{h}$ . Further increase in the quantity of additional gas in the pre-chamber does not bring any benefit in this mode, even though the case with  $Q=0.2 \text{ Nm}^3/\text{h}$  (used for CFD) corresponds approximately to the theoretical stoichiometric mixture for current pre-chamber volume. A very rich mixture within the vicinity of the spark plug and low mixing of the pre-chamber charge can be the reason why it leads to worse combustion (confirmed by CFD, Fig. 5.3).

However, considering that the pre-chamber is an ignition device, it can be understood that for case  $Q = 0.3 \text{ Nm}^3/\text{h}$ , even though a lower fraction of total fuel is burned, the absolute amount of fuel burnt and heat released by burning pre-chamber jets is higher, which provides more ignition energy in the main chamber. Tab. 5.1 shows the theoretical and real pre-chamber heat release for various fuel flows, evaluated from the fuel quantity and combustion efficiency (as a reciprocal value of methane emission index). The pre-chamber heat release (ignition energy) varies between 20 to 30 J, which is a thousand times higher than the spark energy



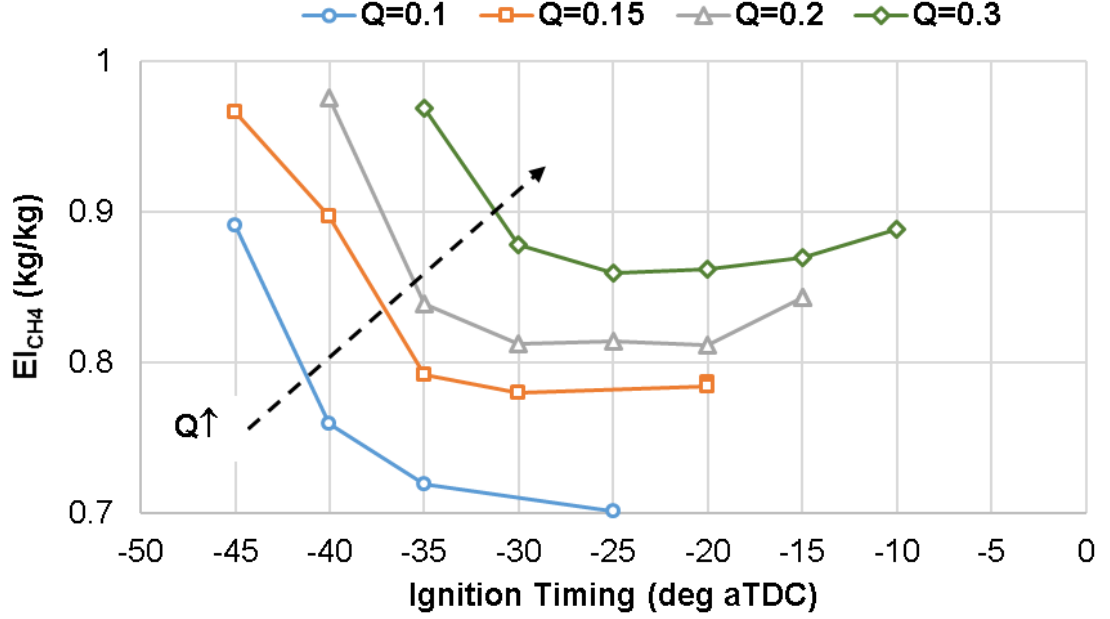


**Figure 5.7:** Sensitivity analysis of ignition timing and fuel quantity, (Mode C).

(ANNEX F).

Q (Nm <sup>3</sup> /h)	0.1	0.15	0.2	0.3
Fuel quantity (mg/cycle)	1.3	2	2.7	4
Theoretical fuel energy (J)	66.4	99.6	132.8	199.2
$EI_{CH_4}$ (kg/kg <sub>fuel</sub> )	0.7	0.78	0.81	0.85
Pre-chamber heat release (J)	19.9	21.9	25.2	29.9

**Table 5.1:** Pre-chamber heat release.

The interior of the pre-chamber is partly separated from the main combustion chamber, and thus is protected from the intensive mixture motion in the cylinder. The idea of the pre-chamber without scavenging in full combustion mode (Mode D) could be used, however, additional gas in the pre-chamber is necessary for scavenging hot residuals from the previous cycle, and keeping the wall surface temperature within the safe operational range (avoiding pre-ignitions).

It is important to note that the operation in this mode (Mode C) is not typical for

normal engine operation. It is used for the CFD validation only. Partially, it reflects the pre-chamber functionality, but the results are distorted by the short circuit scavenging (37% by CFD simulation) and the poor composition (and conditions) in the cylinder leads to flame quenching. The lost fuel would be probably burned in the main combustion chamber in normal operation.

## Full Combustion Mode

Fig. 5.8 displays the basic performance parameters of the naturally aspirated engine with the pre-chamber ignition system at constant engine speed of 1800 rpm, fully open throttle valve and constant pre-chamber fueling flow rate of 0.1Nm<sup>3</sup>/h. The ignition timing was adjusted to keep the constant (position) combustion phasing of 50 percent mass fraction burned ( $CA_{50} = 10^\circ aTDC$ ) for all of the operating conditions. Desired air excess ratio was set by the control of the main gas actuator at the compressor inlet.

The measuring sequence started at  $\lambda \sim 1$  operational point (with IMEP 8.25 bar) which demonstrates the ability to operate the pre-chamber with the mixture composition that is compatible with a three-way catalyst (TWC).

At low loads, the scavenged pre-chamber allows ignition of extremely lean fuel-air mixtures with high combustion rate and significantly expands the flammability limit compared to the conventional spark (see Chapter 4). The curve of peak in-cylinder temperature (TMAX) shows the typical descending tendency with higher air excess values. The low temperature combustion results in low  $NO_X$  emissions, lower thermal losses and higher ratio of specific heats, which leads to increase in thermal efficiency.

At extremely lean operation, the content of nitrogen oxides in raw exhaust gas is very low, offering a good prospect to comply with emission limits given by the legislative for road vehicles, without an exhaust gas  $NO_X$  after-treatment. During the operation with  $\lambda$  above 1.9, the specific values of  $NO_X$  formation remain below the threshold of 0.5 g/kWh, which is considered to be decisive for assessment of acceptability of  $NO_X$  emission from the point of view of current and future emission legislature.

Another aspect of extreme mixture dilution is the increase of hydrocarbons emission. Amount of unburned fuel is expressed in terms of methane emission index ( $EICH_4$ ). At the right side of the graphs ( $\lambda = 2.1$ ), the engine indicated efficiency ( $\eta_{ai}$ ) is low and considerable amount of delivered fuel does not burn at all. This is the major challenge to improve performance of the pre-chamber ignition system.

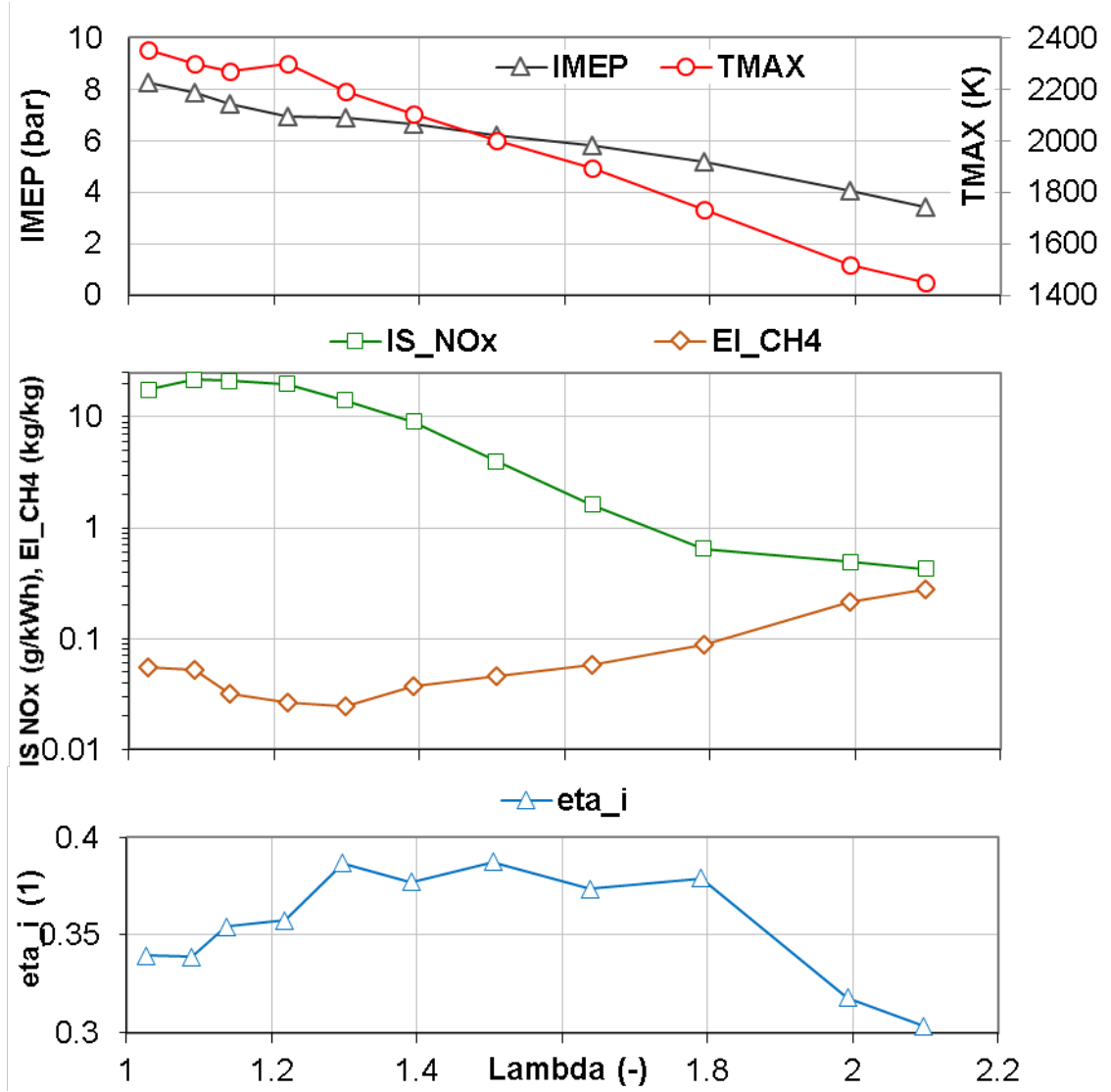


Figure 5.8: Basic performance of pre-chamber engine, (Mode D).

## Transient Test

The following test is presented to describe the pre-chamber behavior during the change of operational modes. The transient test started with the same conditions as the previously mentioned measurement when the full combustion regime ended. During the transient, the main gas supply was stopped. This test demonstrated the change from full combustion mode (Mode D) to combustion in pre-chamber only (Mode C).

The four selected cycles from the high speed data acquisition record of 146 consecutive cycles for this transient test are shown in Fig. 5.9. The measurement started at steady operating point (Mode D) with  $\Lambda = 2.1$  and  $\text{IMEP} = 3.41$  bar. The pressure trace for this point is shown by the curve cycle 0. A visible increase in pressure in the pre-chamber, followed by the start of combustion in the main combustion chamber can be observed.

Transient states are represented by curves from cycle 57 and cycle 73, which show reduced pressure rise rate than that in cycle 0, but steeper than that in cycle 84. The pressure trace of cycle 84 represents the combustion only in the pre-chamber (Mode C). The position of the peak pressure was significantly shifted, when the main gas stopped flowing into the cylinder. The combustion (and its stability) begins to deteriorate significantly until it is hardly visible (identified) at the end of the test.

Possible explanation of the improved functionality at normal engine operation in the “Full combustion mode” is the enlargement of the flammability region in the pre-chamber by the mixture flowing from the cylinder. It leads to stabilization and better combustion in the pre-chamber.

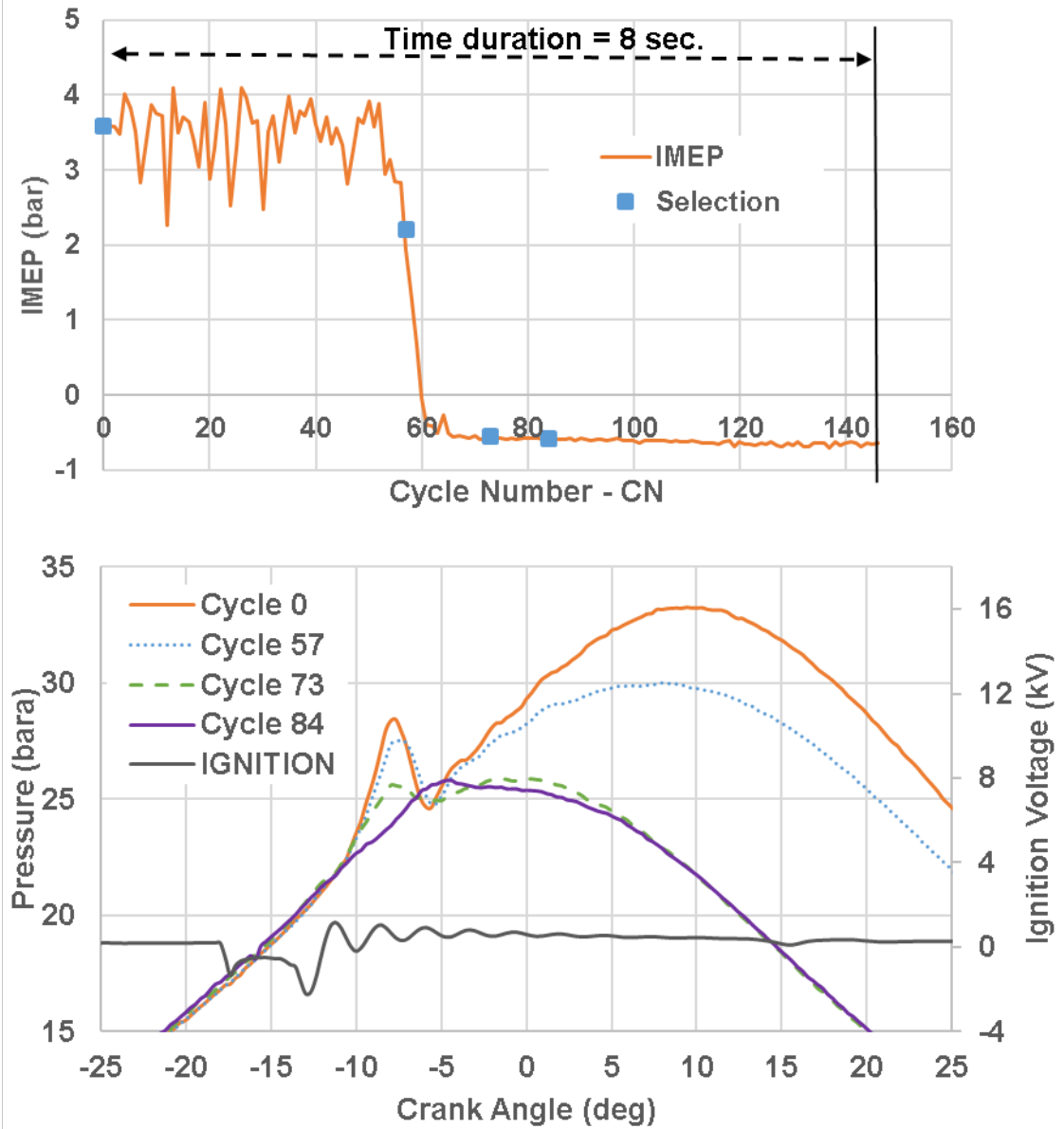


**Figure 5.9:** Transient test - results of high speed data acquisition, pressure in pre-chamber.

## 5.8 Discussion

It has to be mentioned that informative quality and explanatory power of the CFD simulation effort in its current state is limited by introducing a number of simplifications. However, the results acquired so far, allow a deeper insight into the behavior of the pre-chamber charge than previous 0-D and 1-D simulation attempts. Short summarization of the newly acquired knowledge follows.

### Fuel Leakage Assessment:

A simple mechanical control of the fuel supply in the pre-chamber by the check valve, with the appropriate opening pressure and with appropriately adjusted fuel pressure upstream of the valve, provide an acceptable and sufficient fuel supply control. For the pre-chamber fuel rate below 0.2 Nm<sup>3</sup>/h, the results show insignificant fuel leakage during the exhaust stroke into the exhaust due to the short circuit scavenging.

### Mixture Distribution:

The mixing intensity of lean mixture (or pure air in the investigated case), coming from the cylinder into the pre-chamber, with the original pre-chamber charge during the compression stroke, is low. The iso-lines in Fig. 5.3 look as if the two parts of the pre-chamber charge were separated by a diaphragm. If a higher degree of dilution of the original charge in the vicinity of the spark plug gap is desirable, the intensity of mixing of pre-chamber charge has to be enhanced.

### Pre-chamber Scavenging:

Results of the CFD simulations presented in Figure 5 show that at the instant, when the fuel delivery is finished, by closing the check valve, the remaining  $CO_2$  occupies approximately 40 % of the pre-chamber mass, while the rest of the pre-chamber is filled with the delivered methane. After the pre-chamber charge is diluted by the inflow of the working substance from the cylinder during the compression stroke, the content of residuals in the pre-chamber is lower than the typical content of residual gas in conventional SI engines operating with wide open throttle valve (typically around 5%, [33]).

The locally averaged composition of the pre-chamber charge at the instant of the expected spark discharge is favorable. However, the contours in the picture in Fig. 5.5 do not offer a very optimistic prospect. The spark plug gap is positioned to the right of the bulk flow of the working substance. It is expected, that even if the composition of working substance in the vicinity of the spark electrodes would be significantly

improved, until the spark discharge takes place, the mixture stratification shows rather unfavorable patterns with a high content of incombustible components near the spark plug electrodes. A modification of the fuel supply channel inside the pre-chamber body, with changed position and direction of fuel outlet was designed. Modified pre-chamber is now under testing.

## Experiments:

The performed sensitivity analyses serve also as data for control strategy and optimal setting. Experimental results are consistent with performed CFD simulations.

Lean operation potentially allows reduction of nitrogen oxides ( $NO_X$ ) emissions to levels below the legislative limits without the need of  $NO_X$  after-treatment system. At the same time, lean mixture decreases the combustion temperature, hence heat losses are lower and thermal efficiency of the engine increases.

Appropriately designed catalytic exhaust gas after-treatment would probably be able to mitigate unburned hydrocarbons in all operational regimes. However, unburned hydrocarbons lead to lower engine efficiency and therefore we want to improve combustion efficiency by increasing the volume of the pre-chamber, i.e., the value of ignition energy.

## 5.9 Conclusions

The pre-chamber engine was tested in four different fueling modes with or without spark discharge, to allow separate investigations of various phenomena of this advanced combustion system.

From the partly motored mode (Mode C) it can be concluded that the pre-chamber as a source of ignition energy for lean burn engine provides approximately one thousand times higher energy than the energy of conventional spark plug, even though the combustion efficiency in the pre-chamber was around 30% in the best case ( $Q = 0.1 \text{ Nm}^3/h$ ). The (leakage) loss of unburned fuel, by its direct leak from the pre-chamber to the main combustion chamber, will be burned in the main chamber in normal engine operation.

The performed CFD simulations of the scavenged pre-chamber enhance experimentally acquired knowledge. The quality of scavenging evaluated quantitatively as amount of leaked fuel and qualitatively as a spatial distribution of mixture in the pre-chamber were obtained and discussed. Despite the introduced simplifications, which affect the accuracy of the results, this model can be used for efficient evaluation of different variants, geometry optimizations and sensitivity analysis, with

lower computational requirements, and also as a feedback for the calibration of the scavenging object in the 0-D model of the pre-chamber in the GT-Power software.

According to CFD results, the evaluated pre-chamber can be described as a no swirl pre-chamber with the stratified charge. The low mixing in the pre-chamber is the main factor that influences the functionality of the designed version. Due to this fact, which results in rich mixture in the vicinity of spark plug electrodes, the maximum amount of the additional gas in the pre-chamber and thus the ignition energy is limited. However, the very good global functionality (performance) of the whole combustion system in normal operation was confirmed by the presented lambda sweep, which shows sufficient combustion efficiency, together with favorable  $NO_X$  emissions.

The lean mixture flowing from the cylinder increases the flammability region in the pre-chamber and leads to the stabilization and better combustion in the pre-chamber. The enhanced ignition energy, which results from multipoint ignition of the mixture in the main combustion chamber, results in steep rise of combustion rate and expansion of flammability limit compared to conventional spark ignited engine.

The knowledge will be subsequently used in the new prototype design, to improve global functionality of scavenged pre-chamber, e.g., better charge homogeneity and its scavenging. The CFD simulation of the combustion in the pre-chamber will be introduced in the next chapter. The complete engine geometry and combustion process will be solved.



## Chapter 6

# Development of a Pre-chamber Ignition System for Light Duty Truck Engine

Various sensitivity studies of control strategies (pre-chamber fueling rate, ignition timings) and geometrical configurations (number and geometry of nozzles) of the pre-chamber were presented in chapter 4. The most of the analyses then were based only on the detailed thermodynamic analysis of the records of the two pressures in the pre-chamber and the main combustion chamber, coupled with the analysis based on the chemical efficiency from the exhaust gas composition measurements from the raw exhaust gas.

A complexity of the physics inside the combustion chamber demanded the support from simulations to understand the complex physical and chemical processes in the cylinder throughout the entire engine working cycle. Therefore, as a first step a 1-D model of the tested engine was built and calibrated. In the next step a CFD flow model of a pre-chamber geometry with fixed mesh was designed and used for a numerous studies of the scavenging and the investigation of the flow field inside the pre-chamber of the motored engine with and without fuel supply chapter 5 to the pre-chamber.

A CFD engine model with intake and exhaust ports and combustion chamber geometry with moving piston and valves describe the behavior of the whole working substance during the working cycle. Combustion process is involved. Current state of CFD modeling will be described in dedicated section.

## 6.1 Experimental Setup

The engine and all of the experimental equipment for this study is exactly the same as the equipment described in the chapter 4. The pre-chamber variant, investigated in the current chapter is identical to the 12 hole ( $\varnothing 1.2$  mm) variant, described in the chapter 5 in Tab.4.2.

## 6.2 Measurement Results

The measurement results are introduced as they were acquired with pre-chamber configuration described in the previous sections. All measurements were performed at 1800 rpm, fully open throttle and ignition timing adjusted to give constant position of 50% of mass fraction burned ( $CA_{50} = 10^\circ$  aTDC) for each measured point. Constant pre-chamber fueling rate of 2 mg/cycle was adjusted according to the results of the preliminary experimental sensitivity studies (see chapter 4). Confirmation of the correctness of this value is presented in Fig.6.9 later in section CFD Model Results.

The engine was fueled with grid natural gas with 97.1 % (by volume) of methane. Air excess ratio is used as an independent variable in all graphs in this section.

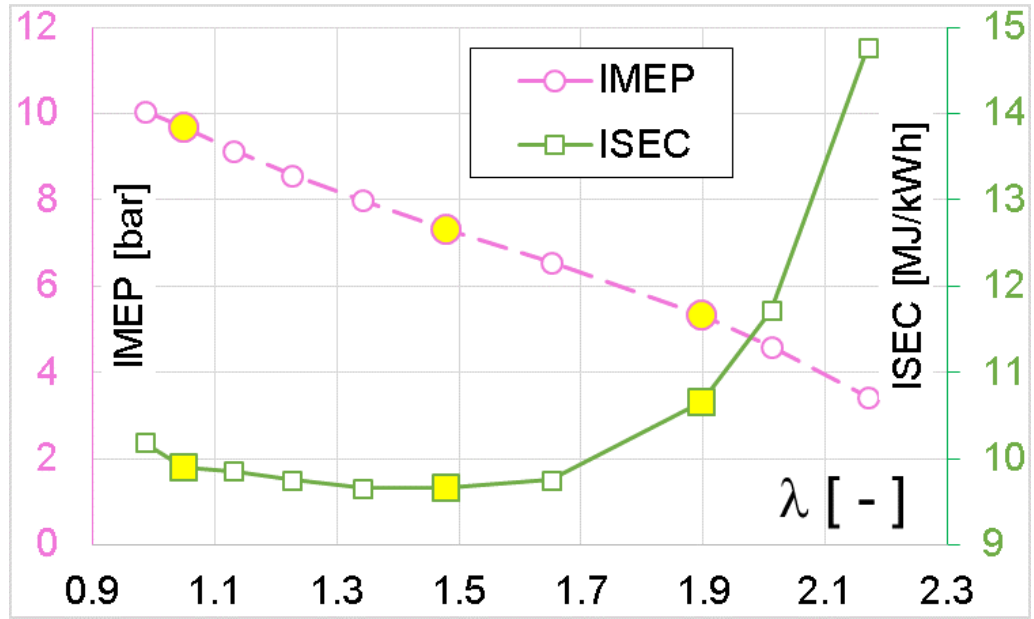


**Figure 6.1:** Basic engine performance as a function of the air excess ratio ( $\lambda$ ).

Engine performance and efficiency is shown in Fig.6.1, where indicated mean

effective pressure (IMEP) and indicated specific energy consumption (ISEC) curves are plotted as a function of the air excess ratio ( $\lambda$ ). In the figure, three points of  $\lambda = 1.05, 1.49$  and  $1.9$ , that were used for CFD simulations are highlighted (yellow markers).

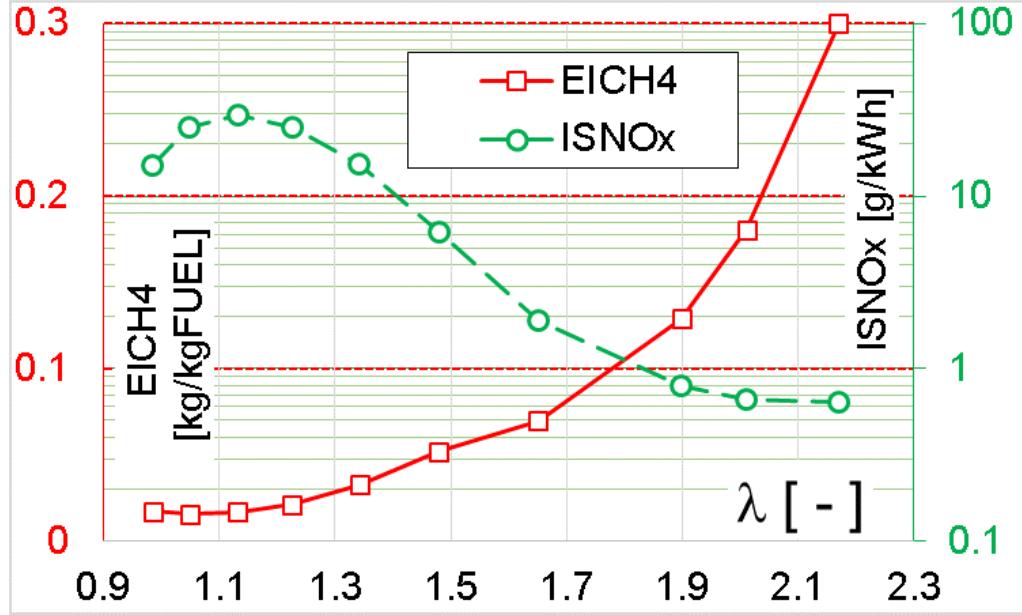


**Figure 6.2:** Engine-out emission as a function of the air excess ratio ( $\lambda$ ).

Engine out emission are introduced in Fig. 6.2 as indicated specific emission of  $NO_X$  (ISNO $_X$ ) and methane emission index (EICH4).

Engine running roughness is presented in Fig. 6.3 by plot of coefficient of variation of indicated mean effective pressure (COVimep). In the same figure combustion phasing is depicted by plot of CA50 and ignition timing (IgnTmg).

The curves in Fig. 6.1 to Fig. 6.3 illustrate typical behavior of the pre-chamber engine. Lean limit of flammability is significantly extended compared with conventional SI engines. While operating with mixture composition at the lean end of the presented curves the content of  $NO_X$  in raw exhaust gas is very low, featuring good prospect to simplify the exhaust gas aftertreatment in the real world operation.

On the other hand, the pre-chamber engine is able to operate with stoichiometric mixture at fully open throttle. This makes possible to operate engine at full load with  $\lambda = 1$  and conventional TWC. Burning velocity within the whole tested range is sufficient, as can be observed from moderate demand for spark advance to maintain  $CA50 = 10^\circ$  aTDC.

Within investigated range of air excess ratio, the constant pre-chamber fueling

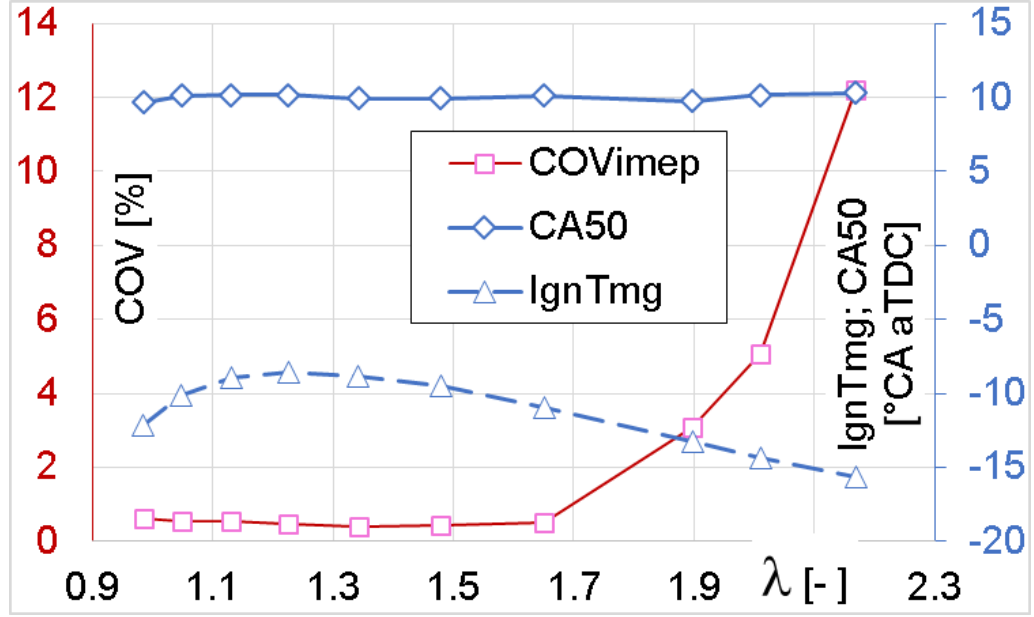


**Figure 6.3:** Running roughness & combustion phasing as a function of air excess ratio.

rate ensures reliable ignition. This observation can simplify the real engine control strategy. Within the range of lean mixture operation, valid for SI engine ( $\lambda \leq 1.7$ ), the engine running roughness is very low. Up to  $\lambda = 2$  the running roughness is still acceptable (COVimep  $\leq 5$ ). The main drawback is high content of unburned methane in engine-out exhaust gas Fig. 6.2. It worsens significantly chemical efficiency with a penalty in overall engine efficiency.

### 6.3 1-D Flow Model for Boundary Conditions Generation

1-D GT-Power model of the investigated system was built and used for generation of physical quantities which are not available from direct measurement (e.g., instantaneous mass flow rate of gas through the check valve which was used as a boundary condition in CFD simulation). The simulation of the “pre-chamber engine” requires modeling of two divided combustion chambers (one for the cylinder and the second one for the pre-chamber). For both volumes, the modeling of combustion, heat transfer and emission formation is needed and therefore the cylinder objects were used. At the first stage, a scavenging reference object was not used, i.e., the gases in the investigated volume are assumed to be ideally mixed (0-D approach).

In case of pipes, the numerical simulation uses 1-D discretization (parameter is the length of pipe). These assumptions lead to good prediction regarding the values of flow velocities and flow rates. On the other hand, the 1-D model cannot correctly determine the composition of the charge in the pre-chamber, to assess a gas leakage and so on, that is a task for CFD.

The influence of throttling in the pre-chamber's nozzles is respected by several pipes with appropriate dimensions (1-D approach). The pressure losses are represented by flow coefficients, calibrated by the data of pressure traces that are directly measured in the cylinder and the pre-chamber from a motored engine. The amount of additional gas flow into the pre-chamber is controlled by the pressure upstream of the check valve. The mechanical check valve prevents backflow from the pre-chamber into the fuel system. This part was modeled by the valve object (connection) with two dimensional array of pressure difference and discharge coefficients (determined experimentally). A dynamic behavior is respected by the valve lift time constant which represents the inertia of the valve (was set to 0.1ms).

The rest of the model was calibrated by a standard three pressure analysis (TPA) procedure [15] from experimental data (in-cylinder, intake and exhaust manifold pressure records) for each operating point. The Fig. IV in Annex E shows the scheme of the pre-chamber engine model with intake and exhaust ports.

## 6.4 CFD Model of Pre-Chamber Engine

Detailed CFD thermodynamic model of the scavenged pre-chamber SI engine was created in AVL FIRE [4]. The main target of this activity was to create a predictive model to evaluate different design variants of the target engine, hence enabling optimization of certain design parameters. The CFD model also allows for understanding the complex phenomena taking place inside engine combustion chamber. The CFD model was built while using the experience from EU FP7 program LESSCCV which was focused on detailed modelling of combustion processes in SI engines including cycle-to-cycle variability – c.f. [85], [77].

### Mesh Generation and Calculation Setup

The mesh was generated using detailed engine geometry from CAD/CAE software tools. The generated mesh is presented in Fig. 6.4. As the engine cycle performance simulation over the entire cycle was needed, the movable mesh of the complete 4-stroke engine cycle had to be created – this is always a complex task to achieve that. The following AVL FIRE tools were needed: FAME Engine+, FAME Hexa. Moreover, all engine ports are present during the whole calculation – this was needed as multiple engine cycles were calculated to study the Cycle to Cycle

Variation (CCV) effects. Due to application of the Large Eddy Simulation (LES) approach, the maximum cell size was set to 0.6 mm while refinement near certain parts/edges was needed. The pre-chamber cell size was set to 0.3 mm while channels connecting the pre-chamber with engine cylinders were modeled even finer: typical cell size was 0.15 mm. The main reason behind the mesh refinement in the pre-chamber domain is the requirement to capture the early flame development in pre-chamber. The amount of mesh cells varies between 7.5 and 13 million depending on engine crank train position.

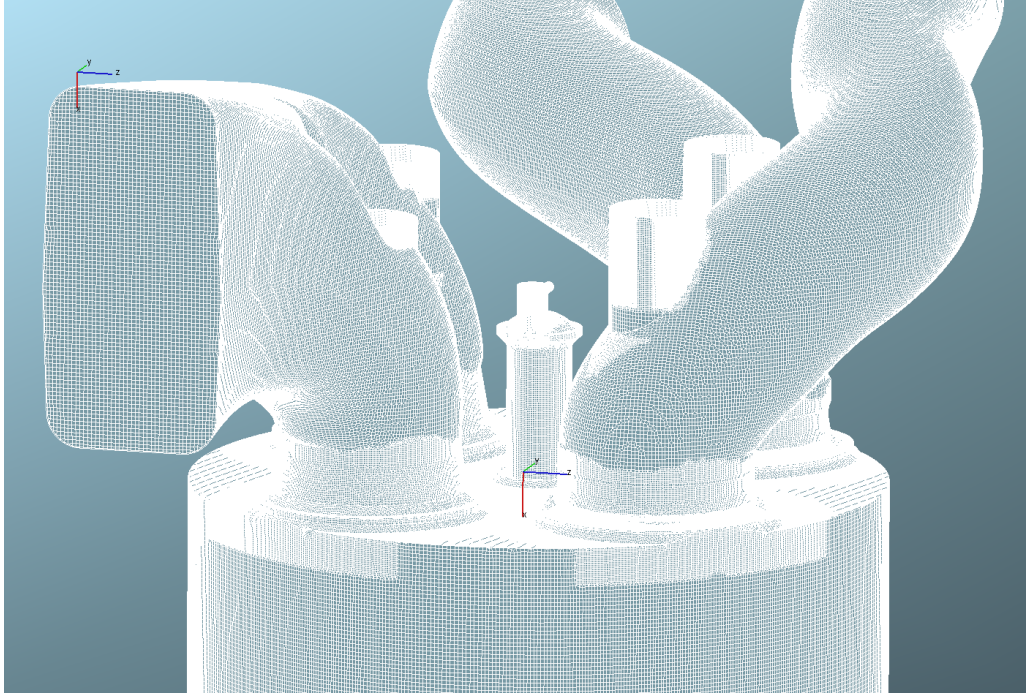


**Figure 6.4:** A snapshot of CFD mesh.

Concerning boundary and initial conditions, they were transferred from the calibrated 0-D/1-D model of the engine created in SW tool [3], described in previous section. To be more precise, surface temperatures were based on simplified predictive FEM model, inlet/outlet boundary pressure/temperature was imposed as function of crank angle. The same applies to fuel mass-flow rate to the pre-chamber, which represents mixture enrichment via dedicated fuel supply system. Initial values of all required thermodynamic parameters (including composition) were directly transferred from the 0-D/1-D model.

Dealing with numerical setup, the following settings were applied. PISO algorithm [37] was selected as time integration method while 2nd order schemes were

used for convective term approximations. Time step was set to 0.1 degCA. Regarding turbulence modelling, coherent structure version of LES approach [51], [46], [45] was selected. Concerning combustion models, the LES version of ECFM-3Z [63] was activated due to positive experience with this model from the past – c.f. [85] and [77]. It should be stressed that this model is turbulence driven, hence it cannot capture local chemical effects (e.g., flame quenching due to low temperature) – this leads to a statement that all fuel is burnt when using this model (provided there is enough oxygen). Dealing with applied chemistry, the turbulence driven combustion models are usually linked with simplified chemistry approaches based on equilibrium. This was also the case for the presented CFD calculations. The only considered pollutant was  $NO_X$ , however its formation was based on standard approach [97], which is to solve certain equations of chemical kinetics.

## CFD Model Calibration

As the applied models are supposed to be detailed and predictive, there are not many parameters to be calibrated. After discussions with experts from AVL (provider of CFD tool [4]), only 2 parameters were selected for tuning of combustion model: initial flame surface density and stretch factor. These parameters were identified with respect to experimental data for the case of air excess 1.05.

After that, these parameters were fixed for all other calculations. The only other parameter, which was also varied, was combustion timing. As the detailed ignition model was not applied, the simplest approach of imposing flame kernel of certain size and flame density was adopted. Hence, there is a need to find a proper phasing of this event (early flame kernel development in the pre-chamber). This was achieved by variation of ignition event to match the 1st pressure peak in the pre-chamber for the case of 1st calculated engine cycle. All other subsequent cycles kept the same combustion phasing as for the 1st cycle. This fine-tuning of combustion phasing was done for every case of calculation (i.e., different levels of air excess).

Fig. 6.5 shows comparison of in cylinder and pre-chamber pressures for average cycle (from 115 measured and from 5 modeled cycles) and for the cycles with the highest and the lowest peak pressure. All graphs correspond to the case of 1800 rpm and air excess of 1.05. In this case the modeled pressures match the measured average curves well. It can be seen that LES modeling approach captures the cycle-to-cycle variation similarly as experiment. Bottom graph (of Fig. 6.5) shows RoHR for the cycles with the highest and the lowest peak pressures both modeled and measured. The shape, phasing and duration of ROHR are closely matched to experimental data. Based on these results, the CFD model was declared to be calibrated.

Similar comparison of model results with experiments was performed for air excess of 1.48 and 1.9. Fig. 6.6 displays the same set of curves as Fig. 6.5 for the air excess of 1.9.

It should be stressed that model results are predicted data and the only tuning was related to the combustion phasing (as described above). A relatively good correspondence was found including CCV effects. However, the modeled pressure traces are over-predicted when compared with experimental data. This is related to above mentioned fact that LES ECFM-3Z combustion model, which is turbulence driven, cannot predict any local chemical phenomena (e.g., flame quenching). That is why all fuel is always burnt in CFD calculations while it is not the case for the real engine. In real engine operation 13% of unburned methane was observed in raw exhaust gas as visible in Fig. 6.2.

It is supposed that these effects are related to local chemistry and only combustion model based on chemical kinetics could capture that. Such model will be employed in the future.



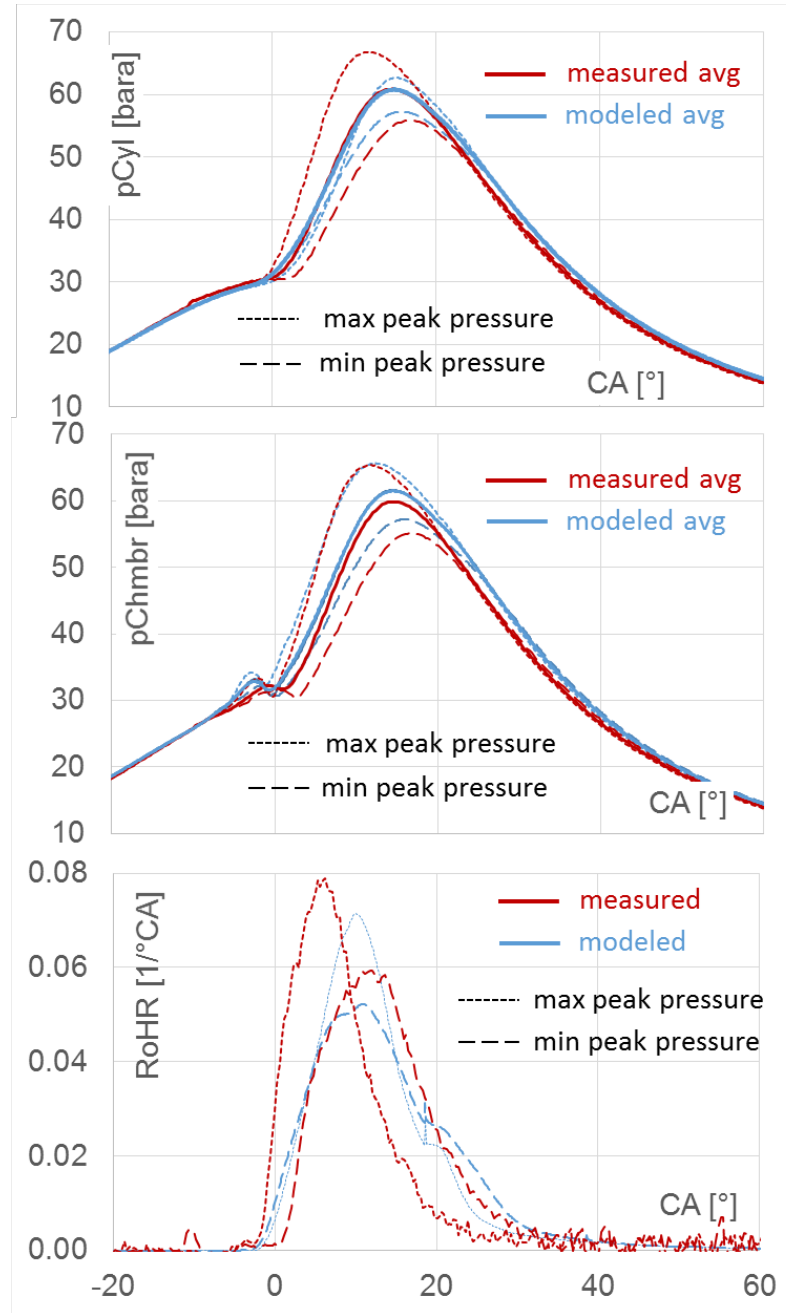


**Figure 6.5:** Comparison of measured and modeled pressure in the cylinder (pCyl - top) and in the pre-chamber (pChmbr - middle) and rate of heat release (RoHR - bottom) for the case of 1800 rpm and air excess of 1.05. Blue color corresponds to CFD calculation. Red color corresponds to measured data.

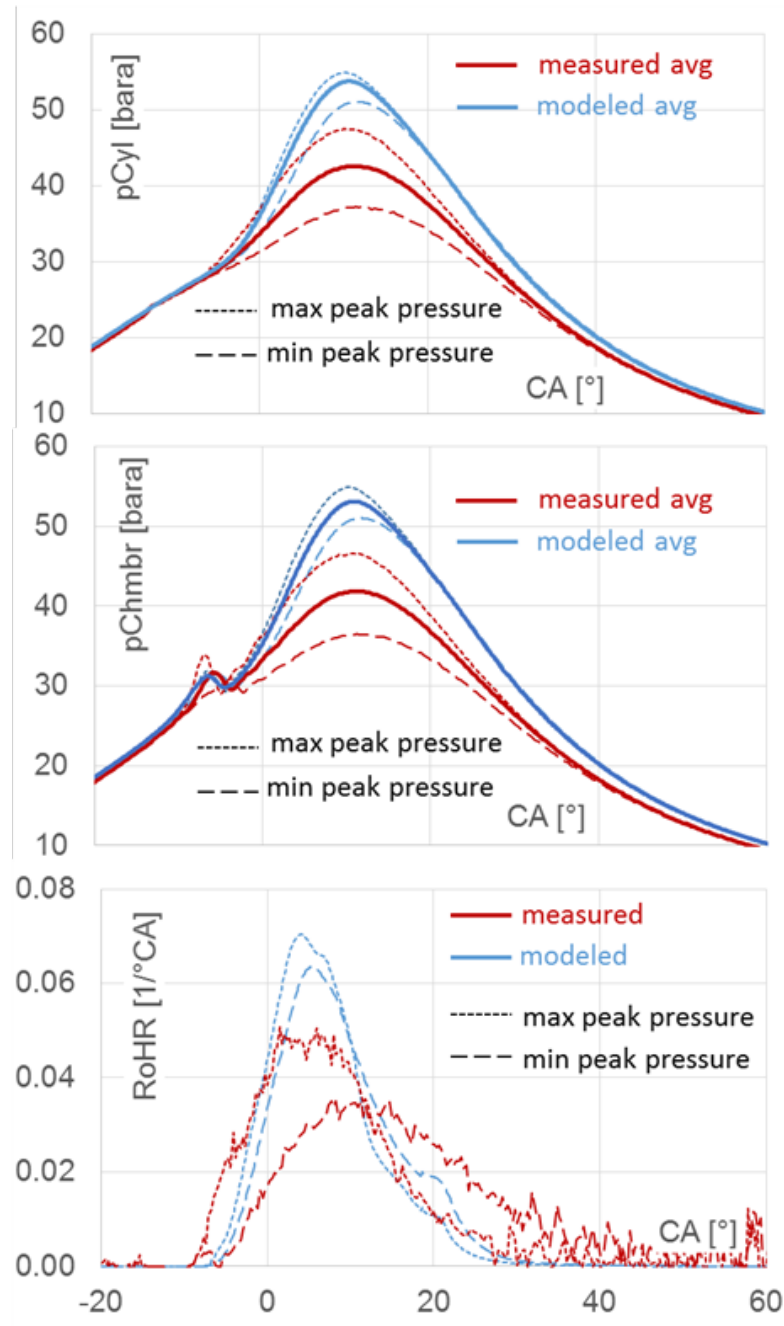


**Figure 6.6:** Comparison of measured and modeled pressure in the cylinder (pCyl - top) and in the pre-chamber (pChmbr - middle) and rate of heat release (RoHR - bottom) for the case of 1800 rpm and air excess of 1.9. Blue color corresponds to CFD calculation. Red color corresponds to measured data.

## 6.5 CFD Model Results

The combustion model assumes the composition of combustion products as equilibrium mixture at given state condition and mass balance. That is why the CFD calculations are not yet able to help with solving the main challenge, we are facing i.e. excessive content of unburned methane in exhaust. Nevertheless, there are certain particular questions which can be well answered by CFD results. The relationship between experimental results and CFD outputs is illustrated in Fig. 6.7 for the operation point with the highest investigated air excess ( $\lambda = 1.9$ ).

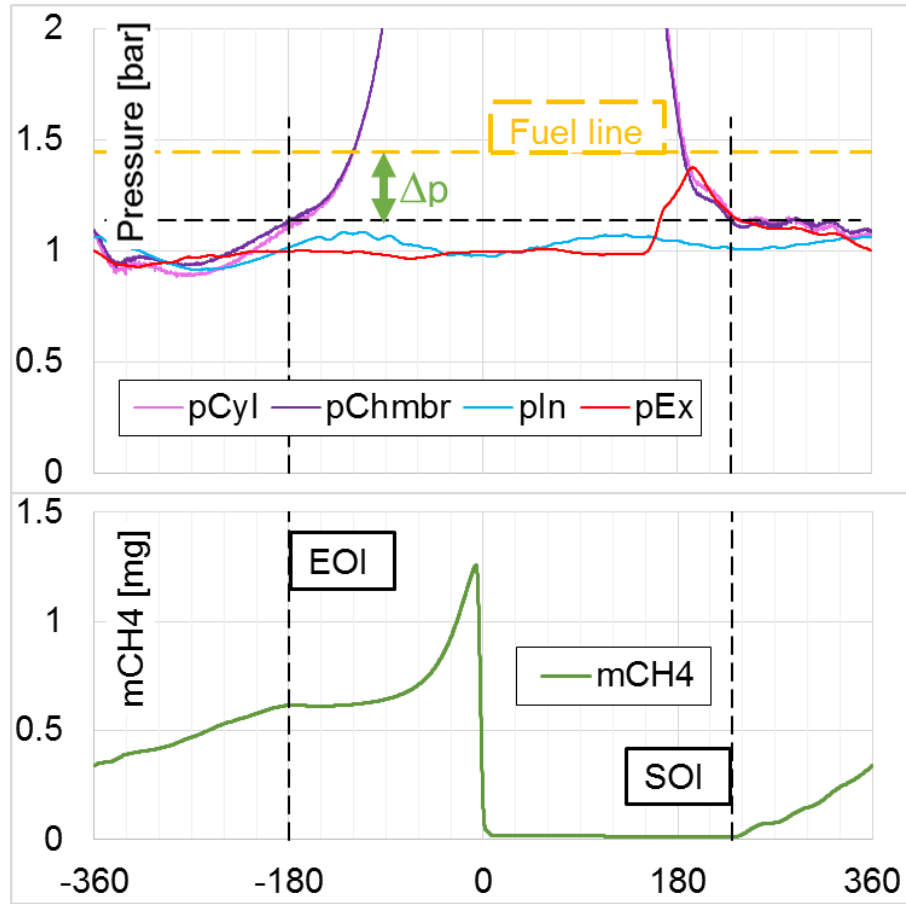


**Figure 6.7:** Measured instantaneous pressures in cylinder (pCyl), pre-chamber (pChmbr), intake port (pIn) and exhaust port (pEx) (top) and modeled mass of methane (mCH4) in the pre-chamber for the case of air excess 1.9 (bottom).

In this figure the scopes of in-cylinder pressure (pCyl), pre-chamber pressure (pChmbr), intake manifold pressure (pIn) and exhaust manifold pressure (pEx) are

transferred from high-speed data acquisition record. The pressure in the fuel line upstream of the check valve is also plotted, as it was measured by low-speed data acquisition system. The pressure difference ( $\Delta p$ ) demanded for opening the check valve is introduced, as it was measured by a separate test on the check valve. The start of injection (SOI) and the end of injection (EOI) points are marked. They were determined by relationship of pressures in the fuel line and in the pre-chamber. The scope of absolute instantaneous mass of methane inside the pre-chamber ( $m_{CH_4}$ ) was transferred from CFD results. Methane content in the pre-chamber increases during the inflow from fuel line and during refilling from cylinder within the compression stroke. During the combustion process the methane content disappears.

The effectiveness of pre-chamber scavenging can be determined neither by measurement nor using 0D or 1D simulation approach. CFD is an appropriate tool for performing this task. For the three tested operational points ( $\lambda = 1.05, 1.48$  and  $1.9$ ), it was stated that, when the fuel delivery is finished by the closing the check valve, the concentration of residual gas in the pre-chamber lies between 24 and 30%. At the time of spark discharge, after the pre-chamber charge is diluted by inflow of fresh mixture from the cylinder, the content of residual gas falls between 4.5 and 5.5 % i.e. to the value typical for SI engine with undivided compression volume. Graphic description of the pre-chamber scavenging is shown in Fig. 6.8 for air excess value  $\lambda = 1.48$  by plot of mass fraction of combustion products.

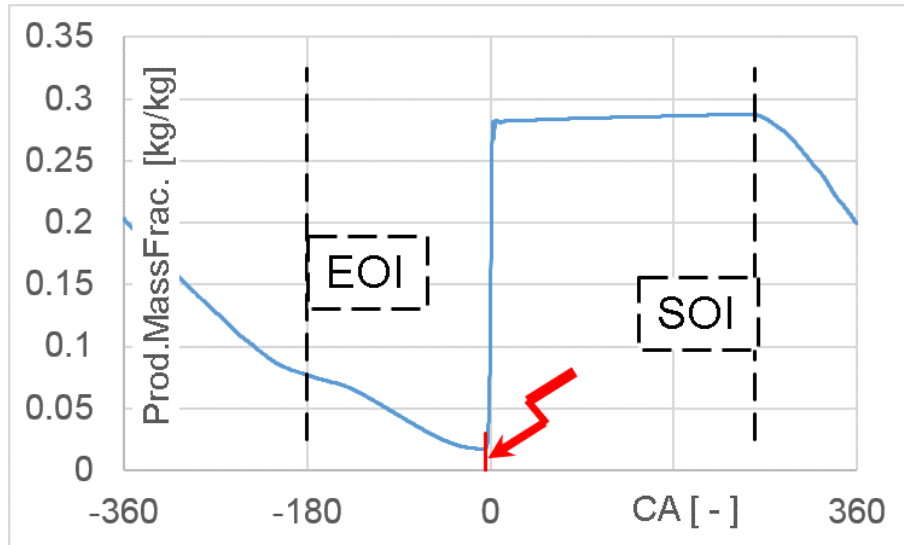


**Figure 6.8:** Modeled mass fraction of combustion products for the case of the air excess ratio 1.48.

The assessment of average mixture composition in pre-chamber while diluted by delivery of (lean) mixture from cylinder during the compression stroke is by CFD

easily possible. From the scopes of instantaneous spatial average of molar fraction of oxygen and methane the course of instantaneous spatial average of air excess can be obtained. The air excess value before the spark discharge lies between 0.7 (for global air excess 1.05) and 1 (for global air excess 1.9), i.e. inside the flammability limits. It needs to be pointed out that constant fueling rate to the pre-chamber (2 mg/cycle) was applied for all three operational points.

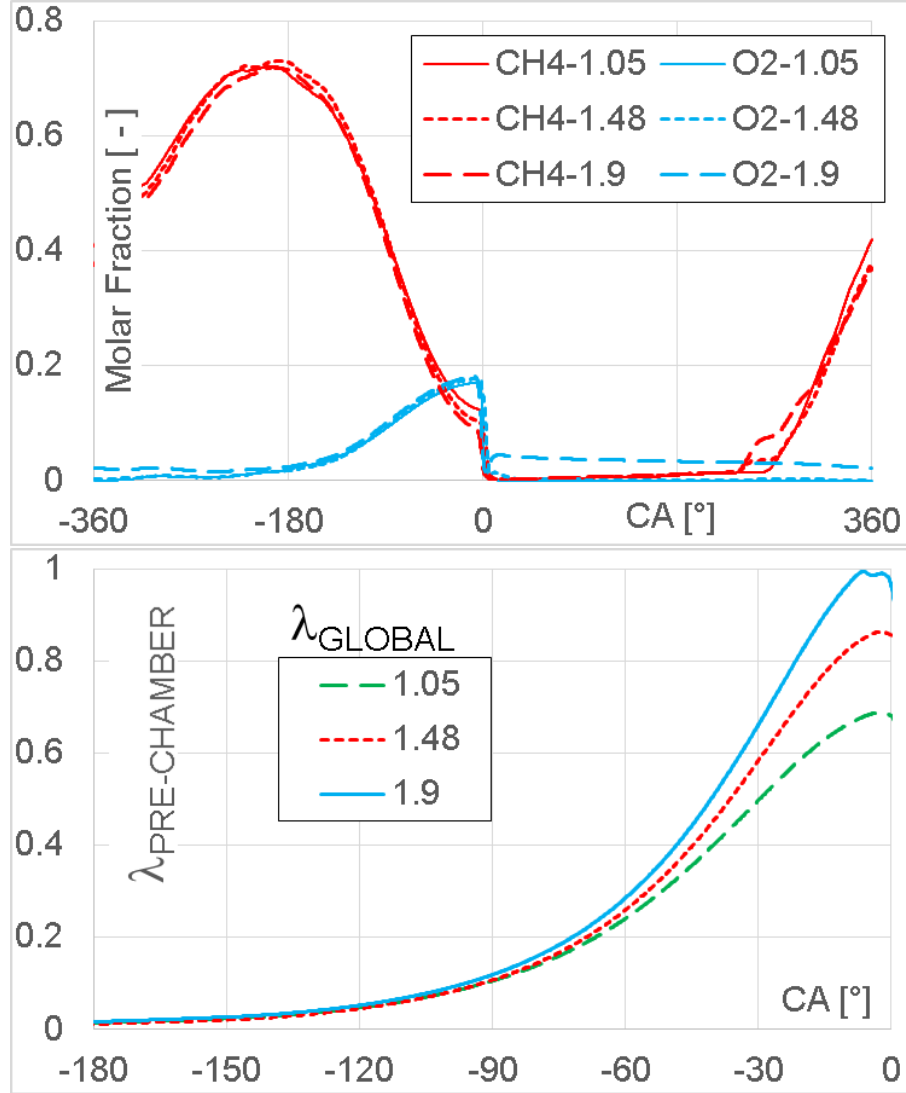


**Figure 6.9:** Pre-chamber mixture composition.

In Fig.6.9 the crank angle indexed methane and oxygen molar fractions (top –along whole cycle) and air excess ratio in the pre-chamber (bottom – within

the compression stroke) are plotted. Spatial average numbers within the whole pre-chamber volume are introduced. In the following figures, the mass fraction of methane contours will be presented in various parts of working cycle in selected cross sectional views of the pre-chamber and cylinder volume.

### Mixture distribution just before spark event

The ignitability of the pre-chamber charge is defined by local mixture composition inside and in the vicinity of the spark gap. The operational point with global air excess close to 1 can be crucial from this point of view. With spatial averaged lack of oxygen in the pre-chamber (Fig. 6.9), the possible local enrichment in the vicinity of spark gap would cause difficulty by initiation of combustion. The CFD shows certain level of mixture stratification, with the richest mixture in the top part of the pre-chamber volume. Nevertheless, even during the engine operation, with global air excess close to 1 (the worst case from this point of view), the enrichment of mixture in the spark gap does not exceed the rich limit of flammability.

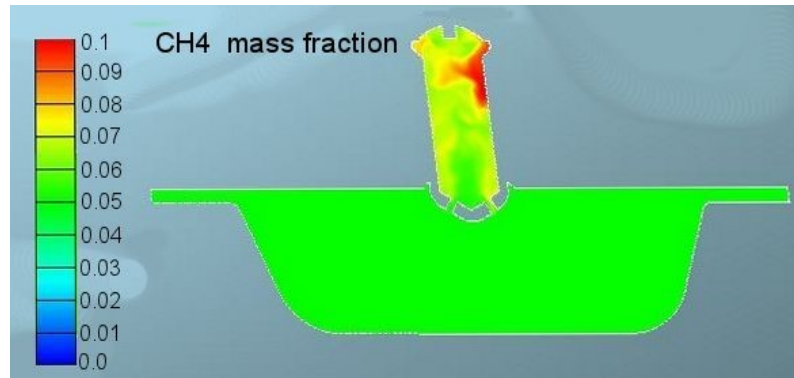


**Figure 6.10:** Methane mass fraction at 3° bTDC. for  $\lambda = 1.05$ .

The contour in Fig. 6.10 outlined the distribution of methane mass fraction at the moment just before start of combustion.

### Mixture distribution at EVC

As already mentioned, the fuel delivery into the pre-chamber is controlled by pressure difference between fuel line upstream of the check valve and the pre-chamber itself. It can be easily derived from the Fig. 6.7 that SOI occurs within the exhaust stroke. Therefore, the fuel inflow into the pre-chamber starts during the late phase of exhaust stroke. In this way, there is a potential for a fuel leakage into the exhaust port when exhaust valve is opened.

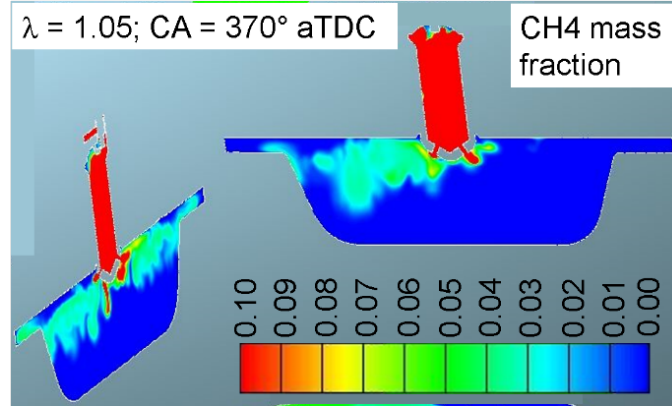


**Figure 6.11:** Assessment of methane leakage to exhaust port.

The CFD boundary conditions were analyzed and methane flow to the exhaust port less than 1% of methane delivery to the pre-chamber was identified for all investigated cases. Fig. 6.11 shows the distribution of methane mass fraction at the crank angle position at EVC. Quite massive inflow of fresh mixture from intake ports takes place. It can also be assessed visually that blow-by through the pre-chamber connecting holes does not influence the contour of CH<sub>4</sub> appearance significantly. It can be stated, that direct leakage of fuel into the exhaust port during the pre-chamber scavenging is negligible. Till now, the mentioned CFD outputs show good agreement with experimental findings. In this way the plausibility of experimental data is enhanced and reciprocally the model's predictive ability is confirmed. Pure model outputs will be used in the next section for further consideration.

## Flame propagation at the start of combustion

In the top picture in Fig. 6.12 (taken 1° after the compression TDC) the flame propagates inside the pre-chamber. Blue colored region represents combustion products. Rich mixture flows through connecting holes, forced by the pressure peak in the pre-chamber. In the presented case 0.7 mg of methane escapes to the cylinder.

From the point of view of ignition energy, the escaped fuel can be considered as a loss, on the other hand the escaped fuel will be burned in the cylinder during the subsequent combustion process. In the mid picture (2° aTDC) the first appearance of flame in the cylinder is visible. At 3° aTDC the flame jets reach the piston surface. The velocity of the flame jet propagation is approximately 200 m/s. The entire process of flame propagation with rugged surface of the flame front significantly differs from spherical surface with continuously growing radius as observed in SI engines with conventional spark plug.

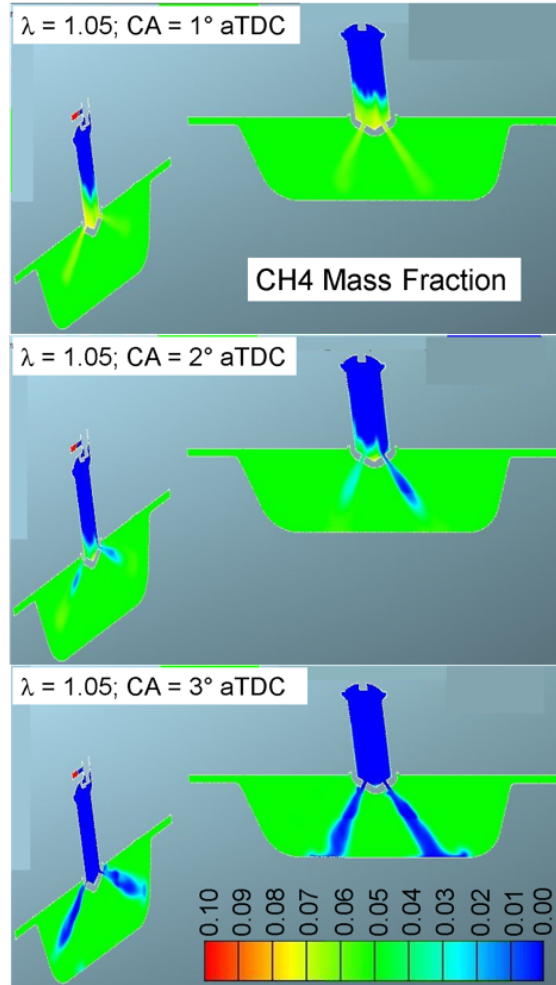


**Figure 6.12:** Flame penetration into the cylinder volume.

## 6.6 Summary and Conclusions

Experimental observations show:

- The engine equipped with the scavenged pre-chamber is capable of running a wide range of  $\lambda$  with constant combustion phasing adjusted to optimum engine efficiency ( $CA_{50} = 10$  deg aTDC). This was achieved by a constant fueling rate to the pre-chamber within the range of tested air excess ratios. The demand for spark advance control is moderate.
- The method of fueling was proven successful. Fuel was delivered via a simple fuel line and check valve, and fuel injection rate was controlled only by the



pressure in the fuel line.

- While operating at the lean end of the investigated range, the  $NO_x$  emissions in the raw exhaust gas are very low, which bodes well for real world operation at low load without exhaust gas aftertreatment.
- The most significant experimental challenge is managing the content of unburned hydrocarbons in the engine-out exhaust gas. The air excess ratio range needs to be trimmed to maintain a reasonable content of unburned methane in the raw exhaust gas.

The results of the CFD model show:

- The effectiveness of pre-chamber scavenging is sufficient. The residual gas content inside the pre-chamber before the start of combustion is on the order of one percent.
- At the time of spark discharge, the mixture composition in the vicinity of spark gap is within the limits of flammability. This statement is valid for all investigated operational points.
- Even if the flow of fuel into the pre-chamber starts during the later phase of the exhaust process, the amount of leaked unburned fuel to the exhaust port during pre-chamber scavenging was identified by CFD as negligible.
- The flame jet propagation in the cylinder occurs very fast. Further flame development differs significantly from conventional hemispherical surfaces typical of SI engines. Our next study will focus on modifying the geometry of both the pre-chamber and the main chamber to cope with this phenomenon.

The detailed CFD model together with calibrated 0-D/1-D model are supposed to introduce a lot of new information which might be difficult to be obtained experimentally. This enables understanding gas exchange process (especially between cylinder and pre-chamber) and turbulent flame development (especially in pre-chamber and early in-cylinder phase). All that is expected to improve overall knowledge of the pre-chamber concept applied to automotive ICE, hence leading to optimizations planned for the near future.

The combustion model used in this study does not capture the local chemistry. Only a combustion model based on chemical kinetics could capture that. Such a model will be employed in the future.

## 6 Development of a Pre-chamber Ignition System for Light Duty Truck Engine

## Chapter 7

# Scavenged Pre-Chamber Volume Effect on Gas Engine Performance and Emissions

Experimental work presented in this study has been performed on a practical, modified multi-cylinder engine. Therefore, the optical access for combustion diagnostics could not be applied. As it is difficult to get detailed (local) thermodynamic properties from the experiments, theoretical approach is needed – in this particular case, 3-D CFD combined with LES was adopted.

Based on the above mentioned the main goals of this chapter are the following:

- To test and compare two design variants of pre-chamber (small and big).
- To build a 3-D CFD model of the target engine (c.f. Tab. 4.1) with the focus on combustion process and cycle-to-cycle variation (CCV) effects.
- To analyze detailed CFD data to understand combustion process of the target engine, which is based on turbulent flame jet concept.

### 7.1 Experimental Setup and Procedures

Experiments were performed on a 4-cylinder 4-stroke natural gas engine which was converted to a single cylinder one by closing the intake and exhaust ports of three cylinders. The setup is identical to the one described in previous sections.

Otherwise the engine configuration remains unchanged from the original four-cylinder one. The original turbocharger was matched to the four-cylinder engine with variable turbine geometry (VTG) and intercooler. This modification allows quick testing of different pre-chamber prototypes. VTG rack was kept constant at

maximum stator nozzle area (minimum boost pressure). In mentioned configuration the boost pressure was limited to several units of kPa. Therefore, single-cylinder engine operated within the range of the naturally aspirated engine. The main engine parameters can be found in Tab. 4.1.

A central mixer is used for an air-fuel mixture formation in intake manifold upstream of the compressor. The engine was fueled with natural gas with methane contents 98.4% (by volume). Mixture inflow is controlled by a conventional throttle valve located downstream from the intercooler and actuated by a stepper motor. The pre-chamber is filled with additional gaseous fuel through a miniature check valve. Fuel flow to the pre-chamber is measured and controlled by an OMEGA FMA2610A mass flow controller. The pressure in the fuel line upstream the check valve is given by the equilibrium state given by the imposed flow, the check valve flow parameters and the pressure in the pre-chamber. The filling and scavenging of the pre-chamber can be partially controlled, based on the engine operating conditions, but with less complexity, required for electronic injection system.

A capacitive ignition system (UNIMA TC+) enables independent adjustment of the spark timing. All actuators and selected set of sensors are connected to the engine electronic control unit (ECU) developed in the authors' department using Field-Programmable-Gate-Array as a HW platform. The ECU is fully accessible and allows an open loop control as well. The detailed test setup description can be found in chapter 4.

In order to determine the influence of the volume of the pre-chamber, an experimental comparison of two pre-chambers with the same geometry of the connection orifices with different volumes was performed. A brief description of a small pre-chamber design is given in Fig. 7.1. The spark plug insulator assembly is asymmetrically located. This allows placement of the check valve as close as possible to the pre-chamber as well as miniature piezoelectric pressure sensor installation (not visible). The fuel enters the pre-chamber via a single channel (approximately 40 mm long with diameter of 1.2 mm) The big pre-chamber uses a redesigned fuel supply system which is shown in Fig. 7.2. The check valve is located outside the pre-chamber body, then the fuel flows through the capillary (with diameter of 1.5 mm) with approximate length of 130 mm and enters the pre-chamber by two opposite channels (visible in the middle part of Fig. 7.1). This configuration allows placing of the standard (M8) spark plug in the pre-chamber axis. Main pre-chambers parameters can be found in Tab. 7.1.

## PRE-CHAMBER DESIGN

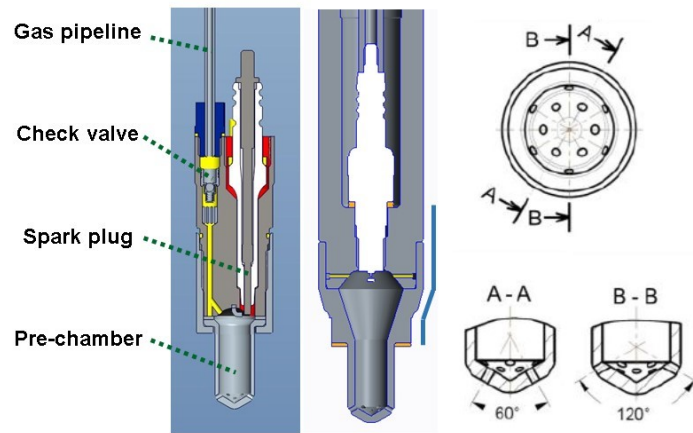


**Figure 7.1:** Pre-chamber design: small pre-chamber (left), big pre-chamber (middle), geometry of orifices (right) for the connecting channel configuration of 12x  $d=1.2$  mm.

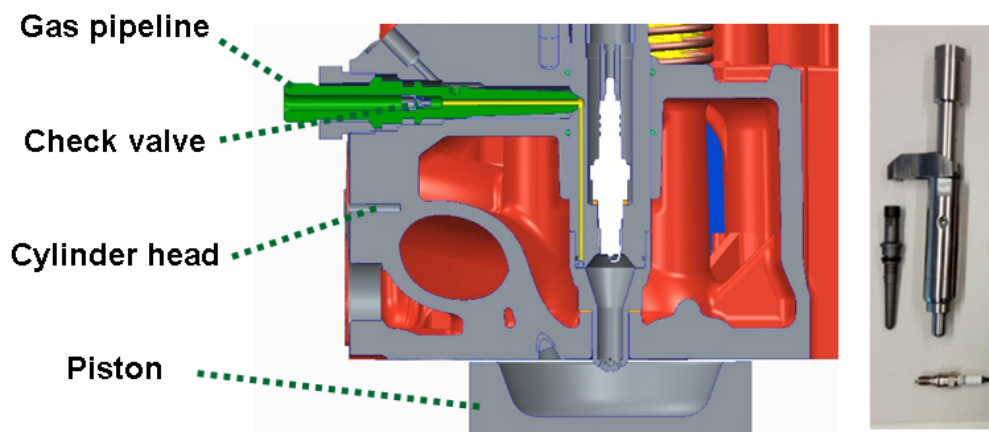


**Figure 7.2:** Installation of big pre-chamber in research engine.

Pre-chamber (PC)	Small	Big
Volume - VPC	1.92 cm <sup>3</sup>	4.1 cm <sup>3</sup>
Fraction of Compression Volume	2.2 %	4.6 %
CR with pre-chamber	12.2:1	12.0:1
Heat transfer (HT) area	8.5 cm <sup>2</sup>	15.4 cm <sup>2</sup>
Ratio of PC to overall HT area	4.3 %	7.4 %
Number of holes	12	12
Hole diameters	1.2	1.2

**Table 7.1:** Main pre-chambers parameters.

## 7.2 Mathematical Model

### 0-D/1-D Model

A GT-Power model of the investigated system was built and used for determination of physical quantities which are not available from direct measurements and for a crosscheck of the experimental results. The simulation of the “pre-chamber engine” requires modeling of two separated combustion chambers (one for the cylinder and the second one for the pre-chamber). For both volumes, the modeling of combustion, heat transfer and emission formation is needed and therefore the cylinder objects were used. The influence of throttling in communication ports (orifices) is respected by several pipes with appropriate dimensions (1-D approach). The pressure losses are represented by flow coefficients calibrated by data of pressure traces that are directly measured in the cylinder and pre-chamber from motored engine. The amount of additional gas flowing into the pre-chamber is controlled by the pressure upstream of the check valve. The mechanical check valve prevents backflow from the pre-chamber into the fuel system. This part was modeled by the valve object (connection) with two dimensional array of pressure difference and discharge coefficients (determined experimentally). The rest of the model was calibrated by a standard three pressure analysis (TPA) procedure [15]. The difference against experimental data was minimized by the calibration parameters, determined by genetic algorithm optimizer – the procedure is explained in [79].

### 3-D CFD Model

For the simulation of the gas flow, spray mixture formation and flame propagation processes in the SI-engine analyzed in the present work, the 3D-CFD code AVL FIRE is adopted [4]. The 3-D CFD SW solves the general conservation equations of mass, momentum and enthalpy plus additional transport equations for turbulence related quantities and for conservation of chemical species. The adopted solution method is based on a fully conservative finite volume approach. All dependent variables, such as momentum, pressure, density, turbulence kinetic energy, dissipation rate, and the scalar quantities are evaluated at the cell centers of the general, unstructured computational grids. A second-order midpoint rule is used for integral approximation and a second order linear approximation for any value at the cell-face. Convection is solved by adopting higher order differencing schemes. In order to offer full flexibility in terms of the structure and topology of the employed computational meshes, the solver allows for each computational cell to consist of an arbitrary number of cell faces. Connectivity and interpolation practices for gradients and cell-face values are set up to accommodate such ‘polyhedral’ calculation volumes. The rate of change (accumulation term) is discretized by using an Euler implicit scheme. The

overall solution procedure is iterative and is based on the Semi-Implicit Method for Pressure-Linked Equations algorithm (SIMPLE) or Pressure-Implicit with Splitting of Operators (PISO, c.f. [37]), applicable to turbulent flows at all speeds. For solving the large sets of linear equation systems evolving from the discretization of the governing equations, an efficient preconditioned conjugate gradient method is employed. More details can be found in documentation of AVL [4].

Dealing with numerical setup, the following settings were applied. PISO algorithm was selected as time integration method while 2nd order schemes were used for convective term approximations. Time step was set to 0.1 °CA.

Regarding turbulence modelling, Large Eddy Simulation (LES) was adopted. It is based on the filtered instantaneous Navier-Stokes equations. Filtering operation actually represents scale separation in space, where large scales are directly resolved and the influence of small scales is taken into account by the sub-grid scale (SGS) model. Coherent structure version of LES approach [51], [46], [45] was selected.

Concerning combustion models, the LES version of ECFM-3Z was activated due to positive experience with this model from the past – c.f. [85],[77]. Premixed turbulent SI-engine combustion is modeled in the present case by using the LES variant of the Extended Coherent Flame Model (CFM) [63] which is based on solving a transport equation for the flame surface density (FSD), suitably linked with the gas-phase thermochemistry. It should be stressed that this model is turbulence driven, hence it cannot capture local chemical effects (e.g., flame quenching due to low temperature or turbulence-related effects) – this leads to a statement that all fuel is (usually) burnt when using this model (provided there is enough oxygen). Dealing with applied chemistry, the turbulence driven combustion models are usually linked with simplified chemistry approaches based on equilibrium. This was also the case for the presented CFD calculations. The only considered pollutant was NO<sub>x</sub>, however its formation was based on standard approach [97], which is to solve certain equations of chemical kinetics.

The CFD model is based on existing engine design (c.f. Tab. 4.1). 3-D CAD data of engine cylinder head, piston and liner were provided by engine manufacturer. All the necessary geometry information was available, hence the meshing procedure could be started. The meshing itself was made by means of hybrid meshing tool of AVL FIRE. Typical mesh cell size was set to 0.6 mm – this is based on experience from the previous work [85],[77] with LES approach to SI ICE modeling. The pre-chamber cell size was set to 0.3 mm while channels connecting the pre-chamber with engine cylinders were modeled even finer: typical cell size was 0.15 mm. The main reason behind the mesh refinement in the pre-chamber domain is the requirement to capture the early flame development in pre-chamber. The important parameters of applied mesh are summarized in Tab. 7.2.

Concerning boundary and initial conditions, they were transferred from the calibrated 0-D/1-D models of the engine created in SW tool [3]. As multiple cycles were



Typical Mesh Size	< 0.6 mm
Min. Amount of Mesh Cells	7.5 x 10 <sup>6</sup>
Max. Amount of Mesh Cells	13 x 10 <sup>6</sup>
Max. Angle Interval of Single Mesh Set	10° CA

**Table 7.2:** Table 3. Main mesh parameters

calculated to estimated CCV effects, all ports were present in the computational domain (hence no port removal when corresponding valves were closed). Hence, inlet BCs are mapped onto surface representing inlet of intake port – inlet boundary pressure/temperature was imposed as function of crank angle. The same applies to outlet BC and outlet of exhaust port. The last BC surface corresponds to dedicated fuel supply system of pre-chamber where fuel mass-flow rate to the pre-chamber was imposed, which represents mixture enrichment in the pre-chamber – the surface is located in small pipe near spark plug in upper part of the pre-chamber itself. Surface temperatures were based on simplified predictive FEM model from simulations using calibrated 0-D/1-D models. Initial values of all required thermodynamic parameters (including composition) were directly transferred from the 0-D/1-D model(s).

The details regarding mesh generation and LES combustion model calibration while using available experimental data are described in [3], [87]. This also includes comparison between measurements and 3-D CFD model predictions.

## 7.3 Experimental Results

### Combustion only in the Pre-chamber

Partly motored mode when fuel was delivered only into the pre-chamber and spark was on is used for testing of the pre-chamber functionality. This mode was investigated experimentally to evaluate the combustion efficiency in the pre-chamber only, to quantify ignition energy from the pre-chamber combustion. Heat release rates of different pre-chamber configurations can be quantified and compared in this way.

The internal volume of the pre-chamber defines the maximum amount of gas that the pre-chamber can accumulate during the filling (scavenging) phase. The actual amount of gaseous fuel is affected by the efficiency of the scavenging of the residual gases from the previous cycle. This mixture is diluted by the incoming mixture from the main combustion chamber during the compression stroke. The dilution ratio is equal (given by) to dynamic compression ratio ( $\epsilon_{Dym}$ ) by the equations Eq. (7.1).

$$\epsilon = \frac{V_{IVC}}{V_{TDC}}, \quad (7.1)$$

where  $V_{IVC}$  is a cylinder volume at intake valve close and  $V_{TDC}$  is the minimum cylinder volume at top dead center. This value represents the compression ratio of the trapped volume. Evaluated dynamic compression ratio for testing engine is 9.5:1. This ratio exactly corresponds to the stoichiometric volume ratio of methane and air. A stoichiometric mixture will be formed in the pre-chamber provided that the pre-chamber is completely filled with gaseous fuel and that only air is in the cylinder. This ideal case can occur in this operating mode (partly motored mode). Conditions inside the pre-chamber for normal engine operation will be described in the next paragraph.

Tab. 7.3 shows the theoretical and real pre-chambers heat release for various fuel flows, evaluated from the fuel quantity and combustion efficiency (evaluated from the methane emission index). The comparison shows that bigger pre-chamber provides approximately two times more heat release. Highest pre-chamber combustion efficiency is achieved when the amount of gas which is delivered to the pre-chamber corresponds to its volume (i.e. volumetric ratio ( $V_{fuel} / V_{PC}$ ) = 1). A further increase in the amount of additional gas into the pre-chamber reduces the pre-chamber combustion efficiency, but increase the total heat release which provides more ignition energy in the main chamber. Excess fuel that leaks from the pre-chamber is not lost because it would be probably burned in the main combustion chamber in normal operation. However, a rich mixture may occur in the vicinity of the orifices. All these trends are confirmed by CFD simulations – comparison of released chemical energy in pre-chamber is shown in Fig. 7.3 in Annex and it relates well with numbers presented in Tab. 7.3. The real pre-chamber heat release is also affected by the position of the spark plug. The fresh charge is forced out from the pre-chamber during combustion. The estimation of this loss is about 45% and it was performed by the multi-zone combustion model described in [34]. It needs to be added that the energy release by the pre-chamber combustion is therefore 700-2000 times higher than the energy released by the spark discharge (see Chapter 6).

## Full Combustion Mode

Full combustion mode represents standard engine operation when homogeneous air-fuel mixture is formed in the intake manifold upstream the compressor. The following charts display the comparison of the basic performance of the naturally aspirated engine with different pre-chambers volumes (Small =  $1.9\text{cm}^3$  and Big =  $4.1\text{cm}^3$ ). The operation conditions were: constant engine speed of 1800 rpm, fully open throttle valve and constant pre-chamber fuelling rate of 0.15 standard  $\text{m}^3/\text{h}$  in case of small pre-chamber and 0.2 standard  $\text{m}^3/\text{h}$  in case of big pre-chamber. The

Pre-chamber (PC)	Small	Small	Big	Big
Fuel avg. vol. flow rate – $Q_{\text{fuel}}$ (m <sup>3</sup> /h)	0.1	0.2	0.2	0.4
Vol. fuel quantity – $V_{\text{fuel}}$ (cm <sup>3</sup> /cycle)	1.9	3.7	3.7	7.6
Volumetric ratio: $V_{\text{fuel}} / V_{\text{PC}}$	0.96	1.93	0.9	1.85
Theoretical fuel energy – Total (J)	66	133	133	273
PC combustion efficiency (-)	0.3	0.19	0.36	0.26
Heat release (J)	19.9	25.2	47	69.5

**Table 7.3:** Pre-chamber heat release

ignition timing was adjusted to maintain the constant combustion phasing of 50 percent mass fraction burned ( $CA_{50} = 10^\circ$  aTDC). This setting is close to the MBT of this set-up for all operational points according to Chapter 4. Simultaneously with ignition timing sweeps, pre-chamber fueling rate was tested and also presented in Chapter 4. Desired air excess ratio was set by the control of the main gas metering valve.

Engine performance and efficiency is shown in Fig. 7.3, where indicated mean effective pressure (IMEP) and indicated efficiency curves are plotted as a function of the air excess ratio ( $\lambda$ ). The comparison shows that the pre-chamber with bigger volume has lower IMEP and lower indicated efficiency compared to the small one. Possible explanation can be: lower compression ratio, less combustion efficiency and higher wall heat losses associated to larger heat transfer surface area of big pre-chamber.

Engine out emissions are introduced in Fig. 7.4 as indicated specific emission of NO<sub>x</sub> (IS NO<sub>x</sub>) and methane emission index (EI CH<sub>4</sub>). In case of the big pre-chamber, the lower formation of NO<sub>x</sub> emissions associated with worse combustion, represented by the higher amount of unburned hydrocarbons in the range of  $\lambda$  from 1 to 1.75 can be observed.

The amount of gas delivered into the big pre-chamber in the experiment ( $Q = 0.2$  standard  $m^3/h$ ) corresponds approximately to 90% of the pre-chamber rated volume, which means that the pre-chamber is not fully scavenged and its potential in terms of fuel filling is not fully utilized. Next, tests of increasing the fuel delivery into the pre-chamber led to a deterioration of the pre-chamber performance due to rich mixture inside the pre-chamber. The explanation for this behavior was provided by the simulation results (Fig. 7.10) and will be discussed in more detail in the section ‘3-D CFD Results’ (located below).

Based on the above mentioned, the un-scavenged mode (passive) big pre-chamber was tested (plotted by the green lines in the figures). The lean flammability limit

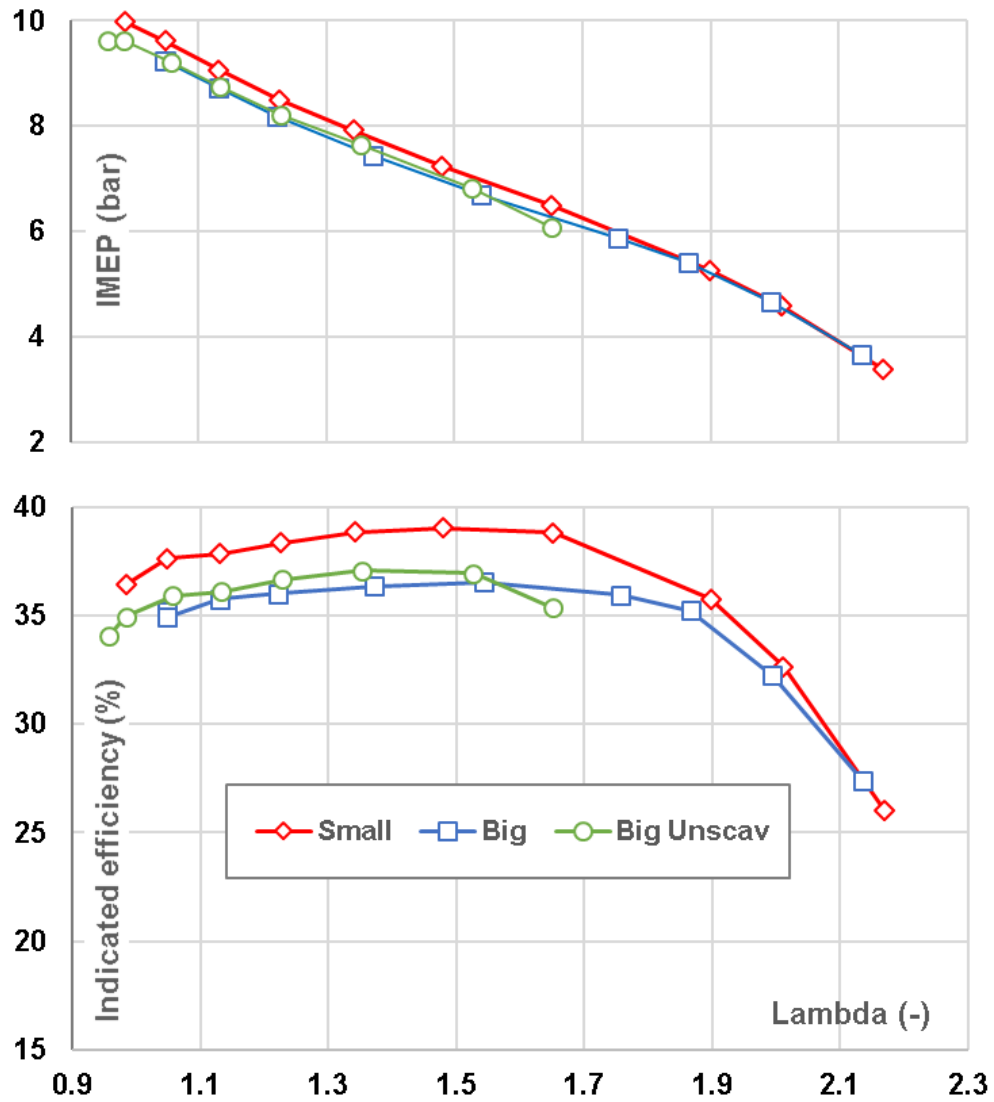


**Figure 7.3:** Indicated mean effective pressure (IMEP) and indicated efficiency as a function of the air excess ratio at engine speed of 1800 rpm. Comparison of the small and the big scavenged pre-chambers and the big un-scavenged pre-chamber.

of un-scavenged pre-chamber was determined at  $\lambda$  1.53. Further increasing of air excess caused unstable combustion and misfiring which is demonstrated by the coefficient of variation of indicated mean effective pressure (COVimep) in Fig. 7.5. It is clear that a passive pre-chamber cannot be used to ignite an extremely lean mixture. However, there was an improvement in the overall function near the stoichiometric mixture which is demonstrated by decreasing of unburned hydrocarbons

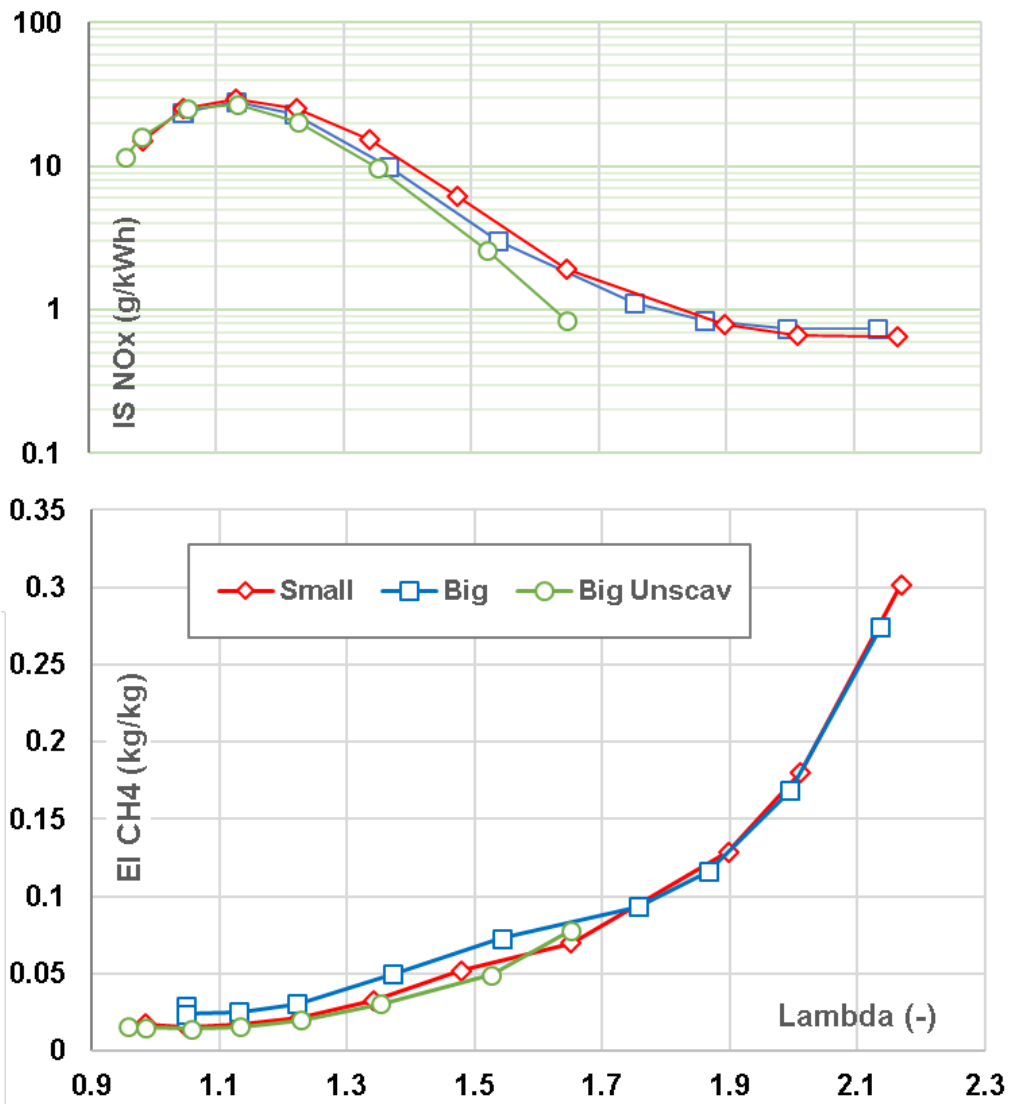


**Figure 7.4:** Engine out emission as a function of the air excess ratio at constant engine speed of 1800 rpm. Comparison of small and big scavenged pre-chambers and big un-scavenged pre-chamber.

and the values are close to (or even better than) the small pre-chamber, without the need for local mixture enrichment. However, a pre-chamber thermal damage might occur (at the bottom part, around the orifices) due to missing scavenging of residual gas and cooling by cold fuel delivery in this regime after a long time of operation. The reduced amount of additional gas will have to be sufficiently compensated at least by external cooling. In the case mentioned in this paper the outer surface of

pre-chamber assembly (marked by the blue line in Fig.7.1) was cooled by engine coolant.

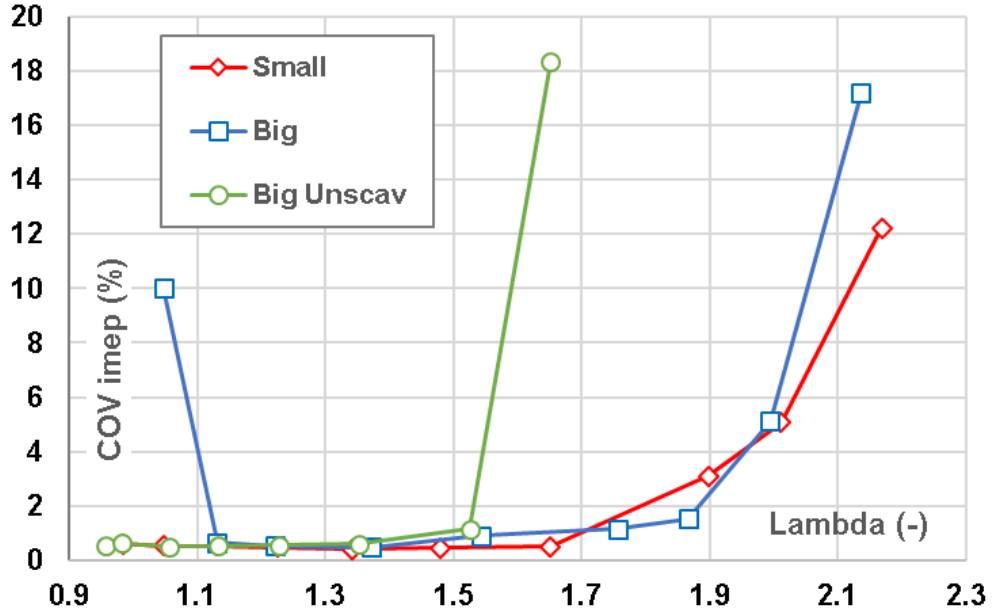


**Figure 7.5:** Coefficient of variation of indicated mean effective pressure (COV imep) as a function of the air excess ratio at constant engine speed of 1800 rpm. Comparison of small and big scavenged pre-chambers and big un-scavenged pre-chamber.

Fig. 7.6 shows the comparison of the rate of heat release for the average cycle (in-cylinder) near the stoichiometric mixture operation. All pre-chamber variants show significantly faster combustion than that with conventional spark ignition (SI). Pre-chamber provides multipoint ignition in the main combustion chamber and increases the ignition energy. There is no significant difference between small and big scavenged pre-chambers' rate of heat release. The un-scavenged pre-chamber shows the highest combustion rate. The reason will be discussed later in the section 'Simulation Results'.

Comparison of the rate of heat release for lean operation at lambda 1.5 is illustrated in Fig. 7.7. The difference between small and big pre-chamber is not significant. The big pre-chamber shows slightly higher combustion rate at the beginning of combustion. The un-scavenged pre-chamber shows the lowest burn rate. The operation of un-scavenged pre-chamber at lambda 1.5 is still acceptable. Combustion instability occurs beyond this point.

Fig. 7.8. shows the comparison of two pre-chamber variants at lambda = 2. The big pre-chamber shows higher rate of heat release then the small one. The increased

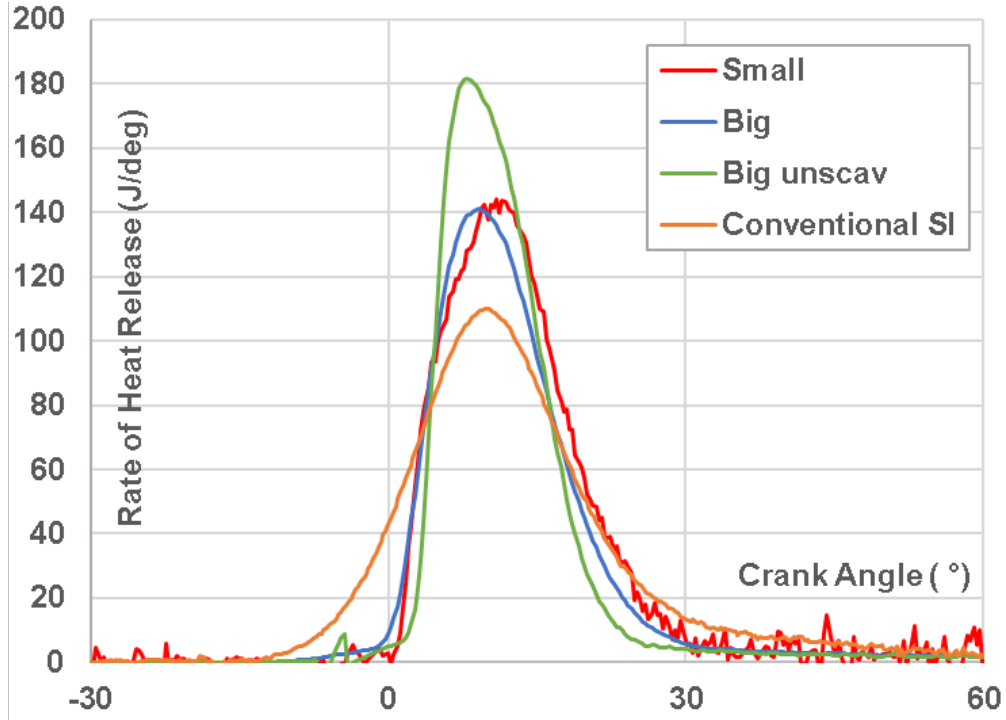


**Figure 7.6:** Comparison of average cycle rate of heat release for the air excess of 1.05 at engine speed of 1800 rpm. Comparison of conventional spark ignition (SI), small and big scavenged pre-chambers and big un-scavenged pre-chamber.

volume of the pre-chamber provides higher ignition energy and accelerates combustion. In this way combustion duration can be shortened and spark advance can be retarded. However, there was no expected reduction in unburned hydrocarbons. The difference in NO<sub>x</sub> emissions is also very subtle.

As already mentioned, the adjustment of ignition timing was set to maintain  $CA_{50} = 10^\circ CA$  aTDC in all cases. Big pre-chamber shows faster combustion which is demonstrated by the values of  $CA_5$ ,  $CA_{90}$  and lower demand for spark advance timing in Fig. 7.9 in lean operation. Near the stoichiometric mixture, the scavenged big pre-chamber shows worse performance compared to small one. The big scavenged pre-chamber cannot be operated at stoichiometric mixture at all due to unstable combustion and misfiring (COV<sub>imep</sub> in Fig. 7.5). With the highest probability, the mixture in the vicinity of the spark gap is extremely rich causing poor ignitability. On the other hand, the un-scavenged big pre-chamber provides best combustion stability and the fastest combustion probably due to better charge homogeneity. It can operate with rich mixture.

The mentioned lambda sweeps were also performed for the big and small pre-

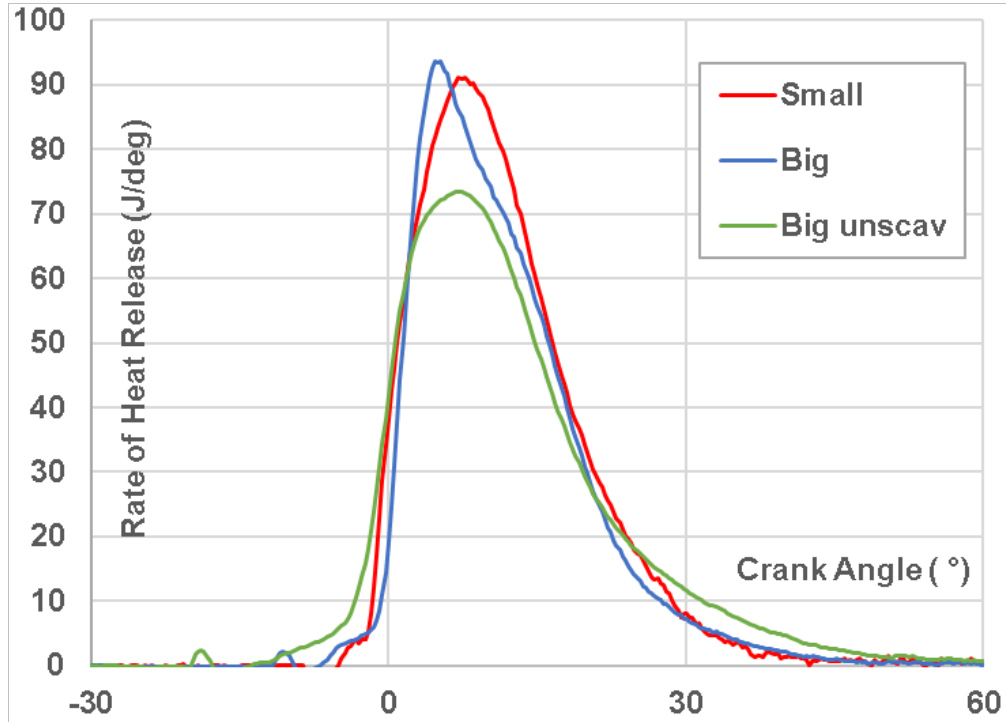


**Figure 7.7:** Comparison of average cycle rate of heat release for the air excess of 1.5 at IMEP = 7 bar and engine speed of 1800 rpm. Comparison of small and big scavenged pre-chamber and big un-scavenged pre-chamber.

chamber at engine speed of 1200 rpm and 2400 rpm. The trends for various engine speeds are very similar, hence the data are not presented here.



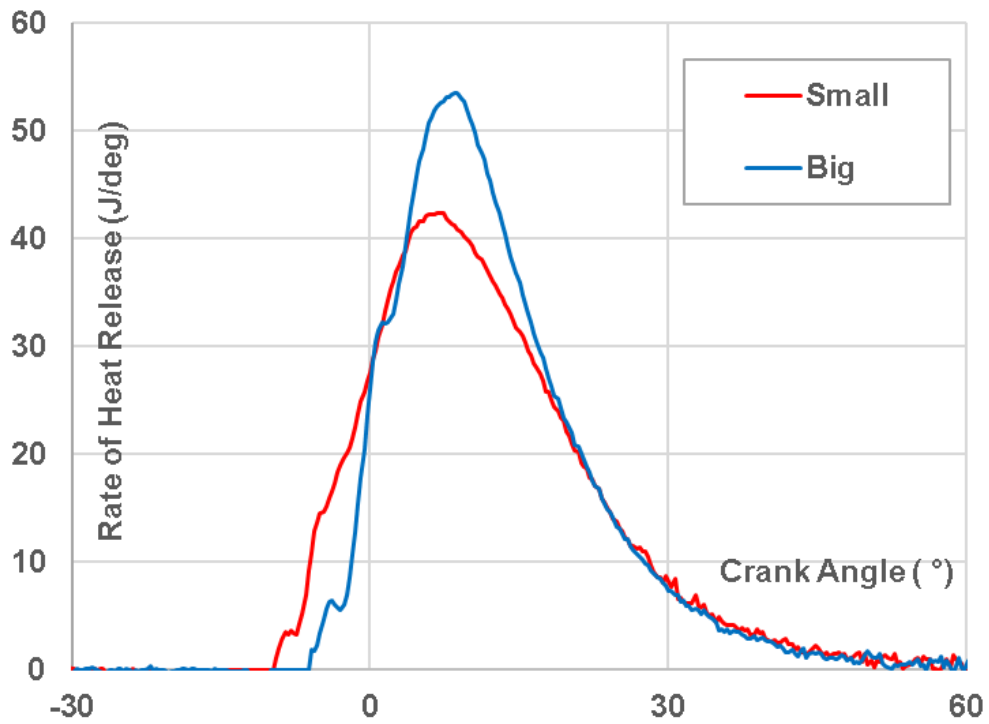


**Figure 7.8:** Comparison of average cycle rate of heat release for the air excess of 2 at IMEP = 4.6 bar and engine speed of 1800 rpm. Comparison of small and big scavenged pre-chambers.

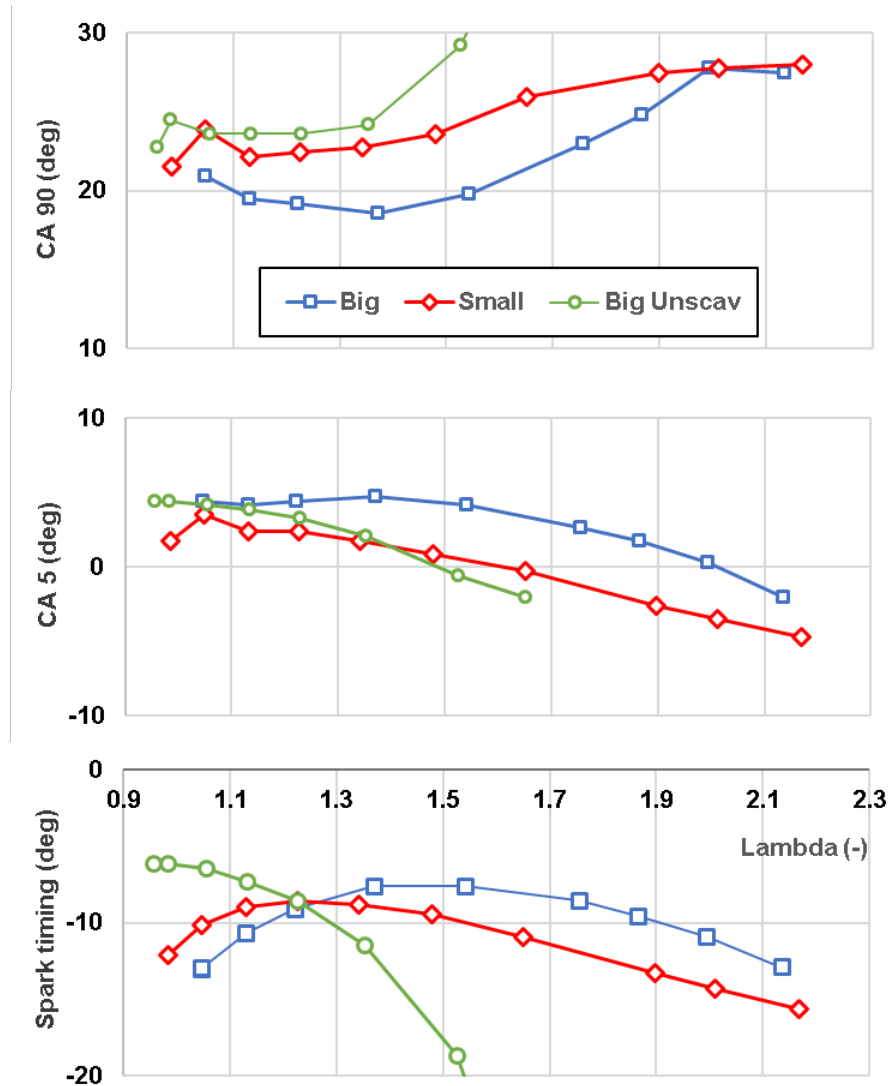


**Figure 7.9:** Spark timing, CA 5 and CA 90 at constant engine speed of 1800 rpm. Comparison of small and big scavenged pre-chambers and big un-scavenged pre-chamber.

## 7.4 Simulation Results

### 0-D/1-D Model

The air excess in the pre-chamber is one of the parameters which cannot be determined experimentally. The GT-power model allows a prediction of the average value of the air excess in the pre-chamber. The simulation uses the 0-D approach that means the gases in the investigated volume are assumed to be ideally homogeneously mixed. Fig. 7.10 shows the air excess in the scavenged pre-chamber before combustion start as a function of the global air excess ratio. It can be observed that ideal stoichiometric mixture in the pre-chamber is achieved at very lean mixture operation. On the other side, the extremely rich mixture in the pre-chamber which is close to the flammability limit occurs at stoichiometric engine operation. This fact leads to deterioration of the combustion stability in the pre-chamber and subsequently in the main combustion chamber as mentioned in comment to the Fig. 7.9.

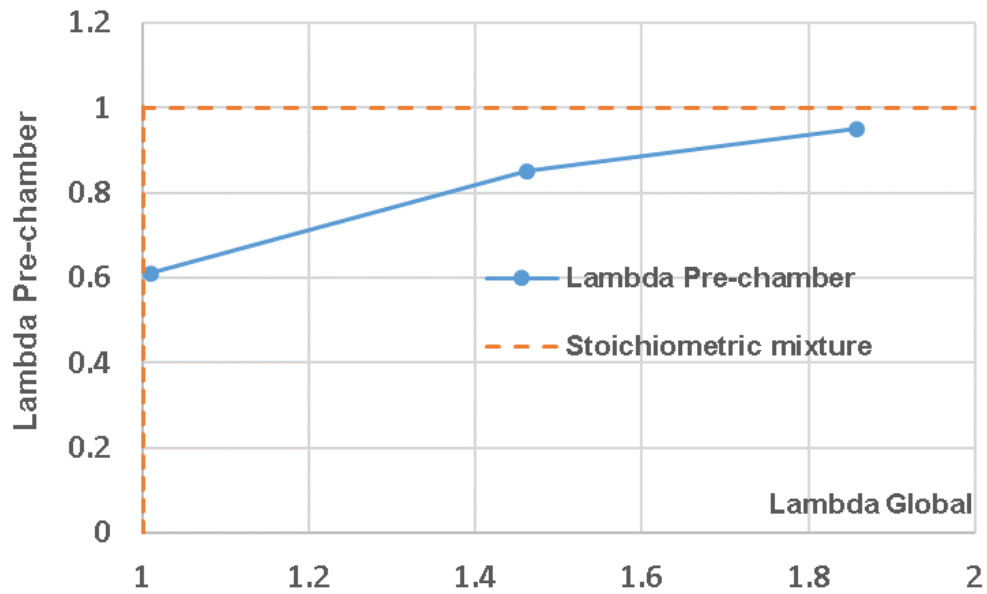


**Figure 7.10:** GT-Power simulation – 1800 rpm, constant pre-chamber fuelling rate of 0.2 standard m<sup>3</sup>/h: air excess in the big scavenged pre-chamber as a function of the global air excess ratio.

### 3-D CFD Results / Computed cases

As mentioned above, the CFD approach was applied to get deeper understanding of all important phenomena taking place in the target engine. This concerns mainly mixing and combustion. Based on previous experience (c.f. [85],[77], the LES approach is supposed to predict the mixing well. Moreover, if flame front propagation is dominated by turbulence effects, LES ECFM-3Z model is expected to provide reasonably accurate results concerning ROHR – however, it cannot capture chemical effects (e.g., local quenching due to low temperature – this effect might be significant when operating at higher levels of air excess).

Regarding combustion timing control, it is a bit more difficult for 3-D CFD. Unlike in the case of experimental data, when CA50 point is kept constant at 10deg ATDC, it would be too time consuming to achieve that – this would require to run at least 5 cycles to determine the location of average CA50 point and then to re-run it again while shifting combustion phasing to achieve CA50=10deg ATDC, which clearly doubles the requirement for calculation time. As a single cycle requires approx. 4 days (while using 192 CPU cores) and we usually run 4-5 consecutive cycles, this would lead to significant decrease of calculated cases. Moreover, empirical experience (based on previous calculations of the target engine) shows that ROHR shape is almost unchanged when making small changes of combustion phasing (i.e., changes of order of few degCA). Hence, only ROHR diagrams are shown when presenting 3-D CFD data from integral point of view. If the corresponding pressure traces are needed, the fastest way to obtain them is to impose ROHR curves (from 3-D CFD) into 0-D/1-D model and run the simulation while changing the combustion phasing to achieve the desired location of CA50 point.

Fig. 7.11, Fig. 7.12 and Fig. 7.13 show comparison of in-cylinder rate of heat release traces for small and big scavenged pre-chambers and big un-scavenged pre-chamber. From the 120 measured cycles the cycles with the highest and the lowest peak pressure (in the graphs labeled as Max p meas and Min p meas) were selected. ROHR data for 3 cycles from CFD results are shown – 1st calculated cycle is skipped due to possible influence of initial conditions (especially thermodynamic state in the pre-chamber might influence subsequent combustion phase). All graphs correspond to the case of 1800 rpm and air excess of 1.05. It can be seen that LES modeling approach also captures the cycle-to-cycle variation. The shape, phasing and duration of ROHR are closely matched to experimental data. All CFD traces are positioned within the limits of experimental data. Based on these results, the CFD model was declared to be calibrated.

Comparison of scavenged regime with un-scavenged one is presented in Fig. VI in Annex G from ROHR point of view and Fig. IX, Fig. X in Annex G show detailed 3-D CFD data. All these data correspond to operation at stoichiometric mixture (global air excess equals to 1.0). The ROHR data (Fig. VI) suggests that when big

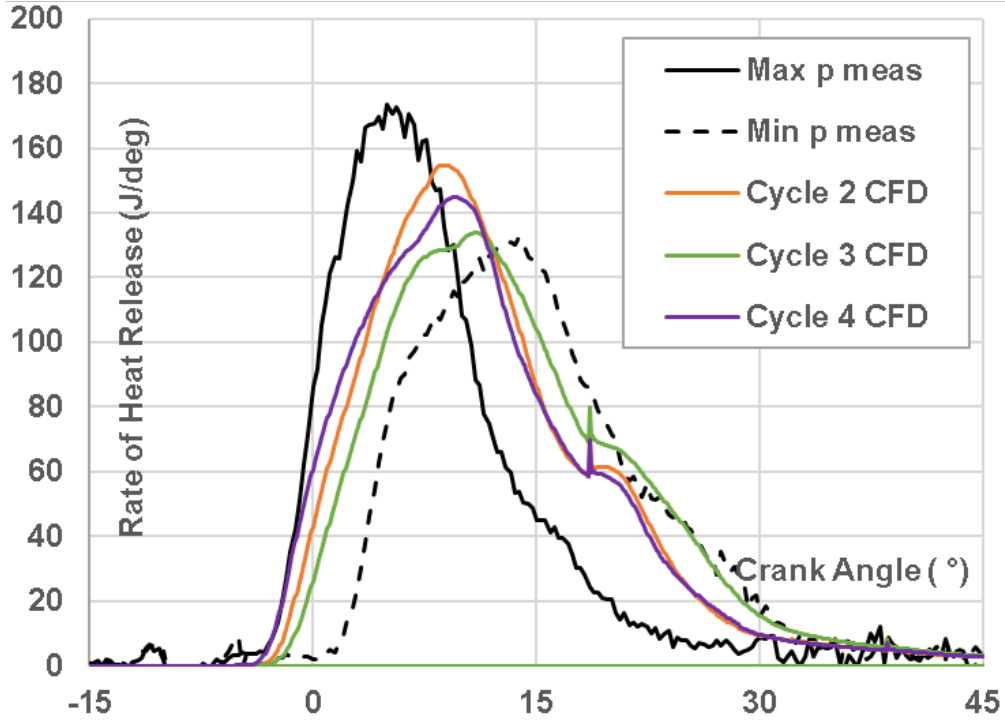


**Figure 7.11:** In-cylinder rate of heat release for small scavenged pre-chamber at  $\lambda = 1.05$  and engine speed of 1800 rpm. Comparison of the measured cycles with the highest and the lowest peak pressures (Max p meas and Min p meas) and CFD data.

pre-chamber is applied, combustion becomes faster regardless if the operation is scavenged or un-scavenged. This is also confirmed by experimental data (Fig. 7.6 ), although the version of big pre-chamber with scavenged operation might be slightly overestimated by the CFD model.

Analysis of mixing process in pre-chamber shows that there is relatively small difference when comparing scavenged case (left column in Fig. IX ) with un-scavenged ones (right column in Fig. IX ). Although scavenging phase leads to the fact that pre-chamber doesn't contain any oxygen at the end of intake stroke, all the mixing with oxidizer has to be done during compression stroke. This leads to the fact that there are still visible inhomogeneities of fuel space distribution just before spark timing event. When dealing with un-scavenged cases, there is lower demand for dilution by mixture incoming from cylinder. Hence, mixture homogeneity is very high and EGR content is low nevertheless it is slightly higher when compared with scavenged case – c.f. Fig. 7.14 . This leads to lower CCV effects for the case of un-scavenged pre-chamber – this is clearly visible in Fig. VI as both combustion phasing and com-

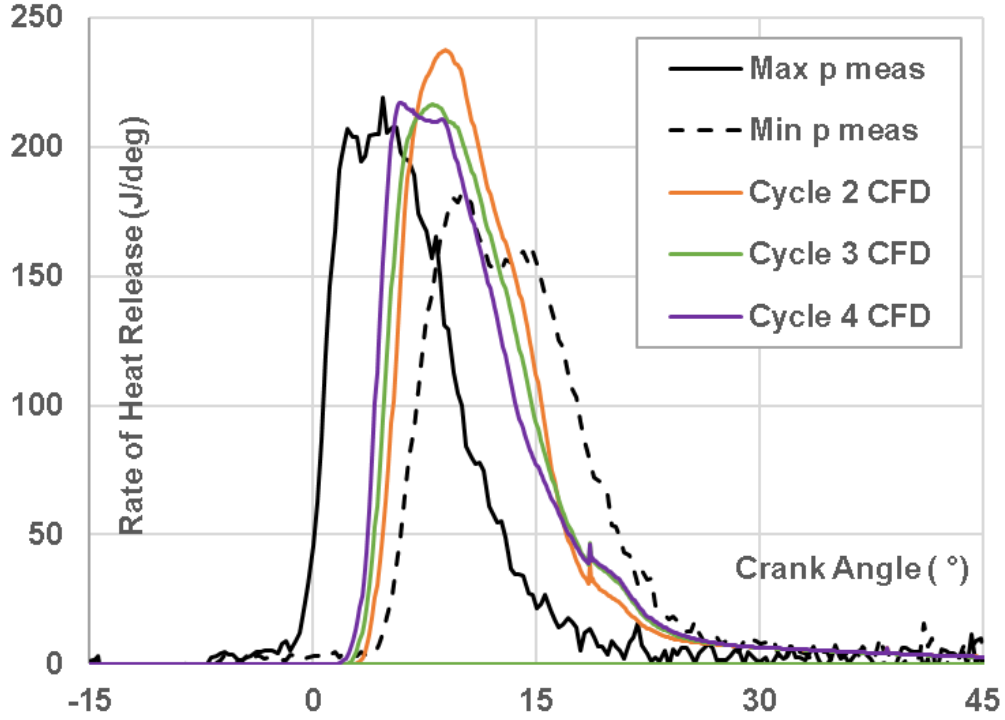


**Figure 7.12:** In-cylinder rate of heat release for big scavenged pre-chamber at  $\lambda = 1.05$  and engine speed of 1800 rpm. Comparison of the measured cycles with the highest and the lowest peak pressures (Max p meas and Min p meas) and CFD data.

bustion shape are less varied when comparing all computed cycles. This confirms that pre-chamber can work properly without scavenging if needed.

Scopes of space-averaged air excess ratio and residual gas content (RGC) in scavenged and un-scavenged big pre-chamber are introduced in Fig. 7.14 for stoichiometric operation. The figure clearly shows different operation of the pre-chamber when using different scavenging strategies. Un-scavenged operation is suitable for near stoichiometric operation as significant dilution would lead to too high air excess in pre-chamber (at spark plug location), hence causing problems with reliable ignition. At the global air excess of 1 the average value of  $\lambda$  in the scavenged pre-chamber at spark discharge is 0.61 and matches with the simulation in the GT-power (Fig. 7.10 , left point). A very rich mixture is a reason for deterioration of pre-chamber functionality and bad combustion stability. The differences in the residual gas content between scavenged and un-scavenged pre-chamber is 6,3% vs 10,7% at combustion start. Functionality of the pre-chamber is primarily influenced by the air excess and by the spatial distribution of the mixture in the vicinity of spark plug

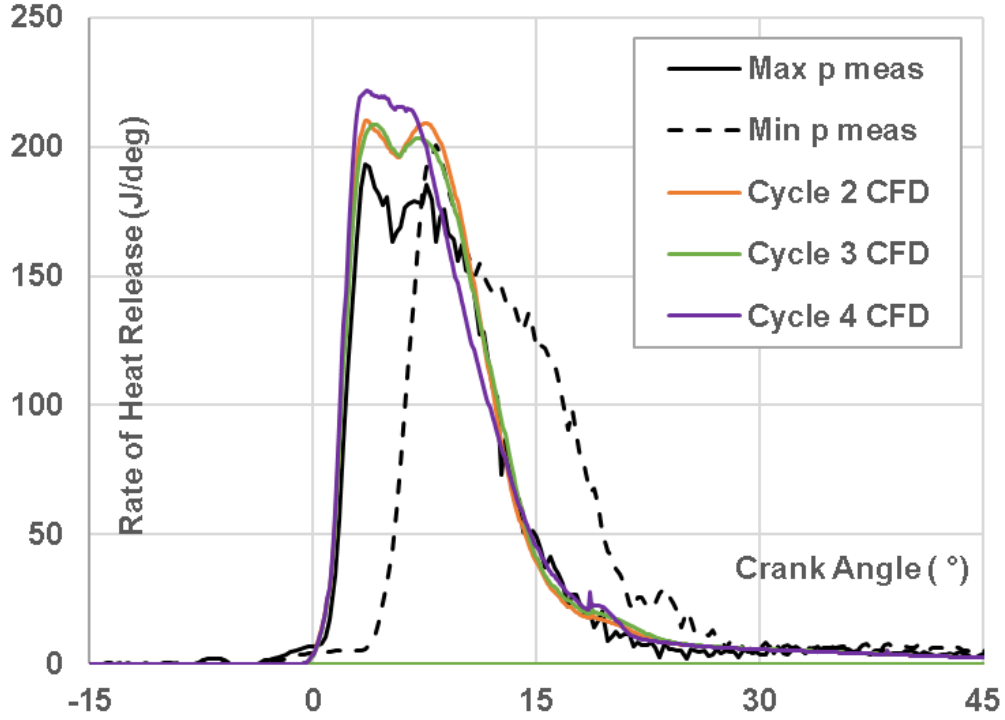


**Figure 7.13:** In-cylinder rate of heat release for big un-scavenged pre-chamber at  $\lambda = 1.05$  and engine speed of 1800 rpm. Comparison of the measured cycles with the highest and the lowest peak pressures (Max p meas and Min p meas) and CFD data.

electrodes.

Scavenging is supposed to push away hot exhaust gases out of pre-chamber and cool down pre-chamber inner surface by relatively cold fuel gas. This is supposed to improve pre-chamber cooling. Based on design of pre-chamber cooling circuit, it was estimated that pre-chamber inner surface temperature is approx. 500 K. Temperature space distribution is shown in Fig. X in the Annex. There is surprisingly little difference between scavenged case and un-scavenged one – 3-D CFD data suggest that there is almost no difference during major part of the whole engine cycle. This is caused by strong effect of wall heat transfer as pre-chamber has high ratio of surface-to-volume and by high turbulence level which supports mixing (surface temperature of 500 K was applied for un-scavenged case as well). Comparison of different pre-chamber designs at global air excess of 1.5 is shown in Fig. VII (ROHR) and Fig. XI, Fig. XII in the Annex. These set of figures are the outcome of pre-chamber optimization with the main focus put on connecting channel configuration – more details can be found in [21]. Unlike in case of data presented above, pre-chamber

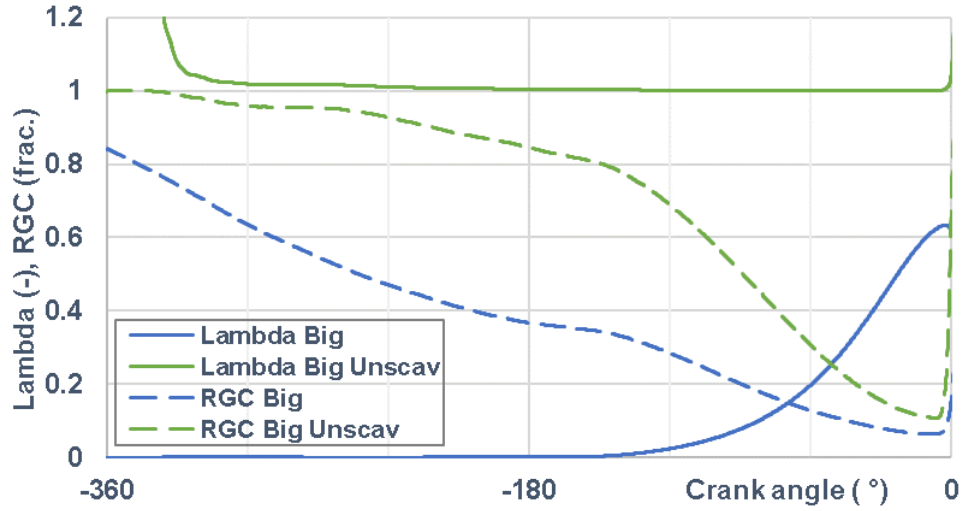


**Figure 7.14:** CFD simulation of stoichiometric operation: air excess and residual gas content in the big pre-chamber as a function of crank angle. Scavenged and un-scavenged versions are compared

is always operated in scavenged mode. The ROHR data (Fig. VII) correspond well with experimental ones (Fig. 7.7) – and it again suggests that increasing pre-chamber size leads to faster combustion. The qualitative trends are similar to those presented above for the case of global air excess of 1.0. Mixture quality space distribution is shown in Fig. 7.15, Fig. 7.16 and more comprehensive presentation is shown in Fig. XI in the Annex. It confirms that mixture homogeneity in pre-chamber is relatively low. Relatively high space variations of local air excess can be observed – this also varies significantly among the cycles, hence leading to higher level of CCV. When big pre-chamber is applied, these variations become even stronger due to the fact that it is taller (when compared with small pre-chamber), hence more time is needed to perform mixing inside pre-chamber. On the other hand, the space distribution of equivalence ratio follows required trend that rich/stoichiometric mixture is located near spark plug to enable reliable ignition and robust/stable early flame kernel development and propagation. This enables stable pre-chamber operation at high air excess levels (up to the value of 2.0), which was also confirmed by experiments.

Flame front space/time development is plotted in Fig. XII for the case of air excess of 1.5. It confirms that application of big pre-chamber leads to faster combustion, which is primarily driven by higher level of released chemical energy (Fig. VIII) and faster turbulent flame jet (related to size and number of connecting channels with respect to total pre-chamber volume). This figure is also supposed to stress that pre-chamber combustion is clearly different to classical SI one in terms of flame



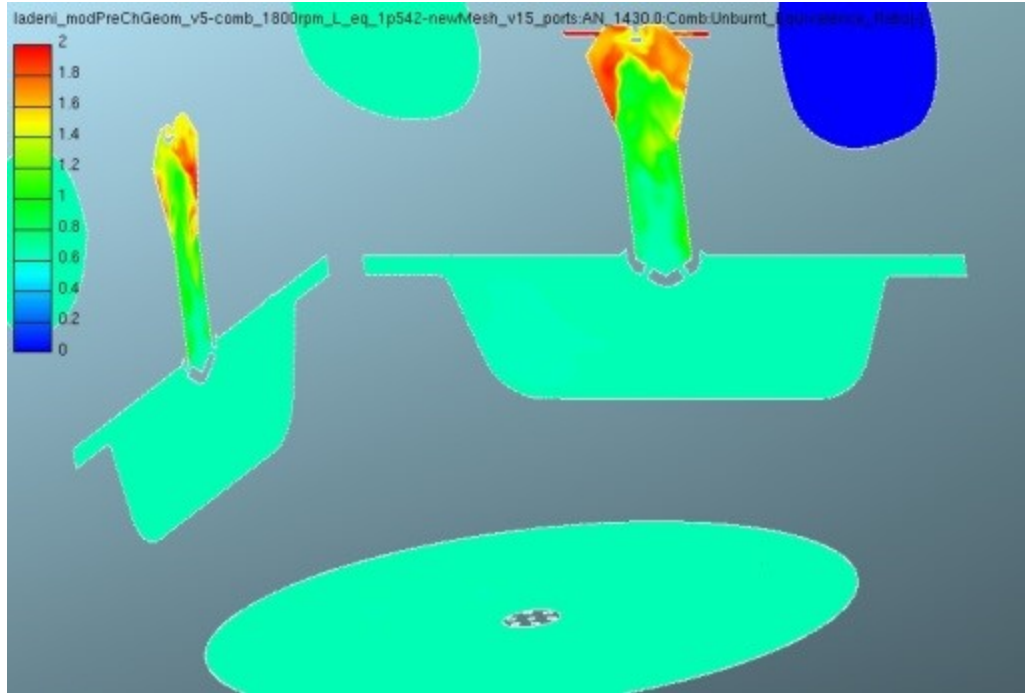


**Figure 7.15:** Equivalence ratio as a marker of mixture quality at air excess of 1.5, ‘big version (12x d=1.2mm)’, 10 degCA bTDC (legend: blue color corresponds to value 0.0 while red one represents 2.0).

structure and the direction of flame propagation. In the case of turbulent flame jet (i.e., application of pre-chamber), the flame front is created near piston top surface and it then propagates towards cylinder head. As there are many jets (due to many connecting channels), the flame surface in the main combustion chamber is large, hence leading to fast combustion progress. Both experimental data and simulation ones confirm this.

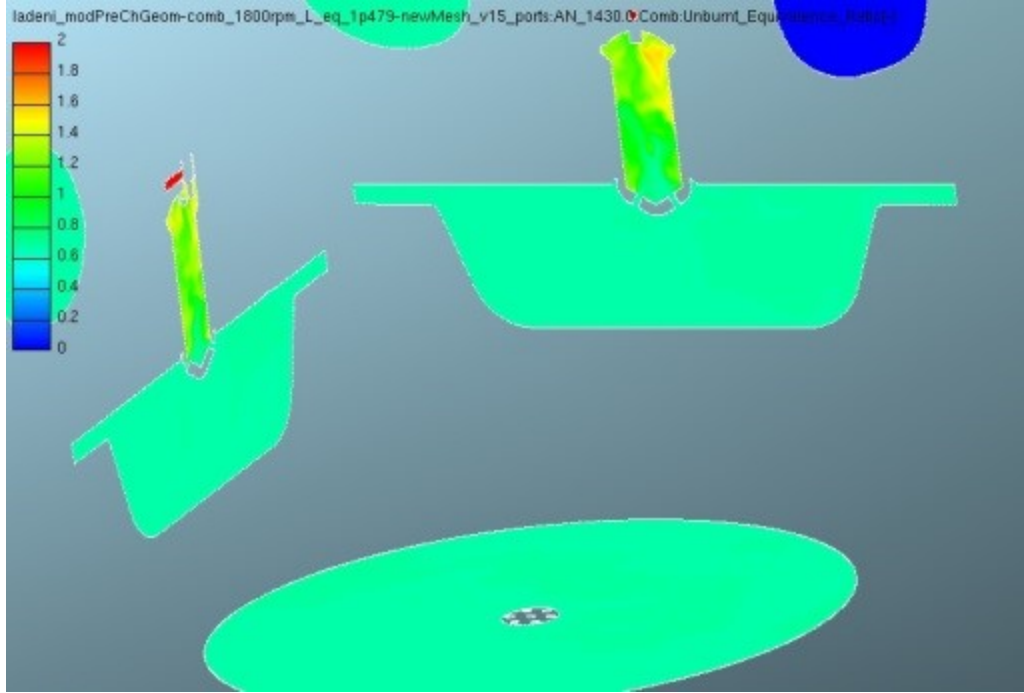


**Figure 7.16:** Equivalence ratio as a marker of mixture quality at air excess of 1.5, ‘small version (12x d=1.2mm)’, 10 degCA bTDC (legend: blue color corresponds to value 0.0 while red one represents 2.0).

## 7.5 Summary and Conclusions

In order to determine the influence of the volume of the pre-chamber, an experimental comparison of two pre-chambers with the same geometry of the connection orifices with different volumes was performed. From the partly motored mode, it can be concluded that the big pre-chamber provides approximately two times higher ignition energy than the small one. Nevertheless, the expected reduction in unburned hydrocarbon production and the extension of the engine operating range (air excess range) have not been achieved at full combustion mode. The benefit of the big pre-chamber is a faster combustion and lower demand for spark advance timing. On the other hand, the big scavenged pre-chamber shows a worse function and degradation of performance in the vicinity of stoichiometric mixture. Behavior of big pre-chamber in vicinity of stoichiometric mixture can be improved when un-scavenged (passive) mode of operation is adopted. The un-scavenged pre-chamber can be used up to the value of air excess 1.5. Combustion instability and misfiring occurs beyond this point.

At lean operation, the increased pre-chamber volume could not be completely

exploited due to low mixing intensity in the pre-chamber. The amount of gas delivery into the pre-chamber and thus potential ignition energy are limited. This statement is consistent with performed experiments and simulations.

The CFD model is based on LES approach while turbulence driven combustion model (LES ECFM-3Z) was applied, hence no chemical effects (e.g., flame quenching due to low local temperature) are taken into account. All the testing was done at single operating point – engine speed 1800 rpm while considering different levels of global air excess (the data related to values of 1.0 and 1.5 are presented in the paper). Two design variants of pre-chamber were tested with pre-chamber volume of 2.3 and 4.6% of cylinder compression volume.

Both scavenged operation and un-scavenged one were analyzed with big pre-chamber. Although there are differences related to specific pre-chamber operation, space distribution of important parameters just before ignition event is similar. Hence, combustion is fast in both cases while un-scavenged mode features lower levels of CCV. These trends are supported by experimental results.

3-D CFD results show that combustion process of SI ICE equipped with pre-chamber is very complex one. The flame structure is far away from classical spherical flame front shape of typical SI ICEs – its shape and topology is more similar to CI ICE although it is still a deflagration flame front propagation process.

The performed 3-D CFD simulations allow determining the spatial mixture distribution within the pre-chamber. The CFD results show rich mixture in the vicinity of the spark plug gap due to significantly stratified charge and low mixing in the pre-chamber. The low mixing limits the maximum amount of additional gas, and thus potential ignition energy of the pre-chamber volume, and further deteriorates its function.

As a next step, it is necessary to focus on improvement of the pre-chamber mixing to obtain better charge homogeneity. Further investigations with various connection orifice geometries and a new design of the main chamber geometry are in preparation.

## 7 Scavenged Pre-Chamber Volume Effect on Gas Engine Performance and Emissions

## Chapter 8

# Use of Hydrogen in a Combustion Engine with Advanced Combustion

### 8.1 INTRODUCTION

Replacing conventional fossil fuels with hydrogen is one possible way of decarbonising land transport activities. Efforts to implement this basic idea are mainly focused on the use of  $H_2$ -powered *PEM FC* (proton exchange membrane fuel cells), which would produce electricity on board for traction electric motors to power the vehicle. Even though cars powered by  $H_2$  fuel cells are already on the market, there are still serious problems that need to be addressed in order for fuel cells electric vehicle (*FCEV*) to be widely used in the real world.

While the range of vehicles and the refueling time of *FCEV* are comparable to vehicles powered by *ICEs*, the cost of *PEM FC* is a major disadvantage caused by the demand for special materials and production technologies. Another important issue is the requirement for the purity of hydrogen for use as *FC* fuel. Therefore, it makes sense to explore a different strategy for the use of hydrogen as a fuel for transport, which could overcome the "chicken and egg" syndrome, at least in the initial period of using hydrogen-powered vehicles and building hydrogen infrastructure.

Internal combustion engines (*ICE*) are the most widespread power units in the world, used in freight and passenger transport. For spark ignition (*SI*) engines, it is possible to use the design, based on natural gas engines for construction of hydrogen fueled *ICEs*. Modification of a diesel engine to burn hydrogen is also possible, while the engine remains capable of burning pure diesel (or renewable liquid fuels), i.e., the vehicle is not dependent on a sparse network of hydrogen filling stations. The *ICE* is insensitive to the purity of hydrogen, so it allows the gradual development of the hydrogen infrastructure without the need for expensive purification (initially, before the major deployment of PEMFC).

Internal combustion engines are not considered 100% emission-free propulsion (so called “Zero tailpipe emissions”), because even when using hydrogen, they emit nitrogen oxides (if atmospheric air is used as an oxidant). However, nitrogen oxide emissions can be eliminated virtually to a zero level by the exhaust gas aftertreatment system. A selective catalytic reduction (*SCR*) can be applied, where hydrogen can also be used as a reducing agent. Lean NO<sub>x</sub> traps (*LNT*) are another possible means for *NO<sub>x</sub>* reduction.

Other carbonaceous pollutants, such as carbon monoxide (*CO*), hydrocarbons (*THC*), carbon dioxide (*CO<sub>2</sub>*) and particulate matter (*PM*) can be almost eliminated by hydrogen combustion. In hydrogen engines, carbon containing gaseous exhaust gas components and particle matter are formed only by the combustion of lubricating oil, which escapes either through the piston rings or around the valve stems or from the turbocharger bearings. The oil penetrates into the combustion chamber also from the ventilation of the crankcase due to the imperfect separation of the oil from the crankcase gas, as it returns to the engine intake manifold by the positive crankcase ventilation system. Oil combustion and subsequent emissions can be almost eliminated by careful design optimization of the mentioned subassemblies.

In the past, several car and truck manufacturers brought the development of hydrogen-powered internal combustion cars to near-series production. Automotive companies such as Ford [29], [55], [71], [38], [74], [76] and BMW [44], [13], [19] presented hydrogen vehicle projects with internal combustion engines. Among the most interesting was the BMW 7 Series with a six-liter naturally aspirated dual-fuel twelve-cylinder engine with a power output of 191 kW. The vehicle allowed a range of about 200 km on about 8 kg of liquid hydrogen in a cryogenic tank and another 500 km on gasoline [90].

For a transitional period in the development of hydrogen infrastructure, the concept of a bifuel propulsion system seems to make sense, as it will ensure the range of the vehicle in the absence of hydrogen filling stations. This concept is similar to natural gas vehicles as today that are equipped with a small gasoline tank (eg Fiat, VW, Škoda vehicles in Europe). The reduction in carbon dioxide emissions will therefore not be maximized immediately with the deployment of these systems. A gradual decrease in *CO<sub>2</sub>* emissions can be expected. In practice, the intensity of the desired effect will depend on the density of the hydrogen filling stations and the societal benefits of using hydrogen as a motor vehicle fuel. The question arises, why previously developed hydrogen cars have not started the hydrogen era yet? The answer is not hard to guess. Hydrogen has not yet economically been a competitive fuel compared to fossil petroleum-based fuels or natural gas.

The current trend in internal combustion engines lays in so-called downsizing of the engines. Downsizing means reducing the displacement of engines (usually associated with a usage of a low number of cylinders) and increasing their power density by turbocharging. There has been a vast progress in turbocharging recently.

Increasing the charge air pressure, while maintaining the optimum mixing ratio, allows more fuel to be delivered to the engine and thus achieve higher performance with better efficiency than can be achieved with the higher number of cylinders or high engine speeds. Another benefit of downsizing can be found in low loads that are dominant in real life car operations. Passive resistances (friction loss and energy to drive accessories, etc.) are lower for a small engine than for a large one. This extends the area of high efficiency of the internal combustion engine even to the low load region.

One of the significant aspects associated with the operation of a hydrogen fueled internal combustion engine is the very high demand for working substance flow (or air consumption). The mixture calorific value of the hydrogen / air mixture is approximately 20% lower than that of the gasoline / air one (See Tab. II in Annex H).

In addition, in the case of hydrogen engines with homogeneous mixture combustion, the stoichiometric concept with a three-way catalyst for aftertreatment of pollutants in exhaust gas is problematic. Since hydrogen-air mixtures in the stoichiometric condition are highly inflammable, possible ignition sources must be avoided [44]. For a safe operation of the hydrogen engine, it is therefore necessary to operate the engine with a lean mixture. One reason is a prevention of abnormal combustion, i.e., pre-ignition, knocking, and back firing in case of mixture formation in the intake manifold. An additional advantage of engine operation with an extremely lean mixture lies in the low combustion temperature. The low-temperature combustion (*LTC*) increases a thermal efficiency by the reduction of the heat transfer to the walls of the combustion chamber and thanks to a more favorable ratio of specific heat capacity (so-called Poisson's constant). Another benefit is the possibility of increasing the compression ratio of the engine due to greater resistance to abnormal combustion. Higher compression ratio also leads to the relatively high efficiency of the hydrogen fueled engine [53].

Low temperature combustion is also beneficial in terms of *NOx* emissions. As already indicated in the introduction, the only significant pollutants in *H<sub>2</sub>ICE* exhaust gas, are nitric oxides (*NOx*). In the case of combustion of a premixed homogeneous mixture, the *NOx* emissions are reduced by lowering the combustion temperature.

For conventional hydrocarbon fuels, the flammability range of the mixture in conventional spark ignition engine is limited [33]. When burning lean mixtures, the burning velocity decreases with the air excess ratio increase. The combustion instability increases, which leads to misfire as the air excess ratio exceeds approximately the value of 1.6. This is associated with the higher emissions of hydrocarbons and deterioration of chemical efficiency.

On the other hand, due to the low initiation energy and high burning velocity, even for lean mixtures with air, hydrogen can be used in the engine with air excess

ratio higher than 4, even with a conventional ignition system, i.e. with inductive high-voltage spark ignition. The so-called lean burn concept for hydrogen engines leads to extremely low nitrogen oxide emissions and, unlike for hydrocarbon fuels, the combustion of very lean hydrogen mixtures does not degrade the chemical efficiency of incomplete combustion.

The authors decided to experimentally investigate the potential of low-temperature hydrogen combustion in a spark ignition experimental single-cylinder engine, supercharged with an externally driven compressor, while respecting the realistic turbocharging. The study will first describe the test engine with accessories. Then, the methodology and evaluation of the experiments will be described. The results of the initial mapping of hydrogen engine properties in the range of engine maps will be presented.

## 8.2 Experimental setup

Experiments were performed on a spark ignition experimental single-cylinder engine in the engine laboratory of the Center for Sustainable Mobility Vehicles (CVUM) at the Czech Technical University in Prague. The engine was designed by bachelor's, master's, and doctoral students of the Faculty of Mechanical Engineering together with CVUM researchers in cooperation with designers from the engine development department of ŠKODA AUTO Company, where the engine was also manufactured and assembled. The engine is derived from the cylinder unit of current ŠKODA engines with a displacement of  $375\text{ cm}^3$  per cylinder. The basic parameters of the engine are displayed in Tab. 8.1.

The engine is installed on an AVL Single-Cylinder Compact Test Bed with an alternating asynchronous dynamometer enabling both motoring and loading of the engine. The engine is liquid cooled and lubricated with an external AVL 733 conditioning unit. The engine is externally supercharged by an Atlas Copco compressor, the boost pressure and air temperature were adjusted by the AVL 515 boost unit, see Fig. 8.1.

The test cell is complemented by a gas mixing station, which allows a preparation of mixed gaseous fuel from up to five gaseous components ( $C_2H_6$ ,  $C_3H_8$ ,  $N_2$ ,  $CO_2$ , and  $H_2$ ). Mass flows of gases are controlled and measured by Brooks SLA5853 controller. A mixture of fuel and air is formed in the engine intake manifold. Fuel is injected into the intake manifold metered by low-pressure pulse-driven port fuel injection system with an originally CNG injector. The timing and length of the pulses have been optimized to eliminate back firing.

The air is compressed or throttled by an external AVL 515 boost unit. The air temperature at the engine inlet was set to a constant value of  $40^\circ\text{C}$  to emulate the function of a conventional vehicle intercooler. The exhaust back pressure was ad-



Bore / Stroke	74.5 / 85.9 mm
Maximum engine speed	6000 rpm
Compression ratio	Max 11.6:1 (adjustable)
Maximum cylinder pressure	100 bar
Boosting	external (0.3 to 4 bar air absolute pressure)
Air temperature	30 - 130°C
Exhaust back pressure	adjustable by exhaust throttle
Engine control unit	Bosch MS6.1 ECU
ECU calibration	ETAS INCA 7 software
Valve control	electrohydraulic variable timing
Throttle control	electronic throttle
Fuel injection	gas/liquid fuel port injection
Ignition	high voltage inductive ignition coil
Lambda control	closed/open loop control
Knock control	knock sensor based
Fuel	hydrogen (purity 4.0)

**Table 8.1:** Basic parameters of the ŠKODA single cylinder research engine.

justed by a throttle valve in the exhaust manifold downstream the 60 L exhaust plenum. The back-pressure value is controlled to emulate the exhaust back pressure of the exhaust turbocharger with a total efficiency of about 50% (compressor isentropic efficiency  $\eta_{SC} = 73\%$ , turbine isentropic efficiency  $\eta_{ST} = 73\%$  and turbocharger mechanical efficiency  $\eta_{TCmech} = 95\%$ ).

Exhaust gas sample was taken from the exhaust manifold for analysis using a set of laboratory gas analyzers AVL AMAi60 (*NDIR* for measuring the molar fraction of  $CO$  and  $CO_2$ , *PMD* for measuring of  $O_2$ , *FID* for detecting the molar fraction of  $THC$  and  $CH_4$  and *CLA* for detecting the molar fraction of  $NO$  and  $NO_x$ ). The H-Sense mass spectrometer was used to determine the fraction of unburned hydrogen in the exhaust gas. Cooled piezoelectric pressure transducer (AVL GC24D) with a M8 thread was installed in the separate drill in the cylinder head. The cylinder pressure is a crank angle indexed with a resolution of  $0.1^\circ$  by the *AVL 365C* incremental rotational encoder, attached to the crankshaft. The AVL Indicom Mobile system was used for a high speed data acquisition, online evaluation, and display of the rate

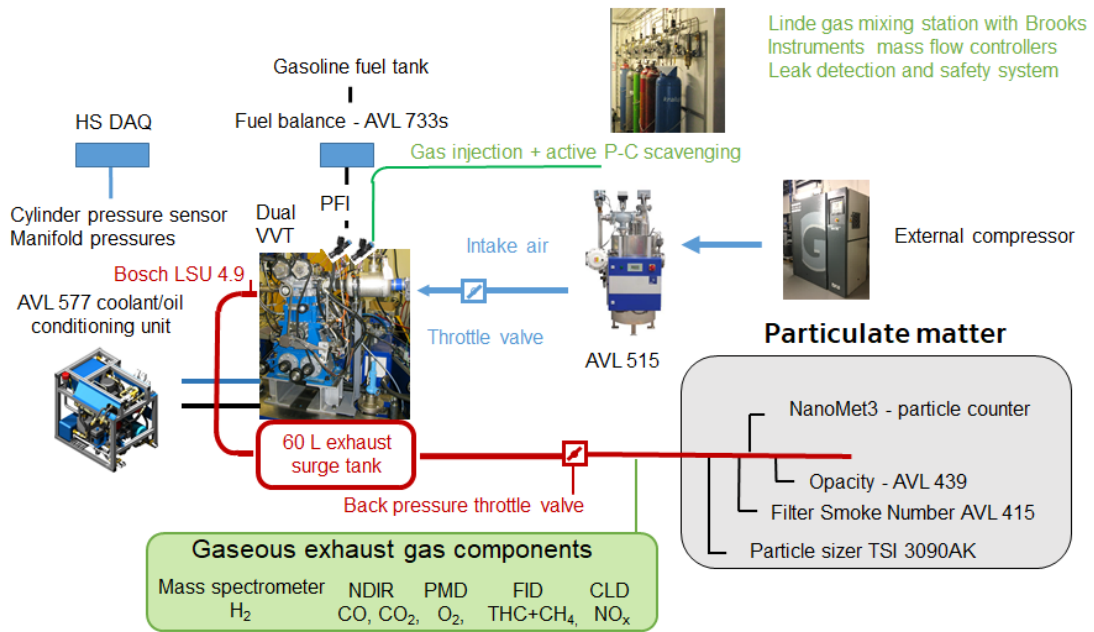


**Figure 8.1:** Schematic of a test cell with an experimental single-cylinder ŠKODA-ČVUT engine in the CTU engine laboratory.

of heat release, the crank angle indexed value of integral of the mass fraction burnt.

### 8.3 Methodology of experiments

The experiments were performed at steady state, as a sequence of part-load curves, each of them taken at constant speed and with the engine throttle valve fully open. The intake air pressure and thus the mixture inflow were adjusted solely by the external boost unit. The required engine power was set by the injected fuel amount. To reduce the number of degrees of freedom, the ignition timing was set for all measured points to maintain a phasing of 50% of the mixture burn ( $CA_{50}$ ) at  $10^\circ$  after the top dead center. This value is generally considered close to the optimal combustion phasing in most cases. An exception was the operation at high loads, where the combustion phasing was delayed with respect to compliance with the maximum combustion pressure limit (100 bar).

The engine is equipped with a dual knock detection. The engine control unit works with the signal of the piezoelectric knock sensor, located on the engine block. During the ECU parameterization, the so-called adaptive knock control was switched on. The ignition timing was automatically set according to the knock intensity in individual working cycles. Simultaneously, the high speed *DAQ* processed the signal from the piezoelectric pressure sensor installed in the cylinder head and evaluated the knock level for individual cycles by filtering the high-frequency component of the pressure signal. The test cell operator adjusted and adapted the default ignition advance map in the ECU according to the intensity of the knock.

Based on consultations with ŠKODA AUTO a.s. R&D workers and according to previous experience in the evaluation of vehicle emissions in driving cycles, to comply with the  $NO_x$  limit in the exhaust after catalytic converter, the engine should not emit more than 10 ppm of  $NO_x$  at any time of the cycle. For laboratory experiments at the engine dynamometer at steady state, the air to fuel ratio of the mixture was adjusted by the inlet air pressure regarding maintaining the molar fraction of  $NO_x$  in the raw exhaust gas below 10 ppm. For each point, at which the boost pressure was higher than the atmospheric one, the exhaust back pressure was adjusted so that the efficiency of the fictitious exhaust gas driven turbocharger corresponded to the value of 50%. With this measure, a more or less realistic backpressure was emulated as for a turbocharged multicylinder engine.

### 8.4 Experimental results

#### Initial lean operation mapping

Fig. 8.2 presents results from the initial mapping of the the lambda range for the required limit of  $NO_x$  at a constant speed of 2000 rpm, constant engine load at a mean indicated pressure of 6 bar, and at constant combustion phasing. Fig. 8.2 on

the left shows the dependence of molar fractions of  $NO_x$  and  $H_2$  in exhaust gas on the air excess ratio ( $\lambda$ ). The required boost pressure and exhaust back pressure are shown in Fig. 8.2 on the right.

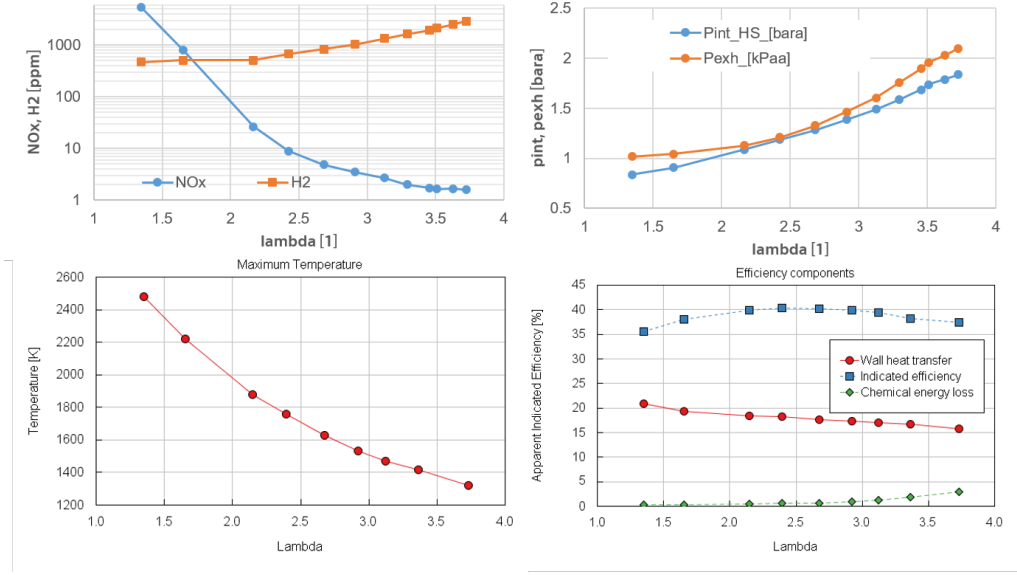


**Figure 8.2:** Influence of the air excess ratio on molar fraction of  $NO_x$  and molar fraction of  $H_2$  in the exhaust gas (top left), the boost pressure and the exhaust back pressure in the exhaust manifold (top right) and maximum cylinder charge temperature (bottom). Traces measured at a constant speed of 2000 rpm, at constant mean indicated pressure of 6 bar and at constant combustion phasing.

Molar fraction of  $NO_x$  can be significantly reduced to a one-digit level in ppm for the leaner mixture by maintaining a constant power by boosting. The proportion of hydrogen in the exhaust increases with increasing air excess ratio as can be seen in Fig. 8.2 in the top left diagram. The trend in maximum cylinder charge temperature is shown in the bottom left in Fig. 8.2. Bottom right part displays the results of the thermodynamic analysis performed in the GT Power using the three pressure analysis [15]. Blue curve shows the trend in indicated efficiency, the red curve shows the heat losses in the cylinder and the green curve plots the loss in chemical energy by the measured fuel molar fraction in the exhaust. The optimum indicated efficiency occurs around  $\lambda = 2.5$ , where the combustion rate and chemical efficiency remain high (Fig. 8.3).

At bottom graph in Fig. 8.3) cylinder charge gas constant traces are displayed. A molar contraction in hydrogen combustion causes decrease of the cylinder charge gas constant. This effect reduces the pressure increment by combustion and hence deteriorates the engine indicated efficiency.

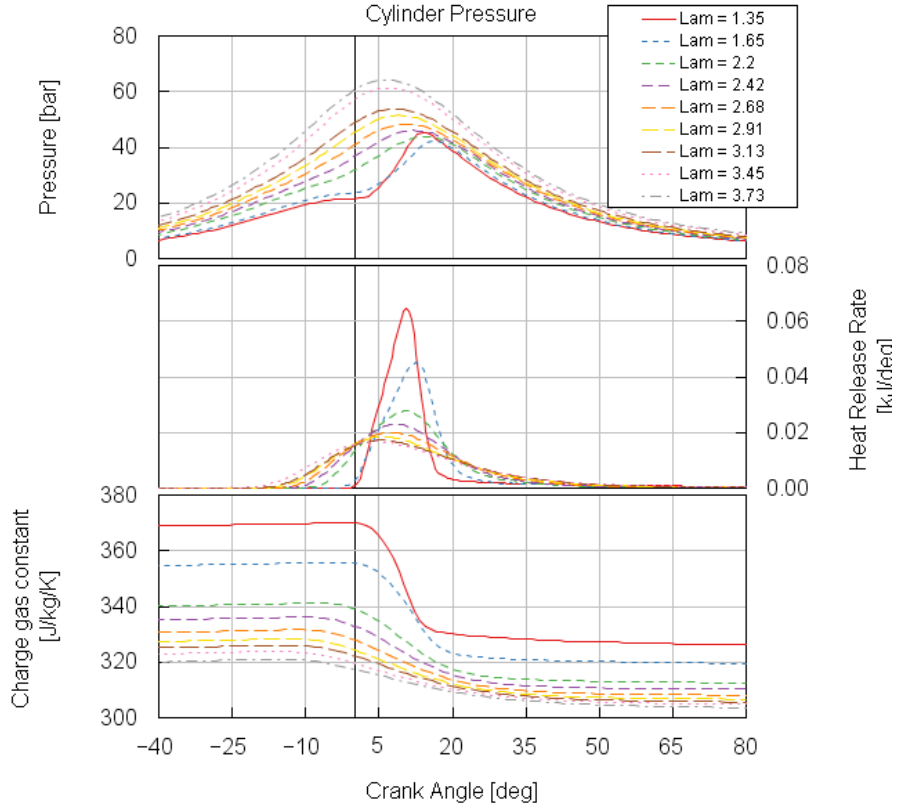


**Figure 8.3:** Crank angle indexed traces of the cylinder pressure and heat release rate in dependence of lambda values.

## Engine performance maps

All subsequent measurement results will be presented in this study in the form of the performance characteristics with coordinates of the brake mean effective pressure  $bme_p$ . Due to the atypical arrangement of the test engine and its accessories compared to conventional multicylinder engines, the directly measured effective values (i.e., related to the brake torque and power) do not have sufficient significance. Therefore, the effective quantities have been recalculated from the indicated parameters using the values of passive resistance taken from a modern turbocharged multicylinder gas engine [22].

Fig. 8.4 shows the performance maps of a single cylinder engine. The symbols (+) show the measured points, the blue continuous line indicate the envelope of the measurement. The values of the maximum combustion pressure ( $p_{max}$ ) are marked in figure on the left by colored isolines. The achievable maximum load (vertical axis)

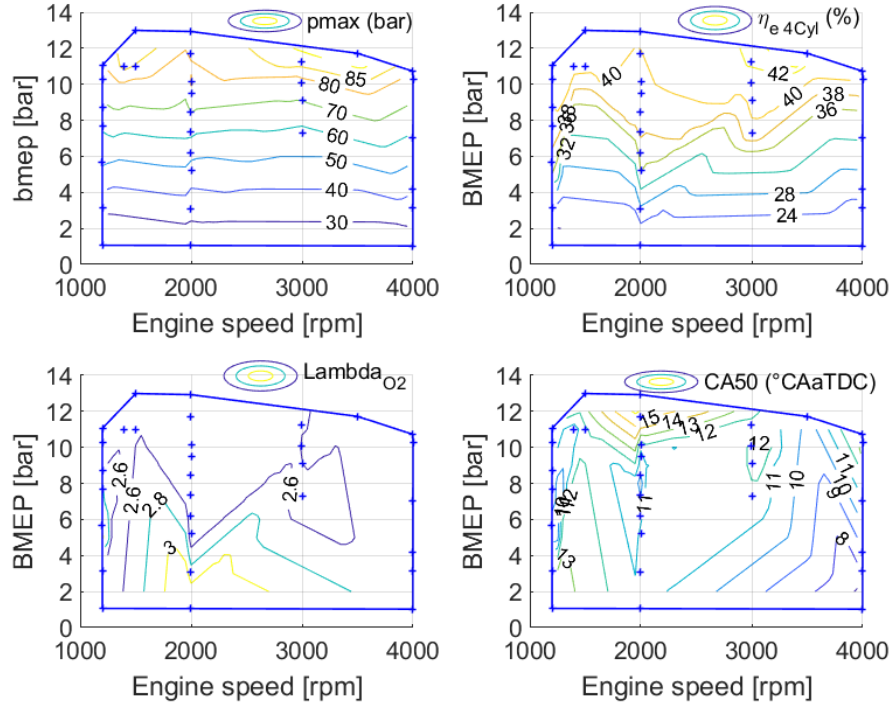


**Figure 8.4:** Performance maps of the four-cylinder engine: top left isolines of maximum cylinder pressure and top right isolines of the brake efficiency, lower left isolines of air excess ratio (determined from molar fraction of  $O_2$  in the exhaust), lower right isolines of the crank angle of 50% of the mass fraction burned.

of this engine is limited by a limit of maximum combustion pressure of 100 bar. The diagram on the right in Fig. 8.4 shows the isolines of engine brake efficiency. The peak value is 43.3% in maximum load at a speed of 3500 rpm.

According to preliminary evaluations of thermodynamics, the low temperature combustion concept is a significant contributor to the high efficiency of the hydrogen engine. The air excess ratio ranged from 2.4 to 3.3, see Fig. 8.4 bottom left. The high burning rate of such a lean mixture of hydrogen and air has also a positive effect on the efficiency of the engine, and the possibility of maintaining optimal combustion phasing, see Fig. 8.4 bottom right. Low maximum combustion temperature and low heat loss on the combustion chamber walls improve the engine's efficiency.

Fig. 8.5 shows the isolines of the boost pressure and exhaust back pressure. The overall efficiency of the fictitious turbocharger was maintained at 50% during the tests by adjusting the back pressure in the exhaust. The test bed operators tried to emulate the pressures in the intake and exhaust manifold of the externally super-

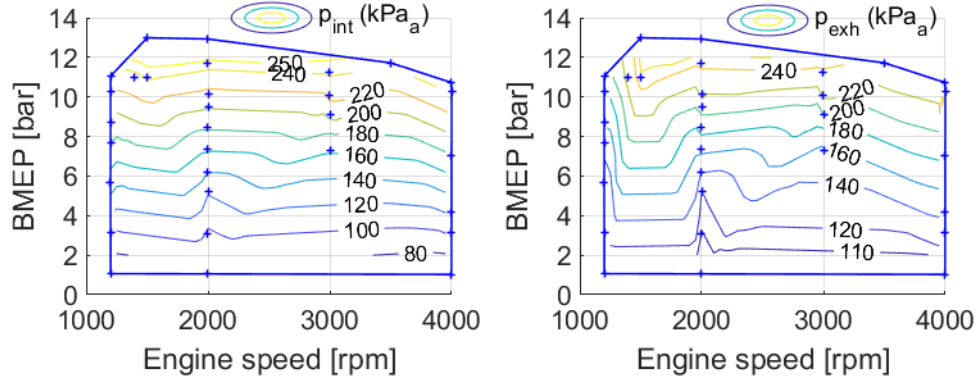


**Figure 8.5:** Plots the isolines of the absolute intake air pressure (left) and isolines of the absolute exhaust gas pressure (right).

charged single-cylinder engine as realistic as possible regarding the possibilities of current turbochargers. The maximum boost pressure of 250 kPa<sub>a</sub> was reached at a maximum load at an engine speed of 4000 rpm. The exhaust back pressure at this point was 276 kPa<sub>a</sub>.

## Hydrogen engine emission parameters

Only two main emission parameters will be discussed in the study, i.e.,  $NO_x$  and  $CO_2$  emissions.  $NO_x$  emissions are formed at high temperatures by the oxidation of atmospheric nitrogen. Due to the low combustion temperature of lean mixtures and the high air excess ratio, it was possible to keep the molar fraction of  $NO_x$  in raw exhaust gas at one-digit values in ppm at all points of the map, see Fig. 8.6 left. Specific  $NO_x$  emissions range from 6 to 17 percent of the current emission limit (e.g., the EU6 limit for heavy duty applications is 0.46 g / kWh [1] (as a result of running the WHTC cycle).

Exhaust emissions of  $CO_2$  are important in terms of global emissions. In the case of hydrogen fueled internal combustion engine,  $CO_2$  is formed only by the combustion of lubricating oil penetrating into the combustion chamber. Fig. 8.7 on the left shows the isolines of measured  $CO_2$  molar fraction in exhaust. The intake air entering the engine contained 420 ppm  $CO_2$ . The right half of Fig. 8.7 shows isolines of specific  $CO_2$  emissions, untreated for the proportion of  $CO_2$  in the intake air. Specific  $CO_2$  emissions range from 3.8 to 17 g/kWh.

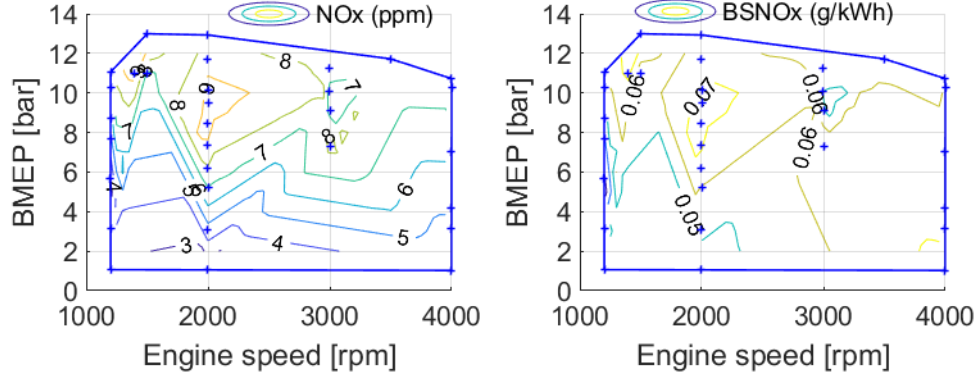


**Figure 8.6:** Plot of isolines of NOX molar fraction in raw exhaust gas (left), isolines of specific NOX emission (right).

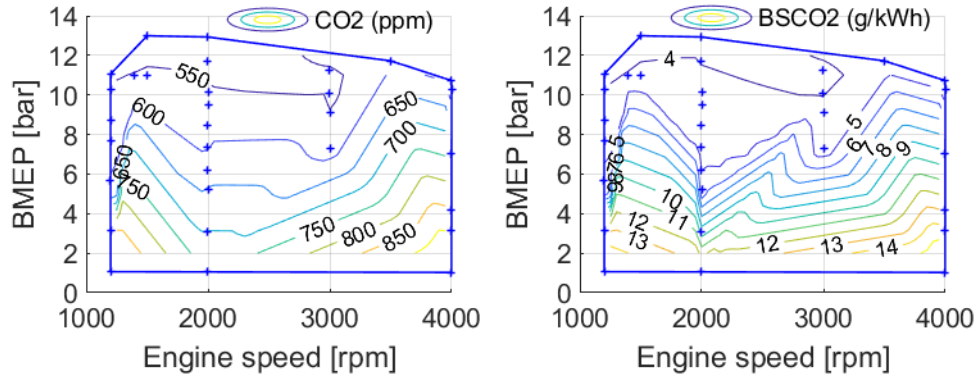


**Figure 8.7:** Isolines of the molar fraction of  $CO_2$  in exhaust (left) and isolines of specific  $CO_2$  emissions (right).

## 8.5 Conclusions

Low  $NOx$  values indicate the potential to meet the driving cycle emission limits of a passenger car without additional exhaust gas treatment. Regarding  $CO_2$  emissions, it is worth noting that a modern diesel engine with a specific diesel consumption of  $220 \text{ g/kWh}$  emits around  $700 \text{ gCO}_2/\text{kWh}$ . Even with a simplified evaluation, without subtracting the amount of  $CO_2$  in the intake manifold, the hydrogen engine can reduce exhaust  $CO_2$  emissions by 97.6 to 99.5% compared to a modern diesel engine.



The proposed use of hydrogen as a fuel in transport allows a reduction in the emissions of all monitored pollutants as well as carbon dioxide by several orders of magnitude.

At high loads, the engine efficiency is comparable to the efficiency of a fully loaded fuel cell. The design of the engine and accessories is practically no different from engines using more conventional gaseous fuels, and the introduction of primary production will not cause requirements for changes in production and assembly technologies.

Adaptation to the use of hydrogen as a fuel is also realistic for vehicles in service. Tolerance to the impurities in hydrogen and the possibility of operating on a conventional fuel in the absence of hydrogen, make the hydrogen engine an ideal means of supporting the development of hydrogen infrastructure during the transitional period in building the hydrogen economy.

The use of hydrogen as a fuel for internal combustion engines will allow carmakers to apply a de facto reduction in greenhouse gas emissions to their products by using physical processes, governed by natural laws rather than by an administrative reduction of the fleet average  $CO_2$  emissions by combination of sales of (supposedly zero emission) electric vehicles and vehicles with internal combustion engines.



## Chapter 9

# Summary and Conclusions of the Thesis

### Summary of gasoline engine low temperature combustion studies

The first study, carried out on a gasoline fueled experimental engine with the fully flexible valve actuation system, showed that stable, dilute, and efficient combustion could be achieved with SACI at loads above the allowable limits for naturally aspirated HCCI. The SACI combustion mode provided a pathway of transition from pure HCCI to pure SI. The following results were also obtained.

Lean HCCI without spark assistance was achieved up to  $\sim 3.7$  bar NMEP. Combustion phasing was heavily dependent on the degree of NVO and the fraction of hot internal residual under certain conditions. A large degree of NVO introduced complex cycle-to-cycle feedback, which greatly affected the combustion stability at higher loads.

Load extension was achieved using a combination of spark assist and EGR dilution. Maintaining a dilute mixture limited the maximum in-cylinder temperature, increasing  $\gamma$  and allowing for more efficient operation than conventional SI at the same load conditions. At these loads, NO<sub>x</sub> emissions exceeded US-2010 standards; however, conventional after-treatment could be used due to the stoichiometric mixture.

SACI allowed for successful engine operation above the HCCI ringing limit and below the SI misfire limit, bridging the gap between the two combustion regimes. Just above the HCCI limit, the increased unburned temperatures allowed weak flames to be sustained at very low  $\phi$  mixtures. These flames helped induce auto-ignition when the mixture was too cold to auto-ignite consistently without spark. As the load increased, the flame development became stronger and the total internal residual was reduced, resulting in lower unburned temperatures.

Three knock metrics have been applied to HCCI, SACI, and SI combustion in a FFVA engine and the results are compared over a range of loads.

For all metrics, the transition from HCCI to SACI, and from SACI to SI results in reduced knock values.

Variability as measured by standard deviation and frequency distribution, is increased as the combustion transitions from HCCI through the SACI region to SI, consistent with the increasing proportion of flame-induced heat release.

In the SACI combustion mode, no general agreement was found among the metrics. Furthermore, all metrics showed a significant decrease as the engine transitioned between HCCI through SACI to SI despite the presence of significant audible knock as SI combustion was approached.

## Initial scavenged prechamber ignition study on a gas engine

Initially, three geometries of a scavenged prechamber equipped with a miniature pressure sensor were designed and tested on a natural gas light duty truck engine at a fixed engine speed under the steady state operation.

The best engine performance was achieved with the prechamber with the largest volume and the greatest cross section area of the nozzles. At extremely lean operation, it shows the best efficiency and the lowest emissions of hydrocarbons with favorable  $NO_X$  emissions.

Despite the high amount of unburned hydrocarbons in exhaust, the tested engine equipped with the scavenged prechamber showed significant improvements compared to the engine with a conventional spark plug.

The prechamber engine was able to operate at high load with a stoichiometric mixture strategy that is compatible with a three-way catalyst. At low loads, the scavenged prechamber allows to ignite extremely lean fuel-air mixtures with high combustion rate. Lean operation potentially allows the reduction of nitrogen oxide ( $NO_X$ ) emissions to levels below the legislative limits without the need of using a  $NO_X$  after-treatment system. At the same time, the lean mixture reduces the combustion temperature, hence the heat losses are reduced and the thermal efficiency of the engine is increased.

The prechamber engine was then tested in four different fueling modes with or without spark discharge, to allow separate investigations of various phenomena of this advanced combustion system.

From the partly motored mode (Mode C), it can be concluded that the prechamber as a source of ignition energy for the lean burn engine provides approximately a thousand times higher energy than the energy of the conventional spark plug. Further experimental observations show:

- The engine equipped with the scavenged prechamber is capable of running a

wide range of  $\lambda$  with constant combustion phasing adjusted to the optimum engine efficiency ( $CA_{50} = 10$  deg aTDC). This was achieved by a constant fueling rate to the prechamber within the range of tested air excess ratios. The demand for spark advance control is moderate.

- The simple method of fueling the prechamber was proven successful. Fuel was delivered via a simple fuel line and check valve, and the fuel injection rate was controlled only by the pressure in the fuel line.
- While operating at the lean end of the investigated range, the  $NO_X$  emissions of the raw exhaust gas are very low, which bodes well for real world operation at low load without exhaust gas aftertreatment.
- The most significant experimental challenge is managing the content of unburned hydrocarbons in the engine-out exhaust gas. The range of the air excess ratio needs to be trimmed to maintain a reasonable content of unburned methane in the raw exhaust gas.

To determine the influence of the volume of the prechamber, an experimental comparison of two prechambers with the same geometry of the connection orifices with different volumes of 2.3 and 4.6% of cylinder compression volume was performed.

From the partly motored mode, it can be concluded that the big prechamber provides approximately two times higher ignition energy than the small one. Nevertheless, the expected reduction in unburned hydrocarbon production and the extension of the engine operating range (air excess range) have not been achieved at full combustion mode. The benefit of the big prechamber is a faster combustion and lower demand for spark advance timing. On the other hand, the big scavenged prechamber shows a worse function and degradation of performance near the stoichiometric mixture. Behavior of the big prechamber near the stoichiometric mixture can be improved when un-scavenged (passive) mode of operation is adopted. The un-scavenged prechamber can be used up to the value of air excess 1.5. Combustion instability and misfiring occurs beyond this point.

At lean operation, the increased prechamber volume could not be completely exploited due to the low mixing intensity in the prechamber. The amount of gas delivery into the prechamber and thus the potential ignition energy are limited. This statement is consistent with the performed experiments and simulations.

Initial CFD simulations show:

- Using the CFD modeling, the quality of scavenging was evaluated quantitatively as the amount of leaked fuel and qualitatively as a spatial distribution of mixture in the prechamber. Despite the introduced simplifications, which

affect the accuracy of the results, the simple CFD model of the prechamber was used for efficient evaluation of different variants, geometry optimization, and sensitivity analysis, with lower computational requirements,

- The CFD results were used also as a feedback for the calibration of the scavenging object in the 0-D model of the prechamber in the GT-Power software.
- The evaluated prechamber can be described as a no-swirl prechamber with the stratified charge. The low mixing in the prechamber is the main factor that influences the functionality of the designed version. Due to this fact, which results in a rich mixture near the spark plug electrodes, the maximum amount of additional gas in the prechamber and thus the ignition energy is limited.

## Complete engine geometry, CFD study

The detailed CFD model together with the calibrated 0-D/1-D model are supposed to introduce a lot of new information which might be difficult to be obtained experimentally. This enables understanding the gas exchange process (especially between the cylinder and the prechamber) and the turbulent flame development (especially in the prechamber and early in-cylinder phase). All that is expected to improve the overall knowledge of the prechamber concept applied to automotive ICE, hence leading to optimizations planned for the near future.

The combustion model used in this study does not capture the local chemistry. The model is based on LES approach while the turbulence driven combustion model (LES ECFM-3Z) was applied, hence no chemical effects (e.g., flame quenching due to low local temperature) were taken into account. Only a combustion model based on chemical kinetics could capture that. Such a model will be employed in the future.

- The effectiveness of prechamber scavenging is sufficient. The residual gas content inside the prechamber before the start of combustion is on the order of one percent.
- At the time of spark discharge, the mixture composition near the spark gap is within the limits of flammability. This statement is valid for all investigated operational points.
- Even if the flow of fuel into the prechamber starts during the later phase of the exhaust process, the amount of leaked unburned fuel to the exhaust port during prechamber scavenging was identified by CFD as negligible.
- The flame jet propagation in the cylinder occurs very fast. Furthermore, flame development differs significantly from conventional hemispherical surfaces typical of SI engines. Our next study will focus on modifying the geometry of both the prechamber and the main chamber to cope with this phenomenon.

- Both the scavenged operation and un-scavenged one were analyzed with a big prechamber. Although there are differences related to the specific prechamber operation, the space distribution of important parameters just before the ignition event is similar. Hence, combustion is fast in both cases while un-scavenged mode features lower levels of CCV. These trends are supported by experimental results.
- 3-D CFD results show that the combustion process of SI ICE equipped with prechamber is a very complex one. The flame structure is far away from the classical spherical flame front shape of typical SI ICEs – its shape and topology is more similar to CI ICE, although it is still a deflagration flame front propagation process.
- The performed 3-D CFD simulations allow determining the spatial mixture distribution within the prechamber. The CFD results show a rich mixture near the spark plug gap due to significantly stratified charge and low mixing in the prechamber. The low mixing limits the maximum amount of additional gas, and thus the potential ignition energy of the prechamber volume, and further deteriorates its function.
- As a next step, it is necessary to focus on the improvement of the prechamber mixing to obtain better charge homogeneity. Further investigations with various connection orifice geometries and a new design of the main chamber geometry are in preparation.

## Hydrogen low temperature combustion in SI engine

Regarding the application of low temperature combustion in spark ignition engines. The low  $NO_x$  values indicate the potential to meet the driving cycle emission limits of a passenger car without additional exhaust gas treatment.

Regarding  $CO_2$  emissions, it is worth noting that a modern diesel engine with a specific diesel consumption of  $220\text{ g/kWh}$  emits around  $700\text{ gCO}_2/\text{kWh}$ . Even with a simplified evaluation, without subtracting the amount of  $CO_2$  in the intake manifold, the hydrogen engine can reduce exhaust  $CO_2$  emissions by 97.6 to 99.5% compared to a modern diesel engine.

The proposed use of hydrogen as a fuel in transport allows a reduction in the emissions of all monitored pollutants as well as carbon dioxide by several orders of magnitude.

At high loads, the engine efficiency is comparable to the efficiency of a fully loaded fuel cell. The design of the engine and accessories is practically no different from engines using more conventional gaseous fuels, and the introduction of primary

production will not cause requirements for changes in production and assembly technologies.

Adaptation to the use of hydrogen as a fuel is also realistic for vehicles in service. Tolerance to the impurities in hydrogen and the possibility of operating on a conventional fuel in the absence of hydrogen, make the hydrogen engine an ideal means of supporting the development of hydrogen infrastructure during the transitional period in building the hydrogen economy.

The use of hydrogen as a fuel for internal combustion engines will allow car makers to apply a real reduction in greenhouse gas emissions to their products by using physical processes, governed by natural laws rather than by an administrative reduction of the fleet average  $CO_2$  emissions by combination of sales of (supposedly zero emission) electric vehicles and vehicles with internal combustion engines.



# References

- [1] URL: <https://dieselnet.com/standards/eu/hd.php>.
- [2] Paris agreement, report of the conference of the parties on its twenty-first session, held in paris from 30 november to 13 december 2015. URL: <https://unfccc.int/process/conferences/pastconferences/paris-climate-change-conference-november-2015/paris-agreement>.
- [3] GT-Power User's Manual, GT-Suite version 7.3. Gamma Technologies Inc., 2012.
- [4] FIRE 2014 SP2 [DVD]. AVL List GmbH, 2015.
- [5] Morgan M. Andreae, Wai K. Cheng, Thomas Kenney, and Jialin Yang. On hcci engine knock. In *JSAE/SAE International Fuels & Lubricants Meeting*. SAE International, jul 2007. URL: <https://doi.org/10.4271/2007-01-1858>.
- [6] Tanet Aroonsrisopon, Philipp Werner, John O. Waldman, Volker Sohm, David E. Foster, Takeshi Morikawa, and Minoru Iida. Expanding the hcci operation with the charge stratification. In *SAE 2004 World Congress Exhibition*. SAE International, mar 2004. URL: <https://doi.org/10.4271/2004-01-1756>.
- [7] William P. Attard and Hugh Blaxill. A single fuel pre-chamber jet ignition powertrain achieving high load, high efficiency and near zero nox emissions, aug 2011. URL: <https://doi.org/10.4271/2011-01-2023>.
- [8] Graz Austria AVL List GmbH. *Evaluation of Combustion Noise from Cylinder Pressure, AVL Combustion Noise Meter 450 manual, 2010*.
- [9] Christian Bach, Christian Lämmle, Rolf Bill, Patrik Soltic, David Dyntar, Philippe Janner, Konstantinos Boulouchos, Chris Onder, Tilo Landenfeld, Lutz Kercher, Oliver Seel, and Jörg D. Baronick. Clean engine vehicle a natural gas driven euro-4/sulev with 30% reduced co2-emissions. In *SAE 2004 World Congress and Exhibition*. SAE International, mar 2004. URL: <https://doi.org/10.4271/2004-01-0645>.

- [10] D.R. Ballal and A. H. Lefebvre. The Influence of Flow Parameters on Minimum Ignition Energy and Quenching Distance, Proceeding of Fifteenth International Symposium on Combustion, pp. 1473-1481, The Combustion Institute, 1974.
- [11] Laura Sophie Baumgartner, Sebastian Wohlgemuth, Sebastian Zirngibl, and Georg Wachtmeister. Investigation of a methane scavenged prechamber for increased efficiency of a lean-burn natural gas engine for automotive applications, apr 2015. URL: <https://doi.org/10.4271/2015-01-0866>.
- [12] Kevin D. Beaty, Rolf Egnell, and Mats Ekelund. Development of a low emission volvo 9.6 liter natural gas fueled bus engine. In *Future Transportation Technology Conference & Exposition*. SAE International, aug 1992. URL: <https://doi.org/10.4271/921554>.
- [13] Edgar Berger, Christian Bock, Hubert Fischer, Manfred Gruber, Gerrit Kiesgen, and Hermann Rottengruber. The new bmw 12-cylinder hydrogen engine as clean efficient and powerful vehicle powertrain. In *2006 FISITA World Automotive Congress*. Society of Automotive Engineers of Japan, oct 2006.
- [14] F. T. BORGHI, T. A. A. MOREIRA, R. WHANCO, J. E. M BARROS, and R. M. VALLE. Aerodynamic in-cylinder flow simulation in an internal combustion engine with torch ignition system. In *23rd SAE Brasil International Congress and Display*. SAE International, sep 2014. URL: <https://doi.org/10.4271/2014-36-0298>.
- [15] J. Boyde. GT-Power to enhance Single Cylinder Measurements, GT-User Conference, MTU Friedrichshafen GmbH, 2015. URL: [https://www.gtisoft.com/wp-content/uploads/2015/11/Enhance\\_Single\\_Cylinder\\_Measurements.pdf](https://www.gtisoft.com/wp-content/uploads/2015/11/Enhance_Single_Cylinder_Measurements.pdf).
- [16] Alasdair Cairns and Hugh Blaxill. The effects of combined internal and external exhaust gas recirculation on gasoline controlled auto-ignition. In *SAE 2005 World Congress and Exhibition*. SAE International, apr 2005. URL: <https://doi.org/10.4271/2005-01-0133>.
- [17] Junseok Chang, Orgun Güralp, Zoran Filipi, Dennis N. Assanis, Tang-Wei Kuo, Paul Najt, and Rod Rask. New heat transfer correlation for an hcci engine derived from measurements of instantaneous surface heat flux. In *2004 Powertrain & Fluid Systems Conference & Exhibition*. SAE International, oct 2004. URL: <https://doi.org/10.4271/2004-01-2996>.

- [18] Kwang Min Chun and John B. Heywood. Characterization of knock in a spark-ignition engine. In *SAE International Congress and Exposition*. SAE International, feb 1989. URL: <https://doi.org/10.4271/890156>.
- [19] Stefan Danner and Sigmund Fuerst. Bmw hydrogen 7 series a safe way to a clean future. In *2006 FISITA World Automotive Congress*. Society of Automotive Engineers of Japan, oct 2006.
- [20] John E. Dec and Yi Yang. Boosted hcci for high power without engine knock and with ultra-low nox emissions - using conventional gasoline, apr 2010. URL: <https://doi.org/10.4271/2010-01-1086>.
- [21] Adam B. Dempsey and Rolf D. Reitz. Computational optimization of a heavy-duty compression ignition engine fueled with conventional gasoline, apr 2011. URL: <https://doi.org/10.4271/2011-01-0356>.
- [22] Vit Dolecek, Jiri Vavra, and Marcel Skarohlid. Optimized driving cycle oriented control for a highly turbocharged gas engine. In *WCX SAE World Congress Experience*. SAE International, apr 2019. doi:<https://doi.org/10.4271/2019-01-0193>.
- [23] V. Doleček and J. Vávra. Development of pure cng vehicle supported by a 1d simulations of driving cycle  $co_2$  emissions. *L. International Scientific Conference of Czech and Slovak Universities and Institutions Dealing with Motor Vehicles and Internal Combustion Engines Research*, 2019.
- [24] J. A. Eng. Characterization of pressure waves in hcci combustion. In *SAE Powertrain and Fluid Systems Conference and Exhibition*. SAE International, oct 2002. URL: <https://doi.org/10.4271/2002-01-2859>.
- [25] J. T. Farrell, J. G. Stevens, and W. Weissman. A second law analysis of high efficiency low emission gasoline engine concepts. In *SAE 2006 World Congress & Exhibition*. SAE International, apr 2006. doi:<https://doi.org/10.4271/2006-01-0491>.
- [26] M. Ferrera. Cng 2.0. in *CO2 Reduction for Transportation Systems Conference*, 2019.
- [27] Russell P. Fitzgerald, Richard Steeper, Jordan Snyder, Ronald Hanson, and Randy Hessel. Determination of cycle temperatures and residual gas fraction for hcci negative valve overlap operation, apr 2010. URL: <https://doi.org/10.4271/2010-01-0343>.

- [28] José Geiger, Stefan Pischinger, Robert Böwing, Hans-Jürgen Koß, and Jörg Thiemann. Ignition systems for highly diluted mixtures in si-engines. In *International Congress & Exposition*. SAE International, mar 1999. URL: <https://doi.org/10.4271/1999-01-0799>.
- [29] Ravi Gopalakrishnan, M.J. Throop, Alan Richardson, and John Lapetz. Engineering the ford h2 ic engine powered e-450 shuttle bus. In *Powertrain & Fluid Systems Conference and Exhibition*. SAE International, oct 2007. URL: <https://doi.org/10.4271/2007-01-4095>.
- [30] Börje Grandin, Ingemar Denbratt, Joakim Bood, Christian Brackmann, and Per-Erik Bengtsson. The effect of knock on the heat transfer in an si engine: Thermal boundary layer investigation using cars temperature measurements and heat flux measurements. In *International Fuels & Lubricants Meeting & Exposition*. SAE International, oct 2000. URL: <https://doi.org/10.4271/2000-01-2831>.
- [31] Göran Haraldsson, Per Tunestål, Bengt Johansson, and Jari Hyvönen. Hcci combustion phasing with closed-loop combustion control using variable compression ratio in a multi cylinder engine. In *2003 JSAE/SAE International Spring Fuels and Lubricants Meeting*. SAE International, may 2003. URL: <https://doi.org/10.4271/2003-01-1830>.
- [32] E. Hellström, A. Stefanopoulou, J. Vávra, A. Babajimopoulos, D. Assanis, L. Jiang, and H.: Yilmaz. Understanding the dynamic evolution of cyclic variability at the operating limits of hcci engines with negative valve overlap. *SAE Technical Paper 2012-01-1106*, 2012. doi:10.4271/2012-01-1106.
- [33] John B. Heywood. *Internal Combustion Engine Fundamentals*. New York: McGraw-Hill, 1998.
- [34] J. Hvězda, Z. Syrovátka, M. Takáts, and J. Vávra. Evaluation of ignition pre-chamber geometry by multi-zone model of combustion, koka 2017 - xlviii. international scientific conference of the czech and slovak universities and institutions dealing with research of internal combustion engines. 2017. pp. 12-22. isbn 978-80-7494-354-6.
- [35] Jari Hyvönen, Göran Haraldsson, and Bengt Johansson. Supercharging hcci to extend the operating range in a multi-cylinder vcr-hcci engine. In *SAE Powertrain Fluid Systems Conference Exhibition*. SAE International, oct 2003. URL: <https://doi.org/10.4271/2003-01-3214>.
- [36] Jari Hyvönen, Göran Haraldsson, and Bengt Johansson. Operating conditions using spark assisted hcci combustion during combustion mode transfer

- to si in a multi-cylinder vcr-hcci engine. In *SAE 2005 World Congress and Exhibition*. SAE International, apr 2005. URL: <https://doi.org/10.4271/2005-01-0109>.
- [37] R.I Issa. Solution of the implicitly discretised fluid flow equations by operator-splitting. *Journal of Computational Physics*, 62(1):40 – 65, 1986. URL: <http://www.sciencedirect.com/science/article/pii/0021999186900999>, doi:[https://doi.org/10.1016/0021-9991\(86\)90099-9](https://doi.org/10.1016/0021-9991(86)90099-9).
- [38] Sury A. Janarthanam, John R. Blankenship, Richard E. Soltis, Steve J. Szwabowski, and Arun K. Jaura. Architecture and development of a hydrogen sensing and mitigation system in h2rv - ford’s concept hev propelled with a hydrogen engine. In *SAE 2004 World Congress & Exhibition*. SAE International, mar 2004. URL: <https://doi.org/10.4271/2004-01-0359>.
- [39] Ming Jia, Maozhao Xie, and Zhijun Peng. Prediction of the operating range for a hcci engine based on a multi-zone model. In *2008 SAE International Powertrains, Fuels and Lubricants Congress*. SAE International, jun 2008. URL: <https://doi.org/10.4271/2008-01-1663>.
- [40] Thomas Johansson, Bengt Johansson, Per Tunestål, and Hans Aulin. Hcci operating range in a turbo-charged multi cylinder engine with vvt and spray-guided di. In *SAE World Congress & Exhibition*. SAE International, apr 2009. URL: <https://doi.org/10.4271/2009-01-0494>.
- [41] E. W. Kaiser, J Yang, T Culp, N Xu, and M. M. Maricq. Homogeneous charge compression ignition engine-out emission-does flame propagation occur in homogeneous charge compression ignition? *International Journal of Engine Research*, 3(4):185–195, 2002. doi:10.1243/146808702762230897.
- [42] N Kallian, H Zhao, and C Yang. Effects of spark-assistance on controlled auto-ignition combustion at different injection timings in a multicylinder direct-injection gasoline engine. *International Journal of Engine Research*, 10(3):133–148, 2009. doi:10.1243/14680874JER03209.
- [43] Yasuharu Kawabata and Daichi Mori. Combustion diagnostics & improvement of a prechamber lean-burn natural gas engine. In *SAE 2004 World Congress & Exhibition*. SAE International, mar 2004. URL: <https://doi.org/10.4271/2004-01-0979>.
- [44] Gerrit Kiesgen, Manfred Klütting, Christian Bock, and Hubert Fischer. The new 12-cylinder hydrogen engine in the 7 series: The h2 ice age has begun. In *SAE 2006 World Congress & Exhibition*. SAE International, apr 2006. URL: <https://doi.org/10.4271/2006-01-0431>.

- [45] H. Kobayashi, F. Ham, and X. Wu. Application of a local sgs model based on coherent structures to complex geometries. *International Journal of Heat and Fluid Flow*, 29(3):640 – 653, 2008. The Fifth International Symposium on Turbulence and Shear Flow Phenomena (TSFP5). URL: <http://www.sciencedirect.com/science/article/pii/S0142727X08000313>, doi: <https://doi.org/10.1016/j.ijheatfluidflow.2008.02.008>.
- [46] Hiromichi Kobayashi. The subgrid-scale models based on coherent structures for rotating homogeneous turbulence and turbulent channel flow. *Physics of Fluids*, 17(4):045104, 2005. arXiv:<https://doi.org/10.1063/1.1874212>, doi:10.1063/1.1874212.
- [47] G. König and C. G. W. Sheppard. End gas autoignition and knock in a spark ignition engine. In *International Fuels & Lubricants Meeting & Exposition*. SAE International, oct 1990. URL: <https://doi.org/10.4271/902135>.
- [48] G. König, R. R. Maly, D. Bradley, A. K. C. Lau, and C. G. W. Sheppard. Role of exothermic centres on knock initiation and knock damage. In *International Fuels & Lubricants Meeting & Exposition*. SAE International, oct 1990. URL: <https://doi.org/10.4271/902136>.
- [49] George A. Lavoie, J. Martz, M. Wooldridge, and D. Assanis. A multi-mode combustion diagram for spark assisted compression ignition. *Combustion and Flame*, 157(6):1106 – 1110, 2010. URL: <http://www.sciencedirect.com/science/article/pii/S0010218010000556>, doi: <https://doi.org/10.1016/j.combustflame.2010.02.009>.
- [50] George A Lavoie, Elliott Ortiz-Soto, Aristotelis Babajimopoulos, Jason B Martz, and Dennis N Assanis. Thermodynamic sweet spot for high-efficiency, dilute, boosted gasoline engines. *International Journal of Engine Research*, 14(3):260–278, 2013. URL: <https://doi.org/10.1468087412455372>.
- [51] M. Lesieur, O. Métais, and P. Comte. *Large-Eddy Simulations of Turbulence*. Cambridge University Press, 2005. doi:10.1017/CB09780511755507.
- [52] Laura Manofsky, Jiri Vavra, Dennis N. Assanis, and Aristotelis Babajimopoulos. Bridging the gap between hcci and si: Spark-assisted compression ignition. In *SAE 2011 World Congress and Exhibition*. SAE International, apr 2011. URL: <https://doi.org/10.4271/2011-01-1179>.
- [53] Nicholas S. Matthias, Thomas Wallner, and Riccardo Scarcelli. A hydrogen direct injection engine concept that exceeds u.s. doe light-duty efficiency targets, apr 2012. URL: <https://doi.org/10.4271/2012-01-0653>.

- [54] Daniel Mohr, Timothy Shipp, and Xueting Lu. The thermodynamic design, analysis and test of cummins' supertruck 2 50% brake thermal efficiency engine system. In *WCX SAE World Congress Experience*. SAE International, apr 2019. URL: <https://doi.org/10.4271/2019-01-0247>.
- [55] R. J. Natkin, A. R. Denlinger, M. A. Younkins, A. Z. Weimer, S. Hashemi, and A. T. Vaught. Ford 6.8l hydrogen ic engine for the e-450 shuttle van. In *Powertrain & Fluid Systems Conference and Exhibition*. SAE International, oct 2007. URL: <https://doi.org/10.4271/2007-01-4096>.
- [56] Laura Manofsky Olesky, Jiri Vavra, Dennis Assanis, and Aristotelis Babajimopoulos. Effects of Charge Preheating Methods on the Combustion Phasing Limitations of an HCCI Engine With Negative Valve Overlap. *Journal of Engineering for Gas Turbines and Power*, 134(11), 09 2012. 112801. arXiv:[https://asmedigitalcollection.asme.org/gasturbinespower/article-pdf/134/11/112801/5894335/112801\\_1.pdf](https://asmedigitalcollection.asme.org/gasturbinespower/article-pdf/134/11/112801/5894335/112801_1.pdf), doi:10.1115/1.4007319.
- [57] Jan-Ola Olsson, Per Tunestål, and Bengt Johansson. Boosting for high load hcci. In *SAE 2004 World Congress and Exhibition*. SAE International, mar 2004. URL: <https://doi.org/10.4271/2004-01-0940>.
- [58] E.A. Ortiz-Soto, J. Vávra, and A.: Babajimopoulos. Assessment of residual mass estimation methods for cylinder pressure heat release analysis of hcci engines with negative valve overlap. *Journal of Engineering for Gas Turbines and Power*, 134(8), 2012. doi:10.1115/1.4006701.
- [59] Gary J. Patterson and Richard S. Davis. Geometric and topological considerations to maximize remotely mounted cylinder pressure transducer data quality, apr 2009. URL: <https://doi.org/10.4271/2009-01-0644>.
- [60] H. Persson, A. Hultqvist, B. Johansson, and A. Remón. Investigation of the early flame development in spark assisted hcci combustion using high speed chemiluminescence imaging. In *SAE World Congress and Exhibition*. SAE International, apr 2007. URL: <https://doi.org/10.4271/2007-01-0212>.
- [61] Ludek Pohorelsky, Pavel Brynych, Jan Macek, Pierre-Yves Vallaude, Jean-Charles Ricaud, Philippe Obernesser, and Pascal Tribotté. Air system conception for a downsized two-stroke diesel engine. In *SAE 2012 World Congress & Exhibition*. SAE International, apr 2012. URL: <https://doi.org/10.4271/2012-01-0831>.
- [62] Andrew L. Randolph. Cylinder-pressure-transducer mounting techniques to maximize data accuracy. In *International Congress & Exposition*. SAE International, feb 1990. URL: <https://doi.org/10.4271/900171>.

- [63] S. Richard, O. Colin, O. Vermorel, A. Benkenida, C. Angelberger, and D. Veynante. Towards large eddy simulation of combustion in spark ignition engines. *Proceedings of the Combustion Institute*, 31(2):3059 – 3066, 2007. URL: <http://www.sciencedirect.com/science/article/pii/S1540748906001040>, doi:<https://doi.org/10.1016/j.proci.2006.07.086>.
- [64] M. F. Russell and R. Haworth. Combustion noise from high speed direct injection diesel engines. In *SAE Surface Vehicle Noise and Vibration Conference*. SAE International, may 1985. URL: <https://doi.org/10.4271/850973>.
- [65] M. Ruth. Vehicle technologies office merit review 2018:cummins-peterbilt supertruck ii,” in 2018 doe vehicle technologies office annual merit review and peer evaluation meeting about advanced combustion systems, jun. 2018. URL: [www.energy.gov/sites/prod/files/2018/06/f52/acs102\\_ruth\\_2018\\_o.pdf](http://www.energy.gov/sites/prod/files/2018/06/f52/acs102_ruth_2018_o.pdf).
- [66] Ashish Shah, Per Tunestål, and Bengt Johansson. Cfd simulations of pre-chamber jets’ mixing characteristics in a heavy duty natural gas engine. In *JSAE/SAE 2015 International Powertrains, Fuels & Lubricants Meeting*. SAE International, sep 2015. URL: <https://doi.org/10.4271/2015-01-1890>.
- [67] Magnus Sjöberg and John E. Dec. An investigation of the relationship between measured intake temperature, bdc temperature, and combustion phasing for premixed and di hcci engines. In *2004 SAE Fuels and Lubricants Meeting and Exhibition*. SAE International, jun 2004. URL: <https://doi.org/10.4271/2004-01-1900>.
- [68] Magnus Sjöberg and John E. Dec. Effects of engine speed, fueling rate, and combustion phasing on the thermal stratification required to limit hcci knocking intensity. In *2005 SAE Brasil Fuels & Lubricants Meeting*. SAE International, may 2005. URL: <https://doi.org/10.4271/2005-01-2125>.
- [69] L. Souček. *Nepřímý zážeh pro průmyslový plynový motor, Diploma Thesis No. D93-M15*. Faculty of Mechanical Engineering, Czech Technical University in Prague, Prague, 1993.
- [70] Donald L. Stivender. Development of a fuel-based mass emission measurement procedure. In *International Mid-Year Meeting*. SAE International, feb 1971. URL: <https://doi.org/10.4271/710604>.
- [71] William F. Stockhausen, Robert J. Natkin, Daniel M. Kabat, Lowell Reams, Xiaoguo Tang, Siamak Hashemi, Steven J. Szwabowski, and Vance P. Za-



- nardelli. Ford p2000 hydrogen engine design and vehicle development program. In *SAE 2002 World Congress & Exhibition*. SAE International, mar 2002. URL: <https://doi.org/10.4271/2002-01-0240>.
- [72] Michalis Syrimis, Kei Shigahara, and Dennis N. Assanis. Correlation between knock intensity and heat transfer under light and heavy knocking conditions in a spark ignition engine. In *International Congress & Exposition*. SAE International, feb 1996. URL: <https://doi.org/10.4271/960495>.
- [73] Z. Syrovatka, M. Takats, and J.: Vávra. Analysis of scavenged pre-chamber for light duty truck gas engine. *SAE Technical Paper 2017-24-0095*, 2017-September(September), 2017. doi:10.4271/2017-24-0095.
- [74] Steven J. Szwabowski, Siamak Hashemi, William F. Stockhausen, Robert J. Natkin, Lowell Reams, Daniel M. Kabat, and Curtis Potts. Ford hydrogen engine powered p2000 vehicle. In *SAE 2002 World Congress & Exhibition*. SAE International, mar 2002. URL: <https://doi.org/10.4271/2002-01-0243>.
- [75] James P. Szybist, Eric Nafziger, and Adam Weall. Load expansion of stoichiometric hcci using spark assist and hydraulic valve actuation, oct 2010. URL: <https://doi.org/10.4271/2010-01-2172>.
- [76] Xiaoguo Tang, Daniel M. Kabat, Robert J. Natkin, William F. Stockhausen, and James Heffel. Ford p2000 hydrogen engine dynamometer development. In *SAE 2002 World Congress & Exhibition*. SAE International, mar 2002. URL: <https://doi.org/10.4271/2002-01-0242>.
- [77] Reinhard Tatschl, Michael Bogensperger, Zoran Pavlovic, Peter Priesching, Henrik Schuemie, Oldrich Vitek, and Jan Macek. Les simulation of flame propagation in a direct-injection si-engine to identify the causes of cycle-to-cycle combustion variations. In *SAE 2013 World Congress & Exhibition*. SAE International, apr 2013. URL: <https://doi.org/10.4271/2013-01-1084>.
- [78] Bryce Charles Thelen and Elisa Toulson. A computational study of the effects of spark location on the performance of a turbulent jet ignition system. In *SAE 2016 World Congress and Exhibition*. SAE International, apr 2016. URL: <https://doi.org/10.4271/2016-01-0608>.
- [79] R. Toman and J. Macek. Evaluation of the predictive capabilities of a phenomenological combustion model for natural gas si engine, journal of middle european construction and design of cars, 15(2), 37-48., 2017. URL: doi:<https://doi.org/10.1515/mecdc-2017-0007>.

- [80] Elisa Toulson, Harold J. Schock, and William P. Attard. A review of pre-chamber initiated jet ignition combustion systems. In *SAE 2010 Powertrains Fuels & Lubricants Meeting*. SAE International, oct 2010. URL: <https://doi.org/10.4271/2010-01-2263>.
- [81] Tomonori Urushihara, Koichi Yamaguchi, Koudai Yoshizawa, and Teruyuki Itoh. A study of a gasoline-fueled compression ignition engine - expansion of hcci operation range using si combustion as a trigger of compression ignition -. In *SAE 2005 World Congress and Exhibition*. SAE International, apr 2005. URL: <https://doi.org/10.4271/2005-01-0180>.
- [82] J. Vávra, Z. Syrovátka, O. Vitek, J. Macek, and M.: Takáts. Development of a pre-chamber ignition system for light duty truck engine. *SAE Technical Paper 2018-01-1147*, 2018-April, 2018. doi:10.4271/2018-01-1147.
- [83] Jiri Vavra, Stanislav V. Bohac, Laura Manofsky, George Lavoie, and Dennis Assanis. Knock In Various Combustion Modes in a Gasoline-Fueled Automotive Engine. *Journal of Engineering for Gas Turbines and Power*, 134(8), 06 2012. 082807. URL: <https://doi.org/10.1115/1.4006694>.
- [84] Jiri Vavra, Michal Takats, Vojtech Klir, and Marcel Skarohlid. Influence of natural gas composition on turbocharged stoichiometric si engine performance. In *SAE 2012 International Powertrains, Fuels & Lubricants Meeting*. SAE International, sep 2012. URL: <https://doi.org/10.4271/2012-01-1647>.
- [85] Oldrich Vitek, Jan Macek, Reinhard Tatschl, Zoran Pavlovic, and Peter Priesching. Les simulation of direct injection si-engine in-cylinder flow. In *SAE 2012 World Congress & Exhibition*. SAE International, apr 2012. URL: <https://doi.org/10.4271/2012-01-0138>.
- [86] J. Vávra, M. Takáts, and S. Bohac. Mixture dilution on a natural gas si engine operating at low load. *MECCA, Journal of Middle European Construction and Design of Cars*, 2014. doi:10.2478/mecdc-2014-0007.
- [87] O. Vitek, V. Doleček, Z. Syrovátka, and J. Macek. Identification of cycle-to-cycle variability sources in si ice based on cfd modeling”, mecca journal of middle european construction and design of cars., 2018, XVI(01), ISSN 1214-0821.
- [88] Oldřich Vitek, Jan Macek, and Miloš Polášek. Simulation of pre-chambers in an engine combustion chamber using available software. In *SAE 2003 World Congress & Exhibition*. SAE International, mar 2003. URL: <https://doi.org/10.4271/2003-01-0373>.

- [89] Robert M. Wagner, K. Dean Edwards, C. Stuart Daw, Johnney B. Green, and Bruce G. Bunting. On the nature of cyclic dispersion in spark assisted hcci combustion. In *SAE 2006 World Congress and Exhibition*. SAE International, apr 2006. URL: <https://doi.org/10.4271/2006-01-0418>.
- [90] Thomas Wallner, Hennning Lohse-Busch, Stephen Gurski, Mike Duoba, Wolfgang Thiel, Dieter Martin, and Thomas Korn. Fuel economy and emissions evaluation of bmw hydrogen 7 mono-fuel demonstration vehicles. *International Journal of Hydrogen Energy*, 33(24):7607 – 7618, 2008. URL: <http://www.sciencedirect.com/science/article/pii/S0360319908011439>, doi: <https://doi.org/10.1016/j.ijhydene.2008.08.067>.
- [91] Willson B. Walter T., Gossweiler C. *Pressure Sensors, Application of an Improved Model for the Determination of Acoustic Resonances in Indication Passages for Combustion Pressure Measurements in Large Bore Gas Engines, Kistler Special Print 920-352e-02.07*.
- [92] Z. Wang, J. Wang, S. Shuai, X. He, F. Xu, D. Yang, and X. Ma. Research on spark induced compression ignition (sici). In *SAE World Congress & Exhibition*. SAE International, apr 2009. URL: <https://doi.org/10.4271/2009-01-0132>.
- [93] Zhi Wang, Jian-Xin Wang, Shi-Jin Shuai, Guo-Hong Tian, Xinliang An, and Qing-Jun Ma. Study of the effect of spark ignition on gasoline hcci combustion. *Proceedings of the Institution of Mechanical Engineers, Part D: Journal of Automobile Engineering*, 220(6):817–825, 2006. URL: <https://doi.org/10.1243/09544070JAUT0151>.
- [94] Rikard Wellander, Joakim Rosell, Mattias Richter, Marcus Alden, Oivind Andersson, Bengt Johansson, Jeudi Duong, and Jari Hyvonen. Study of the early flame development in a spark-ignited lean burn four-stroke large bore gas engine by fuel tracer plif, apr 2014. URL: <https://doi.org/10.4271/2014-01-1330>.
- [95] G. Woschni. A universally applicable equation for the instantaneous heat transfer coefficient in the internal combustion engine. In *National Fuels and Lubricants, Powerplants, Transportation Meetings*. SAE International, feb 1967. URL: <https://doi.org/10.4271/670931>.
- [96] Hanho Yun, Nicole Wermuth, and Paul Najt. Extending the high load operating limit of a naturally-aspirated gasoline hcci combustion engine, apr 2010. URL: <https://doi.org/10.4271/2010-01-0847>.

- [97] Y. B. Zeldovich, P. Y. Sadovnikov, and D. A. Frank-Kamenetskii. Oxidation of Nitrogen in Combustion. Translation by M. Shelef, Academy of Sciences of USSR, Institute of Chemical Physics, Moscow-Leningrad, 1947.
- [98] Yuzhong Zhang, Ritesh Gautam, Sudhanshu Pandey, Mark Omara, Joannes D. Maasackers, Pankaj Sadavarte, David Lyon, Hannah Nesser, Melissa P. Sulprizio, Daniel J. Varon, Ruixiong Zhang, Sander Houweling, Daniel Zavala-Araiza, Ramon A. Alvarez, Alba Lorente, Steven P. Hamburg, Ilse Aben, and Daniel J. Jacob. Quantifying methane emissions from the largest oil-producing basin in the united states from space. *Science Advances*, 6(17), 2020. URL: <https://advances.sciencemag.org/content/6/17/eaaz5120>, doi:10.1126/sciadv.aaz5120.
- [99] Hua Zhao, Jian Li, Tom Ma, and Nicos Ladommatos. Performance and analysis of a 4-stroke multi-cylinder gasoline engine with cai combustion. In *SAE 2002 World Congress and Exhibition*. SAE International, mar 2002. URL: <https://doi.org/10.4271/2002-01-0420>.
- [100] B. Zigler. *An experimental investigation of the ignition properties of low temperature combustion in an optical engine*. Dissertation (Ph.D.), University of Michigan, Ann Arbor, Michigan, 2008. URL: <http://hdl.handle.net/2027.42/60655>.

# Annexes

## A UM-FFVA Engine

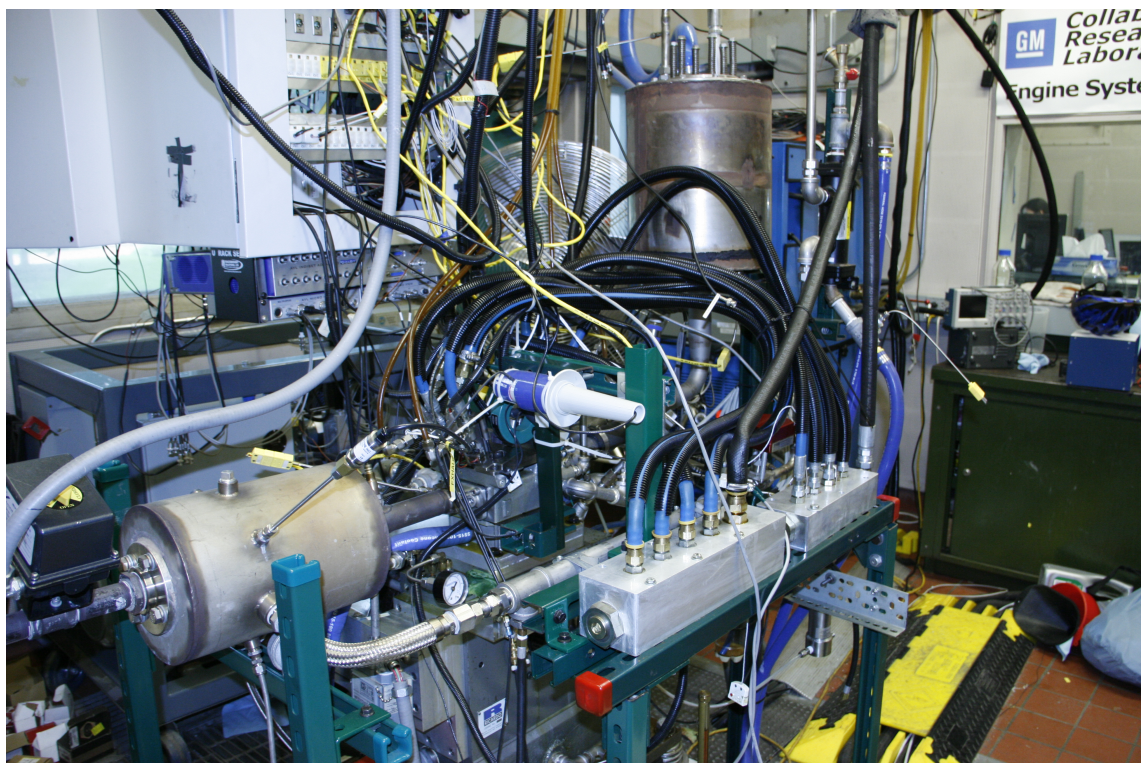


**Figure I:** A FFVA engine test bed, a hydraulic system distribution rail for the Sturman valve system (in front), an exhaust plenum on the left and an egr line.

## B Fuel supply into the pre-chamber

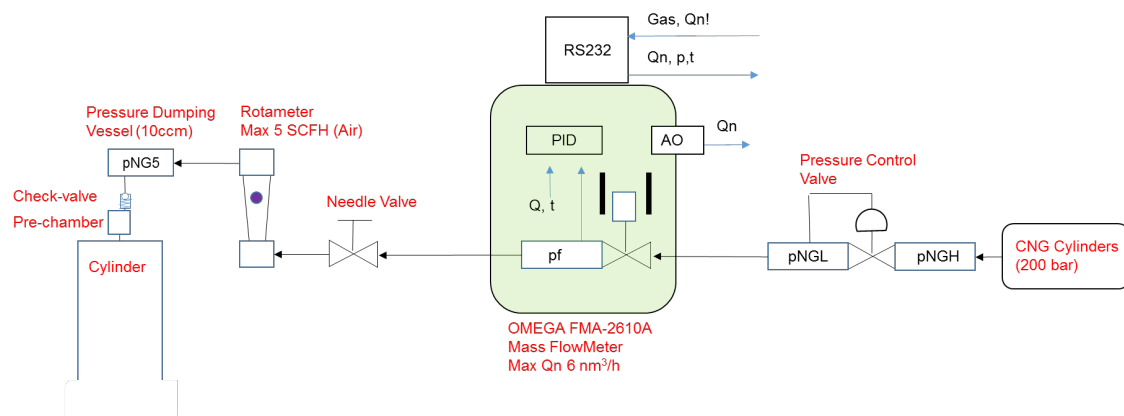


**Figure II:** Schematics of the fuel supply into the pre-chamber.

## C Heat release analysis results for various Lambda values

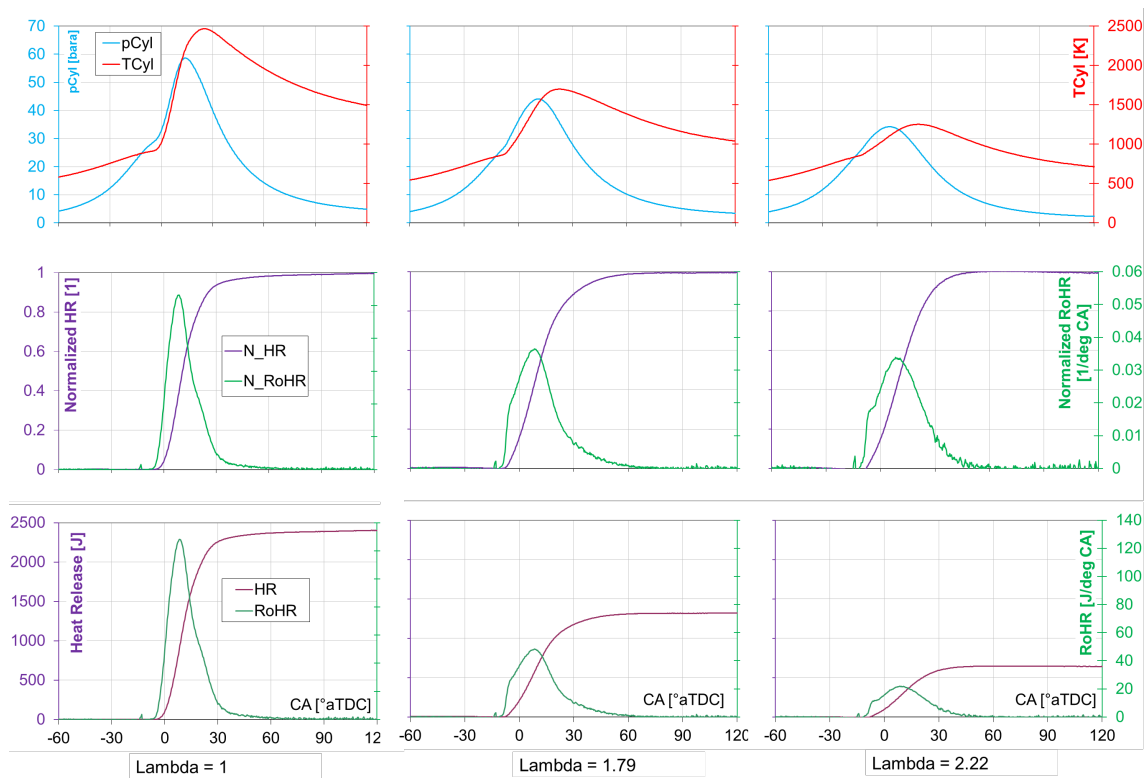


**Figure III:** Heat release analysis results for various Lambda values.

## D Results of natural gas composition analysis

Component	Avg. composition, [% mol.]
carbon dioxide	0.105
nitrogen	0.856
methane	97.098
ethane	1.562
2-methylpropane (i-butane)	0.048
n-butane	0.040
2,2 dimethylpropane (neo-pentane)	0.002
2- methylbutane	0.006
n-pentane	0.004
C6 (sum)	0.003
C7+ (sum)	0.001
Total	100
LHV [MJ/m <sup>3</sup> ], V(15°C, 101.325 kPa)	34.45
HHV [MJ/m <sup>3</sup> ], V(15°C, 101.325 kPa)	38.23

**Table I:** Results of natural gas composition analysis using gas chromatograph HP 6980.



## E Scheme of the GT-power model

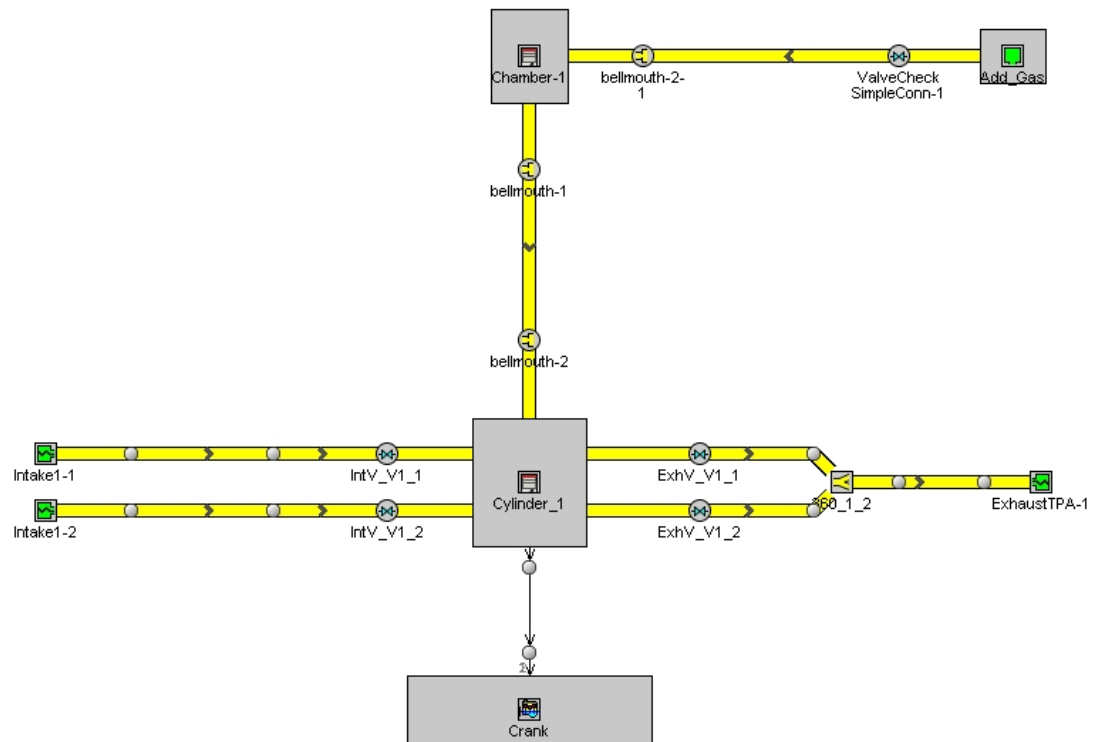


**Figure IV:** Scheme of the GT-power TPA model.

## F Measured traces of ignition energy

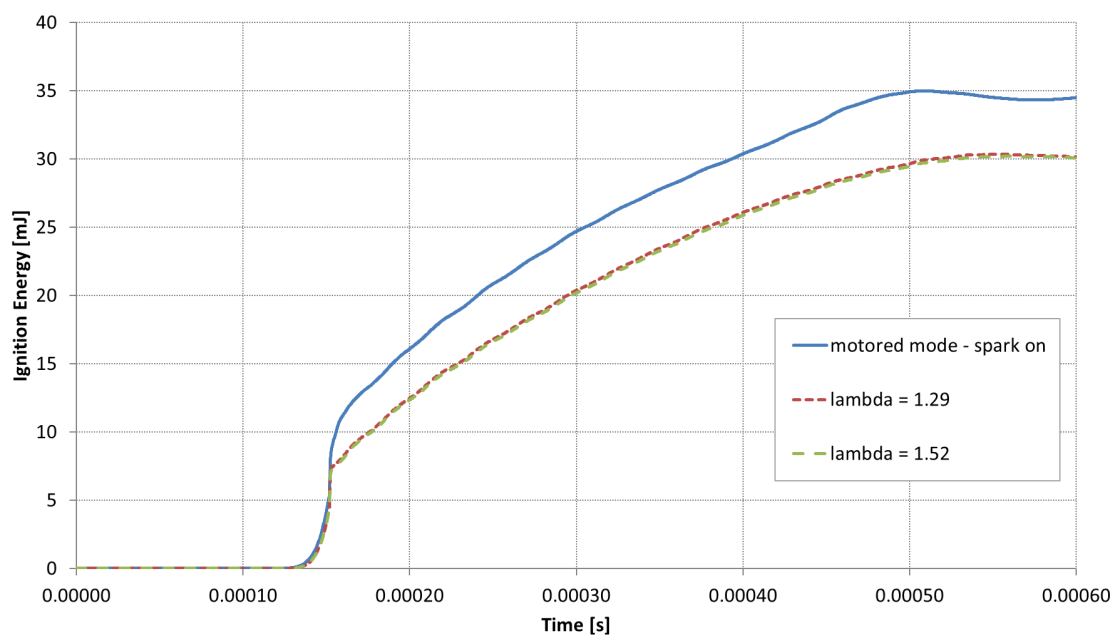


**Figure V:** Comparison of spark energy profiles measured at 1800 rpm and fully open throttle valve for various air excess ratio ( $\lambda$ ). Spark voltage was measured by high voltage probe Tektronics P6015A, the electric current was measured by Pearson Model 110 current probe, connected to digital oscilloscope.

## G CFD Results

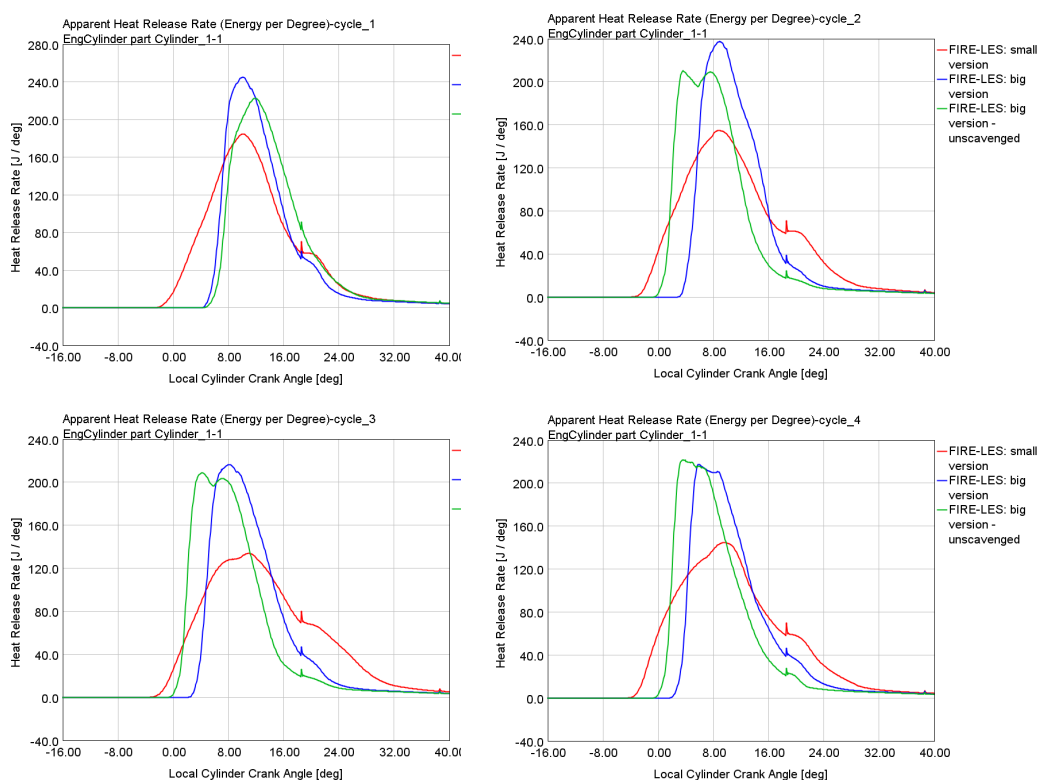


**Figure VI:** Comparison of individual cycle simulation data related to combustion (ROHR) at air excess of 1.0 while comparing different pre-chamber design configurations and scavenging strategies (scavenged/un-scavenged) – top left subfigure corresponds to 1st calculated cycle while bottom right subfigure represents 4th calculated cycle.

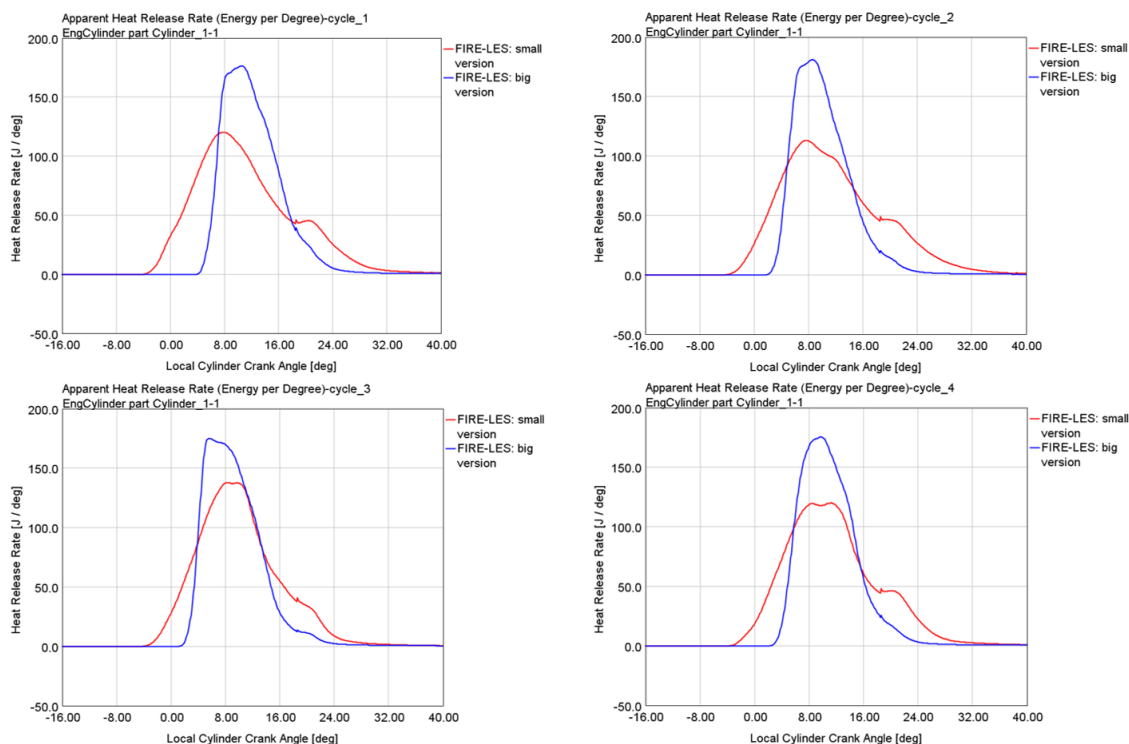


**Figure VII:** Comparison of individual cycle simulation data related to combustion (ROHR) at air excess of 1.5 while comparing different pre-chamber design – top left subfigure corresponds to 1st calculated cycle while bottom right subfigure represents 4th calculated cycle.

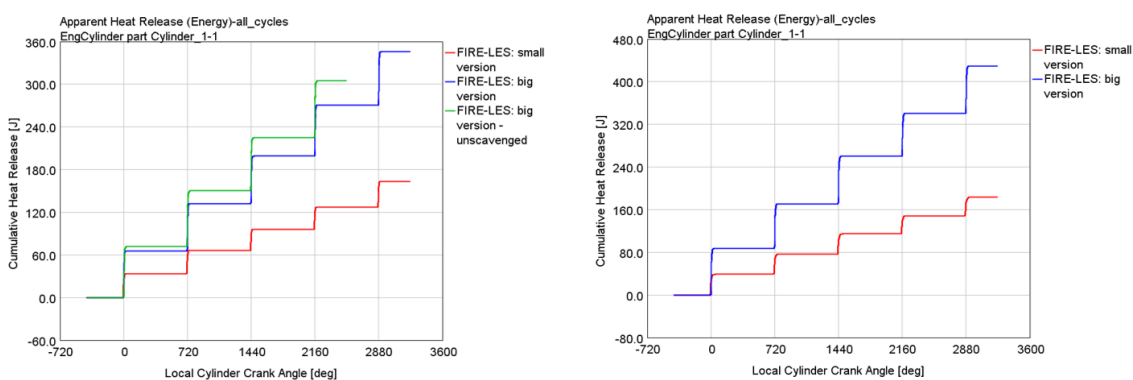


**Figure VIII:** Comparison of cumulative released chemical energy in pre-chamber at air excess of 1.0 (left) and 1.5 (right) while comparing different pre-chamber design configurations – left subfigure corresponds to Fig. VI while right subfigure represents Fig. VII.

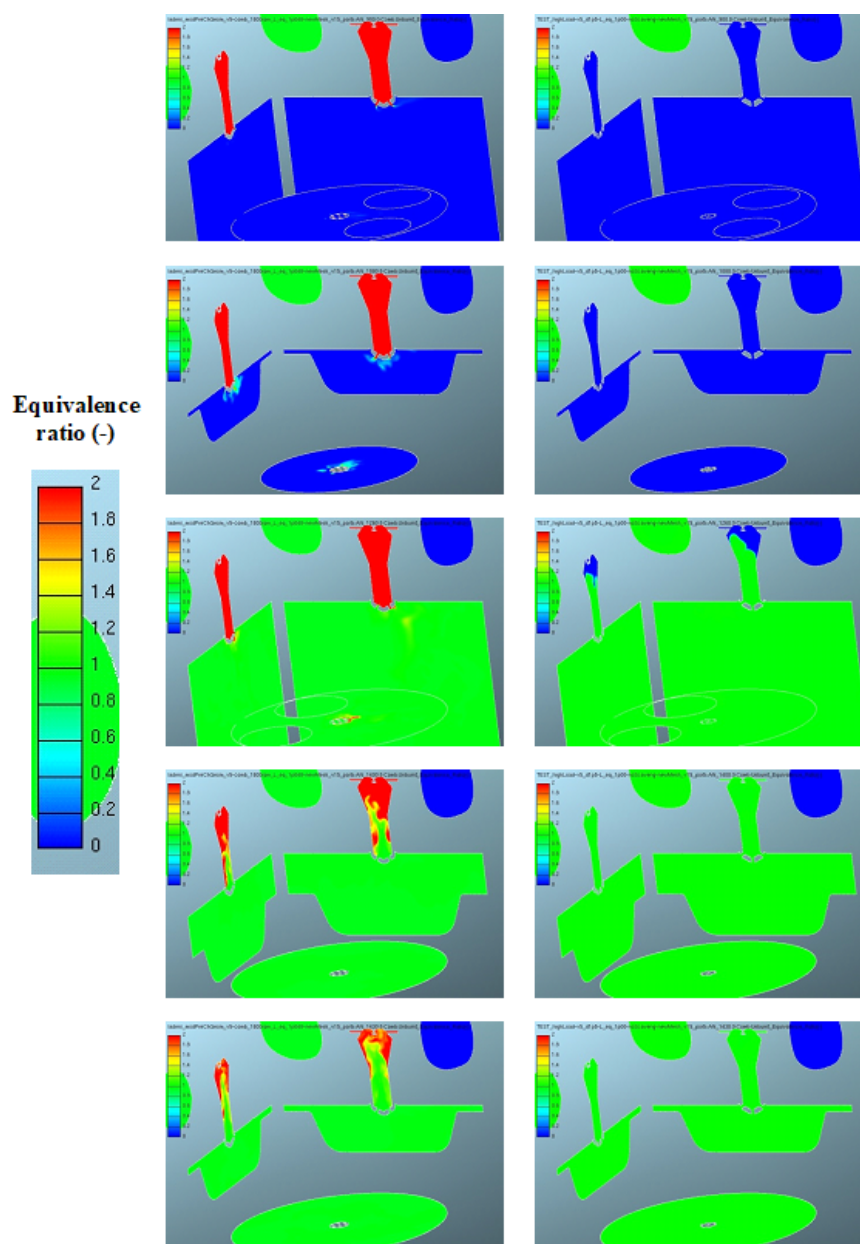


**Figure IX:** Comparison of individual cycle simulation data related to mixing (equivalence ratio as a marker of mixture quality) at air excess of 1.0 while comparing scavenging strategies (scavenged/un-scavenged); presented data correspond to 2nd cycle – left column corresponds to variant ‘big version’, right one to ‘big version – un-scavenged’; 1st row corresponds to 180 °CA, 2nd one to 360 °CA, 3rd one to 540 °CA, 4th one 680 °CA and 5th one to 710 °CA.

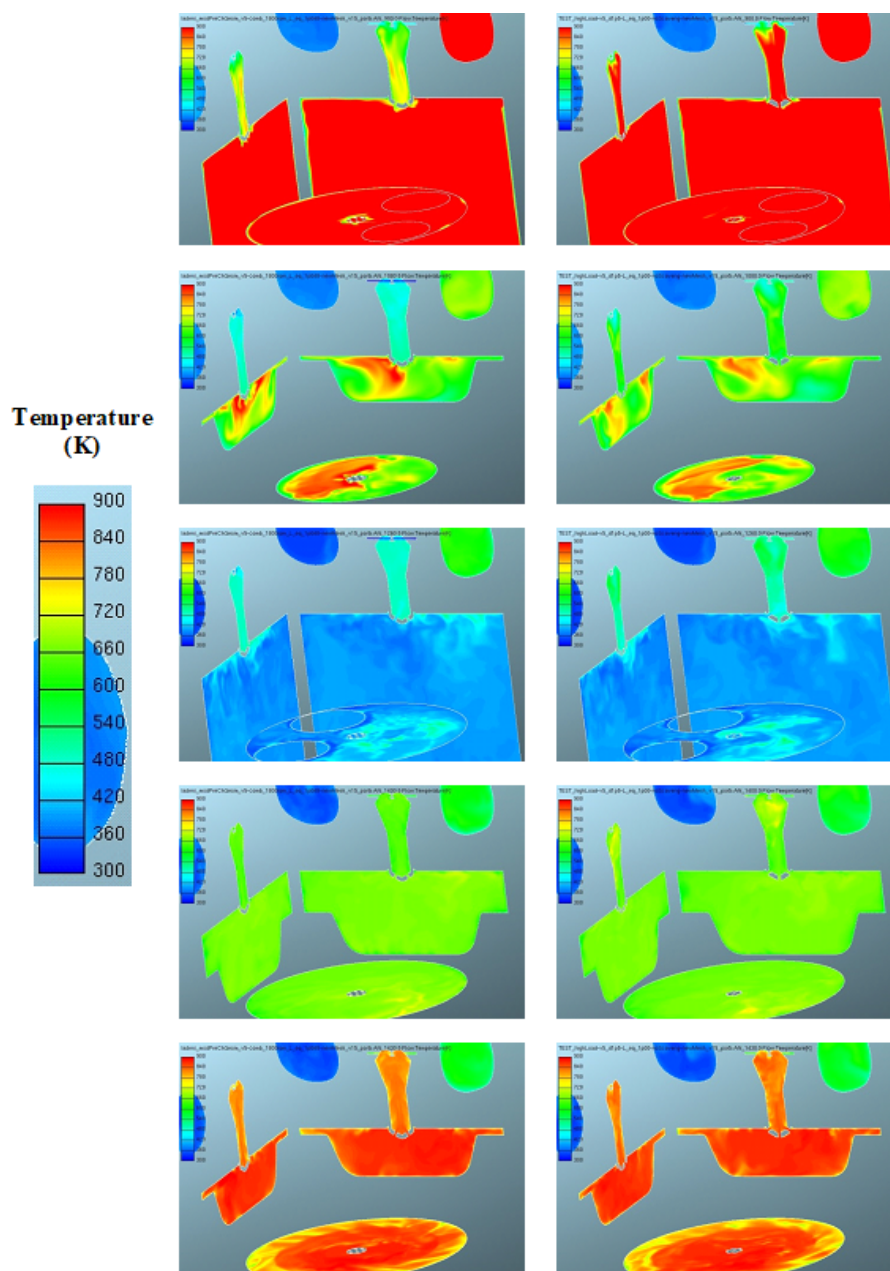


**Figure X:** Comparison of individual cycle simulation data related to heat transfer (local temperature as a marker of heat flux) at air excess of 1.0 while comparing different scavenging strategies (scavenged/un-scavenged); presented data correspond to 2nd cycle – left column corresponds to variant ‘big version’ right one to ‘big version – un-scavenged’; 1st row corresponds to 180 °CA, 2nd one to 360 °CA, 3rd one to 540 °CA, 4th one 680 °CA and 5th one to 710 °CA.

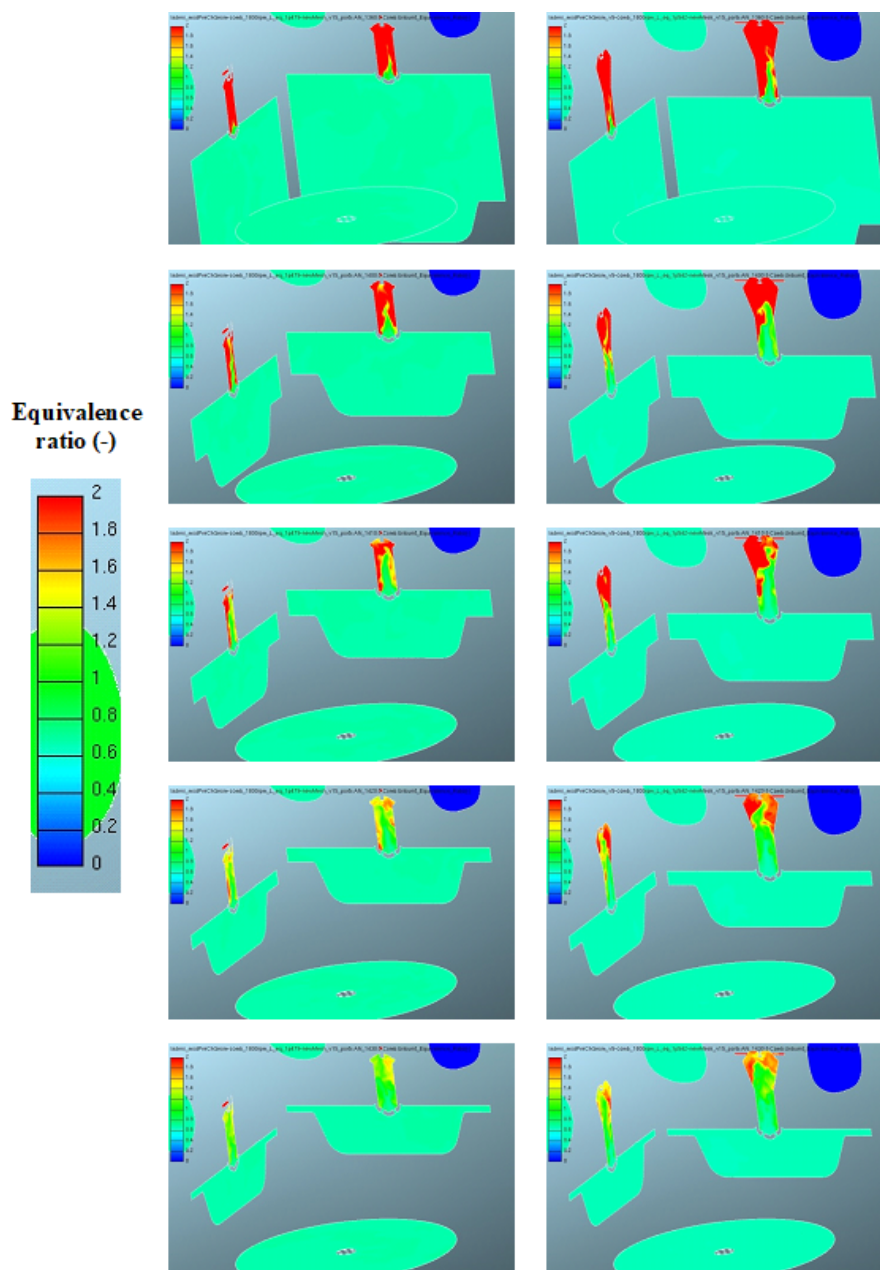


**Figure XI:** Comparison of individual cycle simulation data related to mixing (equivalence ratio as a marker of mixture quality) at air excess of 1.5 while comparing different pre-chamber design configurations; presented data correspond to 2nd cycle – left column corresponds to variant ‘small version’, right one to ‘big version’– 1st row corresponds to 640 °CA, 2nd one to 680 °CA, 3rd one to 690 °CA, 4th one 700 °CA and 5th one to 710 °CA.



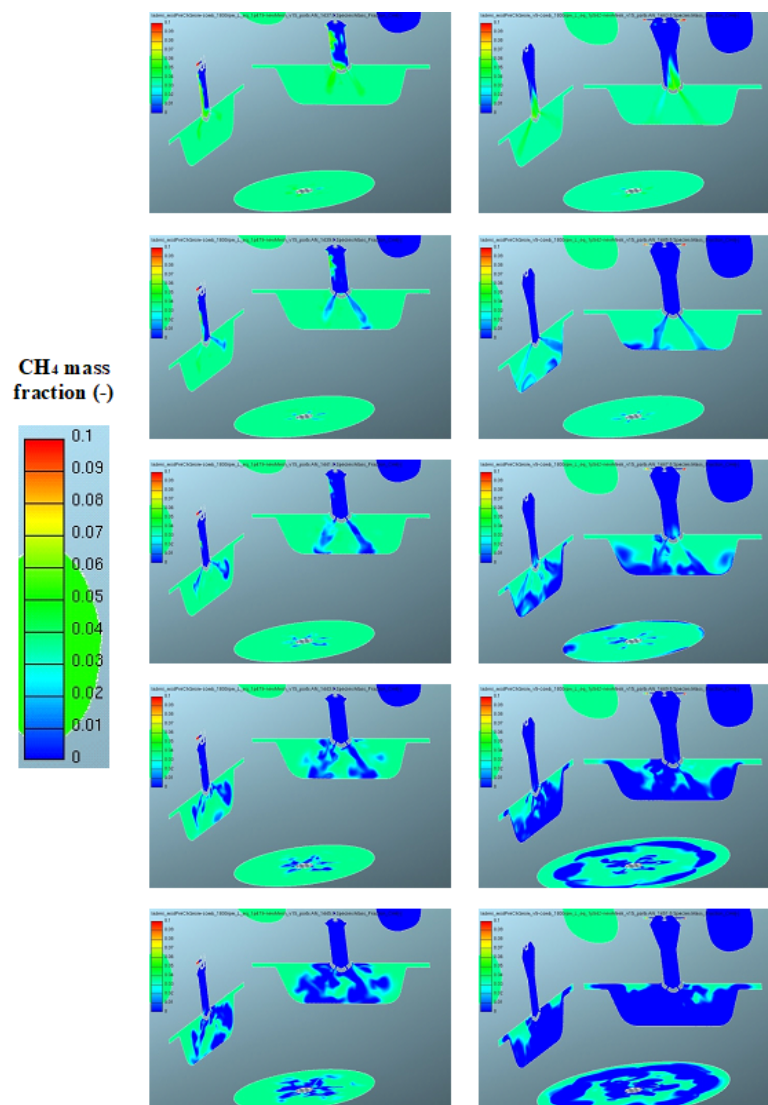


**Figure XII:** Comparison of individual cycle simulation data related to mixing (CH4 mass fraction as a marker of flame – blue color represents burnt zone) at air excess of 1.5 while comparing different pre-chamber design configurations; presented data correspond to 2nd cycle – left column corresponds to variant ‘small version’, right one to ‘big version’ – top row subfigures correspond to early combustion phase (flame front reaches connecting channels in pre-chamber), all other sub-figures represent increase by 2 °CA.



## H Basic properties of various fuels

Fuel	Gasoline A <sup>[33]</sup>	Gasoline B <sup>[33]</sup>	Gasoline E10*	$CH_4$	$H_2$
Carbon mass fraction [kg/kg]	0.865	0.877	0.850	0.750	0.000
Hydrogen mass fraction [kg/kg]	0.135	0.123	0.133	0.250	1.000
Oxygen mass fraction [kg/kg]	0.000	0.000	0.017	0.000	0.000
Oxygen/Fuel stoichio- metric ratio [kg/kg]	3.388	3.324	3.310	4.000	8.000
Air/Fuel sto- ichiometric ratio [kg/kg]	14.640	14.365	14.305	17.285	34.569
Fuel lower calorific value [MJ/kg]	44.000	44.000	41.500	50.042	119.827
Stoichiometric mixture calorific value [MJ/m <sup>3</sup> ]	3.884	3.958	3.749	3.387	3.164

**Table II:** Basic properties of various fuels. \* Composition determined by laboratory analysis.